/N -39
33191

NASA Contractor Report 194457
CU–CSSC–93–06–II

Coupled Structural, Thermal, Phase-Change and Electromagnetic Analysis for Superconductors Volume II

C.A. Felippa, C. Farhat, K.C. Park, C. Militello, and J.J. Schuler
University of Colorado
Boulder, Colorado

January 1996

National Aeronautics and
Space Administration

TABLE OF CONTENTS

VOLUME II

Part I - Parametrized Variational Principles for Linear Electromagnetodynamics.

Part II - Finite Element Analysis of Time-Independent Superconductivity, Ph.D. thesis, Report CU-CSSC-93-02, Center for Space Structures and Control, College of Engineering, University of Colorado, Boulder, Colorado, 1993.

SUMMARY

Described are the theoretical development and computer implementation of reliable and efficient methods for the analysis of coupled mechanical problems that involve the interaction of mechanical, thermal, phase-change and electromagnetic subproblems. The focus application has been the modeling of superconductivity and associated quantum-state phase-change phenomena. In support of this objective the work has addressed the following issues: (1) development of variational principles for finite elements, (2) finite element modeling of the electromagnetic problem, (3) coupling of thermal and mechanical effects, and (4) computer implementation and solution of the superconductivity transition problem. The main accomplishments have been: (1) the development of the theory of parametrized and gauged variational principles, (2) the application of those principled to the construction of electromagnetic, thermal and mechanical finite elements, and (3) the coupling of electromagnetic finite elements with thermal and superconducting effects, and (4) the first detailed finite element simulations of bulk superconductors, in particular the Meissner effect and the nature of the normal conducting boundary layer. The theoretical development is described in two volumes. Volume I describes mostly formulations for specific problems. Volume II describes generalization of those formulations.

PART I

PARAMETRIZED VARIATIONAL PRINCIPLES FOR LINEAR ELECTROMAGNETODYNAMICS

ABSTRACT

Two families of parametrized mixed variational principles for linear electromagnetodynamics are constructed. The first family is applicable when the current density distribution is known *a priori*. Its six independent fields are magnetic intensity and flux density, magnetic potential, electric intensity and flux density and electric potential. Through appropriate specialization of parameters the first principle reduces to more conventional principles proposed in the literature. The second family is appropriate when the current density distribution is an additional unknown, giving a total of seven independently varied fields. In this case it is shown that a conventional variational principle exists only in the time-independent (static) case. Two static functionals with reduced number of varied fields are investigated. The application of one of these principles to construct finite elements with current prediction capabilities is illustrated with a numerical example.

1. INTRODUCTION

The application of energy and variational methods in electromagnetodynamics to construct finite element approximations has not received to date the same level of attention gained in continuum and structural mechanics. Part of this lag can be attributed to the dominance of analytical and semi-analytical methods. Over the past century (since Heaviside's landmark papers) these methods have been refined and tuned to routinely treat special but important classes of application problems such as circuits, antennas and waveguides. The most comprehensive exposition of EM energy methods in book form is that of Hammond [1], who applies these methods to hand-computed Rayleigh-Ritz and Galerkin approximations.

The use of EM finite elements has received modest but increasing attention for calculations that involve multidimensional, complex geometries and intricate field distributions. Much of the work to date appears to have been done in England, most likely because of the strong influence of the Swansea group formerly headed by O. C. Zienkiewicz. The work is well described in survey articles by Davies [2], Trowbridge [3], Simkin and Trowbridge [4] and the textbook by Silvester and Ferrari [5]. The overall impression given by these expositions is that of an unsettled subject, reminiscent of the early period (1955–1968) of finite elements in structural mechanics.[1] A great number of single-field formulations based on flux, intensity, scalar and reduced potentials are described with the recommended choice varying according to the application, medium involved (polarizable, dielectric, semiconductors, etc.) number of space dimensions, temporal variation characteristics (static, quasi-static, harmonic or transient) as well as other factors of lesser importance.

The present work is part of an ongoing research project to develop one- and two-dimensional finite element models for superconductors [6–8]. During the course of this project several variational principles of increasing generality were constructed. This paper presents a partial unification of mixed variational principles for linear electromagnetics. Two families of parametrized variational principles are considered. These two families, identified by the number of independently varied fields in the sequel, are intended for two different types of source data.

The *six-field family* is appropriate when the current density distribution **J** is a source field (that is, is known *a priori*). Its general functional is denoted by

$$R^{(6)}(\mathbf{E}, \mathbf{D}, \mathbf{B}, \mathbf{H}, \mathbf{A}, \Phi), \tag{1}$$

where **E**, **D**, **B** and **H** are the classical electromagnetic fields that appear in Maxwell's equations, and Φ and **A** are the electromagnetic potentials. This functional is found to depend on 21 numerical coefficients that specify the weights of various fields. The coefficients must satisfy 12 consistency constraints, leaving 9 free parameters. Through appropriate specialization of these parameters all specific functionals of this form that contain the potentials **A** and Φ as independent fields can be produced. These functionals are applicable to both static and dynamic problems.

---

[1] For example, mixed multifield variational principles are not mentioned.

The *seven-field family* is a generalization of $R^{(6)}$ that is appropriate when the current density distribution $\mathbf{J}$ is unknown. Its general functional is denoted by

$$R^{(7)}(\mathbf{E}, \mathbf{D}, \mathbf{B}, \mathbf{H}, \mathbf{A}, \Phi, \mathbf{J}). \tag{2}$$

This functional depends on 36 coefficients that must satisfy 24 constraints, apparently leaving 12 free parameters. These constraints, however, can only be fully satisfied only if the system is time-independent; thus a variational principle of the assumed quadratic form exists only in the static case. For the dynamic case a four-field *restricted* variational principle in the sense of Rosen-Prigogine can be readily constructed. For static problems specialized principles with two to four variables are investigated. One of these static principles is applied to the finite element calculation of current distribution in a wire of varying conductivity.

The two families do not exhaust[2] the totality of variational principles for linear electromagnetics because two classes of functionals are excluded:

(I)   Functionals in which the distribution of volume charges is also varied independently are not covered. The techniques of Sections 3 and 4 can be applied to derive an eight-field family that provides a true variational principle for the static case. This principle would have limited practical application, however, because in electrostatics free charges migrate to the surface of conductors; consequently the internal charge distribution is known to be zero. It is doubtful whether conventional principles for the dynamic case exist.

(II)   Functionals that lack the EM potentials $\mathbf{A}$ and Φ as independently varied fields are not covered. These would be analogous to the complementary energy principles of mechanics. Although occasionally used for bound estimation purposes, complementary EM principles lack appeal in our research program because of three reasons: (1) $\mathbf{A}$ and Φ appear naturally in the volume-source and boundary-closure terms, (2) potentials are excellent variables to treat material interface discontinuities in finite element discretizations, and (3) $\mathbf{A}$ is a key variable in superconductor modeling.

Extensions of the present variational principles to nonlinear and coupled-field problems are outlined in the Conclusions. Our main research thrust has been the generalization to the highly nonlinear problem of superconductivity. Such problems usually display a mix of conducting and superconducting regions. As a result the current density varies enormously in space. Finding this distribution, which reflects the separation of the material into normal and superconducting regions, is an essential part of the problem. It follows that the seven-field family is of particular interest as a point of departure for constructing variational principles for superconductors. Such developments will be reported in a sequel paper.

---

[2] Thus the qualification "partial unification" used above.

2. FIELD EQUATIONS

The Maxwell Equations

The Maxwell equations of electromagnetodynamics, developed in the 1860s, are used here in the classical '3+1' format. These equations involve six space-time fields: $\mathbf{B}$, $\mathbf{D}$, $\mathbf{E}$, $\mathbf{H}$, $\mathbf{J}$ and ρ. Vectors $\mathbf{E}$ and $\mathbf{H}$ represent the electric and magnetic field strengths (also called intensities), respectively, whereas $\mathbf{D}$ and $\mathbf{B}$ represent the electric and magnetic flux densities, respectively.[3] All of these are three-vector quantities, that is, vector fields in three-dimensional space ($x_1 \equiv x$, $x_2 \equiv y$ $x_3 \equiv z$):

$$\mathbf{B} = \left\{ \begin{array}{c} B_1 \\ B_2 \\ B_3 \end{array} \right\}, \quad \mathbf{D} = \left\{ \begin{array}{c} D_1 \\ D_2 \\ D_3 \end{array} \right\}, \quad \mathbf{E} = \left\{ \begin{array}{c} E_1 \\ E_2 \\ E_3 \end{array} \right\}, \quad \mathbf{H} = \left\{ \begin{array}{c} H_1 \\ H_2 \\ H_3 \end{array} \right\}. \tag{3}$$

Each component may depend on space and time. Other field quantities are the total current density $\mathbf{J}$ (a three-vector) and the electric free-charge density ρ (a scalar). Using superposed dots to denote differentiation with respect to time t, we can state Maxwell's equations in a *fixed* Galilean frame[4]

$$\boxed{\begin{array}{ll} \nabla \times \mathbf{H} - \dot{\mathbf{D}} = \mathbf{J}, & \nabla \times \mathbf{E} + \dot{\mathbf{B}} = \mathbf{0}, \\ \nabla \cdot \mathbf{B} = 0, & \nabla \cdot \mathbf{D} = \rho, \end{array}} \tag{4}$$

in which the use of a mks-Giorgi system of units is assumed.[5] The first three equations are also called Ampère-Maxwell, Faraday's and Gauss' laws, respectively.

The system (4) supplies a total of eight partial differential equations, which as stated are independent of the properties of the underlying medium. If $\mathbf{J}$ and ρ are prescribed source fields the eight equations are insufficient, however, to determine the twelve spatial components of fields $\mathbf{B}$, $\mathbf{D}$, $\mathbf{E}$ and $\mathbf{H}$.

Constitutive Equations

The field intensities $\mathbf{E}$ and $\mathbf{H}$ and the corresponding flux densities $\mathbf{D}$ and $\mathbf{B}$ are not independent but connected by electromagnetic constitutive equations. For an electromagnetically isotropic material the equations are

$$\boxed{\mathbf{B} = \mu \mathbf{H}, \qquad \mathbf{D} = \epsilon \mathbf{E}.} \tag{5}$$

---

[3] $\mathbf{B}$ is also called the magnetic induction vector and $\mathbf{D}$ the electric displacement vector. Many authors note, however, that the last term may be highly misleading.

[4] Corrections, whether relativistic or not, required as a result of the motion of the reference system are not considered here.

[5] In a cgs-unit system, factors of 4π appear in the nonhomogeneous Maxwell equations.

where μ and ϵ are the permeability and susceptibility, respectively, of the material[6]. These coefficients may be functions of position but (for static or harmonic fields) do not depend on time. For a general non-isotropic material both μ and ϵ become tensors. Even in isotropic media μ may be a complicated function of **H**; in ferromagnetic materials that exhibit hysteretic effects μ depends on the previous magnetization history.

In free space $\mu = \mu_0$ and $\epsilon = \epsilon_0$, which are connected by

$$c_0^2 = 1/(\mu_0 \epsilon_0), \tag{6}$$

where c_0 is the speed of light in vacuum.

Many conductors obey Ohm's law, which relates the electrical field strength **E** to the current density **J**:

$$\boxed{\mathbf{J} = \sigma \mathbf{E},} \tag{7}$$

where σ is the conductivity of the material. Again for a non-isotropic material σ is generally a tensor that for time-harmonic fields may contain real and imaginary components; in which case the above relation becomes a generalized Ohm's law. In the sequel σ is assumed to be time-independent. For good conductors $\sigma >> \epsilon$; for bad conductors $\sigma << \epsilon$. In free space, $\sigma = 0$.

The Electromagnetic Potentials

The electric scalar potential Φ and the magnetic vector potential **A** are introduced by the standard definitions

$$\boxed{\mathbf{E} = -\nabla \Phi - \dot{\mathbf{A}}, \qquad \mathbf{B} = \nabla \times \mathbf{A},} \tag{8}$$

upon which the two homogeneous Maxwell equations in (4) become identically satisfied. The definition of **A** leaves its divergence $\nabla \cdot \mathbf{A}$ arbitrary. A common choice to fix **A** is the Lorentz gauge:

$$\boxed{\nabla \cdot \mathbf{A} + \mu \epsilon \dot{\Phi} = 0.} \tag{9}$$

With this choice the two non-homogeneous Maxwell equations written in terms of Φ and **A** separate into the wave equations

$$\nabla^2 \Phi - \mu \epsilon \ddot{\Phi} = -\rho/\epsilon, \qquad \nabla^2 \mathbf{A} - \mu \epsilon \ddot{\mathbf{A}} = -\mu \mathbf{J}, \tag{10}$$

For a conducting medium, these equations are indirectly coupled on the right-hand side through Ohm's law (7).

---

[6] Other names for these quantities, such as inductivity and permittivity, are also used

Summary of Field Equations

For further use in the derivation of variational principles, we summarize and label the field equations as follows:

$$
\begin{aligned}
M_H &: \quad \nabla \times \mathbf{H} - \dot{\mathbf{D}} - \mathbf{J} = 0, \\
M_D &: \quad \nabla \cdot \mathbf{D} - \rho = 0, \\
C_\epsilon &: \quad \mathbf{D} - \epsilon\mathbf{E} = 0, \\
C_\mu &: \quad \mathbf{B} - \mu\mathbf{H} = 0, \\
P_E &: \quad \mathbf{E} + \nabla\Phi + \dot{\mathbf{A}} = 0, \\
P_B &: \quad \mathbf{B} - \nabla \times \mathbf{A} = 0, \\
C_\sigma &: \quad \mathbf{E} - \sigma\mathbf{J} = 0, \\
M_B &: \quad \nabla \cdot \mathbf{B} = 0, \\
M_E &: \quad \nabla \times \mathbf{E} + \dot{\mathbf{B}} = 0, \\
G_L &: \quad \nabla \cdot \mathbf{A} + \mu\epsilon\dot{\Phi} = 0.
\end{aligned}
\tag{11}
$$

The set $(M_H, M_D, C_\mu, C_\epsilon, P_E, P_B)$ supplies 16 equations for the $5 \times 3 + 1 = 16$ unknown spatial components of $(\mathbf{E}, \mathbf{D}, \mathbf{B}, \mathbf{H}, \mathbf{A}, \Phi)$. Equations (M_B, M_E) are in fact redundant, being identically satisfied by (P_E, P_B). Equation G_L is only a normalization condition on $\mathbf{A}$. Ohm's law C_σ may be adjoined if the current density $\mathbf{J}$ is not given, in which case we obtain 19 equations for 19 unknown component functions.

Notational Conventions

In the following derivation of parametrized variational principles, the notational conventions of references [9–13] are followed. An *independently varied field* is identified by a superposed tilde; for example $\widetilde{\mathbf{E}}, \widetilde{\mathbf{B}}$. A *derived field* is identified by writing its independent "parent" field as superscript; for example:

$$
\mathbf{D}^E = \epsilon\widetilde{\mathbf{E}}, \quad \mathbf{B}^A = \nabla \times \widetilde{\mathbf{A}}, \quad \mathbf{H}^A = \mu^{-1}\mathbf{B}^A = \mu^{-1}\nabla \times \mathbf{A}.
\tag{12}
$$

If a derived quantity depends on two parent fields, both are listed starting with the most significant one:

$$
\mathbf{D}^{\Phi A} = \epsilon\mathbf{E}^{\Phi A} = -\epsilon(\nabla\Phi + \dot{\mathbf{A}}).
\tag{13}
$$

The integral of a function f over volume V or surface S is often abbreviated to

$$
\left(f\right)_V = \int_V f\, dV, \qquad \left[f\right]_S = \int_S f\, dS.
\tag{14}
$$

6

Integrals over space-time $V \times [t_1, t_2]$ or $S \times [t_1, t_2]$ may be shortened to

$$\left(f \right)_{V \times t} = \int_{t_1}^{t_2} \int_V f \, dV \, dt, \qquad \left[f \right]_{S \times t} = \int_{t_1}^{t_2} \int_S f \, dS \, dt \qquad (15)$$

If $\mathbf{f}$, $\mathbf{g}$ are two vector functions, their inner-product over V may be abbreviated in the usual manner:

$$\left(\mathbf{f}, \mathbf{g} \right)_V \overset{\text{def}}{=} \int_V \mathbf{f}^T \mathbf{g} \, dV, \qquad (16)$$

and similarly for surface, volume × time, and surface × time integrals.

3. SIX-FIELD VARIATIONAL PRINCIPLES

The functionals considered in this and following sections have the general form

$$\boxed{R = U - P + B = L + B} \qquad (17)$$

where U is a quadratic form that characterizes the internal (stored) energy of the electromagnetic field, P is a linear form that characterizes the potential of volume-source contributions, and B contains boundary closure integrals. We often use L (the volume Lagrangian) for $U - P$.

The first two components can be expressed as space-time integrals:

$$U = \int_{t_1}^{t_2} \int_V \mathcal{U} \, dV \, dt = \left(\mathcal{U} \right)_{V \times t}, \qquad P = \int_{t_1}^{t_2} \int_V \mathcal{P} \, dV \, dt = \left(\mathcal{P} \right)_{V \times t}, \qquad (18)$$

where $\mathcal{U}$ and $\mathcal{P}$ are the electromagnetic energy density and source density, respectively. We also denote $\mathcal{L} = \mathcal{U} - \mathcal{P}$ as Lagrangian volume density. The boundary closure term is treated later as it emerges from the first variation of $L = U - P$. The functionals and densities in (17) and (18) will be superscripted with the number of independent fields as appropriate.

The six-field source density is given by

$$\mathcal{P}^{(6)} = \mathbf{J}^T \mathbf{A} + \rho \Phi, \qquad (19)$$

because $\mathbf{J}$ and ρ are prescribed. As for $\mathcal{U}^{(6)}$, making use of the "undetermined coefficient template" technique of references [11-13], the following parametrized form is postulated:[7]

$$\mathcal{U}^{(6)} = \frac{1}{2} \begin{Bmatrix} c^{-1}\widetilde{\mathbf{H}} \\ c^{-1}\mathbf{H}^B \\ c^{-1}\mathbf{H}^A \\ \widetilde{\mathbf{D}} \\ \mathbf{D}^E \\ \mathbf{D}^{\Phi A} \end{Bmatrix}^T \begin{bmatrix} g_{11}\mathbf{I} & g_{12}\mathbf{I} & g_{13}\mathbf{I} & g_{14}\mathbf{I} & g_{15}\mathbf{I} & g_{16}\mathbf{I} \\ g_{21}\mathbf{I} & g_{22}\mathbf{I} & g_{23}\mathbf{I} & g_{24}\mathbf{I} & g_{25}\mathbf{I} & g_{26}\mathbf{I} \\ g_{31}\mathbf{I} & g_{32}\mathbf{I} & g_{33}\mathbf{I} & g_{34}\mathbf{I} & g_{35}\mathbf{I} & g_{36}\mathbf{I} \\ g_{41}\mathbf{I} & g_{42}\mathbf{I} & g_{43}\mathbf{I} & g_{44}\mathbf{I} & g_{45}\mathbf{I} & g_{46}\mathbf{I} \\ g_{51}\mathbf{I} & g_{52}\mathbf{I} & g_{53}\mathbf{I} & g_{54}\mathbf{I} & g_{55}\mathbf{I} & g_{56}\mathbf{I} \\ g_{61}\mathbf{I} & g_{62}\mathbf{I} & g_{63}\mathbf{I} & g_{64}\mathbf{I} & g_{65}\mathbf{I} & g_{66}\mathbf{I} \end{bmatrix} \begin{Bmatrix} c\mathbf{B}^H \\ c\widetilde{\mathbf{B}} \\ c\mathbf{B}^A \\ \mathbf{E}^D \\ \widetilde{\mathbf{E}} \\ \mathbf{E}^{\Phi A} \end{Bmatrix}, \qquad (20)$$

---

[7] Following a nomenclature similar to that used in developing parametrized variational principles for continuum mechanics, $\mathcal{U}$ may be called the generalized electromagnetic field energy density. As a rough guide in comparing to such principles, $c^{-1}\mathbf{H}$ and $\mathbf{D}$ may be regarded as analogous to mechanical stresses whereas $c\mathbf{B}$ and $\mathbf{E}$ are analogous to mechanical strains. The potentials $\mathbf{A}$ and Φ are analogous to displacements. The analogy, however, does not readily extend to boundary conditions.

7

where g_{ij} are *dimensionless* scalar coefficients to be selected, $\mathbf{I}$ denotes the 3×3 identity matrix and

$$c^2 = 1/(\mu\epsilon), \tag{21}$$

is the speed of propagation of EM disturbances in matter. The scaling of $\mathbf{B}$ and $\mathbf{H}$ by c and c^{-1} in (19) "equilibrates" the physical units. The derived fields that appear there are:

$$\mathbf{B}^H = \mu\widetilde{\mathbf{H}}, \quad \mathbf{B}^A = \nabla \times \widetilde{\mathbf{A}}, \quad \mathbf{E}^D = \epsilon^{-1}\widetilde{\mathbf{D}}, \quad \mathbf{E}^{\Phi A} = -\nabla\widetilde{\Phi} - \dot{\widetilde{\mathbf{A}}},$$
$$\mathbf{H}^B = \mu^{-1}\widetilde{\mathbf{B}}, \quad \mathbf{H}^A = \mu^{-1}\mathbf{B}^A = \mu^{-1}\nabla \times \mathbf{A}, \quad \mathbf{D}^E = \epsilon\widetilde{\mathbf{E}}, \quad \mathbf{D}^{\Phi A} = \epsilon\mathbf{E}^{\Phi A}. \tag{22}$$

Relations (22) may be expressed in matrix form as

$$\begin{Bmatrix} c\mathbf{B}^H \\ c\widetilde{\mathbf{B}} \\ c\mathbf{B}^A \\ \mathbf{E}^D \\ \widetilde{\mathbf{E}} \\ \mathbf{E}^{\Phi A} \end{Bmatrix} = \begin{bmatrix} \mu c\mathbf{I} & 0 & 0 & 0 & 0 & 0 \\ 0 & c\mathbf{I} & 0 & 0 & 0 & 0 \\ 0 & 0 & c\Lambda & 0 & 0 & 0 \\ 0 & 0 & 0 & \epsilon^{-1}\mathbf{I} & 0 & 0 \\ 0 & 0 & 0 & 0 & \mathbf{I} & 0 \\ 0 & 0 & -\frac{\partial}{\partial t}\mathbf{I} & 0 & 0 & -\nabla \end{bmatrix} \begin{Bmatrix} \widetilde{\mathbf{H}} \\ \widetilde{\mathbf{B}} \\ \widetilde{\mathbf{A}} \\ \widetilde{\mathbf{D}} \\ \widetilde{\mathbf{E}} \\ \widetilde{\Phi} \end{Bmatrix}, \tag{23}$$

$$\begin{Bmatrix} c^{-1}\widetilde{\mathbf{H}} \\ c^{-1}\mathbf{H}^B \\ c^{-1}\mathbf{H}^A \\ \widetilde{\mathbf{D}} \\ \mathbf{D}^E \\ \mathbf{D}^{\Phi A} \end{Bmatrix} = \begin{bmatrix} c^{-1}\mathbf{I} & 0 & 0 & 0 & 0 & 0 \\ 0 & (\mu c)^{-1}\mathbf{I} & 0 & 0 & 0 & 0 \\ 0 & 0 & (\mu c)^{-1}\Lambda & 0 & 0 & 0 \\ 0 & 0 & 0 & \mathbf{I} & 0 & 0 \\ 0 & 0 & 0 & 0 & \epsilon\mathbf{I} & 0 \\ 0 & 0 & -\frac{\partial}{\partial t}\epsilon\mathbf{I} & 0 & 0 & -\epsilon\nabla \end{bmatrix} \begin{Bmatrix} \widetilde{\mathbf{H}} \\ \widetilde{\mathbf{B}} \\ \widetilde{\mathbf{A}} \\ \widetilde{\mathbf{D}} \\ \widetilde{\mathbf{E}} \\ \widetilde{\Phi} \end{Bmatrix}. \tag{24}$$

in which $\Lambda \equiv \nabla \times$ denotes the curl operator for typographical convenience; note that $\Lambda^T \equiv - \times \nabla$. Let

$$\mathbf{z}^{(6)} = \begin{Bmatrix} \widetilde{\mathbf{H}} \\ \widetilde{\mathbf{B}} \\ \widetilde{\mathbf{A}} \\ \widetilde{\mathbf{D}} \\ \widetilde{\mathbf{E}} \\ \widetilde{\Phi} \end{Bmatrix}, \quad \mathbf{C}^{(6)} = \begin{bmatrix} \mathbf{C}_{11} & \mathbf{C}_{12} & \mathbf{C}_{13} & \mathbf{C}_{14} & \mathbf{C}_{15} & \mathbf{C}_{16} \\ \mathbf{C}_{21} & \mathbf{C}_{22} & \mathbf{C}_{23} & \mathbf{C}_{24} & \mathbf{C}_{25} & \mathbf{C}_{26} \\ \mathbf{C}_{31} & \mathbf{C}_{32} & \mathbf{C}_{33} & \mathbf{C}_{34} & \mathbf{C}_{35} & \mathbf{C}_{36} \\ \mathbf{C}_{41} & \mathbf{C}_{42} & \mathbf{C}_{43} & \mathbf{C}_{44} & \mathbf{C}_{45} & \mathbf{C}_{46} \\ \mathbf{C}_{51} & \mathbf{C}_{52} & \mathbf{C}_{53} & \mathbf{C}_{54} & \mathbf{C}_{55} & \mathbf{C}_{56} \\ \mathbf{C}_{61} & \mathbf{C}_{62} & \mathbf{C}_{63} & \mathbf{C}_{64} & \mathbf{C}_{65} & \mathbf{C}_{66} \end{bmatrix} \tag{25}$$

be the complete 16-component state vector of six independent fields and the 16×16 kernel matrix, respectively, obtained by changing the variables in (20) according to (23) and the transpose of (24). Then

$$\mathcal{U}^{(6)} = \tfrac{1}{2}\mathbf{z}^{(6)T}\mathbf{C}^{(6)}\mathbf{z}^{(6)}. \tag{26}$$

The component submatrices of $\mathbf{C}^{(6)}$ are given by

$$\mathbf{C}_{11} = g_{11}\mu\mathbf{I}, \qquad \mathbf{C}_{12} = g_{12}\mathbf{I}, \qquad \mathbf{C}_{13} = g_{13}\Lambda - g_{16}c^{-1}\frac{\partial}{\partial t}\mathbf{I},$$

$$\mathbf{C}_{14} = g_{14}\mu c\mathbf{I}, \qquad \mathbf{C}_{15} = g_{15}c^{-1}\mathbf{I}, \qquad \mathbf{C}_{16} = -g_{16}c^{-1}\nabla,$$

$$\mathbf{C}_{21} = g_{21}\mathbf{I}, \qquad \mathbf{C}_{22} = g_{22}\mu^{-1}\mathbf{I}, \qquad \mathbf{C}_{23} = g_{23}\mu^{-1}\Lambda - g_{26}\epsilon c\frac{\partial}{\partial t}\mathbf{I},$$

$$\mathbf{C}_{24} = g_{24}c\mathbf{I}, \qquad \mathbf{C}_{25} = g_{25}\epsilon c\mathbf{I}, \qquad \mathbf{C}_{26} = -g_{26}\epsilon c\nabla,$$

$$\mathbf{C}_{31} = g_{31}\Lambda^T - g_{61}c^{-1}\frac{\partial}{\partial t}\mathbf{I}, \qquad \mathbf{C}_{32} = g_{32}\mu^{-1}\Lambda^T - g_{62}(\mu c)^{-1}\frac{\partial}{\partial t}\mathbf{I},$$

$$\mathbf{C}_{33} = g_{33}\mu^{-1}\Lambda^T\Lambda - (\mu c)^{-1}(g_{36}\Lambda^T + g_{63}\Lambda)\frac{\partial}{\partial t} + g_{66}\epsilon\frac{\partial}{\partial t}\frac{\partial}{\partial t}\mathbf{I},$$

$$\mathbf{C}_{34} = g_{34}c\Lambda^T - g_{64}\frac{\partial}{\partial t}\mathbf{I}, \quad \mathbf{C}_{35} = g_{35}\epsilon c\Lambda^T - g_{65}\epsilon\frac{\partial}{\partial t}\mathbf{I}, \quad \mathbf{C}_{36} = -g_{36}\epsilon c\Lambda^T\nabla + g_{66}\epsilon\frac{\partial}{\partial t}\nabla,$$

$$\mathbf{C}_{41} = g_{41}\mu c\mathbf{I}, \qquad \mathbf{C}_{42} = g_{42}c\mathbf{I}, \qquad \mathbf{C}_{43} = g_{43}c\Lambda - g_{46}\frac{\partial}{\partial t}\mathbf{I},$$

$$\mathbf{C}_{44} = g_{44}\mathbf{I}, \qquad \mathbf{C}_{45} = g_{45}\epsilon^{-1}\mathbf{I}, \qquad \mathbf{C}_{46} = -g_{46}\nabla,$$

$$\mathbf{C}_{51} = g_{51}c^{-1}\mathbf{I}, \qquad \mathbf{C}_{52} = g_{52}\epsilon c\mathbf{I}, \qquad \mathbf{C}_{53} = g_{53}\epsilon c\Lambda - g_{56}\epsilon\frac{\partial}{\partial t}\mathbf{I},$$

$$\mathbf{C}_{54} = g_{54}\epsilon\mathbf{I}, \qquad \mathbf{C}_{55} = g_{55}\mathbf{I}, \qquad \mathbf{C}_{56} = -g_{56}\epsilon\nabla,$$

$$\mathbf{C}_{61} = -g_{61}c^{-1}\nabla^T, \qquad \mathbf{C}_{62} = -g_{62}\epsilon c\nabla^T, \qquad \mathbf{C}_{63} = -g_{63}\epsilon c\nabla^T\Lambda + g_{66}\epsilon\nabla^T\frac{\partial}{\partial t},$$

$$\mathbf{C}_{64} = -g_{64}\nabla^T, \qquad \mathbf{C}_{65} = -g_{65}\epsilon\nabla^T, \qquad \mathbf{C}_{66} = g_{66}\epsilon\nabla^T\nabla. \tag{27}$$

Note that in the above $\epsilon c = (\mu c)^{-1}$; one expression or the other is used to facilitate taking the first variation below. Matrix $\mathbf{C}^{(6)}$ must be symmetric because only its symmetric part participates in the first variation of $\mathcal{U}^{(6)}$. This requirement provides the 21 symmetry conditions:

$$g_{ji} = g_{ij}, \qquad i = 1,\ldots,6, \quad j = 1,\ldots,6. \tag{28}$$

Consequently the functional $U^{(6)}$, and thus $R^{(6)}$, is fully characterized by 21 dimensionless coefficients, which may be arranged as a symmetric 6×6 matrix:

$$\mathbf{G}^{(6)} = \begin{bmatrix} g_{11} & g_{12} & g_{13} & g_{14} & g_{15} & g_{16} \\ & g_{22} & g_{23} & g_{24} & g_{25} & g_{26} \\ & & g_{33} & g_{34} & g_{35} & g_{36} \\ & & & g_{44} & g_{45} & g_{46} \\ & & & & g_{55} & g_{56} \\ symm & & & & & g_{66} \end{bmatrix}. \tag{29}$$

This is called the *functional-generating matrix*. The entries of $\mathbf{G}^{(6)}$ cannot be selected arbitrarily, however, because the consistency conditions derived below impose several constraints.

9

For further use define the six-field source vector $\mathbf{s}^{(6)T} = [\,0 \quad 0 \quad \mathbf{J} \quad 0 \quad 0 \quad \rho\,]$ so that

$$\mathcal{P}^{(6)} = \mathbf{s}^{(6)T}\mathbf{z}^{(6)}. \tag{30}$$

The First Variation

With the definitions (26) and (30) the first variation of the volume terms of the six-field form is given by

$$\delta L^{(6)} = \delta(U^{(6)} - P^{(6)}) = \left(\delta\mathbf{z}^{(6)},\, \mathbf{C}^{(6)}\mathbf{z}^{(6)} - \mathbf{s}^{(6)}\right)_{V \times t} \tag{31}$$

After appropriate manipulations[8] we get

$$\delta L^{(6)} = \left(\Delta\mathbf{B}, \delta\widetilde{\mathbf{H}}\right)_{V \times t} + \left(\Delta\mathbf{H}, \delta\widetilde{\mathbf{B}}\right)_{V \times t} + \left(\mathbf{Q} - \mathbf{J}, \delta\widetilde{\mathbf{A}}\right)_{V \times t} + \left(\Delta\mathbf{E}, \delta\widetilde{\mathbf{D}}\right)_{V \times t}$$
$$+ \left(\Delta\mathbf{D}, \delta\widetilde{\mathbf{E}}\right)_{V \times t} + \left(K - \rho, \delta\widetilde{\Phi}\right)_{V \times t} - \left[\mathbf{H}_n^w, \delta\widetilde{\mathbf{A}}\right]_{S \times t} + \left[D_n^w, \delta\widetilde{\Phi}\right]_{S \times t} \tag{32}$$

where the coefficients of the volume variations are

$$\Delta\mathbf{B} = g_{11}\mathbf{B}^H + g_{12}\widetilde{\mathbf{B}} + g_{13}\mathbf{B}^A + c^{-1}\left(g_{14}\mathbf{E}^D + g_{15}\widetilde{\mathbf{E}}^D + g_{16}\mathbf{E}^{\Phi A}\right) \tag{33}$$

$$\Delta\mathbf{H} = g_{12}\widetilde{\mathbf{H}} + g_{22}\mathbf{H}^B + g_{23}\mathbf{H}^A + c\left(g_{24}\widetilde{\mathbf{D}} + g_{25}\mathbf{D}^E + g_{26}\mathbf{D}^{\Phi A}\right), \tag{34}$$

$$\mathbf{Q} = \nabla \times \left(g_{13}\widetilde{\mathbf{H}} + g_{23}\mathbf{H}^B + g_{33}\mathbf{H}^A\right) + \frac{\partial}{\partial t}\left(g_{46}\widetilde{\mathbf{D}} + g_{56}\mathbf{D}^E + g_{66}\mathbf{D}^{\Phi A}\right)$$
$$+ \epsilon c\left[\frac{\partial}{\partial t}\left(g_{16}\mathbf{B}^H + g_{26}\widetilde{\mathbf{B}} + g_{36}\mathbf{B}^A\right) + \nabla \times \left(g_{34}\mathbf{E}^D + g_{35}\widetilde{\mathbf{E}} + g_{36}\mathbf{E}^{\Phi A}\right)\right], \tag{35}$$

$$\Delta\mathbf{E} = c\left(g_{14}\mathbf{B}^H + g_{24}\widetilde{\mathbf{B}} + g_{34}\mathbf{B}^A\right) + g_{44}\mathbf{E}^D + g_{45}\widetilde{\mathbf{E}} + g_{46}\mathbf{E}^{\Phi A}, \tag{36}$$

$$\Delta\mathbf{D} = c^{-1}\left(g_{15}\widetilde{\mathbf{H}} + g_{25}\mathbf{H}^B + g_{35}\mathbf{H}^A\right) + g_{45}\widetilde{\mathbf{D}} + g_{55}\mathbf{D}^E + g_{56}\mathbf{D}^{\Phi A}, \tag{37}$$

$$K = -\nabla \cdot \left(g_{46}\widetilde{\mathbf{D}} + g_{56}\mathbf{D}^E + g_{66}\mathbf{D}^{\Phi A}\right) - \epsilon c\nabla \cdot \left(g_{16}\mathbf{B}^H + g_{26}\widetilde{\mathbf{B}} + g_{36}\mathbf{B}^A\right), \tag{38}$$

---

[8] In deriving the expressions for the variations of Φ and $\mathbf{A}$, the following integration-by-parts formulas have been used:

$$\left(\mathbf{v}, \delta(\nabla\Phi)\right)_V = \left(\mathbf{v}, \nabla\delta\Phi\right)_V = -\left(\delta\Phi, \nabla\mathbf{v}\right)_V + \left[\delta\Phi, \mathbf{v} \cdot \mathbf{n}\right]_S,$$

$$\left(\mathbf{v}, \delta(\nabla \times \mathbf{A})\right)_V = \left(\mathbf{v}, \nabla \times \delta\mathbf{A}\right)_V = \left(\delta\mathbf{A}, \nabla \times \mathbf{v}\right)_V - \left[\delta\mathbf{A}, \mathbf{v} \times \mathbf{n}\right]_S,$$

where $\mathbf{v}$ is an arbitrary vector and $\mathbf{n}$ denotes the external unit normal on S. Furthermore, the variations of the independent fields at initial and final times, in accordance with the usual procedure in Hamiltonian forms, have been assumed to vanish.

and for the surface variations

$$\mathbf{H}_n^w = \mathbf{H}^w \times \mathbf{n} = \left(g_{13}\widetilde{\mathbf{H}} + g_{23}\mathbf{H}^B + g_{33}\mathbf{H}^A\right) \times \mathbf{n}. \tag{39}$$

$$D_n^w = \mathbf{D}^w \cdot \mathbf{n} = -\left(g_{46}\widetilde{\mathbf{D}} + g_{56}\mathbf{D}^E + g_{66}\mathbf{D}^{\Phi A}\right) \cdot \mathbf{n}, \tag{40}$$

Here $\mathbf{D}^w$ and $\mathbf{H}^w$ denote weighted combinations of independent and derived electric and magnetic fluxes, respectively, on S. It follows that the appropriate boundary term is

$$B^{(6)} = \left[\mathbf{H}^w \times \mathbf{A}, \mathbf{n}\right]_{S \times t} + \left[D_n^w, \Phi\right]_{S \times t}. \tag{41}$$

where the first term follows from $\mathbf{H} \times \mathbf{n} \cdot \mathbf{A} = -\mathbf{H} \times \mathbf{A} \cdot \mathbf{n}$. This term defines essential and natural boundary conditions. For example, either Φ or D_n^w may be prescribed on $S \times t$.

Consistency Conditions

When the varied electromagnetic fields coincide with the exact ones we must have $\mathbf{H} = \widetilde{\mathbf{H}} = \mathbf{H}^B = \mathbf{H}^A$, $\mathbf{E} = \widetilde{\mathbf{E}} = \mathbf{E}^D = \mathbf{E}^{\Phi A}$, and so on. Substituting these conditions into the first variation yields

$$\Delta \mathbf{B} = (g_{11} + g_{12} + g_{13})\mathbf{B} + (g_{14} + g_{15} + g_{16})c^{-1}\mathbf{E},$$

$$\Delta \mathbf{H} = (g_{12} + g_{22} + g_{23})\mathbf{H} + (g_{24} + g_{25} + g_{26})c\mathbf{D},$$

$$\mathbf{Q} = (g_{13} + g_{23} + g_{33})\nabla \times \mathbf{H} + (g_{46} + g_{56} + g_{66})\dot{\mathbf{D}}$$

$$+ \epsilon c \left[(g_{16} + g_{26} + g_{36})\dot{\mathbf{B}} + (g_{34} + g_{35} + g_{36})\nabla \times \mathbf{E}\right], \tag{42}$$

$$\Delta \mathbf{E} = (g_{14} + g_{24} + g_{34}) c\mathbf{B} + (g_{44} + g_{45} + g_{46})\mathbf{E},$$

$$\Delta \mathbf{D} = (g_{15} + g_{25} + g_{35}) c^{-1}\mathbf{H} + (g_{45} + g_{55} + g_{56})\mathbf{D},$$

$$K = -(g_{46} + g_{56} + g_{66}) \nabla \cdot \mathbf{D} - \epsilon c(g_{16} + g_{26} + g_{36}) \nabla \cdot \mathbf{B},$$

The Euler equations that emanate from (32) are $\Delta \mathbf{B} = \mathbf{0}$, $\Delta \mathbf{H} = \mathbf{0}$, $\Delta \mathbf{D} = \mathbf{0}$, $\Delta \mathbf{E} = \mathbf{0}$, $\mathbf{Q} - \mathbf{J} = \mathbf{0}$, and $K - \rho = 0$. Consistency with the field equations (11) requires that

$$
\begin{array}{ll}
g_{11} + g_{12} + g_{13} = 0, & g_{14} + g_{15} + g_{16} = 0, \\
g_{12} + g_{22} + g_{23} = 0, & g_{24} + g_{25} + g_{26} = 0, \\
g_{13} + g_{23} + g_{33} = 1, & g_{16} + g_{26} + g_{36} = 0, \\
g_{34} + g_{35} + g_{36} = 0, & g_{46} + g_{56} + g_{66} = -1, \\
g_{14} + g_{24} + g_{34} = 0, & g_{44} + g_{45} + g_{46} = 0, \\
g_{15} + g_{25} + g_{35} = 0, & g_{45} + g_{55} + g_{56} = 0,
\end{array}
\tag{43}
$$

The 12 constraints reduce the number of free parameters in matrix $\mathbf{G}$ to $21 - 12 = 9$. Notice that this choice also satisfies the consistency requirements for the weighted boundary terms in (39) and (40).

11

Interpretation of Euler Equations

Several of the Euler equations appear in unconventional form because they involve a weighted combination of several field equations. Take for definiteness $\Delta \mathbf{B} = 0$. Split as $\Delta \mathbf{B} = \Delta \mathbf{B}_B + \Delta \mathbf{B}_E = 0$. Each component must vanish separately because of field independence. Consider the first component rewritten in terms of weights w_1, w_2 and w_3 as

$$
\begin{aligned}
\Delta \mathbf{B}_B &= g_{11}\mathbf{B}^H + g_{12}\widetilde{\mathbf{B}} + g_{13}\mathbf{B}^A = (w_1 - w_3)\mathbf{B}^H + (w_2 - w_1)\widetilde{\mathbf{B}} + (w_3 - w_2)\mathbf{B}^A \\
&= w_1(\mathbf{B}^H - \widetilde{\mathbf{B}}) + w_2(\widetilde{\mathbf{B}} - \mathbf{B}^A) + w_3(\mathbf{B}^A - \mathbf{B}^H).
\end{aligned}
\tag{44}
$$

Now the constraint $g_{11} + g_{12} + g_{13} = 0$ is satisfied for *arbitrary* nonzero weights w_1, w_2, w_3. But $\mathbf{B}^H = \widetilde{\mathbf{B}}$ is the constitutive equation labeled C_μ in (11), $\widetilde{\mathbf{B}} = \mathbf{B}^A$ is the potential definition labeled P_B, and $\mathbf{B}^A = \mathbf{B}^H$ is a transitive combination of C_μ and P_B. Thus we conclude that $\Delta \mathbf{B}_B = 0$ is a weighted-residual representation of P_B and C_μ. Similarly one can show that $\Delta \mathbf{B}_E = 0$ is a weighted-residual representation of P_E and C_ϵ.

Similar interpretations can be worked out for $\Delta \mathbf{H} = 0$, $\Delta \mathbf{D} = 0$, and $\Delta \mathbf{E} = 0$. Summarizing, the Euler equations associated with the variations in $\mathbf{H}$, $\mathbf{B}$, $\mathbf{E}$ and $\mathbf{D}$ represent, in weighted form, the constitutive equations C_μ, C_ϵ and the potential definition equations P_B and P_E. Because the latter verify the homogeneous Maxwell equations M_B and M_E by definition, we recover the first 8 equations of (11) except for the Maxwell source equations M_H and M_D. These follow directly from the variations in $\mathbf{A}$ and Φ, respectively, as is obvious from (32) and (42). Should the coefficients be such that the weight of a particular equation turns out to be zero, that relation must be verified in strong (pointwise) form.

Equation C_σ (Ohm's law) is not included in this principle because $\mathbf{J}$ is prescribed. The Lorentz gauge condition G_L does not follow from the variational principle and must be separately imposed by augmenting the variational principle with a Lagrange multiplier [7].

Specializations

The simplest choice (in the sense of having the sparsest $\mathbf{G}^{(6)}$ matrix) that verifies the consistency conditions (43) is

$$
\mathbf{G}^{(6)} = \begin{bmatrix}
0 & 0 & 0 & 0 & 0 & 0 \\
0 & 0 & 0 & 0 & 0 & 0 \\
0 & 0 & 1 & 0 & 0 & 0 \\
0 & 0 & 0 & 0 & 0 & 0 \\
0 & 0 & 0 & 0 & 0 & 0 \\
0 & 0 & 0 & 0 & 0 & -1
\end{bmatrix}
\tag{45}
$$

which supplies the two-field form

$$
\begin{aligned}
L(\mathbf{A}, \Phi) &= \tfrac{1}{2}\left(\mu^{-1}\mathbf{B}^A, \mathbf{B}^A\right)_{V \times t} - \tfrac{1}{2}\left(\epsilon \mathbf{E}^{\Phi A}, \mathbf{E}^{\Phi A}\right)_{V \times t} - (\mathbf{J}, \widetilde{\mathbf{A}})_{V \times t} - (\rho, \widetilde{\Phi})_{V \times t} \\
&= \int_{t_1}^{t_2} \int_V \left\{ \tfrac{1}{2}\mu^{-1}\|\nabla \times \widetilde{\mathbf{A}}\|^2 - \tfrac{1}{2}\epsilon \left\| \nabla \widetilde{\Phi} + \frac{\partial \widetilde{\mathbf{A}}}{\partial t} \right\|^2 - \mathbf{J}^T\widetilde{\mathbf{A}} - \rho\widetilde{\Phi} \right\} dV \, dt.
\end{aligned}
\tag{46}
$$

where $||v||^2 \equiv v^T v$. The integrand is the conventional electromagnetic Lagrangian density expressed in terms of the potentials.[9] In (46) the constitutive relations C_μ and C_ϵ are verified in strong (pointwise) form.

Oden and Reddy [18] present a six-field variational principle for magnetohydrodynamics which, on correcting some sign glitches, may be maneuvered to

$$
\mathbf{G}^{(6)} = \begin{bmatrix}
1 & -1 & 0 & 0 & 0 & 0 \\
-1 & 0 & 1 & 0 & 0 & 0 \\
0 & 1 & 0 & 0 & 0 & 0 \\
0 & 0 & 0 & 0 & 1 & -1 \\
0 & 0 & 0 & 1 & -1 & 0 \\
0 & 0 & 0 & -1 & 0 & 0
\end{bmatrix}.
\tag{47}
$$

It can be observed that the previous two examples pertain to the following "template" subset of (29), in which coupling between electric and magnetic fields is absent:

$$
\mathbf{G}^{(6)} = \begin{bmatrix}
g_{11} & g_{12} & g_{13} & 0 & 0 & 0 \\
g_{12} & g_{22} & g_{23} & 0 & 0 & 0 \\
g_{13} & g_{23} & g_{33} & 0 & 0 & 0 \\
0 & 0 & 0 & g_{44} & g_{45} & g_{46} \\
0 & 0 & 0 & g_{45} & g_{55} & g_{56} \\
0 & 0 & 0 & g_{46} & g_{56} & g_{66}
\end{bmatrix}
\tag{48}
$$

subject to $g_{11} + g_{12} + g_{13} = 0$, $g_{21} + g_{22} + g_{23} = 0$, $g_{31} + g_{32} + g_{33} = 1$, $g_{44} + g_{45} + g_{46} = 0$, $g_{45} + g_{55} + g_{56} = 0$ and $g_{46} + g_{56} + g_{66} = -1$. This leaves three free parameters in each 3×3 block. The parameter selection for each block is then similar to that found for the generalized strain energy of compressible elasticity [11,12].

Given the relative lack of development of mixed principles in electromagnetics, mechanics terminology could perhaps be transliterated to electromagnetodynamics without fear of clashing with existing names. For example, the Hu-Washizu principle of mechanics is obtained by taking $g_{12} = -1$, $g_{13} = g_{22} = 1$, others zero, if mechanical stresses σ, strains e and displacements u are ordered as independent fields 1, 2 and 3, respectively. Insertion of this pattern into the blocks of matrix (48) yields what may be called the "six-field Hu-Washizu principle of electromagnetism" if σ, e and u are identified with H, B and A for magnetic fields and D, E and Φ for electric fields, respectively. Note that (47) displays the (negative of the) Hu-Washizu pattern for the electric fields, but not for the magnetic fields.

4. SEVEN-FIELD FUNCTIONALS

---

[9] This specific form is given for free space by Lanczos [14]. It is worked out (with scaling errors) for a single charge in Yourgrau and Mandelstam [15] and again for free space in Gelfand and Fomin [16]. It is elegantly derived in Finlayson [17], who attributes it to prior mid-1960s work in magnetohydrodynamics referenced therein. Inasmuch as the first edition of [14] was published in 1949, the associated variational principle is undoubtedly much older.

Next we allow the current density $\mathbf{J}$ in a *conducting* medium to be an independent field subject to variation. Then Ohm's law (7) must be adjoined to get a sufficient number of equations; in the sequel $\sigma \neq 0$ is assumed. The internal energy density is redefined as follows:

$$\mathcal{U}^{(7)} = \tfrac{1}{2} \left\{ \begin{array}{c} c^{-1}\widetilde{\mathbf{H}} \\ c^{-1}\mathbf{H}^B \\ c^{-1}\mathbf{H}^A \\ \widetilde{\mathbf{D}} \\ \mathbf{D}^E \\ \mathbf{D}^{\Phi A} \\ \mathbf{D}^J \\ \widetilde{\lambda} \end{array} \right\}^T \left[\begin{array}{cccccccc} g_{11}\mathbf{I} & g_{12}\mathbf{I} & g_{13}\mathbf{I} & g_{14}\mathbf{I} & g_{15}\mathbf{I} & g_{16}\mathbf{I} & g_{17}\mathbf{I} & g_{18}\mathbf{I} \\ g_{21}\mathbf{I} & g_{22}\mathbf{I} & g_{23}\mathbf{I} & g_{24}\mathbf{I} & g_{25}\mathbf{I} & g_{26}\mathbf{I} & g_{27}\mathbf{I} & g_{28}\mathbf{I} \\ g_{31}\mathbf{I} & g_{32}\mathbf{I} & g_{33}\mathbf{I} & g_{34}\mathbf{I} & g_{35}\mathbf{I} & g_{36}\mathbf{I} & g_{37}\mathbf{I} & g_{38}\mathbf{I} \\ g_{41}\mathbf{I} & g_{42}\mathbf{I} & g_{43}\mathbf{I} & g_{44}\mathbf{I} & g_{45}\mathbf{I} & g_{46}\mathbf{I} & g_{47}\mathbf{I} & g_{48}\mathbf{I} \\ g_{51}\mathbf{I} & g_{52}\mathbf{I} & g_{53}\mathbf{I} & g_{54}\mathbf{I} & g_{55}\mathbf{I} & g_{56}\mathbf{I} & g_{57}\mathbf{I} & g_{58}\mathbf{I} \\ g_{61}\mathbf{I} & g_{62}\mathbf{I} & g_{63}\mathbf{I} & g_{64}\mathbf{I} & g_{65}\mathbf{I} & g_{66}\mathbf{I} & g_{67}\mathbf{I} & g_{68}\mathbf{I} \\ g_{71}\mathbf{I} & g_{72}\mathbf{I} & g_{73}\mathbf{I} & g_{74}\mathbf{I} & g_{75}\mathbf{I} & g_{77}\mathbf{I} & g_{77}\mathbf{I} & g_{78}\mathbf{I} \\ g_{81}\mathbf{I} & g_{82}\mathbf{I} & g_{83}\mathbf{I} & g_{84}\mathbf{I} & g_{85}\mathbf{I} & g_{88}\mathbf{I} & g_{87}\mathbf{I} & g_{88}\mathbf{I} \end{array} \right] \left\{ \begin{array}{c} c\mathbf{B}^H \\ c\widetilde{\mathbf{B}} \\ c\mathbf{B}^A \\ \mathbf{E}^D \\ \widetilde{\mathbf{E}} \\ \mathbf{E}^{\Phi A} \\ \mathbf{E}^J \\ \epsilon^{-1}\widetilde{\lambda} \end{array} \right\} - \widetilde{\mathbf{A}}^T \widetilde{\mathbf{J}}, \quad (49)$$

Two additional derived quantities appear in (49): $\mathbf{E}^J = \sigma^{-1}\mathbf{J}$ and $\mathbf{D}^J = \epsilon \mathbf{E}^J$. Furthermore, a 3-vector Lagrange multiplier field λ with physical dimensions of $\mathbf{D}$, has been adjoined to weakly specify Ohm's law (7). Because both $\mathbf{A}$ and $\mathbf{J}$ are now unknown terms, term $\mathbf{A}^T\mathbf{J}$ of (18) must be moved to the quadratic form $\mathcal{U}^{(7)}$, and the source density reduces to $\mathcal{P}^{(7)} = \rho\Phi$. Relations (23) and (24) become

$$\left\{ \begin{array}{c} c\mathbf{B}^H \\ c\widetilde{\mathbf{B}} \\ c\mathbf{B}^A \\ \mathbf{E}^D \\ \widetilde{\mathbf{E}} \\ \mathbf{E}^{\Phi A} \\ \mathbf{E}^J \\ \epsilon^{-1}\widetilde{\lambda} \end{array} \right\} = \left[\begin{array}{cccccccc} \mu c\mathbf{I} & 0 & 0 & 0 & 0 & 0 & 0 & 0 \\ 0 & c\mathbf{I} & 0 & 0 & 0 & 0 & 0 & 0 \\ 0 & 0 & c\Lambda & 0 & 0 & 0 & 0 & 0 \\ 0 & 0 & 0 & \epsilon^{-1}\mathbf{I} & 0 & 0 & 0 & 0 \\ 0 & 0 & 0 & 0 & \mathbf{I} & 0 & 0 & 0 \\ 0 & 0 & -\frac{\partial}{\partial t}\mathbf{I} & 0 & 0 & -\nabla & 0 & 0 \\ 0 & 0 & 0 & 0 & 0 & 0 & \sigma^{-1}\mathbf{I} & 0 \\ 0 & 0 & 0 & 0 & 0 & 0 & 0 & \epsilon^{-1}\mathbf{I} \end{array} \right] \left\{ \begin{array}{c} \widetilde{\mathbf{H}} \\ \widetilde{\mathbf{B}} \\ \widetilde{\mathbf{A}} \\ \widetilde{\mathbf{D}} \\ \widetilde{\mathbf{E}} \\ \widetilde{\Phi} \\ \widetilde{\mathbf{J}} \\ \widetilde{\lambda} \end{array} \right\}, \quad (50)$$

$$\left\{ \begin{array}{c} c^{-1}\widetilde{\mathbf{H}} \\ c^{-1}\mathbf{H}^B \\ c^{-1}\mathbf{H}^A \\ \widetilde{\mathbf{D}} \\ \mathbf{D}^E \\ \mathbf{D}^{\Phi A} \\ \mathbf{D}^J \\ \widetilde{\lambda} \end{array} \right\} = \left[\begin{array}{cccccccc} c^{-1}\mathbf{I} & 0 & 0 & 0 & 0 & 0 & 0 & 0 \\ 0 & (\mu c)^{-1}\mathbf{I} & 0 & 0 & 0 & 0 & 0 & 0 \\ 0 & 0 & (\mu c)^{-1}\Lambda & 0 & 0 & 0 & 0 & 0 \\ 0 & 0 & 0 & \mathbf{I} & 0 & 0 & 0 & 0 \\ 0 & 0 & 0 & 0 & \epsilon\mathbf{I} & 0 & 0 & 0 \\ 0 & 0 & -\frac{\partial}{\partial t}\epsilon\mathbf{I} & 0 & 0 & -\epsilon\nabla & 0 & 0 \\ 0 & 0 & 0 & 0 & 0 & 0 & \epsilon\sigma^{-1}\mathbf{I} & 0 \\ 0 & 0 & 0 & 0 & 0 & 0 & 0 & \mathbf{I} \end{array} \right] \left\{ \begin{array}{c} \widetilde{\mathbf{H}} \\ \widetilde{\mathbf{B}} \\ \widetilde{\mathbf{A}} \\ \widetilde{\mathbf{D}} \\ \widetilde{\mathbf{E}} \\ \widetilde{\Phi} \\ \widetilde{\mathbf{J}} \\ \widetilde{\lambda} \end{array} \right\}. \quad (51)$$

Transforming (49) via (50) and (51) to independently varied fields it is found that symmetry of the resulting kernel matrix $\mathbf{C}^{(7)}$ is satisfied by $g_{ij} = g_{ji}$ for $i, j = 1, \ldots, 8$. Thus functional $L^{(7)}$

14

and $R^{(7)}$ are completely characterized by the symmetric functional-generating matrix

$$\mathbf{G}^{(7)} = \begin{bmatrix} g_{11} & g_{12} & g_{13} & g_{14} & g_{15} & g_{16} & g_{17} & g_{18} \\ & g_{22} & g_{23} & g_{24} & g_{25} & g_{26} & g_{27} & g_{28} \\ & & g_{33} & g_{34} & g_{35} & g_{36} & g_{37} & g_{38} \\ & & & g_{44} & g_{45} & g_{46} & g_{47} & g_{48} \\ & & & & g_{55} & g_{56} & g_{57} & g_{58} \\ & & & & & g_{66} & g_{67} & g_{68} \\ & & & & & & g_{77} & g_{78} \\ symm & & & & & & & g_{88} \end{bmatrix} \tag{52}$$

The first variation of $L^{(7)} = U^{(7)} - P^{(7)}$ may be written

$$\begin{aligned} \delta L^{(7)} &= \left(\Delta\mathbf{B}, \delta\widetilde{\mathbf{H}}\right)_{V\times t} + \left(\Delta\mathbf{H}, \delta\widetilde{\mathbf{B}}\right)_{V\times t} + \left(\mathbf{Q} - \mathbf{J}, \delta\widetilde{\mathbf{A}}\right)_{V\times t} + \left(\Delta\mathbf{E}, \delta\widetilde{\mathbf{D}}\right)_{V\times t} \\ &+ \left(\Delta\mathbf{D}, \delta\widetilde{\mathbf{E}}\right)_{V\times t} + \left(K - \rho, \delta\widetilde{\Phi}\right)_{V\times t} + \left(\sigma^{-1}\mathbf{M} - \mathbf{A}, \delta\widetilde{\mathbf{J}}\right)_{V\times t} + \left(\Delta\mathbf{J}, \delta\widetilde{\lambda}\right)_{V\times t}, \\ &- \left[\mathbf{H}_n^w, \delta\widetilde{\mathbf{A}}\right]_{S\times t} + \left[D_n^w, \delta\widetilde{\Phi}\right]_{S\times t} \end{aligned} \tag{53}$$

where now

$$\Delta\mathbf{B} = g_{11}\mathbf{B}^H + g_{12}\widetilde{\mathbf{B}} + g_{13}\mathbf{B}^A + c^{-1}\left(g_{14}\mathbf{E}^D + g_{15}\widetilde{\mathbf{E}} + g_{16}\mathbf{E}^{\Phi A} + g_{17}\mathbf{E}^J + g_{18}\epsilon^{-1}\lambda\right), \tag{54}$$

$$\Delta\mathbf{H} = g_{12}\widetilde{\mathbf{H}} + g_{22}\mathbf{H}^B + g_{23}\mathbf{H}^A + c\left(g_{24}\widetilde{\mathbf{D}} + g_{25}\mathbf{D}^E + g_{26}\mathbf{D}^{\Phi A} + g_{27}\mathbf{D}^J + g_{28}\widetilde{\lambda}\right), \tag{55}$$

$$\begin{aligned} \mathbf{Q} &= \nabla \times \left(g_{13}\widetilde{\mathbf{H}} + g_{23}\mathbf{H}^B + g_{33}\mathbf{H}^A\right) + \frac{\partial}{\partial t}\left(g_{46}\widetilde{\mathbf{D}} + g_{56}\mathbf{D}^E + g_{66}\mathbf{D}^{\Phi A} + g_{67}\mathbf{D}^J + g_{68}\widetilde{\lambda}\right) \\ &+ \epsilon c\left[\frac{\partial}{\partial t}\left(g_{16}\mathbf{B}^H + g_{26}\widetilde{\mathbf{B}} + g_{36}\mathbf{B}^A\right) + \nabla \times \left(g_{34}\mathbf{E}^D + g_{35}\widetilde{\mathbf{E}} + g_{36}\mathbf{E}^{\Phi A} + g_{37}\mathbf{E}^J + g_{38}\epsilon^{-1}\widetilde{\lambda}\right)\right], \end{aligned} \tag{56}$$

$$\Delta\mathbf{E} = c\left(g_{14}\mathbf{B}^H + g_{24}\widetilde{\mathbf{B}} + g_{34}\mathbf{B}^A\right) + g_{44}\mathbf{E}^D + g_{45}\widetilde{\mathbf{E}} + g_{46}\mathbf{E}^{\Phi A} + g_{47}\mathbf{E}^J + g_{48}\epsilon^{-1}\widetilde{\lambda}, \tag{57}$$

$$\Delta\mathbf{D} = c^{-1}\left(g_{15}\widetilde{\mathbf{H}} + g_{25}\mathbf{H}^B + g_{35}\mathbf{H}^A\right) + g_{45}\widetilde{\mathbf{D}} + g_{55}\mathbf{D}^E + g_{56}\mathbf{D}^{\Phi A} + g_{57}\mathbf{D}^J + g_{58}\widetilde{\lambda}, \tag{58}$$

$$K = -\nabla \cdot \left(g_{46}\mathbf{D}^E + g_{56}\widetilde{\mathbf{D}} + g_{66}\mathbf{D}^{\Phi A} + g_{67}\mathbf{D}^J + g_{78}\widetilde{\lambda}\right) - \epsilon c\nabla \cdot \left(g_{16}\mathbf{B}^H + g_{26}\widetilde{\mathbf{B}} + g_{36}\mathbf{B}^A\right), \tag{59}$$

$$\mathbf{M} = c^{-1}\left(g_{17}\widetilde{\mathbf{H}} + g_{27}\mathbf{H}^B + g_{37}\mathbf{H}^A\right) + g_{47}\widetilde{\mathbf{D}} + g_{57}\mathbf{D}^E + g_{67}\mathbf{D}^{\Phi A} + g_{77}\mathbf{D}^J + g_{78}\widetilde{\lambda}, \tag{60}$$

$$\Delta\mathbf{J} = c\left(g_{18}\mathbf{B}^H + g_{28}\widetilde{\mathbf{B}} + g_{38}\mathbf{B}^A\right) + g_{48}\mathbf{E}^D + g_{58}\widetilde{\mathbf{E}} + g_{68}\mathbf{E}^{\Phi A} + g_{78}\sigma^{-1}\mathbf{J} + g_{88}\epsilon^{-1}\widetilde{\lambda}, \tag{61}$$

$$\mathbf{H}_n^w = \mathbf{H}^w \times \mathbf{n} = \left(g_{13}\widetilde{\mathbf{H}} + g_{23}\mathbf{H}^B + g_{33}\mathbf{H}^A\right) \times \mathbf{n}. \tag{62}$$

$$D_n^w = \mathbf{D}^w \cdot \mathbf{n} = -\left(g_{46}\widetilde{\mathbf{D}} + g_{56}\mathbf{D}^E + g_{66}\mathbf{D}^{\Phi A} + g_{67}\mathbf{D}^J + g_{68}\widetilde{\lambda}\right) \cdot \mathbf{n}, \tag{63}$$

The multiplier field can be obtained from the Euler equation $\sigma^{-1}\mathbf{M} - \mathbf{A} = \mathbf{0}$, which yields

$$\widetilde{\lambda} = \left[\sigma\mathbf{A} - c^{-1}(g_{17}\widetilde{\mathbf{H}} + g_{27}\mathbf{H}^B + g_{37}\mathbf{H}^A) - (g_{47}\widetilde{\mathbf{D}} + g_{57}\mathbf{D}^E + g_{67}\mathbf{D}^{\Phi A} + g_{77}\mathbf{D}^J)\right]/g_{78}. \tag{64}$$

15

Now if all fields reduce to the exact ones the preceding equations become

$$\Delta B = (g_{11} + g_{12} + g_{13})B + (g_{14} + g_{15} + g_{16} + g_{17})c^{-1}E + g_{18}c^{-1}\lambda,$$

$$\Delta H = (g_{12} + g_{22} + g_{23})H + (g_{24} + g_{25} + g_{26} + g_{27})cD + g_{28}c\lambda,$$

$$Q = (g_{13} + g_{23} + g_{33})\nabla \times H + (g_{46} + g_{56} + g_{66} + g_{67})\dot{D} + g_{68}\dot{\lambda}$$
$$+ \epsilon c\left[(g_{16} + g_{26} + g_{36})\dot{B} + (g_{34} + g_{35} + g_{36} + g_{37})\nabla \times E + g_{38}\nabla \times \epsilon^{-1}\lambda\right],$$

$$\Delta D = (g_{14} + g_{24} + g_{34})c^{-1}H + (g_{44} + g_{45} + g_{46} + g_{47})D + g_{48}\lambda,$$

$$\Delta E = (g_{15} + g_{25} + g_{35})cB + (g_{45} + g_{55} + g_{56} + g_{57})E + g_{58}\epsilon^{-1}\lambda,$$

$$K = -(g_{46} + g_{56} + g_{66} + g_{67})\nabla \cdot D - g_{68}\nabla \cdot \lambda - \epsilon c(g_{16} + g_{26} + g_{36})\nabla \cdot B,$$

$$M = c^{-1}(g_{17} + g_{27} + g_{37})H + (g_{47} + g_{57} + g_{67} + g_{77})D + g_{78}\lambda,$$

$$\Delta J = c(g_{18} + g_{28} + g_{38})B + (g_{48} + g_{58} + g_{68})E + g_{78}\sigma^{-1}J + g_{88}\epsilon^{-1}\lambda,$$

$$H_n^w = H^w \times n = (g_{13} + g_{23} + g_{33})H \times n,$$

$$D_n^w = D^w \cdot n = -(g_{46} + g_{56} + g_{66} + g_{67} + g_{68})D \cdot n,$$

$$\lambda = \left[\sigma A - c^{-1}(g_{17} + g_{27} + g_{37})H - (g_{47} + g_{57} + g_{67} + g_{77})D\right]/g_{78}.$$

(65)

Consistency of $\Delta H = \Delta B = \Delta E = \Delta D = 0$, $Q - J = 0$, $K - \rho = 0$ and $\Delta J = 0$ with the field equations M_H through C_σ in (11) requires verification of the 24 conditions

$g_{11} + g_{12} + g_{13} = 0,$	$g_{14} + g_{15} + g_{16} + g_{17} = 0,$	$g_{18} = 0,$
$g_{12} + g_{22} + g_{23} = 0,$	$g_{24} + g_{25} + g_{26} + g_{27} = 0,$	$g_{28} = 0,$
$g_{13} + g_{23} + g_{33} = 1,$	$g_{34} + g_{35} + g_{36} + g_{37} = 0,$	$g_{38} = 0,$
$g_{14} + g_{24} + g_{34} = 0,$	$g_{44} + g_{45} + g_{46} + g_{47} = 0,$	$g_{48} = 0,$
$g_{15} + g_{25} + g_{35} = 0,$	$g_{45} + g_{55} + g_{56} + g_{57} = 0,$	$g_{58} = 0,$
$g_{16} + g_{26} + g_{36} = 0,$	$g_{46} + g_{56} + g_{66} + g_{67} = -1,$	$g_{68} = 0,$
$g_{17} + g_{27} + g_{37} = 0,$	$g_{47} + g_{57} + g_{67} + g_{77} = 0,$	$g_{78} = 1,$
$g_{18} + g_{28} + g_{38} = 0,$	$g_{48} + g_{58} + g_{68} = -1,$	$g_{88} = 0.$

(66)

Conditions (66) also meet the consistency requirements for the weighted boundary terms D^w and H_n^w. The boundary term $B^{(7)}$ has a structure similar to (41) but with D_n^w redefined according to (63). Furthermore, if these constraints are met, the last of (65) shows that the Lagrange multiplier field at the exact solution becomes

$$\lambda = \sigma A. \tag{67}$$

But examination of (66) uncovers a contradiction: $g_{48} + g_{58} + g_{68} = -1$ and $g_{48} = g_{58} = g_{68} = 0$ are incompatible conditions. Consequently a variational principle of the postulated form does not exist in the general time-dependent problem. But in the static case condition $g_{68} = 0$ is no longer necessary, which allows us to select $g_{68} = -1$, $g_{48} = g_{58} = 0$ and thus satisfy $g_{48} + g_{58} + g_{68} = -1$. This particular choice is further explored below.

A Restricted Variational Principle

As discussed above, the simplest $\mathbf{G}^{(7)}$ that "almost" satisfies all constraints (66) is

$$\mathbf{G}^{(7)} = \begin{bmatrix} 0 & 0 & 0 & 0 & 0 & 0 & 0 & 0 \\ 0 & 0 & 0 & 0 & 0 & 0 & 0 & 0 \\ 0 & 0 & 1 & 0 & 0 & 0 & 0 & 0 \\ 0 & 0 & 0 & 0 & 0 & 0 & 0 & 0 \\ 0 & 0 & 0 & 0 & 0 & 0 & 0 & 0 \\ 0 & 0 & 0 & 0 & 0 & -1 & 0 & -1 \\ 0 & 0 & 0 & 0 & 0 & 0 & 0 & 1 \\ 0 & 0 & 0 & 0 & 0 & -1 & 1 & 0 \end{bmatrix}. \tag{68}$$

This choice reduces the general functional to a four-field one, with the volume Lagrangian

$$L(\mathbf{A}, \Phi, \mathbf{J}, \lambda) = \int_{t_1}^{t_2} \int_V \left\{ \tfrac{1}{2}\mu^{-1}(\mathbf{B}^A)^T \mathbf{B}^A - \tfrac{1}{2}\epsilon(\mathbf{E}^{\Phi A})^T \mathbf{E}^{\Phi A} + \lambda(\sigma^{-1}\widetilde{\mathbf{J}} - \mathbf{E}^{\Phi A}) - \widetilde{\mathbf{A}}^T \widetilde{\mathbf{J}} - \rho\widetilde{\Phi} \right\} \, dV \, dt, \tag{69}$$

which may be otherwise constructed by augmenting (46) with the Lagrange multiplier term $\lambda(\sigma^{-1}\mathbf{J} - \mathbf{E}^{\Phi A})$. Its Euler equations are

$$\nabla \times \mathbf{H}^A - \dot{\mathbf{D}}^{\Phi A} - \widetilde{\lambda} = \widetilde{\mathbf{J}}, \qquad \nabla \cdot \mathbf{D}^{\Phi A} - \nabla \cdot \widetilde{\lambda} = \rho, \qquad \widetilde{\lambda} = \sigma\widetilde{\mathbf{A}}, \qquad \sigma^{-1}\widetilde{\mathbf{J}} = \mathbf{E}^{\Phi A}. \tag{70}$$

Under static conditions all field equations are satisfied because $\dot{\lambda} = 0$ and $\nabla \cdot \lambda = 0,$[8] and we have a true variational principle. But in the general (dynamic) case M_H and M_Φ are not satisfied because of the nonvanishing residual terms $\dot{\lambda} = \sigma\dot{\mathbf{A}}$ and $\nabla \cdot \lambda = \nabla \cdot (\sigma\mathbf{A}).$[9]

To render (69) into a true dynamic variational principle requires the use of complicated techniques such as inclusion of the adjoint or "image" system [1] or the method of vanishing parameters [19]. If one is content, however, with a *restricted* variational principle in the sense of Rosen [20], the above functional is augmented with compensating terms:

$$L_R(\mathbf{A}, \Phi, \mathbf{J}, \lambda) = L(\mathbf{A}, \Phi, \mathbf{J}, \lambda) - \widetilde{\mathbf{A}}^T \dot{\lambda}_0 - \widetilde{\Phi}\nabla \cdot \lambda_0. \tag{71}$$

Here field λ_0 is kept "frozen" in the variation process, upon which one sets $\lambda_0 = \lambda$. All dynamic field equations are thereby recovered. As pointed out by Finlayson [17] this technique is equivalent to the use of Galerkin's method for the residual terms, with λ_0 as test function. Note also that the second correction term is not necessary if one normalizes the divergence of that test function with the Coulomb-like gauge $\nabla \cdot \lambda_0 = 0$.

---

[8] If σ varies smoothly in space, the divergence-free condition $\nabla \cdot \lambda = 0$ has to be imposed as an adjunct of the gauge $\nabla \cdot \mathbf{A} = 0$; otherwise integration by parts is required to transform that residual into boundary terms. That transformation is mandatory if σ jumps across some material interface.

[9] The last residual term becomes $-\mu\epsilon\sigma\nabla\dot{\Phi}$ if σ is spatially uniform and the Lorentz gauge (9) is chosen to normalize $\nabla \cdot \mathbf{A}$. But generally σ varies in space when different media are considered.

17

Two- through Four-Field Functionals for Electromagnetostatics

To simplify the construction of finite element approximations it is desirable to reduce the number of fields to be discretized. For dynamic problems, the corrected four-field functional (71) appears to be the simplest one. For *static* problems, however, one may attempt further reductions subject to consistency verification. Assuming $\rho = 0$ in V, setting $\lambda = \sigma \mathbf{A}$ and $\mathbf{J} = \sigma \mathbf{E}^{\Phi} = -\sigma \nabla \Phi$ and eliminating the time dependence yields the two-field functional

$$L(\mathbf{A}, \Phi) = \int_V \left\{ \tfrac{1}{2} \mu^{-1} (\mathbf{B}^A)^T \mathbf{B}^A - \tfrac{1}{2} \epsilon (\nabla \widetilde{\Phi})^T \nabla \widetilde{\Phi} + \sigma \widetilde{\mathbf{A}}^T \nabla \widetilde{\Phi} \right\} dV. \tag{72}$$

Its first variation is

$$\delta L(\mathbf{A}, \Phi) = \left(\nabla \times \mathbf{H}^A - \mathbf{J}^{\Phi}, \delta \widetilde{\mathbf{A}} \right)_V + \left(\nabla \cdot \mathbf{D}^{\Phi} - \nabla \cdot (\sigma \mathbf{A}), \delta \widetilde{\Phi} \right)_V + \left[\mathbf{H}^A \times \mathbf{n}, \delta \widetilde{\mathbf{A}} \right]_S + \left[(\widetilde{\mathbf{D}} - \sigma \widetilde{\mathbf{A}}) \cdot \mathbf{n}, \delta \widetilde{\Phi} \right]_S \tag{73}$$

This provides the correct Euler equations if one enforces the gauge $\nabla \cdot (\sigma \mathbf{A}) = 0$ instead of $\nabla \cdot \mathbf{A} = 0$. If this condition is not enforced *a priori*, a multiplier field $\eta \nabla \cdot (\sigma \mathbf{A})$ has to be adjoined to (72).

For anticipated extensions to superconductivity it would be desirable to have $\mathbf{J}$ as a primary field whereas the electric potential Φ is of little interest. This has motivated us to study whether static principles of the form $\mathbf{L}(\mathbf{A}, \mathbf{J})$ are possible. Replacing $\mathbf{E}^{\Phi} = -\nabla \Phi$ by $\sigma^{-1} \mathbf{J}$ in (72) yields the deceptively simple form

$$L(\mathbf{A}, \mathbf{J}) = \int_V \left\{ \tfrac{1}{2} \mu^{-1} (\mathbf{B}^A)^T \mathbf{B}^A - \tfrac{1}{2} \epsilon \sigma^{-2} \widetilde{\mathbf{J}}^T \widetilde{\mathbf{J}} - \widetilde{\mathbf{A}}^T \widetilde{\mathbf{J}} \right\} dV. \tag{74}$$

Its first variation is

$$\delta L(\mathbf{A}, \mathbf{J}) = \left(\nabla \times \mathbf{H}^A - \widetilde{\mathbf{J}}, \delta \widetilde{\mathbf{A}} \right)_V - \left(\epsilon \sigma^{-2} \widetilde{\mathbf{J}} + \widetilde{\mathbf{A}}, \delta \widetilde{\mathbf{J}} \right)_V + \left[\mathbf{H}^A \times \mathbf{n}, \delta \widetilde{\mathbf{A}} \right]_S. \tag{75}$$

The second Euler equation $\epsilon \sigma^{-2} \mathbf{J} + \mathbf{A} = \mathbf{0}$, which replaces $\nabla \cdot \mathbf{D} = 0$, is generally incorrect: this is due to the elimination of $\nabla \Phi$, which inhibits the necessary integration by parts. The disappearance of the potential Φ has also the effect of forfeiting the automatic verification of the homogeneous Maxwell equation $\nabla \times \mathbf{E} = \mathbf{0}$. Both deficiencies can be corrected by augmenting (74) with two Lagrangian multiplier fields: a 3-vector κ and a scalar η to get

$$L(\mathbf{A}, \mathbf{J}, \kappa, \eta) = \int_V \left\{ \tfrac{1}{2} \mu^{-1} (\mathbf{B}^A)^T \mathbf{B}^A - \tfrac{1}{2} \epsilon \sigma^{-2} \widetilde{\mathbf{J}}^T \widetilde{\mathbf{J}} - \widetilde{\mathbf{A}}^T \widetilde{\mathbf{J}} + \widetilde{\kappa}^T \nabla \times \mathbf{E}^J + \widetilde{\eta} \nabla \cdot \mathbf{D}^J \right\} dV. \tag{76}$$

The first variation becomes

$$\delta L(\mathbf{A}, \mathbf{J}, \kappa, \eta) = \left(\nabla \times \mathbf{H}^A - \widetilde{\mathbf{J}} \right)_V - \sigma^{-1} \left(\epsilon \sigma^{-1} \widetilde{\mathbf{J}} + \widetilde{\mathbf{A}} - \nabla \times \widetilde{\kappa} + \epsilon \nabla \widetilde{\eta}, \delta \widetilde{\mathbf{J}} \right)_V$$
$$+ \left(\nabla \times \mathbf{E}^J, \delta \kappa \right)_V + \left(\nabla \cdot \mathbf{D}^J, \delta \widetilde{\eta} \right)_V + \left[\mathbf{H}^A \times \mathbf{n}, \delta \widetilde{\mathbf{A}} \right]_S + \left[\sigma^{-1} (\widetilde{\kappa} \times \mathbf{n} + \epsilon \widetilde{\eta} \mathbf{n}), \delta \widetilde{\mathbf{J}} \right]_S, \tag{77}$$

which has the correct Euler equations. For finite element work it is convenient to integrate (76) by parts to lower the variational index of $\mathbf{J}$ to zero:

$$L(\mathbf{A}, \mathbf{J}, \kappa, \eta) = \int_V \left\{ \tfrac{1}{2}\mu^{-1}(\mathbf{B}^A)^T \mathbf{B}^A - \sigma^{-1}\left(\tfrac{1}{2}\epsilon\sigma^{-1}\widetilde{\mathbf{J}} + \widetilde{\mathbf{A}} - \nabla \times \widetilde{\kappa} + \epsilon\nabla \cdot \widetilde{\eta}\right)^T \widetilde{\mathbf{J}} \right\} dV$$
$$+ \int_S \sigma^{-1}\left(\widetilde{\kappa} \times \mathbf{n} - \epsilon\widetilde{\eta}\mathbf{n}\right)^T \mathbf{E}^J \, dS. \tag{78}$$

The application of (78) or (76) to finite element discretization is simplified if $\nabla \cdot \mathbf{D}^J = \nabla \cdot (\epsilon\sigma^{-1}\mathbf{J}) = 0$ is enforced automatically on account of the nature of the problem, because if so multiplier field η is not needed. This happens in the one-dimensional axisymmetric case as the analysis of the next section shows.

5. FINITE ELEMENT DISCRETIZATION

In this section we illustrate the application of the preceding static functionals to construct finite element models for treating one-dimensional axisymmetric problems with unknown current distribution. These problems involve cylindrical conductors with hollow or solid circular cross sections carrying current axially, such as the one illustrated in Figure 1. It is convenient to use a cylindrical coordinate system (r, θ, z) as illustrated in that Figure.

The material properties may only vary radially:

$$\mu = \mu(r), \qquad \epsilon = \epsilon(r), \qquad \sigma = \sigma(r). \tag{79}$$

The unknown fields in equations (72)–(78) have the following structure and spatial dependencies:

$$\mathbf{A} = \left\{ \begin{array}{c} 0 \\ 0 \\ A_z(r) \end{array} \right\}, \quad \mathbf{B}^A = \nabla \times \mathbf{A} = \left\{ \begin{array}{c} 0 \\ -\frac{\partial A_z}{\partial r} \\ 0 \end{array} \right\}, \quad \Phi = zE_z(r), \quad \mathbf{E}^\Phi = \nabla\Phi = \left\{ \begin{array}{c} -r\frac{\partial E_z}{\partial r} \\ 0 \\ E_z \end{array} \right\}, \tag{80}$$

$$\mathbf{J} = \left\{ \begin{array}{c} 0 \\ 0 \\ J_z(r) \end{array} \right\}, \quad \mathbf{E}^J = \left\{ \begin{array}{c} 0 \\ 0 \\ \sigma^{-1}J_z \end{array} \right\}, \quad \mathbf{D}^J = \left\{ \begin{array}{c} 0 \\ 0 \\ \epsilon\sigma^{-1}J_z \end{array} \right\}, \quad \kappa = \left\{ \begin{array}{c} 0 \\ \kappa_\theta(r) \\ 0 \end{array} \right\}, \quad \nabla\times\kappa = \left\{ \begin{array}{c} 0 \\ 0 \\ \frac{1}{r}\frac{\partial(r\kappa_\theta)}{\partial r} \end{array} \right\}, \tag{81}$$

For the exact solution $E_z^J = J_z(r)/\sigma(r) = E_z$ must be a constant throughout, for otherwise $E_r^\Phi \neq 0$. Because $\nabla \cdot \mathbf{D}^J = 0$ is verified identically even if E_z (in the numerical approximation) depends on r, the multiplier field η in (76)-(78) may be omitted. Similarly, since $\nabla.(\sigma\mathbf{A})$ vanishes identically, no augmentation of (72) is required.

Over the problem domain $r_i \leq r \leq r_j, 0 \leq \theta \leq 2\pi$ and $-\tfrac{1}{2}H \leq z \leq \tfrac{1}{2}H$, functionals (72) and (78) (with $dV = 2\pi Hr\,dr$, and $dS = 2\pi rH$ on the lateral surfaces) become

$$L(A_z, \Phi) = 2\pi H \int_{r_i}^{r_j} \left\{ \frac{1}{2\mu}\left(\frac{\partial A_z}{\partial r}\right)^2 - \tfrac{1}{2}\epsilon\left(\frac{\partial\Phi}{\partial z} + \sigma A_z\right)^T \frac{\partial\Phi}{\partial z} \right\} r\,dr, \tag{82}$$

19

$$L(A_z, J_z, \kappa_\theta) = 2\pi H \int_{r_i}^{r_j} \left\{ \frac{1}{2\mu} \left(\frac{\partial A_z}{\partial r} \right)^2 - \left(\frac{\epsilon}{2\sigma^2} J_z + A_z - \frac{1}{r} \frac{\partial (r\kappa_\theta)}{\partial r} \right) J_z \right\} r \, dr + 2\pi H \kappa_\theta \sigma^{-1} r J_z \Big|_{r_i}^{r_j},$$

$$(83)$$

The boundary integral in (83) is taken only over the cylinder faces at $r = r_i$ and $r = r_j$ because the integrals over the cross sections at $z = \pm H/2$ cancel out.

Discretization

To treat the one-dimensional axisymmetric problem it is sufficient to use two-node "line" elements that represent rectangular tori of common z-dimension H. Here we consider an individual element identified by superscript e. The two element end nodes are denoted by i and j, with inner and outer radial coordinates r_i^e and r_j^e, respectively. The element radial length is $L^e = r_j^e - r_i^e$ and the mean radius is $r_m^e = \frac{1}{2}(r_i^e + r_j^e)$. The material properties (79) are taken to be constant over each element and are denoted by μ^e, ϵ^e and σ^e.

In functionals (82) and (83) fields Φ, A_z and κ_θ appear with variational index 1 that requires C^0 continuity, and consequently are interpolated linearly over the element:

$$\Phi^e = z\mathbf{N}\Phi^e = z[N_i^e \ N_j^e] \begin{Bmatrix} \Phi_i^e \\ \Phi_j^e \end{Bmatrix}, \quad A_z^e = \mathbf{N}A_z^e = [N_i^e \ N_j^e] \begin{Bmatrix} A_{z_i}^e \\ A_{z_j}^e \end{Bmatrix}, \quad \kappa_\theta^e = \mathbf{N}\kappa_\theta^e = [N_i^e \ N_j] \begin{Bmatrix} \kappa_{\theta_i}^e \\ \kappa_{\theta_j}^e \end{Bmatrix}.$$

$$(84)$$

Here row vector $\mathbf{N}$ (with element superscript suppressed for simplicity) contains the linear-in-r finite element shape functions $N_i^e = (r_j^e - r)/L^e$ and $N_j^e = (r - r_i^e)/L^e$. On the other hand J_z in functional (83) has variational index 0 thus admitting C^{-1} continuity, and will be approximated as a constant (step) function J_z^e over the element.

Substituting the finite element assumptions into (82)–(83) and taking variations with respect to the nodal values yields the following element contributions:

$$\delta L(A_z^e, \Phi_z^e) = \begin{Bmatrix} \delta A_z^e \\ \delta \Phi^e \end{Bmatrix}^T \begin{bmatrix} \mathbf{K}_{AA}^e & \mathbf{K}_{A\Phi}^e \\ \mathbf{K}_{\Phi A}^e & \mathbf{K}_{\Phi\Phi}^e \end{bmatrix} \begin{Bmatrix} A_z^e \\ \Phi^e \end{Bmatrix},$$

$$(85)$$

$$\delta L(A_z^e, J_z^e, \kappa_\theta^e) = \begin{Bmatrix} \delta A_z^e \\ \delta J_z^e \\ \delta \kappa_\theta^e \end{Bmatrix}^T \begin{bmatrix} \mathbf{K}_{AA}^e & \mathbf{K}_{AJ}^e & 0 \\ \mathbf{K}_{JA}^e & K_{JJ} & \mathbf{K}_{JK}^e \\ 0 & \mathbf{K}_{KJ}^e & 0 \end{bmatrix} \begin{Bmatrix} A_z^e \\ J_z^e \\ \kappa_\theta^e \end{Bmatrix},$$

$$(86)$$

20

in which

$$\mathbf{K}^e_{AA} = 2\pi H \int_{r^e_i}^{r^e_j} (\mu^e)^{-1} \left(\frac{\partial \mathbf{N}}{\partial r}\right)^T \frac{\partial \mathbf{N}}{\partial r} r\, dr = 2\pi H r^e_m (\mu^e L^e)^{-1} \begin{bmatrix} 1 & -1 \\ -1 & 1 \end{bmatrix},$$

$$\mathbf{K}^e_{\Phi\Phi} = 2\pi H \int_{r^e_i}^{r^e_j} \epsilon^e \mathbf{N}^T \mathbf{N} r\, dr = 2\pi H \epsilon^e L^e \tfrac{1}{6} \begin{bmatrix} 2r^e_m - \tfrac{1}{2}L^e & r^e_m \\ r^e_m & 2r^e_m + \tfrac{1}{2}L^e \end{bmatrix},$$

$$\mathbf{K}^e_{A\Phi} = 2\pi H \int_{r^e_i}^{r^e_j} \epsilon^e \sigma^e \left(\frac{\partial \mathbf{N}}{\partial r}\right)^T \mathbf{N} r\, dr = 2\pi H \epsilon^e \sigma^e \tfrac{1}{2} \begin{bmatrix} -r^e_m + \tfrac{1}{6}L^e & -r^e_m - \tfrac{1}{6}L^e \\ r^e_m - \tfrac{1}{6}L^e & r^e_m + \tfrac{1}{6}L^e \end{bmatrix} = (\mathbf{K}^e_{\Phi A})^T$$

$$\mathbf{K}^e_{AJ} = 2\pi H \int_{r^e_i}^{r^e_j} \mathbf{N}^T r\, dr = 2\pi H L^e \tfrac{1}{2} [\, r^e_m - \tfrac{1}{6}L^e \quad r^e_m + \tfrac{1}{6}L^e \,] = (\mathbf{K}^e_{JA})^T,$$

$$K^e_{JJ} = 2\pi H \int_{r^e_i}^{r^e_j} \epsilon^e (\sigma^e)^{-2} r\, dr = 2\pi H \epsilon^e (\sigma^e)^{-2} r^e_m L^e,$$

$$\mathbf{K}^e_{J\kappa} = 2\pi H \int_{r^e_i}^{r^e_j} (\sigma^e)^{-1} \frac{1}{r} \frac{\partial(r\mathbf{N})}{\partial r} r\, dr = 2\pi H (\sigma^e)^{-1} [\, -r^e_i \quad r^e_j \,] = (\mathbf{K}^e_{\kappa J})^T.$$

$$(87)$$

The finite element equations may now be assembled in the usual manner and result in the master stiffness equations

$$\mathbf{Kv} = \mathbf{p},\tag{88}$$

where, using terminology and notation analogous to structural mechanics, $\mathbf{K}$ denotes the master stiffness matrix, $\mathbf{v}$ the array of degrees of freedom, and $\mathbf{p}$ the corresponding force vector. More details as regards the structure of this system and the application of boundary and global-constraint conditions are given below for the finite element model based on the functional (83).

Finite Element Model and Boundary Conditions

Element models (85) and (86) have the same number (four) of end-node degrees of freedom. The second one also has an internal degree of freedom J^e_z. In the sequel we shall consider only model (86) formulated from the $L(A_z, J_z, \kappa_\theta)$ functional because imposition of the total-current constraint condition is easier.

For this model the axisymmetric "line" elements may be regarded as having four nodes:

1. The two element end nodes i and j at which A_z and κ_θ are assigned.

2. One interior node at the element center where J^e_z is assigned.

3. A "global" node shared by all conducting elements where the Lagrange multiplier λ_g defined below is assigned. This is conventionally placed at the outer end of the mesh.

The magnetic potential $A_z(r)$ is determined up to an arbitrary constant. Conventionally we fix that constant by setting $A_z = 0$ on the outermost node of the mesh, located in free space. The "reaction force" corresponding to this constraint can be readily worked out [6] to be $-I$, where I is the total current flowing through the wire. This "force" is in fact obtained from Ampère's law by integrating the flux H over a circular path on the wire boundary.

21

This boundary term can be given two different physical interpretations. The first interpretation has a current I in the conductor and a field $-\mathbf{H}_b$ at the boundary. $\mathbf{H}_b$ is generated by the current within the conductor. The second interpretation has zero current in the conductor and an external applied field equal to $\mathbf{H}_b$ at the boundary. Distinguishing between these two interpretations is crucial in superconductivity modeling [8] so as to start from the physically correct state in nonlinear path continuation procedures.

For normal (nonsuperconducting) conductors the first interpretation is the most practically important one. To impose the current conservation constraint, $I - \int_\Gamma \mathbf{J}_z \cdot \mathbf{d}\Gamma = 0$, where Γ is the wire cross section area, the functional (84) is augmented by that constraint weighted by a Lagrange multiplier λ_g. The discretized form of that term is

$$\lambda_g \left(I - \sum_{e=1}^{N_{ce}} \int_{\Gamma_e} J_z^e \, d\Gamma_e \right), \tag{89}$$

where N_{ce} is the number of conducting elements, and $\Gamma_e = 2\pi r_m^e L^e$ is the normal-to-z element cross section. The Lagrange multiplier freedom λ_g is assigned to a "global" node shared by all elements as discussed above.

The complete degree of freedom vector $\mathbf{v}$ has the following structure:

$$\mathbf{v} = \{ A_{z_1} \quad A_{z_2} \quad \dots \quad A_{z_{N_n}} \quad J_{z_1} \quad J_{z2} \quad \dots \quad J_{z_{N_e}} \quad \kappa_{\theta_1} \quad \kappa_{\theta_2} \quad \dots \kappa_{\theta_{N_{cn}}} \quad \lambda_g \}^T, \tag{90}$$

where $N_n = N_e + 1$ is the total number of nodes and $N_{cn} = N_{ce} + 1$ the number of "conducting nodes" (nodes attached to conducting elements). The associated force vector $\mathbf{p}$ in (88) has all zero entries except for the last one (that corresponding to λ_g), which is $-I$ to enforce the total current constraint. The last row and colum of $\mathbf{K}$ are modified to implement the bilinear terms in (89).

Finally, an essential boundary condition on κ_θ can be obtained in the following manner. The second Euler equation in (83) yields for the exact solution

$$\frac{1}{r} \frac{\partial(r \kappa_\theta)}{\partial r} = \epsilon \sigma^{-2} J_z + \sigma^{-1} A_z. \tag{91}$$

Integration of this differential equation shows that κ_θ must have the form $\kappa_\theta = r k(r)$, where $k(r)$ is regular at the origin. It follows that $\kappa_\theta(0) = 0$. Consequently the value κ_{θ_1} at a node on the z-axis must be prescribed to be zero.

Test Problems

The formulation presented in the previous subsection has been applied to two one-dimensional axisymmetric test problems discussed below. Both problems involve conduction along the solid wire of circular cross section depicted in Figure 1.

All elements have a unit thickness $H = 1$ in the z direction. The finite element mesh is terminated at a finite size outside the wire. For both test problems, the outer radial end of the mesh
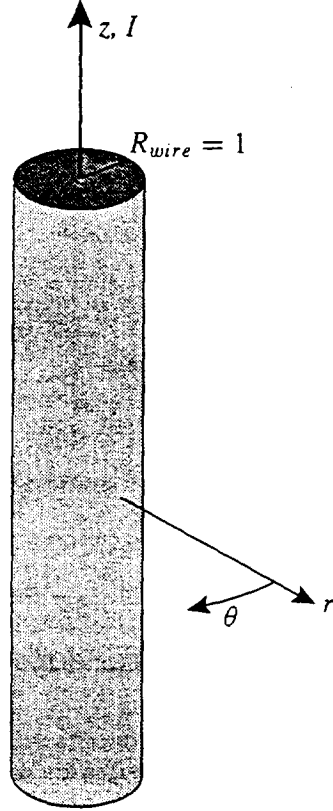
Figure 1. Infinite wire of circular cross section carrying total current I, referred to a cylindrical coordinate system r, θ, z.

is defined as the truncation radius $r = R_T$. The outer radial end of the conductor's mesh is defined as the wire radius $r = R_{wire}$. Because current is only carried in the conductor, the J_z^e freedoms between R_{wire} and R_T are constrained to be zero.

The components of the element stiffness matrix corresponding to the conducting elements (1 to N_{ce}) are calculated and merged into the master stiffness matrix. The components for the free-space elements are next determined and merged. The total-current constraint (89) is imposed on the master stiffness and the load vector. Finally, essential boundary conditions on individual node values are set as previously explained. The master equations modified for B.C. are processed by a standard symmetric skyline solver, which returns the computed $\mathbf{v}$ vector.

The physical quantities of interest are not $A_{z_j}^e$, but the magnetic field B_θ and the current density J_z. According to (80) $B_\theta = -(\partial N/\partial r) A_z^e$. Since A_z^e is linearly interpolated over the element, only a mean value B_θ^e can be recovered with that formula. Plots for B_θ are not included here because of space constraints, but may be found in Ref. [8]. Instead, the results for J_z are presented to illustrate the accuracy that may be obtained by using the variational approach.

The ability of the potential-based variational principles to accurately model discontinuities in the **B** field at a conductor/free space interface has already been established for one- and two-
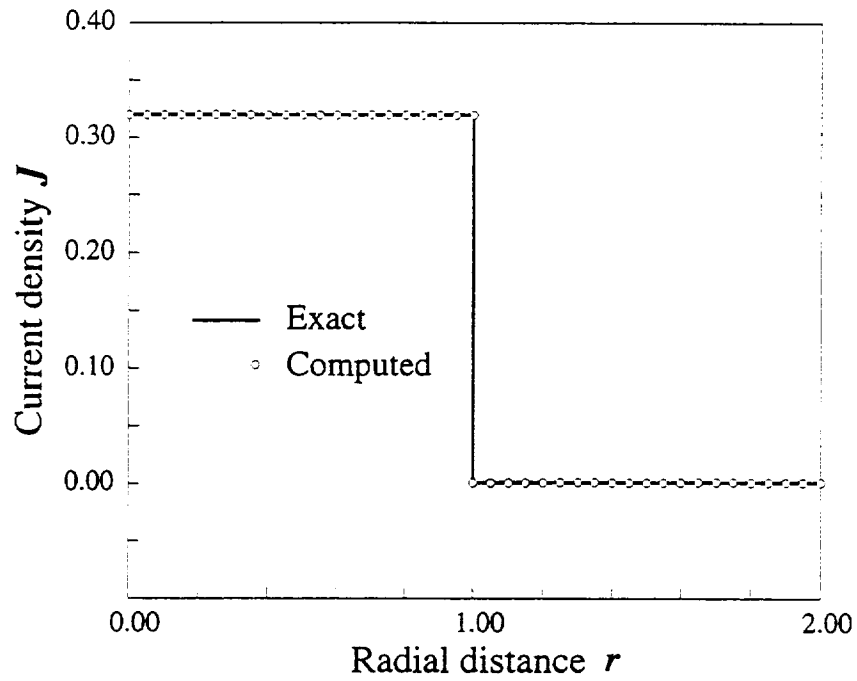
23

Figure 2. Current density J_z versus radial distance r for equal-conductivity test case. Computed solution plotted as points to highlight accuracy of method in matching exact solution.
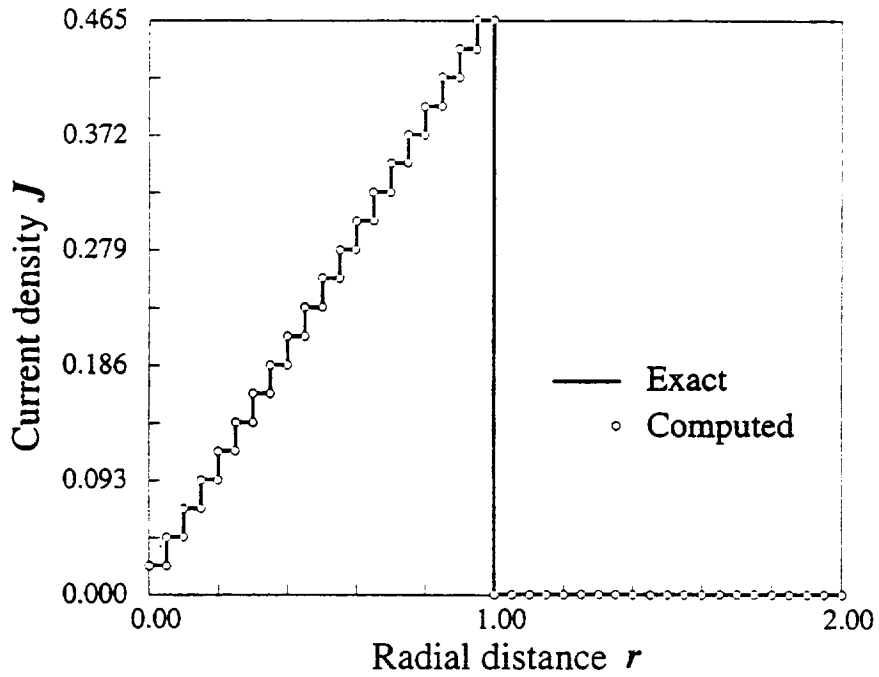

Figure 3. Current density J_z versus radial distance r for conductivity set equal to element index. Computed solution plotted as points to highlight accuracy of method in matching exact solution.

dimensional problems in previous work [6, 7]. Consequently in both test problems μ and ϵ are set to unity in the wire and free space. In the first test problem the conductivity σ^e is set to one for all wire elements. In the second problem this is set to the element number, *i.e.* $\sigma^e = e$. Since the wire elements have equal radial width, this admittedly artificial assumption models a "layered" wire with conductivity varying in linear stepwise fashion from $r = 0$ to $r = R_{wire}$.

Discussion of Test Results

The first test problem is identical to that reported in Schuler and Felippa [6], where the current density was assumed *a priori* to be uniform. As shown in Figure 1, it consists of a wire conductor of radius R_{wire} transporting a total current I equal to one ampere in the z direction. The radial direction is discretized with N_{wire} elements inside the wire and N_{free} elements outside the wire in free space. The mesh is truncated at a "truncation radius" R_T, where $A_z = 0$. Other boundary conditions are set as previously stated. The conductivity σ is unity everywhere.

The results obtained with $R_T = 2R_{wire}$, $N_{wire} = N_{free} = 20$ for the potentials and B_θ matched those generated by the prescribed-current potential-based finite elements [6]. Figure 2 shows the analytical and computed solutions for the current density J_z. The computed results differ from the exact uniform current distribution by less than 10^{-6}, thus providing a check on the element calculations.

The second problem is identical to the first one in all respects except that $\sigma^e = e$ for $e = 1, \ldots, N_{free}$. The exact current distribution is an element-driven step function. Figure 3 shows the exact and computed solutions for J_z. The results were as accurate as those reported in the first problem. The computed potentials and magnetic fields (not shown here) displayed the same order of accuracy obtained for the prescribed-current finite elements in previous work [6,7].

6. CONCLUSIONS

Two families of parametrized functionals for linear electromagnetodynamics have been presented. The six-field family is applicable to problems where the current density is given, and is valid in static and dynamic situations. The seven-field family allows the current density to be an independent field. This family yields true variational principles for time-independent problems. In the dynamic case it supplies a basis for the development of restricted variational principles from which Galerkin approximations can be constructed. In the static case it supplies a framework for obtaining "problem customized" principles with reduced number of varied fields.

The results obtained in test problems show that it is possible to extend our previous finite element formulations to cover the situation where the current distribution is not known *a priori*. This is encouraging for its application to superconductivity. The two reduced-field static functionals analyzed in some detail are computationally similar in the one-dimensional axisymmetric idealization. The functional with J_z as primary variable permits, however, a simpler implementation of a total-current conservation constraint. For two- and three-dimensional problems, however, (72) is likely to be computationally superior over (78) because it has less degrees of freedom per connected

node.[10]

We finally comment on the feasibility of extending these variational principles in the following directions.

Anisotropy. The principles are not affected in any way by making μ, ϵ and σ tensors as long as they do not depend on time (or frequency). Space dependence *per se* does not introduce difficulties.

Ferromagnetism. If μ is a unique nonlinear function of the magnetic intensity, extension is straight-forward as long as $\mu > 0$. If path dependence (hysteretic) effects are considered, only rate forms can be constructed.

Mechanical Motion. To account for motion of the reference frame, the Maxwell equations have to be modified for velocity effects. A hierarchy of corrections may be built depending on the relative speed of these motions with respect to the light. For many practical problems in electric machinery the first-order correction, which retains Galilean frames and ignores relativistic effects, is sufficient.

Interaction with Mechanical and Thermal Fields. Including effects such as piezoelectricity, magnetostrictivy and thermomagnetics (see, for example, Parkus [21]) into the linear theory require expanding the number of field variables and equations, much in the same manner as one passes from six-field to seven-field functionals. The complexity of the systems, however, may make use of symbolic computations a necessity.[11]

Superconductivity. As noted in the Introduction, this is our primary goal. The principles (17) of linear electromagnetics may be extended to cover superconductivity by appending a term G:

$$\boxed{R = U - P + B + G = L + B + G} \tag{92}$$

This additional term, which is highly nonlinear and vanishes on normal-conducting volume portions, depends on the superconducting model. The London and Ginsburg-Landau models for Type I and II superconductors [22,23] have been investigated [8]. The Ginsburg-Landau model requires the introduction of an additional complex-valued field Ψ, which models quantum-mechanics effects. Interaction with temperature and accounting for phase changes remain important objectives of the superconductor simulation.

---

[10] Assuming that the η field need to be retained in (78), the "element connector" degree-of-freedom ratio between $L(\mathbf{A}, \Phi)$ and $L(\mathbf{A}, \mathbf{J}, \kappa, \eta)$ is 3/5 in two dimensions and 4/7 in three dimensions. In addition (78) requires one internal node for the $\mathbf{J}$ components.

[11] In fact most derivations in Sections 3 and 4 of the present paper were carried out with MACSYMA.

REFERENCES

1. P. Hammond, *Energy Methods in Electromagnetism*, Clarendon Press, Oxford, 1981

2. J. B. Davies, 'The finite element method,' Chapter 2 in *Numerical Techniques for Microwave and Millimeter-Wave Passive Structures*, ed. by T. Itoh, Wiley, New York, 1989

3. C. W. Trowbridge, 'Numerical solution of electromagnetic field problems in two and three dimensions,' Chapter 18 in *Numerical Methods in Coupled Problems*, ed. by R. Lewis *et.al.*, Wiley, London, 1984

4. J. Simkin and C. W. Trowbridge, 'Finite Elements and Magnetic Scalar Potentials,' in *The Finite Element Method in the 1990's*, ed. by E. Oñate, J. Perriaux and A. Samuelsson, CIMNE, Barcelona and Springer-Verlag, Berlin, 509–517 (1991)

5. A. Silvester and R. L. Ferrari, *Finite Elements for Electrical Engineers*, Cambridge, 2ed. 1990

6. J. J. Schuler and C. A. Felippa, 'Electromagnetic Finite Elements Based on a Four-Potential Variational Principle', *Finite Elements in Analysis and Design*, **6**, 273–284 (1990)

7. J. J. Schuler and C. A. Felippa, 'Electromagnetic Axisymmetric Finite Elements Based on a Gauged Four-Potential Variational Principle', presented at the *Symposium on Computational Technology for Flight Vehicles*, November 5–7, 1990, Washington, D.C. also in in *J. Computing Systems in Engineering*, **1**, 273–285 (1991)

8. J. J. Schuler and C. A. Felippa, 'Analysis of Superconducting Electromagnetic Finite Elements Based on a Magnetic Vector Potential Variational Principle', CSSC report CU-CSSC-91-28, Department of Aerospace Engineering Sciences, Center for Space Structures and Controls, University of Colorado at Boulder, October 1991.

9. C. A. Felippa, 'Parametrized Multifield Variational Principles in Elasticity: I. Mixed Functionals,' *Communications in Applied Numerical Methods*, **5**, 79–88 (1989)

10. C. A. Felippa, 'Parametrized Multifield Variational Principles in Elasticity: II. Hybrid Functionals and the Free Formulation,' *Communications in Applied Numerical Methods*, **5**, 89–98 (1989)

11. C. A. Felippa and C. Militello, 'Developments in Variational Methods for High-Performance Plate and Shell Elements,' in *Analytical and Computational Methods for Shells*, CAD Vol. 3, ed. by A. K. Noor, T. Belytschko and J. C. Simo, American Society of Mechanical Engineers, ASME, New York, 191–216 (1989)

12. C. A. Felippa and C. Militello, 'The Variational Formulation of High-Performance Finite Elements: Parametrized Variational Principles,' *Computers & Structures*, **36**, 1–11 (1990)

13. C. A. Felippa, 'Parametrized Variational Principles Encompassing Compressible and Incompressible Elasticity,' *Int. J. Solids Structures*, **29**, 57–68 (1991)

14. C. Lanczos, *The Variational Principles of Mechanics*, Dover, New York, 4th ed., 1970

15. W. Yourgrau and S. Mandelstam, *Variational Principles in Dynamics and Quantum Theory*, Dover, New York, 1968

16. I. M. Gelfand and S. V. Fomin, *Calculus of Variations*, Prentice-Hall, Englewood Cliffs, NJ, 1963

17. B. A. Finlayson, *The Method of Weighted Residuals and Variacional Principles*, Academic Press, New York, 1972

18. J. T. Oden and J. N. Reddy, *Variational Methods in Theoretical Mechanics*, Springer-Verlag, Berlin, 1983

19. B. D. Vujanovic and S. E. Jones, *Variational Methods in Nonconservative Phenomena*, Academic Press, New York, 1989

20. P. Rosen, 'On Variational Principles for Irreversible Processes,' *J. Chem. Phys.*, **21**, 1220–1221 (1953)

21. H. Parkus (ed.), *Electromagnetic Interactions in Elastic Solids*, Springer-Verlag, Berlin, 1979

22. C. Kittel, *Introduction to Solid State Physics*, 6th. ed, Wiley, New York, 1986

23. M. Tinkham, *Introduction to Superconductivity*, Krieger Pub. Co., Malabar, FA, 1975

PART II

FINITE ELEMENT ANALYSIS OF
TIME-INDEPENDENT SUPERCONDUCTIVITY

ABSTRACT

The focus of this part is the development of electromagnetic (EM) finite elements

based upon a generalized four-potential variational principle. The final goal of this research

is to formulate, develop and validate finite element models that can accurately capture elec-

tromagnetic, thermal and material phase changes in a superconductor. The use of the four-

potential variational principle allows for downstream coupling of electromagnetic fields with

the thermal, mechanical and quantum effects exhibited by superconducting materials. The

use of variational methods to model an electromagnetic system allows for a greater range

of applications than just the superconducting problem. In fact, the four-potential variational

principle can be used to solve a broader range of EM problems than any of the currently

available formulations. It also reduces the number of independent variables from six to four

while easily dealing with conductor/insulator interfaces.

This methodology has been applied to a range of EM field problems. Seven

problems are presented here. These applications show the power of the four-potential

variational method, when augmented by Lagrange multiplier weighted constraint equations,

to solve diverse EM field problems. All of the finite element models predict EM quantities exceptionally well and match the expected physical behavior.

The results obtained with these finite element models display in previously unseen detail the physics of the superconducting charge carriers within the boundary layer of a Ginzburg-Landau superconductor. These results are compared to the physics of a low viscosity fluid problem. From this analogy, a physical argument is advanced about superconductors. This argument is that the small resistance that exists within a superconductor is similar in origin to the viscous effects of fluid and can be attributed to collisions that occur between moving and static charge carriers.

INTRODUCTION

1.1 MOTIVATION AND BACKGROUND.

The computer simulation of electromagnetic (EM) field problems has received considerable attention during the past thirty years. This is a direct result of the realization among scientists and engineers that the computer could be exploited to solve EM problems that had previously been too complex or cumbersome to be treated by established analytical techniques. Before the advent of computer technology, solutions of EM field problems were often limited to relatively simple problems or geometries. Generally, the intractability of standard analytical techniques and the nonlinearity of solutions of EM problems is largely a result of the coupling between electric and magnetic fields. With the aid of computers, the inherent nonlinearity of EM field problems became more manageable and more complex EM systems problems could be and were solved. When problem solving capabilities advanced, so did computer and electrical engineering technology. These new technologies were then increasingly used in aerospace applications. These applications were in control and guidance as well as more efficient servos, motors, generators and electronic sensing and surveillance gear. More recently, high-temperature superconductors (HTS) have been discovered. These composite materials are presently the subject of intensive experimental research

31

and are expected to have a major impact in space propulsion, digital computing, power systems and communications in the next century.

The present work is part of a research program for the numerical simulation of EM/mechanical systems that involve superconductors. The point of departure from previous works is the use of finite elements based upon a four-potential variational principle to predict desired EM quantities.

The simulation involves the interaction of the following four components:

(1) *Thermal Fields*: temperature and heat fluxes.

(2) *Electromagnetic Fields*: electric and magnetic field strengths and fluxes, currents and charges.

(3) *Quantum Mechanics*: the constitutive behavior of the superconducting system is governed by quantum mechanical effects. Particularly important is the superconducting phase change, governed by phenomena at the quantum level, and triggered by thermal, mechanical and EM field energy levels.

All three components can be treated by the finite element method. This treatment produces the spatial discretization of the continuum into mechanical, thermal, quantum mechanical and electromagnetic meshes of a finite number of degrees of freedom. The finite element discretization may be developed in two ways:

(1) *Simultaneous Treatment*. The whole problem is treated as an indivisible whole. The four meshes noted above become tightly coupled, with common nodes and elements.

(2) *Staged Treatment.* The mechanical, thermal and electromagnetic components of the problem are treated separately. Finite element meshes for these components may be developed separately. Coupling effects are viewed as information that has to be transferred between these four meshes.

The present research follows the staged treatment. More specifically, we develop finite element models for the fields in isolation, and then treat coupling effects as interaction forces between these models. This "divide and conquer" strategy is ingrained in the partitioned treatment of coupled problems [2,3], which offers significant advantages in terms of computational efficiency and software modularity. Another advantage relates to the way research into complex problems can be made more productive. It centers on the observation that some aspects of the problem are either better understood or less physically relevant than others. These aspects may then be temporarily left alone while efforts are concentrated on the less developed and/or more physically important aspects. The staged treatment is better suited to this approach. Of the four components listed previously, the last two are less developed in a modeling and computational sense.

Mechanical elements for this research have been derived using general variational principles that decouple the element boundary from the interior, thus providing efficient ways to work out coupling with non-mechanical fields. The point of departure was the previous research into the free-formulation variational principles presented by Felippa [4]. A more general formulation for the mechanical elements, which includes the assumed natural deviatoric strain formulation was established and reported in Refs. [5,6,7,8]. New representations of thermal fields have not been addressed as standard formulations

33

are considered adequate for the coupled-field phases of this research. However, research in thermomechanical interactions supported by this program has resulted in the construction of robust and efficient staggered solution procedures [9].

The development of EM finite elements to date has not received the same degree of attention given to mechanical and thermal elements. Part of the reason is the widespread use of analytical and semianalytical methods in electrical engineering. These methods have been highly refined for specialized but important problems such as circuits and wave guides. Thus the advantages of finite elements in terms of generality have not been enough to counterweight established techniques. Much of the EM finite element work to date has been done in England and is well described in the surveys by Davies [10] and Trowbridge [11]. The general impression conveyed by these surveys is one of an unsettled subject, reminiscent of the early period (1960-1970) of finite elements in structural mechanics. A great number of formulations that combine flux, intensity, and scalar potentials are described with the recommended choice varying according to the application, medium involved (polarizable, dielectric, semiconductors, etc.), number of spatial dimensions, time-dependent characteristics (static, quasi-static, harmonic, or transient), as well as other factors of lesser importance. The possibility of a general variational formulation has not been recognized.

1.2 REVIEW OF EXISTING TECHNIQUES

As mentioned previously, the computer simulation and modeling of EM field problems is presently an unsettled subject especially in nonlinear problems. A rich variety of mathematical techniques have been used to solve these complex problems. Some of these techniques involve using integral transforms to find a solution, while other techniques yield solutions to the integral or differential EM field equations that contain Bessel, Airy, Gamma, and Legendre functions [12]. A common method of computer implementation involves taking the analytical representation of the solution to a problem and making a numerical approximation to that solution. In time-independent problems the implementation may take the form of discretizing the analytical differential or integral EM field equations over the system's spatial dimensions [13]. Linear time-dependent problems may be transformed to Fourier or Laplace space, solved, and then converted back to the real time domain. The computer is simply used to make good approximations to an integral which is an analytical solution to the problem, but for which no closed form solution of the integral exists. While these methods are effective for specific problems, they are rarely of a general enough nature that they can be used on most EM system problems. A recognition of the interest in and the need for more generalized computer solution techniques for EM field problems led to the first COMPUMAG series of conferences in 1976 [11, p. 506].

Prior to this time, few finite element techniques existed but the power of more generalized schemes were demonstrated in finite difference codings that used the differential forms of *Maxwell's* field equations. Usually the conventional field quantities were replaced by potentials and the resultant

EM field equations were discretized over space [14, pp. 101-105;15,16]. Finite difference schemes generally are not as amenable to Neumann boundary conditions or an easy change to a higher variational order as finite element methods. Because of the prevelance of Neumann boundary conditions in EM field problems, especially when conventional field quantities are replaced by a potential formulation, as well as difficulties associated with a change in the variational order of variables when finite difference methods are used, finite difference techniques are rarely used for the spatial discretization of EM field equations.

Maxwell's EM field equations may be recast in a potential formulation. This reduces the number of independent variables for the electric field $\mathbf{E}$ from three to one through the substitution $\mathbf{E} = -\nabla \Phi$, where Φ is the electrostatic potential. The reformulation of the magnetic field is more complicated. In free space, the magnetic field $\mathbf{B}$ can be defined as the negative gradient of the magnetostatic potential φ (i.e., $\mathbf{B} = -\nabla \varphi$). This substitution reduces the number of independent variables from three to one for the magnetic field but this potential is neither single valued nor defined in a conductor that is carrying a steady current [14, p.139]. Another reformulation substitutes the curl of the magnetic vector potential $\mathbf{A}$ for $\mathbf{B}$ (i.e., $\nabla \times \mathbf{A} = \mathbf{B}$). Although this formulation does not reduce the number of independent variables in an EM field problem, it does require that the solution of $\mathbf{A}$ be C^o continuous across material interfaces, thus simplifying finite element development. Formulations that use the $\mathbf{B}$ field as a primary variable are not required to be C^o continuous across material boundaries. In spite of the difficulties presented by a discontinuous variable, the majority of EM

field finite element formulations to date are based on the original EM fields, *e.g.*, see Refs. [17,18].

Some researchers have also experimented with magnetic vector potential based finite elements [11]. These formulations use a Galerkin weighted residual method applied to the strong form of the EM field equations. The drawback with this approach is that the uniqueness of a numerical solution is questionable because the divergence of $\mathbf{A}$ is not specified. A variational approach based upon $\mathbf{A}$ can easily overcome this difficulty by specifying a function or *gauge* for the divergence of $\mathbf{A}$, weighting it by a Lagrangian multiplier, and augmenting it to the energy functional of the EM system. The only requirement on the choice of gauge is that the Euler equations of the weighted gauge choice equal zero. Another statement of this requirement is that the augmented energy functional should differ from the EM field energy functional by a constant [19, p. 36]. In fact, by an appropriate use of the *Lorentz* gauge, the Lagrangian, or energy functional, of the EM field equations can be used to perform a canonical transformation to produce the Hamiltonian of the system [20, pp. 72-91]. The only EM finite elements that use the approach of energy functionals augmented by a weighted gauge equation are the ones presented in this work.

As mentioned on the previous page, the magnetic scalar potential can be used to calculate the $\mathbf{B}$ field in free space and reduce the number of independent variables from three to one. To increase computational speed and reduce memory allocation, Trowbridge [11] has coupled $\mathbf{A}$ with φ to produce a new independent variable vector quantity $\mathbf{R}$. $\mathbf{R}$ requires that three variables be solved in a conducting media and only one variable be solved in free space. This method has drawbacks, specifically that $\mathbf{R}$ and φ are not

unique, and that in the interior of conductors cancellation problems arise that can give erroneous values for **B** [11, pp. 521-525].

To model EM fields in a superconductor, another field variable must be included: the wave order parameter ψ. This function can be complex and the absolute value of ψ times its complex conjugate ($|\psi\psi^*| = |\psi|^2$) is defined as the number density of superconducting electron pairs. This new variable accounts for the quantum mechanical effects that appear in the interior of a superconductor. These quantum effects change the value of the **B** field and current density vector **j** within a superconductor.

A widely used mathematical model that describes quantum and EM interactions within a superconductor are the *Ginzburg-Landau* equations [21, p. 104] . These equations reduce to Maxwell's equations, the same equations that govern EM fields in normal conductors and in vacuum. The Ginzburg-Landau equations are derived using variational principles and require a unique gauge choice to ensure that a superconducting current can only exist in a conductor as physics demands. The gauge choice used in the present work is called the *London* gauge and is equivalent to the Lorentz gauge for magnetostatic problems. The Ginzburg-Landau equations also contain **A** explicitly as well as the vector curl of **A**. To model superconductors numerically, the optimal choice of independent variables is to use **A**. The use of a field based formulation requires the numerical integration of **B** to remove terms in the Ginzburg-Landau equations that contain **A**. This integration can easily become the source of additional numerical error, an error that is not present when the choice of independent variable is **A**.

A finite difference formulation of the Ginzburg-Landau equations has been developed that producs reasonable results [15,16]. The formulation uses

A as a primary variable, but thermal effects are neglected when this model is in the normal state. This formulation also suffers from the previously mentioned drawbacks of finite difference methods in the treatment of arbitrary geometries.

1.3 THESIS CONTENT.

The objective of this thesis is to develop EM finite elements for type I and II superconductors based upon a gauged four-potential variational principle. At present, the physics of high temperature superconductors (HTS) are not well enough understood to permit the development of an adequate mathematical model. The last elements developed in this work include thermal coupling, but are magnetostatic. This restriction is motivated by the fact that the time-independent problem exhibits strong nonlinearities; furthermore, no completely satisfactory mathematical model has been developed for the time-dependent case [21, p. 273]. The highly nonlinear nature of the problem is the result of a boundary layer effect exhibited at a superconductor/normal conductor or superconductor/vacuum interface. Extremely strong gradients of the independent variables ψ, $\mathbf{A}$, $\mathbf{B}$, and $\mathbf{j}$ are present in this regime. These gradients bring about serious numerical difficulties, the most important ones being a highly ill-conditioned system of incremental equations and the need for specialized mesh discretization. The final superconducting finite element developed is of a general enough nature that it works equally well in both the boundary layer and the bulk of the superconductor. Unlike the previously mentioned field based formulations, this element requires no special treatment for material interfaces, in particular, the superconductor/vacuum interface.

The derivation of all of the EM finite elements in this thesis are based upon a four-potential variational formulation that uses the four-potential as the primary variable. The electric field is represented by a scalar potential and the magnetic field by a vector potential. When the superconductor is modeled, the electric field scalar potential is dropped, because it does not couple with the magnetic field in the magnetostatic case. The modulus and phase of ψ are then added as new independent variables. The formulation of the four-potential variational principle proceeds along lines previously developed for the acoustic fluid problem [22,23]. The appropriate gauge normalization is incorporated in the variational (weak) form through the adjunction of a Lagrange multiplier field.

The main advantages of developing finite elements using a potential based variational formulation in contrast to using existing EM numerical techniques are summarized as follows.

(1) Interface discontinuities are automatically taken care of without any special intervention.

(2) No approximations are invoked *a priori* since the general Maxwell equations are used.

(3) The number of degrees of freedom per finite element node is kept modest as the problem dimensionality increases.

(4) Higher order and hybrid elements are more easily accomodated.

(5) The Ginzburg-Landau equations naturally possess **A** as an independent variable; possibilities for errors from an additional numerical integration are removed.

(6) A generalized formulation that posesses a broad range of applicability.

REMARK 1.3.1
An interesting byproduct of this formulation is that with minor modifications, it can be used to describe the physics of a superfluid. See Ref. [20], pp. 152-158.

1.3.1 FINITE ELEMENTS.

A total of eight finite elements were developed in the course of the the author's research. Seven of these are based upon the four-potential variational principle, and the last is a thermal conduction element developed from a different variational principle according to Ref.[24]. They are in order of development:

(1) a one-dimensional Coupled Linear Electric and Magnetic field (CLEM1D) finite element

(2) a two-dimensional axisymmetric Coupled Linear Electric and Magnetic field (CLEM2D) finite element

(3) a one-dimensional Coupled Linear Electric and Magnetic field INFinite (CLEMINF) finite element

(4) a one-dimensional CUrrent Predicting Linear Electromagnetic (CU-PLE1D) finite element

(5) a one-dimensional Superconducting Thermal, Electromagnetic and Phase coupled (STEP1D) finite element

(6) a one-dimensional Superconducting ThErmAl, and eLectromagnetic field (STEAL1D) finite element

(7) a one-dimensional LINear Thermal conduction (LINT1D) finite element

(8) a one-dimensional Linear Electromagnetic and Thermally coupled (LET1D) finite element

Elements (1), (2) and (3) predict only electric and magnetic fields. Element (3) was developed as a term project, but has limited practical usage except for the development of an EM finite element that is time-dependent. Elements (4), (5), (6), and (8) can predict EM fields, but also have the ability to predict the current density distribution, $\mathbf{j}$, given the scalar input I, the total current. Element (6) is not presented here, because it can easily be derived from element (5) by constraining the variable $|\psi|$ to be a constant. This formulation is known as the the London formulation for superconductors. This element was developed solely for the purpose of troubleshooting element(5) [25]. Element (5) also predicts the quantum mechanical quantity $|\psi|$. It also contains two thermally dependent material parameters. These two parameters couple the superconductor to thermal fields. Element (7) was constructed to predict the temperature distribution within the conductor. Element(8) can predict $\mathbf{j}$ and EM fields, but is coupled to thermal fields by the electrical resistivity, ω.

REMARK 1.3.2
Appropriate changes to the Ginzburg-Landau theory and finite element formulation for the construction of element (6) are listed in this thesis. Results for (6) are deleted as they are not as accurate as the results obtained from the STEP1D finite element which is based upon the complete Ginzburg-Landau theory where ψ is allowed to vary.

1.3.2 DISSERTATION OUTLINE.

The dissertation is organized as follows. Chapter II is devoted to a review of basic EM theory, and the development of four-potential theory. Variational functionals for two cases where the current density vector $\mathbf{j}$ is known are also discussed. Chapter III is devoted to the development of variational functionals for conductors where $\mathbf{j}$ is undetermined. In this chapter,

functionals for the normal and superconducting states of a conductor are presented. Chapter IV introduces the variational functionals necessary for the time-independent heat conduction and convection problems. Some generalized solutions for one-dimensional conductors are also presented here. This chapter also includes formulas that express the values of a conductor's EM material properties as a function of the temperature T. Accurate numerical approximations for the values of these material properties are also developed.

The first four chapters outlined above comprise the first step in the development of EM finite elements that can model the quantum and thermal effects that appear within a superconducting material. The main goal of these chapters is to develop variational functionals that are later discretized to produce finite elements. These finite elements are then used to analyze the thermal, quantum and electromagnetic properties of a conductor for some specific EM field problems. The following seven chapters are devoted to developing finite elements and solving those specific EM field problems. Where an analytical solution to the field problem exists, it is presented in that chapter. If special numerical procedures are necessary for the solution of the field problem, the procedures are also discussed in that chapter. Chapters V and VI deal with one and two-dimensional axisymmetric EM field problems respectively, where the current density vector $\mathbf{j}$ is known and the conductor remains in the normal state. Chapter VII presents the finite element solution of a one-dimensional axisymmetric conductor in its normal state where the current density vector $\mathbf{j}$ is unknown. Chapter VIII is concerned with finding the values of EM fields within a one-dimensional time-independent axisymmetric superconductor. Chapter IX develops a one-dimensional heat

conduction finite element. This element is employed with a modified version of the element of Chapter VII to solve the coupled problem of a one-dimensional axisymmetric conductor that is subjected to a varying thermal load. Chapter X employs appropriately modified versions of the elements of Chapter IX to solve the coupled EM-thermal system where the electric current through a one-dimensional axisymmetric wire is varied. Chapter XI models the complete quantum, themal and EM field problem for a one-dimensional axisymmetric wire. The temperature T and the electric current are allowed to vary, but the wire is also allowed to change its quantum state and be either a normal conductor or a superconductor.

The last chapter, Chapter XII, contains a broad summary of the dissertation. This chapter highlights some of the more important aspects of the variational methods used here. It concludes the dissertation with a small section on new research directions that the thesis research has suggested.

EM AND FOUR-POTENTIAL THEORY

2.1 ELECTROMAGNETIC FIELD EQUATIONS.

2.1.1 THE MAXWELL EQUATIONS.

The original Maxwell equations (1873) involve four three-vector quantities: **B**, **D**, **E**, and **H**. Vectors **E** and **H** represents the electric and magnetic field strengths, respectively, whereas **D** and **B** represent the electric and magnetic fluxes, respectively. All of these are three-vector quantities, that is, vector fields in three-dimensional space (e.g., in Cartesian space, $x_1 \equiv x$, $x_2 \equiv y$, $x_3 \equiv z$):

$$\mathbf{E} = \left\{ \begin{array}{c} E_1 \\ E_2 \\ E_3 \end{array} \right\} \quad \mathbf{D} = \left\{ \begin{array}{c} D_1 \\ D_2 \\ D_3 \end{array} \right\} \quad \mathbf{B} = \left\{ \begin{array}{c} B_1 \\ B_2 \\ B_3 \end{array} \right\} \quad \mathbf{H} = \left\{ \begin{array}{c} H_1 \\ H_2 \\ H_3 \end{array} \right\} \qquad (2.1.1)$$

Other quantities are the electric current 3-vector **j** and the electric charge density ρ (a scalar).

With this notation, and using superposed dots to denote differentiation with respect to time t, Maxwell equations can be stated as

$$\boxed{\begin{array}{ll} \dot{\mathbf{B}} + \nabla \times \mathbf{E} = 0 & \nabla \times \mathbf{H} - \dot{\mathbf{D}} = \mathbf{j} \\[2mm] \nabla \cdot \mathbf{D} = \rho & \nabla \cdot \mathbf{B} = 0 \end{array}} \qquad (2.1.2)$$

The first and second equation are also known as Faraday's and Ampère-Maxwell laws, respectively.

45

The system (2.1.2) supplies a total of eight partial differential equations, which as stated are independent of the properties of the underlying medium.

REMARK 2.1.1
Some authors, for example, Eyges [26], include 4π factors and the speed of light c in the Maxwell equations. Other textbooks, *e.g.* [27, 28], follow Heaviside's advice in using technical units that eliminate such confusing factors.

2.1.2 CONSTITUTIVE EQUATIONS.

The field intensities **E** and **H** and the corresponding flux densities **D** and **B** are not independent but are connected by the electromagnetic constitutive equations. For an electromagnetically isotropic, non-polarized material the equations are

$$\boxed{\mathbf{B} = \mu \mathbf{H} \qquad \mathbf{D} = \epsilon \mathbf{E}} \qquad (2.1.3)$$

where μ and ϵ are the permeability and permitivity, respectively, of the material. These coefficients are functions of position but (for static or harmonic fields) do not depend on time. In the general case of a non-isotropic material both μ and ϵ become tensors. Even in isotropic media μ in general is a complicated function of **H**; in ferromagnetic materials it depends on the previous history (hysteresis effect).

In free space $\mu = \mu_0$ and $\epsilon = \epsilon_0$, which are connected by the relation

$$c_0^2 = \frac{1}{\mu_0 \epsilon_0} \qquad (2.1.4)$$

where c_0 is the speed of light in a free vacuum. In rationalized MKS units, $c_0 \approx 3.10^8$ m/sec and

$$\mu_0 = 4\pi \times 10^{-7} \text{ henry/m}, \quad \epsilon_0 = \mu_0^{-1} c_0^{-2} = (36\pi)^{-1} \times 10^{-11} \text{ sec}^2/(\text{henry} \cdot \text{m})$$

$$(2.1.5)$$

46

The condition $\mu \approx \mu_0$ holds well for most practical purposes in such media as air and copper; in fact $\mu_{air} = 1.0000004\mu_0$ and $\mu_{copper} = .99999\mu_0$.

The electric field strength **E** is further related to the current density **j** by Ohm's law:

$$\mathbf{j} = \sigma \mathbf{E} \tag{2.1.6}$$

where σ is the conductivity of the material. Again for a non-isotropic material σ is generally a tensor which may also contain real and imaginary components; in which case the above relation becomes the generalized Ohm's law. For good conductors $\sigma >> \epsilon$; for bad conductors $\sigma << \epsilon$. In free space, $\sigma = 0$.

2.1.3 MAXWELL EQUATIONS IN TERMS OF E AND B.

To pass to the four-potential considered in this work it is convenient to express Maxwell's equations in terms of the electric field strength **E** and the magnetic flux **B**. In fact this is the pair most frequently used in electromagnetic work that involve arbitrary media. On eliminating **D** and **H** through the constitutive equations (2.1.3), we obtain

$$\boxed{\begin{array}{cc} \dot{\mathbf{B}} + \nabla \times \mathbf{E} = 0 & \nabla \times \mathbf{B} - \mu \epsilon \dot{\mathbf{E}} = \mu \mathbf{j} \\ \nabla \cdot \mathbf{E} = \rho / \epsilon & \nabla \cdot \mathbf{B} = 0 \end{array}} \tag{2.1.7}$$

The second equation assumes that ϵ is independent of time; otherwise $\epsilon \dot{\mathbf{E}} = \epsilon \, d\mathbf{E}/dt$ should be replaced by $d(\epsilon \mathbf{E})/dt$. In charge-free vacuum the equations reduce to

$$\begin{array}{cc} \dot{\mathbf{B}} + \nabla \times \mathbf{E} = 0 & \nabla \times \mathbf{B} - \dfrac{1}{c_0^2}\dot{\mathbf{E}} = 0 \\ \nabla \cdot \mathbf{E} = 0 & \nabla \cdot \mathbf{B} = 0 \end{array} \tag{2.1.8}$$

2.1.4 THE ELECTROMAGNETIC POTENTIALS.

The electric scalar potential Φ and the magnetic vector potential $\mathbf{A}$ are introduced by the definitions

$$\boxed{\mathbf{E} = -\nabla\Phi - \dot{\mathbf{A}} \qquad \mathbf{B} = \nabla\times\mathbf{A}} \qquad (2.1.9)$$

This definition satisfies the two homogeneous Maxwell equations in (2.1.7). The definition of $\mathbf{A}$ leaves its divergence $\nabla \cdot \mathbf{A}$ arbitrary. We shall use the Lorentz gauge [29]

$$\boxed{\nabla \cdot \mathbf{A} + \mu\epsilon\dot{\Phi} = 0} \qquad (2.1.10)$$

With this choice the two non-homogeneous Maxwell equations written in terms of Φ and $\mathbf{A}$ separate into the wave equations

$$\nabla^2\Phi - \mu\epsilon\ddot{\Phi} = -\rho/\epsilon \qquad \nabla^2\mathbf{A} - \mu\epsilon\ddot{\mathbf{A}} = -\mu\mathbf{j} \qquad (2.1.11)$$

2.2 THE ELECTROMAGNETIC FOUR-POTENTIAL.

Maxwell's equations can be presented in a compact manner (a form compatible with special relativity) in the four-dimensional spacetime defined by the coordinates

$$x_1 \equiv x, \quad x_2 \equiv y, \quad x_3 \equiv z, \quad x_4 = ict \qquad (2.2.1)$$

where x_1, x_2, x_3 are spatial Cartesian coordinates, $i^2 = -1$ is the imaginary unit, and $c = 1/\sqrt{\mu\epsilon}$ is the speed of EM waves in the medium under consideration. In the sequel Roman subscripts will consistently go from 1 to 4 and the summation convention over repeated indices is used unless otherwise stated.

2.2.1 THE FIELD STRENGTH TENSOR.

The unification can be expressed most conveniently in terms of the *field-strength tensor* **F**, which is a four-dimensional *antisymmetric* tensor constructed from the components of **E** and **B** as follows:

$$\mathbf{F} = \begin{bmatrix} 0 & F_{12} & F_{13} & F_{14} \\ -F_{12} & 0 & F_{23} & F_{24} \\ -F_{13} & -F_{23} & 0 & F_{34} \\ -F_{14} & -F_{23} & -F_{34} & 0 \end{bmatrix} \overset{\text{def}}{=} \gamma \begin{bmatrix} 0 & cB_3 & -cB_2 & -iE_1 \\ -cB_3 & 0 & cB_1 & -iE_2 \\ cB_2 & -cB_1 & 0 & -iE_3 \\ iE_1 & iE_2 & iE_3 & 0 \end{bmatrix} \tag{2.2.2}$$

Here γ is an adjustment factor to be determined later. Similarly, we can introduce the *four-current* vector **J** as

$$\mathbf{J} = \begin{Bmatrix} J_1 \\ J_2 \\ J_3 \\ J_4 \end{Bmatrix} \overset{\text{def}}{=} \gamma \begin{Bmatrix} c\mu j_1 \\ c\mu j_2 \\ c\mu j_3 \\ i\rho/\epsilon \end{Bmatrix} = \gamma c \begin{Bmatrix} \mu j_1 \\ \mu j_2 \\ \mu j_3 \\ i\sqrt{\mu/\epsilon}\,\rho \end{Bmatrix} \tag{2.2.3}$$

Then, for arbitrary γ, the non-homogeneous Maxwell equations, namely $\nabla \times \mathbf{B} - \mu\epsilon \dot{\mathbf{E}} = \mu \mathbf{j}$ and $\nabla \cdot \mathbf{E} = \rho/\epsilon$, may be presented in the compact "continuity" form (the covariant form of these two equations):

$$\frac{\partial F_{ik}}{\partial x_k} = J_i \tag{2.2.4}$$

The other two Maxwell equations, $\nabla \cdot \mathbf{B} = 0$ and $\nabla \times \mathbf{E} + \dot{\mathbf{B}} = 0$, can be presented as

$$\frac{\partial F_{ik}}{\partial x_m} + \frac{\partial F_{mi}}{\partial x_k} + \frac{\partial F_{km}}{\partial x_i} = 0, \tag{2.2.5}$$

where the index triplet (i, k, m) takes on the values (1,2,3), (4,2,3), (4,3,1) and (4,1,2).

2.2.2 THE FOUR-POTENTIAL.

The EM "four-potential" ϕ is a four-vector whose components are constructed with the electric and magnetic potential components of $\mathbf{A}$ and Φ:

$$\phi = \gamma \left\{ \begin{array}{c} \phi_1 \\ \phi_2 \\ \phi_3 \\ \phi_4 \end{array} \right\} \overset{\text{def}}{=} \left\{ \begin{array}{c} cA_1 \\ cA_2 \\ cA_3 \\ i\Phi \end{array} \right\} \tag{2.2.6}$$

It may then be verified that $\mathbf{F}$ can be expressed as the four-curl of ϕ, that is

$$F_{ik} = \frac{\partial \phi_k}{\partial x_i} - \frac{\partial \phi_i}{\partial x_k}, \tag{2.2.7}$$

or in more detail and using commas to abbreviate partial derivatives:

$$\mathbf{F} = \begin{bmatrix} 0 & \phi_{2,1} - \phi_{1,2} & \phi_{3,1} - \phi_{1,3} & \phi_{4,1} - \phi_{1,4} \\ \phi_{1,2} - \phi_{2,1} & 0 & \phi_{3,2} - \phi_{2,3} & \phi_{4,2} - \phi_{2,4} \\ \phi_{1,3} - \phi_{3,1} & \phi_{2,3} - \phi_{3,2} & 0 & \phi_{4,3} - \phi_{3,4} \\ \phi_{1,4} - \phi_{4,1} & \phi_{2,4} - \phi_{4,2} & \phi_{3,4} - \phi_{4,3} & 0 \end{bmatrix} \tag{2.2.8}$$

2.2.3 THE UNGAUGED LAGRANGIAN.

With these definitions, the basic Lagrangian of electromagnetism can be stated as

$$L = \tfrac{1}{4} F_{ik} F_{ik} - J_i \phi_i = \tfrac{1}{4} \gamma^2 \left(\frac{\partial \phi_k}{\partial x_i} - \frac{\partial \phi_i}{\partial x_k} \right)^2 - J_i \phi_i$$

$$= \tfrac{1}{2} \gamma^2 \left(c^2 B^2 - E^2 \right) - \frac{\gamma^2}{\epsilon} (j_1 A_1 + j_2 A_2 + j_3 A_3 - \rho \Phi) \tag{2.2.9}$$

in which

$$B^2 = \mathbf{B}^T \mathbf{B} = B_1^2 + B_2^2 + B_3^2, \quad E^2 = \mathbf{E}^T \mathbf{E} = E_1^2 + E_2^2 + E_3^2 \tag{2.2.10}$$

Comparing the first term with the magnetic and electric energy densities [26,27,28]

$$U_M = \tfrac{1}{2} \mathbf{B}^T \mathbf{H} = \frac{1}{2\mu} B^2, \qquad U_E = \tfrac{1}{2} \mathbf{D}^T \mathbf{E} = \tfrac{1}{2} \epsilon E^2, \tag{2.2.11}$$

we must have $\gamma^2 c^2 = \gamma^2/(\mu\epsilon) = 1/\mu$, from which

$$\gamma = \sqrt{\epsilon} \qquad (2.2.12)$$

Consequently, the required Lagrangian is

$$\boxed{L = \frac{1}{2\mu}B^2 - \tfrac{1}{2}\epsilon E^2 - (j_1 A_1 + j_2 A_2 + j_3 A_3 - \rho\Phi).} \qquad (2.2.13)$$

The associated variational form is

$$R = \int_{t_0}^{t_1} \int_V L\, dV dt \qquad (2.2.14)$$

where V is the integration volume considered in the analysis. In theory V extends over the whole space, but in the numerical simulation the integration is truncated at a known boundary or special devices are used to treat the decay behavior at infinity.

REMARK 2.2.1
Lanczos [30] presents this Lagrangian for free space, but the expression (2.2.13) for an arbitrary material was found in none of the textbooks on electromagnetism listed in the References.

2.2.4 THE GAUGED LAGRANGIAN.

If the fields $\mathbf{A}$ and Φ to be inserted into L do not satisfy the Lorentz gauge relation (2.1.10) *a priori*, this condition has to be imposed as a constraint using a Lagrange multiplier field $\lambda_g(x_i)$, leading to the modified or "gauged" Lagrangian:

$$L_g = L + \lambda_g(\nabla \cdot \mathbf{A} + \mu\epsilon\dot{\Phi}) \qquad (2.2.15)$$

2.2.5 THE FOUR-FIELD EQUATIONS.

On setting the variation of the functional (2.2.15) to zero we recover the field equations (2.2.4) and (2.2.5), as well as the gauge constraint (2.1.10) as Euler-Lagrange equations. Taking the divergence of both sides of (2.2.4) and observing that $\mathbf{F}$ is an antisymmetric tensor so that its divergence vanishes we get

$$\frac{\partial J_i}{\partial x_i} = c\mu(\nabla \cdot \mathbf{j} + \dot{\rho}) = 0 \qquad (2.2.16)$$

The vanishing term in parenthesis is the equation of continuity, which expresses the law of conservation of charge. The Lorentz gauge condition (2.1.10) may be stated as $\partial \phi_i / \partial x_i$. Finally, the potential wave equations (2.1.11) may be expressed in compact form as

$$\Box \phi_i = -J_i \qquad (2.2.17)$$

where $\Box$ denotes the "four-wave-operator", also called the D'Alembertian:

$$\Box \overset{\text{def}}{=} \frac{\partial^2}{\partial x_k \partial x_k} = \frac{\partial^2}{\partial x_1^2} + \frac{\partial^2}{\partial x_2^2} + \frac{\partial^2}{\partial x_3^2} - \frac{\partial^2}{c^2 \partial t^2} \qquad (2.2.18)$$

Hence each component of the four-potential ϕ satisfies an inhomogeneous wave equation. In free space, $J_i = 0$ and each component satisfies the homogeneous wave equation.

The following sections of this chapter are devoted to derivations of the appropriate expression for L_g for selected cases. The first variation of R with respect to the independent variables is also taken. With few exceptons, the solutions of the independent variables Φ is not determined. The variation is performed primarily to determine the natural boundary conditions of each test case for the eventual extension of the four-potential method to finite

element analysis. The variation is also performed to confirm the validity of the four-potential method as an analytical tool by directly comparing the resultant Euler equations minus the Lagrange multiplier terms with Maxwell's field equations.

2.3 THE ONE-DIMENSIONAL AXISYMMETRIC CASE.

The simplest application for the four-potential variational principle is to an infinitely long, straight conductor of circular cross section which carries a known, time-independent uniform current in the longitudinal direction (Fig. 2.1.). To take advantage of the axisymmetric geometry a cylindrical coordinate system is chosen with the wire centerline as the longitudinal z-axis. The vector components in the cylindrical coordinate directions r, θ and z are denoted by

A_1, B_1, E_1 $\equiv$ A_r, B_r, E_r in the r (radial) direction,

A_2, B_2, E_2 $\equiv$ A_θ, B_θ, E_θ in the θ (circumferential) direction,

A_3, B_3, E_3 $\equiv$ A_z, B_z, E_z in the z (longitudinal) direction.

The first step in solving for the fields is to express the gauged Lagrangian

$$L_g = \frac{1}{2\mu}B^2 - \tfrac{1}{2}\epsilon E^2 - (\mathbf{j}^T\mathbf{A} - \rho\Phi) + \lambda_g(\nabla \cdot \mathbf{A} + \mu\epsilon\dot{\Phi}), \qquad (2.3.1)$$

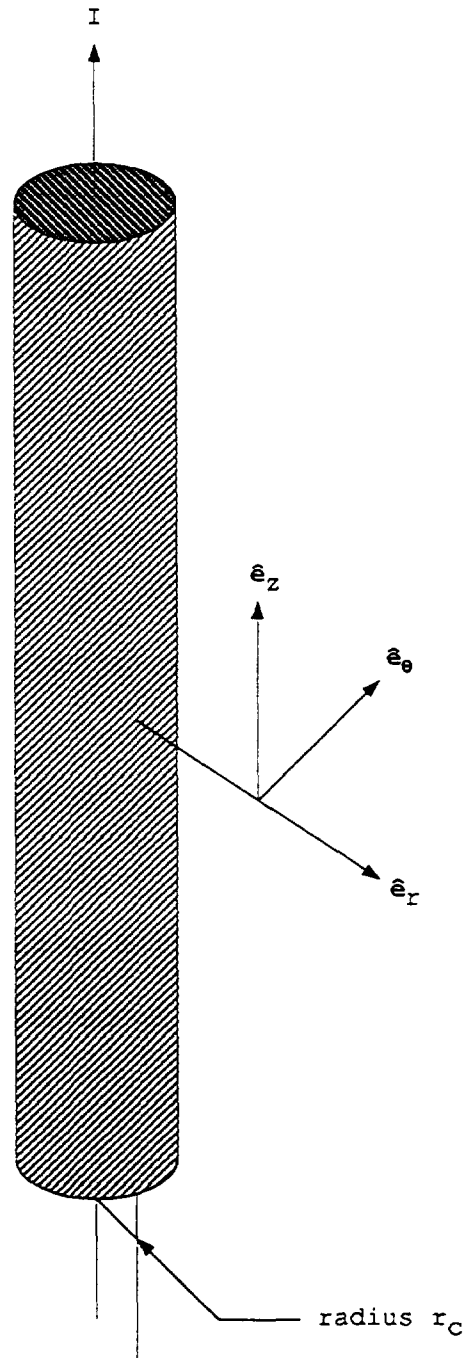in terms of the potentials written in cylindrical coordinates.

53

Figure 2.1: One-dimensional axisymmetric wire.

For B^2 we use (2.1.9), (2.2.10) and the cylindrical-coordinate curl formulas to get

$$B^2 = \left(\frac{1}{r}\frac{\partial A_z}{\partial \theta} - \frac{\partial A_\theta}{\partial z}\right)^2 + \left(\frac{\partial A_r}{\partial z} - \frac{\partial A_z}{\partial r}\right)^2 + \left(\frac{1}{r}\frac{\partial(rA_\theta)}{\partial r} - \frac{1}{r}\frac{\partial A_r}{\partial \theta}\right)^2 \quad (2.3.2)$$

For E^2 we use (2.1.9) and the cylindrical-coordinate gradient formulas to produce

$$\mathbf{E} = \left\{\begin{array}{c} E_1 \\ E_2 \\ E_3 \end{array}\right\} = \left\{\begin{array}{c} E_r \\ E_\theta \\ E_z \end{array}\right\} = -\left\{\begin{array}{c} \frac{\partial \Phi}{\partial r} + \dot{A}_r \\ \frac{1}{r}\frac{\partial \Phi}{\partial \theta} + \dot{A}_\theta \\ \frac{\partial \Phi}{\partial z} + \dot{A}_z \end{array}\right\} \quad (2.3.3)$$

so that (2.2.10) becomes

$$E^2 = \mathbf{E}^T\mathbf{E} = \left(\frac{\partial \Phi}{\partial r} + \frac{\partial A_r}{\partial t}\right)^2 + \left(\frac{1}{r}\frac{\partial \Phi}{\partial \theta} + \frac{\partial A_\theta}{\partial t}\right)^2 + \left(\frac{\partial \Phi}{\partial z} + \frac{\partial A_z}{\partial t}\right)^2 \quad (2.3.4)$$

For the Lorentz gauge we use the cylindrical-coordinate divergence formula to get

$$\nabla \cdot \mathbf{A} + \mu\epsilon\dot{\Phi} = \frac{1}{r}\frac{\partial(rA_r)}{\partial r} + \frac{1}{r}\frac{\partial A_\theta}{\partial \theta} + \frac{\partial A_z}{\partial z} + \mu\epsilon\dot{\Phi} \quad (2.3.5)$$

The electromagnetic fields, for the one-dimensional case, only vary in the radial (r) direction and any partials with respect to θ and z vanish. In the time-independent case, all partials with respect to t also vanish. With no static charge density, $\rho = 0$, and with only a longitudinal current, the single non-vanishing component of $\mathbf{j}$ is j_z. The constitutive relation (2.1.6) can be used to remove the dependence of L_g on Φ; because j_z is known, $\mathbf{E}$ is known, and it is not necessary to carry the terms in L_g necessary to determine $\mathbf{E}$. These simplifications produce

$$L_g = \frac{1}{2\mu}\left\{\left(\frac{\partial A_z}{\partial r}\right)^2 + \left(\frac{1}{r}\frac{\partial(rA_\theta)}{\partial r}\right)^2 + \lambda_g\left(\frac{1}{r}\frac{\partial(rA_r)}{\partial r}\right) - (j_zA_z)\right\} \quad (2.3.6)$$

55

The first variation of R, with (2.3.6) as the Lagrangian, with respect to λ_g gives the Euler equation:

$$\frac{\partial (rA_r)}{\partial r} = 0 \qquad (2.3.7)$$

The solution for A_r is simply a constant over r. For A_r to remain bounded as r goes to zero, the constant must be zero. The first variation of R with respect to A_θ and integration by parts yields the following Euler equation for A_θ

$$r\frac{\partial}{\partial r} \left(\frac{1}{r} \frac{\partial (rA_\theta)}{\partial r} \right) = 0 \qquad (2.3.8)$$

The solution to this equation is $A_\theta = C_1 r + C_2 r^{-1}$ where C_1 and C_2 are constants of integration. Again C_2 must be zero for A_θ to remain bounded as r approaches zero. If C_1 is nonzero, a magnetic field will exist in the z (longitudinal) direction. For the problems considered here, the only magnetic fields that exist are generated by the current I in the wire and C_1 is also chosen to be zero.

Because A_r and A_θ are identically zero, it is not necessary to carry the terms in (2.3.6) dependent upon A_r and A_θ. Consequently, the expression for the gauged Lagrangian for the one-dimensional, time-independent axisymmetric conductor with a known current density distribution is

$$\boxed{L_g = \frac{1}{2\mu} \left\{ \left(\frac{\partial A_z}{\partial r} \right)^2 - (j_z A_z) \right\}} \qquad (2.3.9)$$

Notice that for this particular geometry, with time-independent fields, the gauge choice for $\mathbf{A}$ does not contribute to the Lagrangian and $\mathbf{A}$ is completely determined by the boundary conditions. For this particular case, L is equal to L_g.

The new expression for R is

$$R = \int_V dV \left\{ \frac{1}{2\mu} \left(\frac{\partial A_z}{\partial r} \right)^2 - (j_z A_z) \right\} \tag{2.3.10}$$

The first variation of R with respect to A_z and integration by parts produces

$$\delta R = - \int_V dV \delta A_z \left\{ \frac{1}{\mu r} \left(\frac{\partial}{\partial r} \left(r \frac{\partial A_z}{\partial r} \right) \right) + j_z \right\} + \int_\Gamma d\Gamma \delta A_z \left\{ \frac{r}{\mu} \frac{\partial A_z}{\partial r} \right\} \Big|_{r_i}^{r_j} \tag{2.3.11}$$

where Γ is the surface of the integration volume considered in the analysis, and r_i and r_j are the inner and outer radial limits respectively of the integration volume. For this problem, $d\Gamma$ is simply $d\theta dz$. Substituting the relation for $\mathbf{B}$ from (2.1.9) (*i.e.*, $\mathbf{B} = \nabla \times \mathbf{A}$) into the Euler equation in (2.3.11) gives the following Maxwell relation and verifys that (2.3.9) is the correct form for L_g.

$$\frac{1}{r} \frac{\partial (r B_\theta)}{\partial r} = \mu j_z \tag{2.3.12}$$

2.4 THE TWO-DIMENSIONAL AXISYMMETRIC CASE.

The next simplest problem with which to test the four-potential method is the two-dimensional axisymmetric case. As in the one-dimensional case, the current is steady (time-independent) and known, ρ is still zero, and cylindrical coordinates are chosen with the rotational axis coinciding with the z axis. The four-potential method is now extended to cover this problem by allowing ϕ to vary in the radial and longitudinal directions $\hat{\mathbf{e}}_r$ and $\hat{\mathbf{e}}_z$ but not in the circumferential direction $\hat{\mathbf{e}}_\theta$. Here, and in the sequel, $\hat{\mathbf{e}}_r$, $\hat{\mathbf{e}}_\theta$, and $\hat{\mathbf{e}}_z$ are defined as the unit direction vectors in the r, θ and z directions respectively. All partials with respect to θ now disappear but partials with respect to z now remain. Since the problem is time-independent, and $\mathbf{j}$ is known,

partials with respect to t and partials containing Φ can be eliminated. The gauged Lagrangian is now

$$
L_g = \frac{1}{2\mu} \left[\left(\frac{\partial A_r}{\partial z} - \frac{\partial A_z}{\partial r} \right)^2 + \left(\frac{\partial A_\theta}{\partial z} \right)^2 + \left(\frac{1}{r} \frac{\partial (rA_\theta)}{\partial r} \right)^2 \right]
$$
$$
+ \lambda_g \left(\frac{1}{r} \frac{\partial (rA_r)}{\partial r} + \frac{\partial A_z}{\partial z} \right) - (j_r A_r + j_\theta A_\theta + j_z A_z)
$$

(2.4.1)

Note that this Lagrangian involves *all* components of **A** although the independence from θ has introduced some simplifications with respect to the full three-dimensional case.

Variation of the above with respect to A_r and integartion by parts produces

$$
\delta R(A_r) = \quad - \int_V dV \delta A_r \left\{ \frac{1}{\mu} \left(\frac{\partial^2 A_r}{\partial z^2} - \frac{\partial^2 A_z}{\partial z \partial r} \right) + j_r + \frac{\partial \lambda_g}{\partial r} \right\}
$$
$$
+ \int_{\Gamma_1} d\Gamma_1 \delta A_r \left\{ \frac{1}{\mu} \left(\frac{\partial A_r}{\partial z} - \frac{\partial A_z}{\partial r} \right) \right\} \Big|_{z_i}^{z_j} + \int_{\Gamma_2} d\Gamma_2 \delta A_r \left\{ r \lambda_g \right\} \Big|_{r_i}^{r_j}
$$

(2.4.2)

where $d\Gamma_1$ and $d\Gamma_2$ are defined as $rdrd\theta$ and $d\theta dz$ in the $\hat{\mathbf{e}}_z$ and $\hat{\mathbf{e}}_r$ directions respectively and z_i and z_j are the lower and upper limits of integration respectively, of the integration volume in the $\hat{\mathbf{e}}_z$ direction. To verify that the first three terms of the volume integral in (2.4.2) represent a Maxwell equation, the expression for **B** in terms of A_r, A_θ and A_z is needed. The correct expression for this problem is

$$
\mathbf{B} = \left\{ \begin{array}{c} B_r \hat{\mathbf{e}}_r \\ B_\theta \hat{\mathbf{e}}_\theta \\ B_z \hat{\mathbf{e}}_z \end{array} \right\} = \left\{ \begin{array}{c} -\frac{\partial A_\theta}{\partial z} \hat{\mathbf{e}}_r \\ \left(\frac{\partial A_r}{\partial z} - \frac{\partial A_z}{\partial r} \right) \hat{\mathbf{e}}_\theta \\ \frac{1}{r} \frac{\partial}{\partial r} (rA_\theta) \hat{\mathbf{e}}_z \end{array} \right\}
$$

(2.4.3)

The following expression for $\nabla \times \mathbf{B}$ in terms of B_r, B_θ and B_z is helpful for verification purposes:

$$\nabla \times \mathbf{B} = \left\{ \begin{array}{c} -\frac{\partial B_\theta}{\partial z}\hat{\mathbf{e}}_r \\[2mm] \left(\frac{\partial B_r}{\partial z} - \frac{\partial B_z}{\partial r}\right)\hat{\mathbf{e}}_\theta \\[2mm] \frac{1}{r}\frac{\partial}{\partial r}\left(rB_\theta\right)\hat{\mathbf{e}}_z \end{array} \right\} \tag{2.4.4}$$

Comparison of the θ component of $\mathbf{B}$ with the Euler equation of (2.4.2) verifies that it is the Maxwell equation $\nabla \times \mathbf{B} = \mu \mathbf{j}$ in the $\hat{\mathbf{e}}_r$ direction.

Variation of (2.4.1) with respect to A_θ and integration by parts produces

$$\delta R\left(A_\theta\right) = -\int_V dV \delta A_\theta \left\{\frac{1}{\mu}\left(\frac{\partial^2 A_\theta}{\partial z^2} + \frac{\partial}{\partial r}\left(\frac{1}{r}\frac{\partial}{\partial r}\left(rA_\theta\right)\right)\right) + j_\theta\right\}$$
$$+ \int_{\Gamma_1} d\Gamma_1 \delta A_\theta \left\{\frac{1}{\mu}\frac{\partial A_\theta}{\partial z}\right\}\Big|_{z_i}^{z_j} + \int_{\Gamma_2} d\Gamma_2 \delta A_\theta \left\{\frac{1}{\mu}\frac{\partial}{\partial r}\left(rA_\theta\right)\right\}\Big|_{r_i}^{r_j} \tag{2.4.5}$$

Comparison of the r and θ components of $\mathbf{B}$ in (2.4.5) verifes that the Euler equations match the desired Maxwell equation in the $\hat{\mathbf{e}}_\theta$ direction.

Finally, variation of (2.4.1) with respect to A_z and integration by parts produces

$$\delta R\left(A_z\right) = \int_V dV \delta A_z \left\{\frac{1}{\mu}\left(\frac{1}{r}\frac{\partial}{\partial r}\left(r\left(\frac{\partial A_r}{\partial z} - \frac{\partial A_z}{\partial r}\right)\right)\right) - j_z - \frac{\partial \lambda_g}{\partial z}\right\}$$
$$+ \int_{\Gamma_1} d\Gamma_1 \delta A_z \left\{r\lambda_g\right\}\Big|_{z_i}^{z_j} + \int_{\Gamma_2} d\Gamma_2 \delta A_z \left\{\frac{1}{\mu}r\left(\frac{\partial A_r}{\partial z} - \frac{\partial A_z}{\partial r}\right)\right\}\Big|_{r_i}^{r_j} \tag{2.4.6}$$

Comparison of the θ component of $\mathbf{B}$ again verifies the derivation of the correct Euler equation, this time for the $\hat{\mathbf{e}}_z$ direction.

59

2.5 SUMMARY.

In this chapter, the terminology and basic background for dealing with EM fields is developed. The four-potential method is also introduced and modified for arbitrary materials. The basic Lagrangian for EM field problems is presented and a gauged form of this Lagrangian is also shown. To show the broad range of applicability of the four-potential method to EM field problems, the gauged Langrangian for two simple time-independent cases is derived. The first variation of this Lagrangian, integrated over the independent variables, is also taken. This variation is performed to verify that the Euler-Lagrange equations for these two particular cases match their respective Maxwell equations and also to determine the natural boundary conditions for each case.

In the next chapter, the four-potential method is extended again to obtain the appropriate Lagrangian for two special cases. These cases are a conductor with an unknown current density vector $\mathbf{j}$ and a conductor in the superconducting state.

CURRENT DENSITY PREDICTING FOUR-POTENTIAL THEORY

In the previous chapter, the current density distribution j is known. Unfortunately, for the general case, neither the path that the current I takes through a conductor nor its distribution is known. In this chapter, two different cases where I is known, but j is not, are examined. The first case is a normal conductor and the second case is a type I or II (Ginzburg-Landau) superconductor. Both cases have an identical geometry, that of a one-dimensional infinite wire and both are time-independent with ρ equal to zero. Cylindrical coordinates are used to describe the problem with the z axis coinciding with the rotational axis of the wire.

The purpose of this chapter is to develop the Lagrangians for each of the two problems, and their residuals (Euler equations), so that they may be extended to a finite element formulation. Also included in this chapter is a brief presentation of the basic theory of superconductivity for types I and II superconductors.

3.1 LINEAR CONDUCTORS.

The previously derived Lagrangian for the time-independent case in three dimensions is

$$\boxed{L_g = \int_V dV \left\{ \frac{1}{2\mu} (\nabla \times A)^T (\nabla \times A) - \frac{1}{2}\epsilon \nabla \Phi^T \nabla \Phi - j^T A + \lambda_g (\nabla \cdot A) \right\}}$$

(3.1.1)

where the superscript T represents the transpose of the matrix or vector.

The constitutive equation for a linear conducting medium is

$$\boxed{\mathbf{j} \;=\; \sigma \mathbf{E} \;=\; -\sigma \nabla \Phi}$$
(3.1.2)

As a first guess, (3.1.2) is used to eliminate $\mathbf{j}$ from (3.1.1) in terms of the variable Φ. The resulting equation for the Lagrangian is

$$L_g = \left\{ \frac{1}{2\mu} (\nabla \times \mathbf{A})^T (\nabla \times \mathbf{A}) - \frac{1}{2} \epsilon \nabla \Phi^T \nabla \Phi + \sigma \nabla \Phi^T \mathbf{A} + \lambda_g (\nabla \cdot \mathbf{A}) \right\}$$
(3.1.3)

Integrating L_g over the volume and taking the first variation yields, after integration by parts, the following equation

$$\delta R = \int_V dV \delta \mathbf{A}^T \left\{ \frac{1}{\mu} \nabla \times \nabla \times \mathbf{A} + \sigma \nabla \Phi - \nabla \lambda_g \right\} - \int_V dV \delta \Phi \nabla \cdot \{ \epsilon \nabla \Phi - \sigma \mathbf{A} \}$$
$$+ \int_\Gamma d\Gamma \delta \mathbf{A}^T \left\{ \frac{1}{\mu} (\nabla \times \mathbf{A} \times \hat{\mathbf{n}}) + (\cdot \hat{\mathbf{n}} \, \lambda_g) \right\} + \int_\Gamma d\Gamma \delta \Phi \{ \epsilon \nabla \Phi + \sigma \mathbf{A} \} \cdot \hat{\mathbf{n}}$$
(3.1.4)

where $\hat{\mathbf{n}}$ is the unit outward normal to the surface of the volume of integration.

The first volume integral is an augmented form of Maxwell's equation $\nabla \times \mathbf{B} = \mathbf{j}$, whereas the first boundary integral ensures that the $\mathbf{B}$ field component parallel to the surface is continuous across boundary surfaces. If σ is constant across the volume of integration, then the second volume integral is a restatement of the Maxwell equation $\nabla \cdot \mathbf{D} = 0$ because $\nabla \cdot (\sigma \mathbf{A})$ $= \sigma \nabla \cdot \mathbf{A} = 0$. The second boundary integral enforces the condition that the normal component of $\mathbf{D}$ be continuous across boundaries. For the one-dimensional problems studied here where the value of ϵ does not change across boundaries, this condition automatically satisfies the homogeneous Maxwell equation $\nabla \times \mathbf{E} = 0$.

If σ is constant across the *whole* volume of a conductor, this formulation presents no difficulties. However, if σ changes as a continuous (smooth) function across a conductor, the second Euler equation is incorrect. This can be corrected by augmenting the Lagangian with the constraint $\nabla \cdot \mathbf{D} = 0$ or by changing the gauge constraint to $\nabla \cdot (\sigma \mathbf{A}) = 0$. If the conductivity changes slowly across the conductor, the conductivity can be approximated by a series of step functions. At low temperatures, for the conductors examined in this work, the conductivity does change slowly across the conductor volume and the step function approximation is used. This formulation also has problems. The second boundary and volume integrals in (3.1.4) combine to produce a series of $n-1$ equations for n unknowns where n is the number of differing regions that $\mathbf{E}$ field passes through. These regions are caused by the choice of integration volumes and changing EM material properties. Augmenting (3.1.4) by the current conservation constraint, $I = \int_\Gamma d\Gamma \hat{\mathbf{n}}_c \cdot \mathbf{j}$, where $\hat{\mathbf{n}}_c$ is the directed unit normal to the surface that the current flows through, solves this problem. $\hat{\mathbf{n}}_c$ is aligned in the direction on current flow. The new functional R_{gcc} is

$$R_{gcc} = \int_V dV \left\{ \frac{1}{2\mu} (\nabla \times \mathbf{A})^T (\nabla \times \mathbf{A}) - \frac{1}{2}\epsilon \nabla \Phi^T \nabla \Phi + \sigma \nabla \Phi^T \mathbf{A} + \lambda_g (\nabla \cdot \mathbf{A}) \right\}$$
$$+ \lambda_c \left(I + \int_\Gamma d\Gamma \sigma \hat{\mathbf{n}}_c \cdot \nabla \Phi \right)$$

$$(3.1.5)$$

Variation with respect to **A** and Φ produces

$$\delta R_{gcc} = \int_V dV \delta \mathbf{A}^T \left\{ \frac{1}{\mu} \nabla \times \nabla \times \mathbf{A} + \sigma \nabla \Phi - \nabla \lambda_g \right\}$$

$$- \int_V dV \delta \Phi \left\{ \nabla \cdot (\epsilon \nabla \Phi - \sigma \mathbf{A}) + \nabla \lambda_c \right\}$$

$$+ \int_\Gamma d\Gamma \delta \mathbf{A}^T \left\{ \frac{1}{\mu} (\nabla \times \mathbf{A} \times \hat{\mathbf{n}}) + (\cdot \hat{\mathbf{n}} \lambda_g) \right\} \qquad (3.1.6)$$

$$+ \int_\Gamma d\Gamma \delta \Phi \left\{ (\epsilon \nabla \Phi + \sigma \mathbf{A}) \cdot \hat{\mathbf{n}} + \lambda_c \hat{\mathbf{n}}_c \right\}$$

$$+ \delta \lambda_c \left(I + \int_\Gamma d\Gamma \sigma \hat{\mathbf{n}}_c \cdot \nabla \Phi \right)$$

For anticipated extensions to superconductivity, it was originally desirable to have **j** as a primary variable whereas the electrical potential was of little interest. R_{gcc} was written in terms of the variables **A** and **j** and the first variation and integration by parts was performed to give

$$\delta R_{gcc} = \int_V dV \delta \mathbf{A}^T \left\{ \frac{1}{\mu} \nabla \times \nabla \times \mathbf{A} - \mathbf{j} - \nabla \lambda_g \right\} - \int_V dV \delta \mathbf{j} \left\{ \epsilon \omega^2 \mathbf{j} + \mathbf{A} \right\}$$

$$+ \int_\Gamma d\Gamma \delta \mathbf{A}^T \left\{ \frac{1}{\mu} (\nabla \times \mathbf{A} \times \hat{\mathbf{n}}) + (\cdot \hat{\mathbf{n}} \lambda_g) \right\} + \lambda_c \int_\Gamma d\Gamma \delta \mathbf{j} \cdot \hat{\mathbf{n}}_c$$

$$+ \delta \lambda_c \left(I - \int_\Gamma d\Gamma \hat{\mathbf{n}}_c \cdot \mathbf{j} \right)$$

$$(3.1.7)$$

where ω, the resistivity, equals $1/\sigma$.

The second Euler equation $\epsilon \omega^2 \mathbf{j} + \mathbf{A} = 0$, which replaces $\nabla \cdot \mathbf{D} = 0$, is generally incorrect: this is due to the elimination of $\nabla \Phi$, which inhibits the necessary integration by parts. The lack of this integration also has the effect of forfeiting the automatic verification of the homogeneous Maxwell equation $\nabla \times \mathbf{E} = 0$. These deficiencies can be corrected by augmenting R_{gcc}

with a Lagrangian multiplier field κ to produce the new functional, R_p, which follows.

$$R_p = \int_V dV \Big\{ \frac{1}{2\mu} (\nabla \times \mathbf{A})^T (\nabla \times \mathbf{A}) - \frac{1}{2} \epsilon \omega^2 \mathbf{j}^T \mathbf{j} + \mathbf{j}^T \mathbf{A}$$
$$+ \lambda_g (\nabla \cdot \mathbf{A}) + \kappa^T (\nabla \times \omega \mathbf{j}) \Big\} + \lambda_c \left(I - \int_\Gamma d\Gamma \hat{n}_c \cdot \mathbf{j} \right) \tag{3.1.8}$$

At the start of the thesis research, for the finite element work, $\omega \mathbf{j}$ was originally substituted for $-\nabla \Phi$ in (3.1.1). The original equations produced a variational index of zero for $\mathbf{j}$. This variational index is a constraint that was kept as an arbitrary choice to make the research proceed more rapidly and results in a formulation that is not the most computationally efficient.

For the one-dimensional problem, Φ as a primary variable, not $\mathbf{j}$, is the better choice. A formulation that uses Φ is better because it only varies in the z direction. This requires only two degrees of freedom over the whole domain of the problem to model $\mathbf{E}$ and $\mathbf{D}$. With $\mathbf{j}$ as the primary variable, one degree of freedom per element is needed to evaluate $\mathbf{j}$, and a minimum of two additional degrees of freedom per element are necessary to evaluate κ. The $\mathbf{j}$ formulation requires three degrees of freedom *per element* to model the $\mathbf{E}$ and $\mathbf{D}$ fields.

Another advantage of the Φ based formulation is that with the gauge choice $\nabla \cdot (\sigma \mathbf{A}) = 0$, only one constraint has to be augmented to the gauged Lagrangian, the current conservation constraint. An additional benefit of the Φ formulation is that it does not exclude a σ that varies smoothly. In the thesis formulation, because $\mathbf{j}$ is C^{-1} continuous, σ must also be C^{-1} continuous to satisfy the homogeneous Maxwell equation $\nabla \times \mathbf{E} = 0$.

However, the formulation that was used to produce numerical results here contains $\mathbf{j}$ as primary variable and not Φ because of time limitations on

the thesis research. To reproduce this formulation, it is necessary to integrate (3.1.8) by parts to lower the variational index of $\mathbf{j}$ to zero. The result is

$$
\begin{aligned}
R_p = \int_V dV \Big\{ \frac{1}{2\mu} \left(\nabla \times \mathbf{A} \right)^T \left(\nabla \times \mathbf{A} \right) - \frac{1}{2} \epsilon \omega^2 \mathbf{j}^T \mathbf{j} + \mathbf{j}^T \mathbf{A} \\
+ \lambda_g \left(\nabla \cdot \mathbf{A} \right) + \omega \mathbf{j}^T \left(\nabla \times \boldsymbol{\kappa} \right) \Big\} \\
+ \int_\Gamma d\Gamma \omega \mathbf{j}^T \left(\boldsymbol{\kappa} \times \hat{\mathbf{n}} \right) + \lambda_c \left(I - \int_\Gamma d\Gamma \hat{\mathbf{n}}_c \cdot \mathbf{j} \right)
\end{aligned}
\tag{3.1.9}
$$

3.1.1 ONE-DIMENSIONAL LINEAR CONDUCTOR.

As in section 2.3, the simplest application arises for an infinitely long, straight conductor of circular cross section. A depiction of the physical problem is illustrated in the upper half of Figure 3.1. Again, ρ equals zero, and all partials with respect to θ and z vanish. The only nonzero components of $\mathbf{A}$ and $\mathbf{j}$ are A_z and j_z. By (3.1.2), the only nonzero component of $\mathbf{E}$ is E_z, consequently the only nonvanishing component of $\boldsymbol{\kappa}$ is in the $\hat{\mathbf{e}}_\theta$ direction. The expression for R_p reduces to

$$
\begin{aligned}
R_p = \int_V dV \left\{ \frac{1}{2\mu} \left(A_z \right)^2 - \frac{1}{2} \epsilon \omega^2 j_z^2 - j_z A_z + \omega j_z \frac{1}{r} \frac{\partial}{\partial r} \left(r \kappa_\theta \right) \right\} \\
- \int_{\Gamma_2} d\Gamma_2 \omega r j_z \kappa_\theta \Big|_{r_i}^{r_j} + \lambda_c \left(I - \int_{\Gamma_1} d\Gamma_1 j_z \right)
\end{aligned}
\tag{3.1.10}
$$

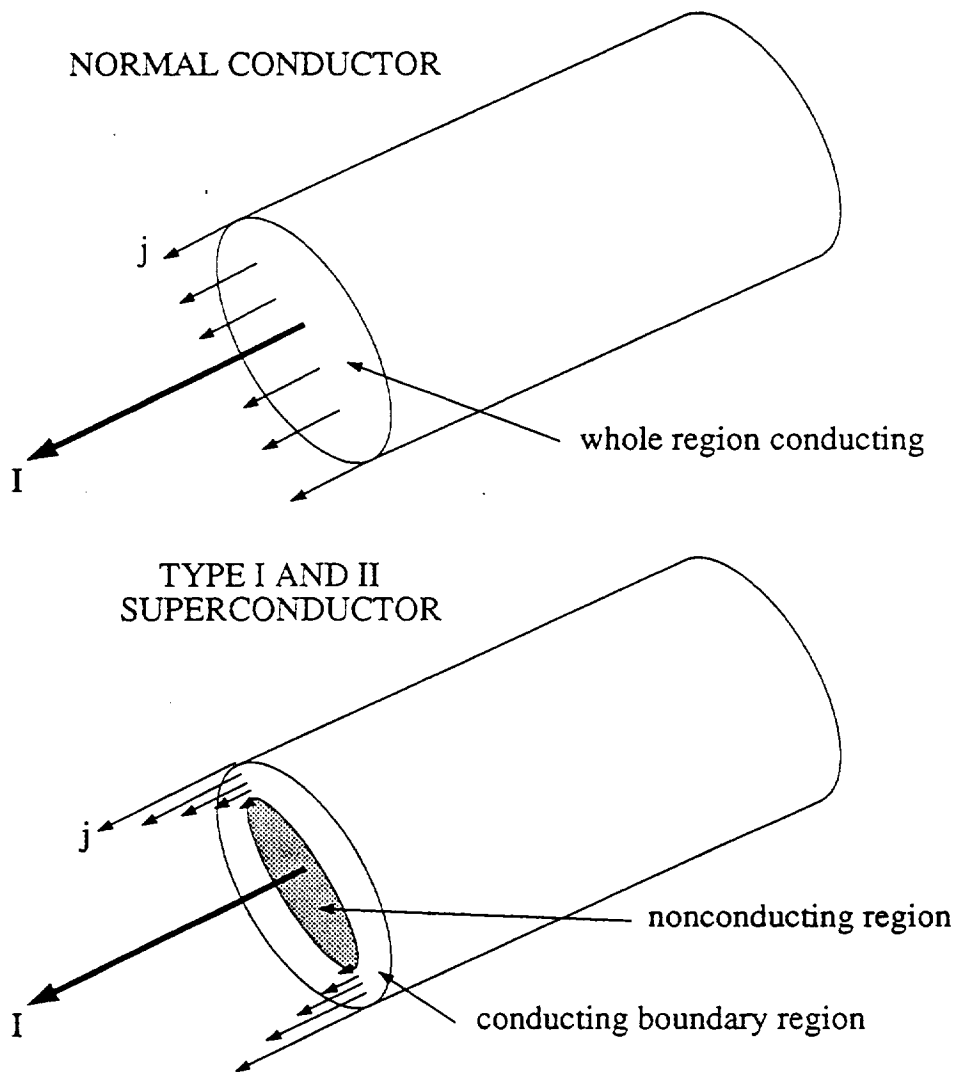where $d\Gamma_2$ and $d\Gamma_1$ are again defined as $d\theta dz$ and $r dr d\theta$ respectively. Varia-

NORMAL CONDUCTOR

whole region conducting

TYPE I AND II
SUPERCONDUCTOR

nonconducting region

conducting boundary region

Figure 3.1: Physical Problem: One-dimensional bulk conductors.

tion with respect to A_z, j_z λ_c and κ_θ and integration by parts produces

$$
\begin{aligned}
\delta R = &- \int_V dV \delta A_z \left\{ \frac{1}{\mu r} \left(\frac{\partial}{\partial r} \left(r \frac{\partial A_z}{\partial r} \right) \right) + j_z \right\} \\
&- \int_V dV \delta j_z \left\{ \epsilon \omega^2 j_z + A_z + \omega \frac{1}{r} \frac{\partial}{\partial r} (r \kappa_\theta) \right\} - \int_{\Gamma_1} d\Gamma_1 \delta j_z \lambda_c \\
&- \int_{\Gamma_2} d\Gamma_2 \omega r \delta j_z \kappa_\theta \Big|_{r_i}^{r_j} - \int_V dV \delta \kappa_\theta \frac{\partial (\omega j_z)}{\partial r} \\
&+ \delta \lambda_c \left(I - \int_{\Gamma_1} d\Gamma_1 j_z \right) + \int_{\Gamma_2} d\Gamma_2 \delta A_z \left\{ \frac{r}{\mu} \frac{\partial A_z}{\partial r} \right\} \Big|_{r_i}^{r_j}
\end{aligned}
$$

(3.1.11)

3.2 SUPERCONDUCTIVITY.

This section presents some of the basic theory of superconductivity and the application of the four-potential method to the solution of the time-independent superconductor problem. For this problem, ρ is taken as zero, and the variable Φ is no longer required. For cases where $\mathbf{E}$ or ρ are not zero, the superconductor behaves as a normal conductor for the $\mathbf{E}$ and $\mathbf{D}$ fields, and these fields can be treated by the methods discussed in the previous chapters. The departure from a normal conductor is exhibited in the $\mathbf{B}$ and $\mathbf{H}$ fields and in the resistance of a superconductor. There is an almost complete absence of resistance and the $\mathbf{B}$ and $\mathbf{H}$ fields are non-linear. The linear constitutive relation (3.1.2) no longer applies, and $\mathbf{j}$ is now a function of $\mathbf{A}$ and the quantum mechanical quantity, the wave order parameter ψ. For these reasons, the non-linear fields and non-linear constitutive equations, this work deals exclusively with magnetostatic superconductor problems.

The most widely accepted microscopic theory of low temperature superconductivity is due to Bardeen, Cooper and Schreifer [21, pp. 16-71] and

is referred to as BCS theory. No attempt is made here to present the BCS theory of superconductivity, as the author's work is based on the Ginzburg-Landau equations. The Ginzburg-Landau equations, which describe types I and II superconducting phenomena, are based upon the BCS theory. The important result of the BCS theory is that below a certain temperature it becomes energetically more favorable for "free" electrons to bind together in pairs, called Cooper pairs, and that the density of these pairs in a volume can be represented by the quantum probability density function ψ. Table 3.1 lists the relevant nomenclature for superconductivity.

Table 3.1   Superconducting Theory Nomenclature

Symbol	Quantities
α, β	Temperature dependent material parameters
ψ	Analgous to a wave/position function in particle mechanics
$|\psi|^2$	Number of superconducting charge carriers per unit volume
ψ^*	Complex conjugate of ψ
q^*	Effective charge of charge carriers
m^*	Effective mass of charge carriers
$\hbar$	Planck's constant divided by 2π
A	Magnetic potential vector
B	Total magnetic field
j	Current distribution
F_s	Helmholtz free energy of superconducting state
F_n	Helmholtz free energy of normal state
ΔF	$F_s - F_n$

3.2.1 THE HELMHOLTZ FREE ENERGY FOR A SUPERCONDUCTOR.

The Helmholtz free energy of a system is expressed as

$$F = U - \mathcal{T}S \qquad (3.2.1)$$

where F, U, $\mathcal{T}$ and S represent the Helmholtz free energy, the potential energy, the temperature and the entropy of the system respectively.

In the general vicinity of the transition or critical temperature for a type I or II superconductor, the difference between the Helmholtz free energy of the superconducting and normal states of a conductor can be approximated as

$$\Delta F = F_s - F_n = \int_V dV \left\{ -\alpha|\psi|^2 + \tfrac{1}{2}\beta|\psi|^4 + \frac{1}{2m^*}|(-i\hbar\nabla - q^*\mathbf{A})\psi|^2 + \tfrac{1}{2}\mathbf{B}\cdot\mathbf{H} \right\}$$
$$(3.2.2)$$

in S.I. units [20], where the quantities α, β and ψ are defined in Table 1. The first two terms represent a typical Landau expansion of the Helmholtz free energy for a second order phase transition. The third term represents the total momentum of the charge carrier. The $-i\hbar\nabla$ term is analogous to the dynamic (kinetic) momentum of a quantum wave-like particle; the $q^*\mathbf{A}$ term represents the field momentum [31, p. 633; 21, pp. 105-108].

REMARK 3.2.1
A good example to illustrate quantum kinetic momentum is provided by a one-dimensional particle in an infinitely deep energy well. The $-i\hbar\nabla$ term in the above functional is similar, in quantum theory, to the momentum of the particle in the well.

Using the identities, $\mathbf{B} = \mu_o\mathbf{H}$, and $\mathbf{B} = \nabla\times\mathbf{A}$, the last term of (3.2.2), which represents the field energy, can be replaced by

$$\frac{1}{2\mu_o}(\nabla\times\mathbf{A})^2 \qquad (3.2.3)$$

70

In (3.2.3), the material's magnetic permeability μ, has been set to μ_o, the value of the permeability of free space. The justification for the use of μ_o is that, in a superconductor, there is an almost total expulsion of the magnetic field $\mathbf{B}$ from the interior of the superconductor. This effect is called the *Meissner* effect. The $\mathbf{B}$ field will only penetrate a small distance into the superconductor. This approximate penetration depth is called the *London* penetration depth. For superconducting samples with dimensions much larger than the London penetration depth, the contribution to F by the difference between $\mu \mathbf{H}$ and $\mu_o \mathbf{H}$ is small and the substitution of μ for μ_o is justified (Ref. [21], p.89). This type of superconductor is referred to as a bulk superconductor. Superconductors with macroscopic dimensions on the order of or smaller than the London penetration depth should use μ instead of μ_o. Only bulk superconductors are dealt with here.

Expanding ΔF in terms of ψ and ψ^* gives

$$\Delta F = \int_V dV \left\{ -\alpha \psi \psi^* + \tfrac{1}{2}\beta \left(\psi \psi^* \right)^2 + \frac{1}{2m^*} \left(-i\hbar \nabla^T \psi - q^* \mathbf{A}^T \psi \right) \right.$$

$$\left. \left(i\hbar \nabla \psi^* - q^* \mathbf{A} \psi^* \right) + \frac{1}{2\mu_o} \left(\nabla \times \mathbf{A} \right)^T \left(\nabla \times \mathbf{A} \right) \right\} \qquad (3.2.4)$$

The quantities ψ and ψ^* are both complex quantities and present no mathematic difficulties when deriving a variational formulation of superconductivity, but they do cause numerical problems. If ψ and ψ^* are used as independent variables in a numerical model, they require twice the amount of memory to store because both a real and imaginary number must be stored for each variable. A preferred numerical formulation will only contain variables that are real. Luckily, the independent variables ψ and ψ^* can be expressed in several different manners, all of which are mathematically

equivalent. If we let ψ equal $\psi_R + i\psi_I$ and ψ^* equal $\psi_R - i\psi_I$, where ψ_R and ψ_I represent the magnitudes of the real and imaginary parts respectively of the old variables, and i the square root of -1, the memory storage problem is solved and the new variables are real. This formulation was used in in Ref. [32] for one-dimensional calculations. Although reasonable results for most quantities were obtained, others lacked accuracy. Later, it was decided to find an improved formulation. In the modified formulation, ψ and ψ^* become $|\psi|e^{i\varpi}$ and $|\psi|e^{-i\varpi}$ respectively, where $|\psi|$ is the modulus and ϖ is the phase angle of ψ and ψ^*. These are the new independent variables used in the functional ΔF. With these substitutions, (3.2.4) becomes

$$
\Delta F = \int_V dV \left\{ -\alpha|\psi|^2 + \tfrac{1}{2}\beta|\psi|^4 + \frac{1}{2m^*}\left(\hbar^2\nabla^T|\psi|\nabla|\psi| \right.\right.
$$
$$
\left. + |\psi|^2\left(\hbar\nabla^T\varpi - q^*\mathbf{A}^T\right)\left(\hbar\nabla\varpi - q^*\mathbf{A}\right)\right) \tag{3.2.5}
$$
$$
\left. + \frac{1}{2\mu_o}(\nabla\times\mathbf{A})^T(\nabla\times\mathbf{A})\right\}
$$

The first variation of ΔF with respect to $|\psi|$ is

$$
\delta\Delta F(\delta|\psi|) = \int_V dV\,\delta|\psi|\left\{ -2\alpha|\psi| + 2\beta|\psi|^3 - \frac{\hbar^2}{m^*}\nabla^2|\psi| \right.
$$
$$
\left. + \frac{|\psi|}{m^*}\left(\hbar\nabla^T\varpi - q^*\mathbf{A}^T\right)\left(\hbar\nabla\varpi - q^*\mathbf{A}\right)\right\} \tag{3.2.6}
$$
$$
+ \int_\Gamma d\Gamma\,\delta|\psi|\left\{ \frac{\hbar^2}{m^*}\hat{\mathbf{n}}\cdot\nabla|\psi|\right\}
$$

The first variation of ΔF with respect to ϖ is

$$
\delta\Delta F(\delta\varpi) = -\int_V dV\,\delta\varpi\left\{ \nabla\cdot\left(|\psi|^2\left(\frac{\hbar^2}{m^*}\nabla\varpi - \frac{q^*\hbar}{m^*}\mathbf{A}\right)\right)\right\}
$$
$$
+ \int_\Gamma d\Gamma\,\delta\varpi\left\{ \hat{\mathbf{n}}\cdot\left(|\psi|^2\left(\frac{\hbar^2}{m^*}\nabla\varpi - \frac{q^*\hbar}{m^*}\mathbf{A}\right)\right)\right\} \tag{3.2.7}
$$

72

The first variation of ΔF with respect to $\mathbf{A}$ is

$$\delta \Delta F(\delta \mathbf{A}) = \int_V dV \delta \mathbf{A}^T \left\{ |\psi|^2 \left(-\frac{q^* \hbar}{m^*} \nabla \varpi + \frac{q^{*2}}{m^*} \mathbf{A} \right) + \frac{1}{\mu_o} (\nabla \times \nabla \times \mathbf{A}) \right\}$$
$$+ \int_\Gamma d\Gamma \delta \mathbf{A}^T \left\{ \frac{1}{\mu_o} (\nabla \times \mathbf{A} \times \hat{\mathbf{n}}) \right\}$$

(3.2.8)

Comparison of the above equations with the Maxwell eqaution $\nabla \times \mathbf{B} = \mathbf{j}$ shows that the constitutive relation for a superconductor is

$$\mathbf{j} = |\psi|^2 \left(\frac{q^* \hbar}{m^*} \nabla \varpi - \frac{q^{*2}}{m^*} \mathbf{A} \right)$$

(3.2.9)

where $\mathbf{j}$ is now a function of $\mathbf{A}$ instead of $\mathbf{E}$. Note that $\mathbf{j}$ and the constitutive relation are already contained in the Euler equations and that $\mathbf{j}$ and λ_c are not needed as separate variables to make the set of equations determinate.

The set of Euler equations obtained by the variation of ΔF is collectively called the *Ginzburg-Landau* equations. They describe the behavior of type I and II superconductors. In the London approximation, ψ is assumed to be constant throughout the conductor volume. For this approximation, equations (3.2.6) and (3.2.7) become zero and equation (3.2.8) becomes

$$\delta \Delta F(\delta \mathbf{A}) = \int_V dV \delta \mathbf{A}^T \left\{ |\psi|^2 \frac{q^{*2}}{m^*} \mathbf{A} + \frac{1}{\mu_o} (\nabla \times \nabla \times \mathbf{A}) \right\}$$

(3.2.10)

This type of conductor is known as a *London* type superconductor. Type I superconductors are commonly referred to as London superconductors because ψ is constant over the majority of the conductor volume and (3.2.10) can be used to get a good approximation of the $\mathbf{B}$ field inside of the conductor.

For the Ginzburg-Landau bulk superconductor, ψ becomes a constant within the superconducting volume at the interior boundary. This

means that $|\psi|$ is a constant there, and the interior boundary integral of (3.2.6) is zero.

Although the curl of **A** has been defined, the divergence of **A** is arbitrary. A common choice and the one used here is the London gauge, $\nabla \cdot \mathbf{A} = 0$, which is equivalent to the time-independent Lorentz gauge. For this gauge choice, **A** must go to zero inside of a bulk superconductor [32, p.12]. ψ must also go to zero at the exterior free space/conductor boundary. This reference shows that, with the London gauge, $\nabla \psi$ also be zero at the exterior boundary. This condition is equivalent to $\nabla |\psi|$ being zero on the exterior boundary. With this condition, the outer boundary integral of (3.2.6) is also zero, and the boundary term disappears completely.

Because of the London gauge choice and the condition that $|\psi|$ is constant deep in the bulk layer, the Euler equation of (3.2.7) becomes, in the bulk region, $\nabla^2 \varpi = 0$, requiring that $\nabla \varpi$ be a constant. The value of the constant is determined by energy considerations. The term $|\psi|/m^*(\hbar \nabla \varpi - q^* \mathbf{A})$ represents the net exchange of field momentum from the magnetic field to the kinetic momentum of the charge carriers. Only in the boundary layer is there an exchange of momentum and in the bulk of a superconductor this term must be zero. Because **A** is zero in the interior of bulk superconductors, $\nabla \varpi$ must also be zero or there will be an exchange of momentum. Therfore, for the London gauge choice, ϖ is a constant [21, p.107]. This reduces the number of independent variables from three to two. The correct augmented

functional for the generalized three-dimensional case is therefore

$$
\Delta F_g = \int_V dV \left\{ -\alpha|\psi|^2 + \tfrac{1}{2}\beta|\psi|^4 + \frac{1}{2m^*}\left(\hbar^2 \nabla^T|\psi|\nabla|\psi| + |\psi|^2\frac{q^{*2}}{m^*}\mathbf{A}^T\mathbf{A}\right) \right.
$$
$$
\left. + \frac{1}{2\mu_o}(\nabla\times\mathbf{A})^T(\nabla\times\mathbf{A}) + \lambda_g(\nabla\cdot\mathbf{A}) \right\}
$$

$$(3.2.11)$$

and its first variation is

$$
\delta\Delta F_g = \int_V dV\,\delta|\psi| \left\{ -2\alpha|\psi| + 2\beta|\psi|^3 - \frac{\hbar^2}{m^*}\nabla^2|\psi| + |\psi|\frac{q^{*2}}{m^*}\mathbf{A}^T\mathbf{A} \right\}
$$
$$
+ \int_V dV\,\delta\mathbf{A}^T \left\{ |\psi|^2\frac{q^{*2}}{m^*}\mathbf{A} + \frac{1}{\mu_o}(\nabla\times\nabla\times\mathbf{A}) + \nabla\lambda_g \right\}
$$
$$
+ \int_\Gamma d\Gamma\,\delta\mathbf{A}^T \left\{ \frac{1}{\mu}(\nabla\times\mathbf{A}\times\hat{\mathbf{n}}) + (\cdot\hat{\mathbf{n}}\,\lambda_g) \right\}
$$

$$(3.2.12)$$

3.2.2 ONE-DIMENSIONAL SUPERCONDUCTORS.

For the one-dimensional Ginzburg-Landau superconductor that has
the same geometry as the linear conductor examined earlier in this chapter,
and no static charge density ρ, (3.2.11) reduces to

$$
\Delta F_g = \int_V dV \left\{ -\alpha|\psi|^2 + \tfrac{1}{2}\beta|\psi|^4 + \frac{1}{2m^*}\left(\hbar^2\left(\frac{\partial|\psi|}{\partial r}\right)^2 \right.\right.
$$
$$
\left.\left. + |\psi|^2 q^{*2} A_z^2\right) + \frac{1}{2\mu_o}\left(\frac{\partial A_z}{\partial r}\right)^2 \right\}
$$

$$(3.2.13)$$

and the first variation is

$$
\begin{aligned}
\delta\Delta F_g = & \int_V dV\,\delta|\psi|\Big\{-2\alpha|\psi| + 2\beta|\psi|^3 \\
& - \frac{\hbar^2}{m^*}\left(\frac{1}{r}\frac{\partial}{\partial r}\left(r\frac{\partial|\psi|}{\partial r}\right)\right) + |\psi|\frac{q^{*2}}{m^*}(A_z)^2\Big\} \\
& - \int_V dV\,\delta A_z\left\{\frac{1}{\mu_o}\left(\frac{1}{r}\frac{\partial}{\partial r}\left(r\frac{\partial A_z}{\partial r}\right)\right) - |\psi|^2\frac{q^{*2}}{m^*}A_z\right\} \\
& + \int_{\Gamma_2} d\Gamma_2\,\delta A_z\left\{r\frac{\partial A_z}{\partial r}\right\}\Big|_{r_i}^{r_j} \\
& + \int_{\Gamma_2} d\Gamma_2\,\delta|\psi|\left\{\frac{\hbar^2}{m^*}r\frac{\partial|\psi|}{\partial r}\right\}\Big|_{r_i}^{r_j}
\end{aligned}
\tag{3.2.14}
$$

An illustration of the physical problem is shown in the lower portion of Figure 3.1.

For a London superconductor, ψ is constant and (3.2.11) and (3.2.12) become

$$
\begin{aligned}
\Delta F_g = & \int_V dV\left\{\frac{1}{2\mu_o}\left(\frac{\partial A_z}{\partial r}\right)^2 + |\psi|^2 q^* A_z^2\right\} \\
\delta\Delta F_g = & -\int_V dV\,\delta A_z\left\{\frac{1}{\mu_o}\left(\frac{1}{r}\frac{\partial}{\partial r}\left(r\frac{\partial A_z}{\partial r}\right)\right) - |\psi|^2\frac{q^{*2}}{m^*}A_z\right\} \\
& + \int_{\Gamma_2} d\Gamma_2\,\delta A_z\left\{r\frac{\partial A_z}{\partial r}\right\}\Big|_{r_i}^{r_j}
\end{aligned}
\tag{3.2.15}
$$

For both cases, the only nonzero component of $\mathbf{j}$ is in the $\hat{e}_z$ direction and is

$$
j_z = -|\psi|^2\frac{q^{*2}}{m^*}A_z
\tag{3.2.16}
$$

3.2.3 EVALUATION OF MATERIAL PARAMETERS α AND β.

The following is a summary of Tinkham's derivation of α and β that is presented in [21, pp.105-109]. Appropriate changes have been made to convert this derivation from CGS units to SI units.

Deep within a superconductor, due to screening effects (the Meissner effect), there are no fields or gradients. The last terms in the functional ΔF drop out and the resulting equation is

$$\Delta F = -\alpha |\psi|^2 + \tfrac{1}{2}\beta |\psi|^4 \qquad (3.2.17)$$

Near the second order phase transition, at the critical temperature T_c, the minimum value for the free energy occurs when

$$\frac{\partial \Delta F}{\partial \psi} = -2\alpha |\psi| + 2\beta |\psi|^3 = 0 \qquad (3.2.18)$$

from which

$$|\psi|^2 = |\psi_\infty|^2 = \frac{\alpha}{\beta} \qquad (3.2.19)$$

where $|\psi_\infty|^2$ is the value for the number density of superconducting charge carriers deep within the conductor. Substituting $|\psi_\infty|^2$ back into the preceding equation for ΔF, gives

$$\Delta F = -\frac{\alpha^2}{\beta} + \frac{\alpha^2}{2\beta} = -\frac{\alpha^2}{2\beta} \qquad (3.2.20)$$

When the critical field $\mathbf{B}_c$ is applied, $\Delta F = -\mathbf{B}_c^2 / 2\mu_o$. Because of this condition, deep within a superconductor, where no gradients are present, the following approximation to ΔF can be made

$$\Delta F = -\frac{\mathbf{B}_c^2}{2\mu_o} = -\frac{\alpha^2}{2\beta} \Rightarrow \frac{\mathbf{B}_c^2}{\mu_o} = \frac{\alpha^2}{\beta} \qquad (3.2.21)$$

77

The work, W, done in setting up a current distribution $\mathbf{j}$ [26] is

$$W = -\tfrac{1}{2} \int_V \mathbf{j}^T \mathbf{A} dV \qquad (3.2.22)$$

From the London theory [21, p. 84], with λ_{eff} equal to the effective London penetration depth, the following equation relating $\mathbf{j}$ and $\mathbf{A}$ can be derived

$$\mathbf{j} = -\frac{1}{\mu_o \lambda_{eff}^2} \mathbf{A} \qquad (3.2.23)$$

Substitution of this expression for $\mathbf{j}$ into the equation for W gives

$$W = \frac{1}{2\mu_o \lambda_{eff}^2} \int_V \mathbf{A}^T \mathbf{A} dV \qquad (3.2.24)$$

From the Ginzburg-Landau theory [21, p. 107], the expression for the work done in setting up a current density $\mathbf{j}$ is defined as being

$$W = \int_V \frac{q^{*2}}{2m^*} \mathbf{A}^T \mathbf{A} |\psi_\infty|^2 dV \qquad (3.2.25)$$

If gradients of the order parameter are zero and there are no external fields present, the two preceding equations are good approximations to W. Equating these two expressions for W gives

$$\frac{1}{2\mu_o \lambda_{eff}^2} = \frac{q^{*2}}{2m^*} |\psi_\infty|^2 \qquad (3.2.26)$$

Algebraic manipulation produces

$$|\psi_\infty|^2 = \frac{m^*}{\mu_o q^{*2} \lambda_{eff}^2} = \frac{\alpha}{\beta} \qquad (3.2.27)$$

Solving for β gives

$$\beta = \alpha \frac{\mu_o q^{*2} \lambda_{eff}^2}{m^*} \qquad (3.2.28)$$

From before

$$\frac{\mathbf{B}_c^2}{\mu_o} = \frac{\alpha^2}{\beta} \tag{3.2.29}$$

Substitution for β finally yields

$$\boxed{\alpha = \frac{q^{*2}}{m^*}\mathbf{B}_c^2\lambda_{eff}^2 \quad \beta = \frac{\mu_o q^{*4}}{m^{*2}}\mathbf{B}_c^2\lambda_{eff}^4} \tag{3.2.30}$$

Allowing $|\psi_\infty|^2$ to equal the number of superconducting electron pairs, it is seen that to be consistent with the London theory

$$\boxed{\begin{array}{lll} q^* & = -2e & = \text{twice the electron charge} \\ m^* & = 2m & = \text{twice the electron mass} \end{array}}$$

3.3 SUMMARY.

In this chapter, the boundary conditions and the appropriate forms of functionals based upon the four-potential method are determined for two conductors with an unknown current density vector. The two types of conductors considered are a normal linear conductor and a superconductor. The only approximation made for the linear conductor is that both ω and $\mathbf{j}$ be step functions. The more general case where they are both C^o continuous is also discussed.

For the superconductor, the Ginzburg-Landau and London type superconductors are discussed. The London type superconductor is shown to be a simplification of the Ginzburg-Landau superconductor based upon the assumption that the quantum mechanical variable ψ becomes a constant throughout the conductor volume.

Also determined are the boundary conditions for the gauge choice $\nabla \cdot \mathbf{A} = 0$. This particular gauge choice reduces the number of independent variables for the Ginzburg-Landau superconductor by one. The appropriate expressions for the two material parameters for this conductor, α and β, are also determined in this chapter.

The primary assumption in determining a functional for the Ginzburg-Landau superconductor is that the conductor is near the phase transition temperature, T_c. Fortunately, there is some experimental support that the Ginzburg-Landau theory is valid in a much wider range of temperature than this narrow range if appropriate values for λ_{eff} and B_c are used.

In the next chapter, the thermal dependence of the two fuctionals derived here is explored. A functional to predict thermal fields is also presented.

THERMAL EFFECTS

In previous chapters thermal effects in conductors have been ignored. Thermal effects are quite important in superconductivity because they determine whether a conductor remains in the normal or superconducting state. Thermal fields also affect the current density distribution in normal linear conductors. In order to develop more accurate models of the EM fields, it is therefore important that thermal effects be included in numerical models of these fields. To accomodate the need to model the thermal fields, this chapter presents the functionals for two simple time-independent thermal field problems, the heat conduction and heat convection problems. These sections summarize material presented in references [24] and [33, pp.90-92].

Typically, the EM material properties α, β, ϵ, μ and ω are temperature-dependent. The dependence of ϵ on thermal fields for conductors is mild and is not addressed here. The thermal dependence of μ is not discussed either because little experimental data for the test material, extremely pure aluminum, could be found. The only available datum found was a room temperature value[34, p.627], and this value is approximately μ_o. If the value of μ remains within an order of magnitude of μ_o (*i.e.*, $\sim 10\mu_o$), the formulations presented in this work experience no numerical difficulties if the correct value for μ is used. Scaling schemes to improve matrix condition numbers and numerical stability are also presented in the sequel, and they

can be implemented to cover cases where μ deviates significantly from μ_o. For the above reasons, the values of μ_o and ϵ_o are substituted for μ and ϵ in all numerical formulations presented here. The temperature dependence of α, β and ω are discussed later in this chapter.

4.1 THERMAL FUNCTIONALS.

For a time-independent three-dimensional system, the functional

$$\Omega_d = \int_V dV \left\{ \tfrac{1}{2} \nabla T^T k \nabla T - \dot{q} T \right\} - \int_\Gamma d\Gamma \left\{ \mathbf{Q} \cdot \hat{n} T \right\} \qquad (4.1.1)$$

can be used to model the heat conduction problem [24, p.2]. $\mathbf{Q}$ represents the heat flux through the boundary of the integration volume, T the temperature, k the thermal conductivity tensor, and $\dot{q}$ the heat generation rate per unit volume. For the time-independent case, all of the above are functions only of the spatial coordinates.

The first variation of the above equation with respect to the independent variable T is

$$\delta\Omega_d = \int_V dV \delta T \left\{ \nabla \cdot (k \nabla T) - \dot{q} \right\} + \int_\Gamma d\Gamma \delta T \hat{n} \cdot \left\{ k \nabla T - \mathbf{Q} \right\} \qquad (4.1.2)$$

For linear conducting media, the heat generation per unit volume depends upon the current density $\mathbf{j}$ and the resistivity of the material ω. Both k and ω for a material are functions of T, but for the purposes of this formulation, they are treated as functions of the space coordinates. When the finite element solution process is discussed, this assumption will be treated in a more complete manner. For now, it is assumed that ω is a function of the

82

space coordinates and the appropriate value of $\dot{q}$ for the time-independent linear conductor is [35, p.117]

$$\dot{q} = \omega \mathbf{j} \cdot \mathbf{j} \qquad (4.1.3)$$

For the case of convection heat transfer, the heat flux across a boundary may be expressed as [24, p.4]

$$\mathbf{Q} = \mathbf{h}\left(\mathcal{T}_{\infty} - \mathcal{T}\right) \qquad (4.1.4)$$

where $\mathbf{h}$ is the heat-transfer coefficient tensor, which is only a function of the spatial coordinates, and $\mathcal{T}_{\infty}$ is the known free-stream temperature. The associated variational functional is

$$\Omega_v = \int_{\Gamma} d\Gamma \mathcal{T} \hat{\mathbf{n}} \cdot \left\{ \mathbf{h}\left(\mathcal{T}_{\infty} - \tfrac{1}{2}\mathcal{T}\right) - \mathbf{Q} \right\} \qquad (4.1.5)$$

whose first variation is

$$\delta\Omega_v = \int_{\Gamma} d\Gamma \delta\mathcal{T} \hat{\mathbf{n}} \cdot \left\{ \mathbf{h}\left(\mathcal{T}_{\infty} - \mathcal{T}\right) - \mathbf{Q} \right\} \qquad (4.1.6)$$

4.1.1 ONE-DIMENSIONAL THERMAL FUNCTIONALS.

For the one dimensional case, the same geometry as that of previous chapters is used. An illustration of the thermal portion of the problem is shown in Figure 4.1. Again there is a long cylindrical conductor that extends to $\pm\infty$ in the $\hat{\mathbf{e}}_z$ direction, the longitudinal axis of the conductor coincides with that of $\hat{\mathbf{e}}_z$ axis, and the conductor carries a steady current I. Due to symmetry, there is no variation of $\mathcal{T}$ in the $\hat{\mathbf{e}}_\theta$ and $\hat{\mathbf{e}}_z$ directions. The functional Ω_d becomes

$$\Omega_d = \int_V dV \left\{ \tfrac{1}{2} k \left(\frac{\partial \mathcal{T}}{\partial r}\right)^2 - \mathcal{T} \omega j_z^2 \right\} - \int_{\Gamma_2} d\Gamma_2 r Q_r \mathcal{T} \Big|_{r_i}^{r_j} \qquad (4.1.7)$$

83

where k is the thermal conductivity, and like ω is a function of r. Q_r is the heat flux in the radial direction $\hat{e}_r$. The first variation of (4.1.7) is

$$\delta\Omega_d = -\int_V dV \delta T \left\{ \frac{1}{r}\frac{\partial}{\partial r}\left(kr\frac{\partial T}{\partial r}\right) + \omega j_z^2 \right\} + \int_{\Gamma_2} d\Gamma_2 \delta T r \left\{ k\frac{\partial T}{\partial r} - Q_r \right\} \Big|_{r_i}^{r_j} \tag{4.1.8}$$

The one dimensional heat convection functional is

$$\Omega_v = \int_{\Gamma_2} d\Gamma_2 T r \left\{ h_{conv}\left(\tfrac{1}{2}T_\infty - T\right) - Q_r \right\} \Big|_{r_i} \tag{4.1.9}$$

where h_{conv} is the convection coefficient. The first variation is

$$\delta\Omega_v = \int_{\Gamma_2} d\Gamma_2 \delta T r \left\{ h_{conv}\left(T_\infty - T\right) - Q_r \right\} \Big|_{r_i} \tag{4.1.10}$$

For the Euler equation of (4.1.8), integrating with respect to r once gives

$$kr\frac{\partial T}{\partial r} = -\int \omega j_z^2 r\, dr + C_1 \tag{4.1.11}$$

and integration with respect to r twice gives

$$T = -\int \frac{1}{kr}\left(\int \omega j_z^2 r\, dr\right) dr + C_1 \int \frac{1}{kr} dr + C_2 \tag{4.1.12}$$

where C_1 and C_2 are constants of integration.

A premise to the analysis of the heat conduction problem presented here is that k varies slowly across the domain of integration, $i.e.$, between r_i and r_j. This premise will be true if the finite elements that are used in the heat conduction analysis can be made small enough to model the temperature distribution within the conductor adequately. The only limit on the size of the elements is machine accuracy. For the cases where the size of the element is smaller than machine accuracy, scaling schemes can be employed to move

84
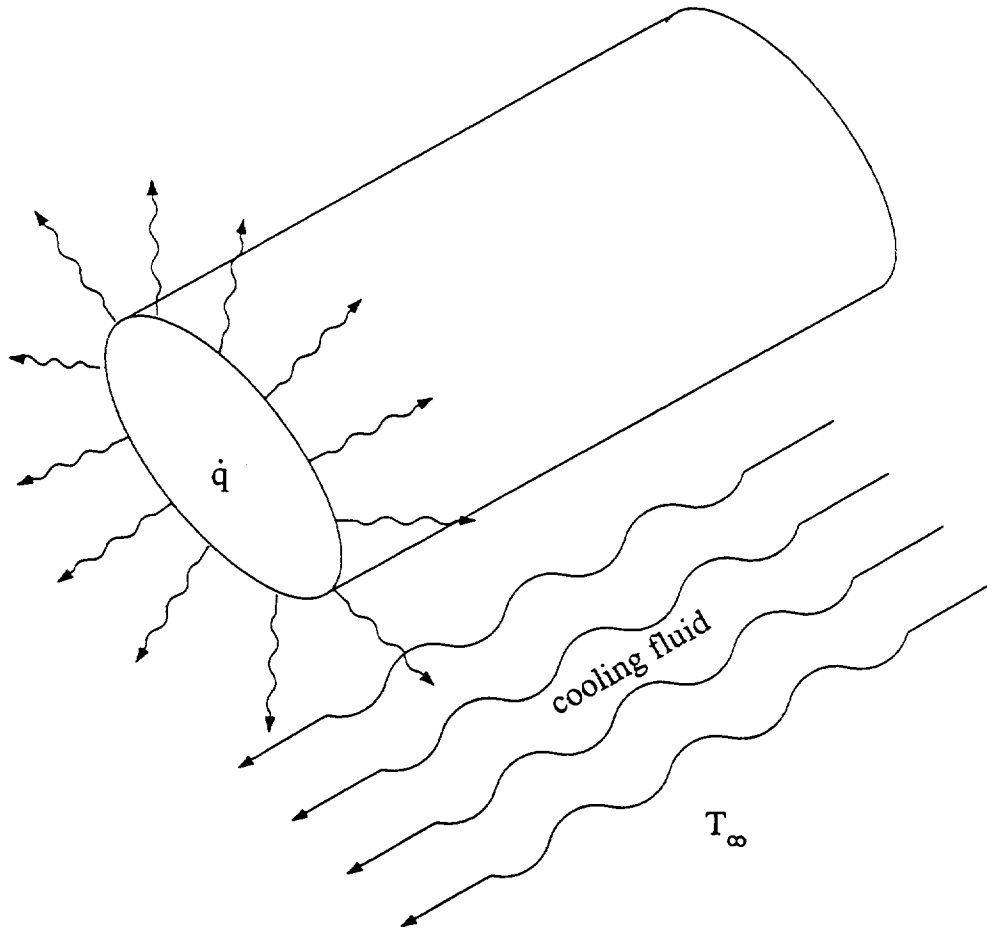
Figure 4.1: Physical Problem: One-dimensional conductor generating a heating load.

finite element solutions back into the machine's range. So, theoretically at least, the assumption that k varies slowly across an element's domain is a valid assumption. This assumption proves to be true for the cases that are presented later in this work. If k varies slowly, it can be approximated by a linear interpolation across an element. This interpolation is

$$k = k_i + \frac{k_j - k_i}{r_j - r_i} r = k_i + \frac{\Delta k}{\Delta r} r \qquad (4.1.13)$$

where k_i and k_j are the values of k at the inner and outer boundaries of integration respectively.

In the previous chapter, it is assumed that over elements (between boundary limits), that ω and j_z are approximated as step functions for a linear conductor. That assumption is made again here. With this assumption, ω and j_z become constants over the range of integration of (4.1.12). Substituting (4.1.13) into (4.1.12), and using the above assumption of constant current density and resistivity, integration of (4.1.12) provides

$$T = \frac{\omega j_z^2}{2} \left(\frac{r\Delta r}{\Delta k} - \frac{k_i \Delta r^2}{\Delta k^2} \ln \left(k_i + \frac{\Delta k}{\Delta r} r \right) \right) + C_1 \frac{1}{k_i} \ln \left(\frac{r\Delta r}{k_i \Delta r + \Delta k} \right) + C_2$$
$$(4.1.14)$$

where ln represents the natural logarithm of the argument.

If ω is allowed to go to zero, as in a superconductor, (4.1.14) becomes

$$T = C_1 \frac{1}{k_i} \ln \left(\frac{r\Delta r}{k_i \Delta r + \Delta k} \right) + C_2 \qquad (4.1.15)$$

For this solution to remain bounded as r_i goes to zero, C_1 *must* be zero. Now T is an undetermined constant, C_2, at r_j. This provides an important boundary condition for *any* cylindrical heat conduction problem that has r_i equal to zero, this boundary condition being that $\partial T / \partial r \big|_0$ equal zero.

Referring to (4.1.8), the interior boundary integral, with C_2 substituted for T shows that

$$Q_r = k\frac{\partial T}{\partial r} = k\frac{\partial C_2}{\partial r} = 0 \qquad (4.1.16)$$

Consequently, the heat flux and the temperature gradient at $r = 0$ vanish if the solution of T is to remain bounded.

Letting r_j now equal an arbitrary interior point of the conductor, r_2, the exterior boundary integral of (4.1.8) also disappears for the case of ω equal to zero. To find the T distribution, another arbitrary point, r_3, between r_2 and the conductor/free space boundary is chosen. The expressions, (4.1.11) and (4.1.15), derived from the heat conduction variational principle, are also used again. At r_2, it is already known that $\partial T/\partial r$ is zero. Using (4.1.11), it is found that C_1 again equals zero and using (4.1.15) determines that T again equals an arbitrary constant. This constant must be the same as that derived for the case where r varied between zero and r_2 in order to satisfy the C^o continuity of T in the variational functional as well as the boundary conditions imposed by the first variation of that functional. Because r_2 and r_3 are arbitrary, this requires for the case of zero resistivity that T become a single constant over the domain of the conductor.

This constant is determined by the use of equations (4.1.8) and (4.1.10). The former states

$$Q_r = k\frac{\partial T}{\partial r} = 0 \qquad (4.1.17)$$

Using this information, (4.1.10) gives

$$T_s = T_\infty \qquad (4.1.18)$$

where T_s and T_∞ represent the surface temperature and the temperature of the cooling fluid outside of the convection cooling boundary layer respectively. This gives the final result, when $\omega = 0$ the temperature distribution within a conductor is the constant T_∞, and also that the thermal properties k and h_{conv} need not be known.

For the more general case of a nonzero ω, equations (4.1.8) and (4.1.10) are used again to find the temperature distribution T. For this case, (4.1.11) must also be used. It is assumed here that r_i is zero and r_j is the conductor radius, r_c. Equation (4.1.11) then gives

$$ kr_c \frac{\partial T}{\partial r} = - \int_0^{r_c} \omega j_z^2 r\, dr \qquad (4.1.19) $$

where r_c is the conductor's radius. Combining this result with the boundary integral of (4.1.8) gives

$$ Q_r = -\frac{1}{r_c} \int_0^{r_c} \omega j_z^2 r\, dr \qquad (4.1.20) $$

Using this result and (4.1.10) gives the following equation

$$ T_s = \frac{1}{h_{conv} r_c} \int_0^{r_c} \omega j_z^2 r\, dr + T_\infty \qquad (4.1.21) $$

At the interior boundary, r_i is equal to zero and the value of C_1 of equation (4.1.12) is zero. The value for C_2 can also be determined to be equal to T_s. The temperature distribution is now

$$ T(r) = - \int_0^r \frac{1}{kr} \left(\int_0^r \omega j_z^2 r\, dr \right) dr + T_s \qquad (4.1.22) $$

REMARK 4.1.1
Strictly speaking, the application of the equation (4.1.15) for T to the superconductors presented in this work is only approximate. For these superconductors j is a function of A and $|\psi|$, both of which are C^o continuous. This makes j C^o

88

continuous, and the integration of the first term in (4.1.11) incorrect because j is assumed to be C^{-1} continuous there. However, because ω is a constant and equal to zero for a superconductor, the first term of (4.1.11) disappears, and integration of the remaining terms gives the previous result, equation (4.1.15).

4.2 VALUES FOR THE THERMAL PARAMETERS k AND h_{conv}.

The first parameter discussed is the thermal conductivity k of a linear conductor. The thermal conductivity of a superconductor is not necessary for the problems studied in this work and will not be discussed. Reference [36] gives a semi-empirical formula for the thermal conductivity of a material. This formula is [36, p.6a]

$$k = \frac{1}{\alpha' \mathcal{T}^n + \beta' / \mathcal{T}} \qquad (4.2.1)$$

where

$$\alpha' = \alpha'' \left(\frac{\beta'}{n\alpha''} \right)^{\frac{(m-n)}{(m+1)}} \qquad (4.2.2)$$

For these formulas, k is given in watt cm^{-1} $\mathcal{T}^{-1}$ where $\mathcal{T}^{-1}$ is in degrees Kelvin. The constants m, n, α'' and β' were determined by a curve fit to experimental data. The values of these constants for well annealed, 99.9999% pure aluminum with a residual resistivity of 0.000593 micro-ohms per cm and a critical temperature of 1.196 degrees Kelvin are [36, p.9]

$$
\begin{array}{ll}
n = 2.0 & \alpha'' = 4.8 \times 10^{-6} \\[2mm]
m = 2.61 & \beta' = .0245
\end{array}
\qquad (4.2.3)
$$

These values are used to determine k for all of the examples presented here. The thermal conductivity returned by this formula is accurate to within 3-5% of experimental values in the temperature range of zero to fifteen degrees Kelvin.

On a microscopic level, all conductors are composed of a lattice structure with tightly bound electrons and protons. Some loosely bound electrons also exist and are called "free" electrons. There are two types of lattice structure interactions, and they determine, in part, how quickly heat may be transported through a conductor. This part is called the lattice structure's contribution to the material's thermal conductivity or the thermal conductivity of the lattice. The first of the two lattice interactions is that due to quantum lattice vibrations called *phonons*, that can be treated quantum-mechanically as both waves and particles, and collisions between these quasi-particles. For this interaction, the thermal conductivity is proportional to T [31, pp.115-121], and is represented by the second term in the denominator of (4.2.1). The second interaction is due to material imperfections, such as a copper ion in an aluminum lattice structure or imperfections in the lattice structure itself, such as dislocations. In this second interaction, the transport of both phonons and "free" electrons are being affected by an imperfect lattice. The net result is that a particle is being scattered by the lattice imperfection. For an essentially pure monocrystaline structure, these effects can be neglected. This assumption is made for the above aluminum sample for k because of its high purity and because it has also been well annealed to remove lattice imperfections.

The "free" electrons provide a third means of energy transport and may either transport an electrical current, heat or both heat and a current. The rate of transport is governed predominantly by electron-phonon collisions. For a conductor, this is the dominant form of heat transport and is called the electronic contribution. This contribution to the thermal conductivity is called the electronic thermal conductivity. Electron-electron

90

collisions also occur, but are so infrequent that they may be neglected here. For the temperature range of interest, zero to fifteen degrees Kelvin, theory predicts that the electronic thermal conductivity is proportional to T^{-2} [37, p.204]. The first term in the denominator of (4.2.1) represents the electronic contribution to the thermal conductivity and illustrates the excellent match of theory to reality for aluminum.

The second parameter necessary to the computational analysis of the problems posed in this work is the heat convection constant h_{conv}. Typically, type I and II superconductors are cooled by liquid helium [38, p.193]. When liquid helium is used, the boundary conditions are not of simple convection cooling, but of combined convection cooling and heat transport by thermal conductivity. At the low temperatures necessary to induce superconductivity in aluminum, liquid helium becomes a two phase fluid. One part of the fluid behaves normally, and the other part becomes a viscosity free (resistanceless) fluid called a superfluid. Not wishing to model the physics of the superfluid, as the focus of the present work is to model thermally coupled superconductor behavior, a simple, arbitrary heat convection boundary term was adopted. For this boundary term, it is assumed that the conductor is in a normal state, the current density j, the resistivity ω, and the thermal conductivity k are constants across the whole domain of the conductor, and the difference between the surface temperature T_s and the cooling fluid does not drop below one hundreth (.01) of a degree Kelvin.

The temperature of the cooling fluid T_∞ is known and, together with the current I, is one of the two independent loading parameters that are varied in the computational analysis of coupled phase-thermal-EM systems presented in later chapters. The maximum values of I and T_s are used to

choose the value of h_{conv}. These values represent the state of the system where the greatest amount of heat transfer occurs. The above choice of state ensures that, by use of the formula for h_{conv} presented below, heat is always being removed from the conductor by the cooling fluid and that the conductor never cools the fluid instead. To simplify the determination of h_{conv}, an overall energy balance approach is used below (e.g., see [33, p.92]. In the steady state, or time-independent system, the heat energy produced by the conductor must equal the amount of heat energy removed by the cooling fluid. For the one-dimensional conductor this is

$$2\pi \int_{z_i}^{z_j} \int_0^{r_c} \omega j_z^2 r \, dr \, dz = 2\pi r_c \int_{z_i}^{z_j} h_{conv} \left(T_s - T_\infty \right) dz \qquad (4.2.4)$$

For a one-dimensional conductor with constant current density, $j_z = I/\pi r_c^2$. Substituting this expression for j_z into (4.2.4), and using all prior assumptions, produces the following expression for h_{conv}.

$$h_{conv} = 50\pi^{-2} r_c^{-3} \omega I^2 \qquad (4.2.5)$$

For this equation, ω is evaluated at T_s which equals $T_\infty + .01$. This choice for ω generates the largest possible amount of heat in the conductor for the two loading parameters.

4.3 THERMAL PROPERTIES OF ω.

Like the thermal conductivity, two primary mechanisms participate to produce a resistance to EM energy transport. For this type of energy transport, the electron-phonon interaction predominates again, but only dominates at high temperatures (above $\sim 20^\circ$ K). Unlike the thermal problem, lattice imperfections can contribute enough to the resistance of EM

energy transport that they must be accounted for. The first type of inter-action is accounted for by the ideal resistivity of a material. The second interaction is accounted for by the residual resistivity of the material. The total resistivity is thus the sum of the residual and ideal resistivities

$$\omega = \omega_i + \omega_o \qquad (4.3.1)$$

where ω_i and ω_o are the ideal and residual resistivities respectively.

Usually, the residual resistivity is a property of the particular sample and is determined by experiment. The value used in the numerical examples contained herein is given at the beginning of the previous section. The following discussion of ideal resistivity is a summary of material presented in Refs. [37] and [39].

The ideal resistivity can be expressed as

$$\omega_i = \mathcal{R} \left(\frac{T}{T_R} \right)^5 \mathcal{J}_5 \left(\frac{T_R}{T} \right) \qquad (4.3.2)$$

where $\mathcal{R}$ is a material constant, T_R is the Debye temperature as determined by resistance methods, and $\mathcal{J}_5$ is

$$\mathcal{J}_5(x) = \int_0^x \frac{z^5 \, dz}{(e^z - 1)(1 - e^{-z})} \qquad (4.3.3)$$

This is the Bloch-Grüneisen formula for the ideal resistivity of a material [37, pp.189-190]. For materials at low temperatures, i.e., $T_R/T \gg 1$, the upper bound on $\mathcal{J}_5$ can be extended to infinity with little error. Integration by parts of (4.3.3) with this new limit produces

$$\mathcal{J}_5(x) = -\frac{x^5}{e^x - 1} \bigg|_0^\infty + 5 \int_0^\infty \frac{z^4}{e^z - 1} dz \qquad (4.3.4)$$

The first term evaluated at the limits is zero and the second term is $5! \times Z(5)$ where $Z(n)$ represents the Riemann zeta function of argument n and $5!Z(5)$ is approximately equal to 124.4. Equation (4.3.2) becomes

$$\omega_i \approx 124.4\mathcal{R} \left(\frac{\mathcal{T}}{\mathcal{T}_R} \right)^5 \qquad (4.3.5)$$

It has been observed experimentally, that for low temperatures, ω is proportional to $\mathcal{T}^5$ [37, pp.190-192]. This validates the general behavior of (4.3.5). For reasons too lengthy to be discussed here (see Ref. [37], pp.182-202), (4.3.2) and (4.3.5) are only good approximations to the ideal resistivity of a material. To bring the formula closer to experimental values, $\mathcal{R}$ can be replaced by an espression quadratic in $\mathcal{T}$ [40, p.470]. Equation (4.3.2) now becomes

$$\omega_i = (\mathcal{C}_0 + \mathcal{C}_1\mathcal{T} + \mathcal{C}_2\mathcal{T}^2) \left(\frac{\mathcal{T}}{\mathcal{T}_R} \right)^5 \mathcal{J}_5 \left(\frac{\mathcal{T}_R}{\mathcal{T}} \right) \qquad (4.3.6)$$

where $\mathcal{C}_0$, $\mathcal{C}_1$ and $\mathcal{C}_2$ are constants determined from experimental data.

4.3.1 VALUES OF CONSTANTS FOR BLOCH-GRÜNEISEN FORMULA.

The value for $\mathcal{T}_r$ is documented as 395° K [39, p.100, 37, p.192]. The values for $\mathcal{R}$ or $\mathcal{C}_0$, $\mathcal{C}_1$, and $\mathcal{C}_2$ were not found after an extensive literature search. Some constants related to $\mathcal{C}_0$, $\mathcal{C}_1$, and $\mathcal{C}_2$ were found in Ref. [40]. Rather than converting these constants, it was decided to do a curve fit of the experimental data in the previously cited reference to determine the desired constants. The software package Mathematica was implemented using the "Fit" option. It was discovered that $\mathcal{C}_0$, $\mathcal{C}_1$, and $\mathcal{C}_2$ are not constants but parameters dependent upon the annealing temperature, $\mathcal{T}_A$. Curve fits

with these parameters assumed to be quadratic functions of T_A returned the following formulas:

$$5C_0 (T_A) = 0.0669523686343453 + 0.00006306135275167563 \, T_A$$
$$- 1.320389349752735 \times 10^{-7} \, T_A^2$$

$$5C_1 (T_A) = -0.001133598163601825 + 0.00000066346229028859 76 \, T_A$$
$$- 7.731210566579611 \times 10^{-9} \, T_A^2$$

$$5C_2 (T_A) = 0.00000318610319948 6918 - 1.840858520126625 \times 10^{-8} \, T_A$$
$$+ 2.147449451671961 \times 10^{-11} \, T_A^2$$

$$(4.3.7)$$

These empirical formulas agree within 5% when compared with the experimental data of Ref. [40] over the range of 2.21-273.16° K. For the numerical examples presented in later chapters, it is assumed that these values can be used down to $\sim 0°$ K with about the same accuracy. This assumption is justified because experimental observation shows that in this temperature range the residual resistivity is the dominant contribution to the total resistivity. Five times the value of each constant is presented in the above formulas. This removes a factor of five from the function $\mathcal{J}_5$ and simplifies of the calculation of $\mathcal{J}_5$. The determination of $\mathcal{J}_5$ is discussed in the next subsection. The value of the annealing temperature used for all numerical experiments was 548.16° K.

4.3.2 NUMERICAL APPROXIMATION TO THE INTEGRAL $\mathcal{J}_5$.

In order to obtain valid values for ω_i, it is also necessary to have a valid numerical approximation to $\mathcal{J}_5$. Although the numerical results presented herein lie in the range where $T_R/T \gg 1$, where the approximation of

equation (4.3.2) is valid, in the interest of additional accuracy, $\mathcal{J}_5$ is evaluated numerically between its actual limits. The evaluation of $\mathcal{J}_5$ between its actual limits also ensures valid results for ω_i should the solution procedure inadvertently step into a range where $\mathcal{T}_r/\mathcal{T}$ is no longer much greater than one.

The range of interest for most of the the author's applications of the Bloch-Grüneisen formula lies between absolute zero and about one hundred degrees above absolute zero. In this range, numerical approximations to the integral in (4.3.3) converges slowly. To improve the rate of convergence, an equivalent expression is substituted that is composed of the difference of two integrals. Formally, this expression is

$$
\begin{aligned}
\mathcal{J}_5(x) &= \int_0^x \frac{z^5\,dz}{(e^z - 1)(1 - e^{-z})} \\
&= \int_0^\infty \frac{z^5\,dz}{(e^z - 1)(1 - e^{-z})} - \int_x^\infty \frac{z^5\,dz}{(e^z - 1)(1 - e^{-z})}
\end{aligned}
\tag{4.3.8}
$$

The first integral, as noted before, is simply $5!Z[5]$, where $Z[n]$ represents the Riemann zeta function of order n. An approximation, good to sixteen decimal places, as determined by the software package Mathematica for $5!Z[5]$, is 124.4313306172044. This is the value used for the numerical experiments contained in this work. Integration of (4.3.8) by parts produces

$$
\begin{aligned}
\mathcal{J}_5(x) &= 5!Z[5] + \left.\frac{z^5}{e^z - 1}\right|_x^\infty - 5\int_x^\infty \frac{z^4}{e^z - 1}\,dz \\
&= 5!Z[5] - \frac{x^5}{e^x - 1} - 5\int_x^\infty \frac{z^4}{e^z - 1}\,dz
\end{aligned}
\tag{4.3.9}
$$

The integral in the above equation is known as a Debye function. Abramowitz and Stegun [41, p.998] give the asymptotic approximation to this integral as:

$$
\int_x^\infty \frac{z^4}{e^z - 1}\,dz = \sum_{n=1}^\infty e^{-nx}\left\{\frac{x^4}{n} + \frac{4x^3}{n^2} + \frac{12x^2}{n^3} + \frac{24x}{n^4} + \frac{24}{n^5}\right\}
\tag{4.3.10}
$$

A thirty term series approximation was used in the numerical experiments presented in this work to evaluate the Debye function. This number of terms enabled the finite element coding to match the Mathematica software results for ω_i to sixteen decimal places.

For the author's numerical experiments, the temperature is evaluated at the nodal points of each element. This is a consequence of the C^o continuity of the variational functionals presented earlier in this chapter. The problem presented by this formulation is that ω for each element is only C^{-1} continuous. To overcome this difficulty, it was decided to evaluate ω at each node, and calculate the mean of the two returned values. This mean value is used as the resistivity of the element. This ensures that a true mean for ω over the element is represented. If the mean temperature is used instead, the resultant value for ω does not represent a true mean because, at low temperatures, ω_i is proportional to T^5. The mean value that is used assumes that ω_i varies linearly over an element whereas the second does not. The assumption of a linear variation here is consistent with the linear variation of all other independent variables of variational functionals presented in this work.

4.4 THERMAL DEPENDENCE OF α, β, AND $|\psi_\infty|^2$.

The thermal behavior of the time-independent superconductor is governed by the material parameters α and β. For numerical purposes, it was found that it was also necessary to know the thermal behavior of $|\psi_\infty|^2$. Equation (3.2.30) of the previous chapter shows that α and β are both functions of λ_{eff} and B_c. Doss gives the empirical thermal dependence of B_c as

[38, p.65]

$$B_c(T) = B_c(0)\left[1 - \left(\frac{T}{T_c}\right)^2\right]$$ (4.4.1)

He also gives the semi-empirical approximation for λ_{eff} as being [38, p.52]

$$\lambda_{eff}(T) = \lambda_{eff}(0)\left[1 - \left(\frac{T}{T_c}\right)^4\right]^{-\frac{1}{2}}$$ (4.4.2)

where $\lambda_{eff}(0)$ and $B_c(0)$ are semi-empirical constants that represent the effective penetration depth and critical magnetic field when the temperature of the system equals zero. For high-purity well-annealed aluminum, $B_c(0)$ equals 99 gauss [42, p.5] and $\lambda_{eff}(0)$ is equal to 500 angstroms [42, p.39]. Substitution of (4.4.1) and (4.4.2) into (3.2.30) gives

$$\boxed{\begin{aligned} \alpha &= \frac{q^{*2}}{m^*}B_c(0)^2\,\lambda_{eff}(0)^2\left[\frac{1 - (T/T_c)^2}{1 + (T/T_c)^2}\right] \\ \beta &= \frac{\mu_o q^{*4}}{m^{*2}}B_c(0)^2\,\lambda_{eff}(0)^4\left[\frac{1}{1 + (T/T_c)^2}\right]^2 \end{aligned}}$$ (4.4.3)

Equation (3.2.27) gives the relation that $|\psi_\infty|^2$ equals α/β. Substitution of (4.4.3) into this equation gives the thermal dependence of $|\psi_\infty|^2$, which is:

$$\boxed{|\psi_\infty(T)|^2 = \frac{m^*}{\mu_o q^{*2}}\lambda_{eff}(0)^{-2}\left[1 - \left(\frac{T}{T_c}\right)^4\right]}$$ (4.4.4)

Note that as T approaches T_c, the critical field goes to zero. The physical interpretation for this behavior is that any field at T_c causes a collapse of the superconducting phase in a conductor. This corresponds to the actual physics of a superconductor. The parameter $|\psi_\infty|^2$ also goes to zero as expected. The parameter λ_{eff} approaches infinity however. The physical interpretation of this result is that the penetration of the magnetic field into the conductor is complete, again in accordance with physical observation.

4.5 SUMMARY.

In this chapter, the variational functionals that describe two methods of heat transfer, conduction and convection, are presented. Important assumptions about these functionals are that the thermal conductivity k and the heat generation terms $\dot{q}$, are functions of the spatial coordinates when used with these functionals. The thermal dependence of k and ω are also discussed, and appropriate numerical approximations for both parameters are also presented. Physical constants necessary to the determination of these parameters for the test material used in this work, high purity, well-annealed aluminum, are also given.

An important assumption about the determination of the value of ω for finite element analysis is also made. In a previous chapter, it was already determined for the specific form of the four-potential formulation chosen for numerical analysis that ω be a step function across an element. In order to evaluate ω, the temperature T must be known. The thermal functionals of this chapter returns two values of T for each element, leaving two choices of how to determine an appropriate value of ω for each element. The first choice is to use the mean value of the two nodal temperatures to determine the elemental ω:

$$\omega^{(e)} = \omega_o + \omega_i \left(\frac{T_i^{(e)} + T_j^{(e)}}{2} \right)$$

The second choice is to evaluate ω at both nodal temperatures and use the mean of these two ω's for the elemental value of ω:

$$\omega^{(e)} = \omega_o + \tfrac{1}{2} \left\{ \omega_i(T_i^{(e)}) + \omega_i(T_j^{(e)}) \right\}$$

The latter approach is used here because it more accurately represents the mean value of ω for an element.

In the discussion of the one-dimensional forms of the heat functionals, it is shown that, for a one-dimensional steady state superconductor, the temperature T is a constant across the domain of the conductor. This result is important for two reasons. First, knowledge of the values of k and h_{conv} for the superconducting state are not necessary and computational effort need not be expended to determine them. Second, since T is constant across the domain, no numerical analysis is required to find the temperature distribution in the conductor.

With the completion of this chapter, all the necessary tools have been developed for the finite element treatment discussed in Chapters V-XI. These chapters show specifically how to construct specific elements based on the four-potential variational principle and their application to the solution of thermal, EM, and quantum phase change problems.

THE CLEM1D FINITE ELEMENT

The first finite element example of the use of the four-potential method for determining EM fields is the simplest. It is the example discussed in Section 2.3, an infinitely long, straight conductor of circular cross section which carries a known, time-independent, uniform current in the longitudinal direction. For comparison purposes, the analytical solutions of A_z inside the conductor and in free space are discussed first.

5.1 ANALYTICAL SOLUTIONS TO THE TEST PROBLEM.

5.1.1 THE FREE SPACE MAGNETIC FIELD.

In Cartesian coordinates the radial component of the magnetic vector potential in free space can be calculated from the expression (see, *e.g.*, [14,26,27,28,43])

$$A_z = \frac{\mu_0}{4\pi} \int_V \frac{j_z}{|\mathbf{r}|} \, dV \qquad (5.1.1)$$

where $|\mathbf{r}|$ is the distance between the elemental charge $j_z \, dV$ and the point in space at which it is desired to find the field potential. The integral extends over the volume containing charges. This expression serves equally well in cylindrical coordinates. In fact, the transformation of z components is one to one if the center of the coordinate systems coincide.

As noted previously, the only non-vanishing component of the current vector is $j_z \, d\Gamma_1$ where $d\Gamma_1$ is the elemental cross sectional area of the conductor $r \, dr \, d\theta$ and j_z is the current density in the z direction. If $d\ell$ represents the differential length of the wire, then $j_z \, dV = j_z \, d\Gamma_1 \, d\ell = I \, d\ell = I \, dz$ and $|\mathbf{r}| = \sqrt{r^2 + z^2}$. Substitution into (5.1.1) yields

$$A_z(r) = \frac{\mu_0 I}{4\pi} \int_{-\infty}^{\infty} \frac{dz}{\sqrt{r^2 + z^2}} \qquad (5.1.2)$$

This integral diverges, but this difficulty can be overcome by taking the wire to have a finite length $2\mathcal{L}$, symmetric with respect to the field point, that is large with respect to its diameter. Integrating between $-\mathcal{L}$ and $+\mathcal{L}$ gives the result

$$A_z(r) = \frac{\mu_0 I}{4\pi} \int_{-\mathcal{L}}^{+\mathcal{L}} \frac{dz}{\sqrt{r^2 + z^2}} = \frac{\mu_0 I}{4\pi} \ln\left(z + \sqrt{r^2 + z^2}\right)\Big|_{-\mathcal{L}}^{+\mathcal{L}} \qquad (5.1.3)$$

Expanding this equation in powers of $r/\mathcal{L}$ and retaining only first-order terms gives

$$A_z = -\left(\frac{\mu_0 I}{2\pi}\right) \ln r + C_1 \qquad (5.1.4)$$

where C_1 is an arbitrary constant. For subsequent developments it is convenient to select $C_1 = (\mu_0 I/2\pi) \ln r_t$, where r_t is the "truncation radius" of the finite element mesh in the radial direction. Then

$$A_z = -\left(\frac{\mu_0 I}{2\pi}\right) \ln\left(\frac{r}{r_t}\right) \qquad (5.1.5)$$

With this normalization, $A_z = 0$ at $r = r_t$. Taking the curl of $\mathbf{A}$ gives the $\mathbf{B}$ field in cylindrical coordinates:

$$\mathbf{B} = \nabla \times \mathbf{A} = \begin{Bmatrix} B_r \\ B_\theta \\ B_z \end{Bmatrix} = \begin{Bmatrix} \frac{1}{r}\frac{\partial A_z}{\partial \theta} - \frac{\partial A_\theta}{\partial z} \\ \frac{\partial A_r}{\partial z} - \frac{\partial A_z}{\partial r} \\ \frac{1}{r}\frac{\partial (r A_\theta)}{\partial r} - \frac{1}{r}\frac{\partial A_r}{\partial \theta} \end{Bmatrix} = \begin{Bmatrix} 0 \\ -\frac{\partial A_z}{\partial r} \\ 0 \end{Bmatrix} \qquad (5.1.6)$$

It is seen that the only non-vanishing component of the magnetic flux density is

$$B_\theta = \mu_0 H_\theta = -\frac{\partial A_z}{\partial r} = \frac{\mu_0 I}{2\pi r} \qquad (5.1.7)$$

This expression is called the law of Biot-Savart in the EM literature.

5.1.2 MAGNETIC FIELD WITHIN THE CONDUCTOR.

Again restricting our consideration to the static case, Maxwell's equations in their integral flux form give

$$\oint_C \mathbf{H} \cdot d\mathbf{s} = \oint_C \mu^{-1} \mathbf{B} \cdot d\mathbf{s} = \int_\Gamma \mathbf{j} \cdot \hat{\mathbf{n}}_c d\Gamma \qquad (5.1.8)$$

where C is a contour around the field point traversed counterclockwise with an oriented differential arclength $d\mathbf{s}$ and $\hat{\mathbf{n}}_c d\Gamma$ is the oriented surface element inside the contour. The term for the electric field disappears in this analysis because $\dot{\mathbf{E}} = 0$. From before, it is known that the right hand side of (5.1.8) is equal to the normal component of the current that flows through the cross sectional area evaluated by the integral. In the free space case, this is the total current that flows through the conductor. But in the conductor the amount of current is a function of the distance r from the center. Again using I to represent the total current carried by the conductor, and r_c the radius of the conductor, and assuming an *uniform* current density $j_z = I/(\pi r_c^2)$, the right hand side of (5.1.8) becomes

$$\int_\Gamma \mathbf{j} \cdot \hat{\mathbf{n}}_c d\Gamma = \int_{\Gamma_1} j_z \, d\Gamma_1 = \frac{I}{\pi r_c^2} \int_{\Gamma_1} d\Gamma_1 = I\frac{r^2}{r_c^2} \qquad (5.1.9)$$

Evaluating the left hand side of the integral and solving for B_θ gives:

$$2\pi r \mu^{-1} B_\theta = I\frac{r^2}{r_c^2}, \qquad B_\theta = \frac{\mu I r}{2\pi r_c^2} \qquad (5.1.10)$$

Comparing this equation with (5.1.5), it is seen that if $\mu = \mu_0$ then B_θ is continuous at the wire surface $r = r_c$ and has the value $\mu_0 I/(2\pi r_c)$. But if $\mu \neq \mu_0$ there is a jump $(\mu - \mu_0)I/(2\pi r_c)$ in B_θ.

The magnetic potential A_z within the conductor is easily computed by integrating $-B_\theta$ with respect to r:

$$A_z = -\frac{\mu I r^2}{4\pi r_c^2} + C_1 \tag{5.1.11}$$

The value of C_1 is determined by matching (5.1.5) at $r = r_c$, since the potential must be continuous. The result can be written as

$$A_z = \frac{I}{2\pi}\left[\tfrac{1}{2}\mu\left(1 - \frac{r^2}{r_c^2}\right) - \mu_0 \ln\left(\frac{r_c}{r_t}\right)\right]. \tag{5.1.12}$$

The preceding expressions (5.1.5),(5.1.12) for A_z can be verified as being correct by substituting them directly into the Euler equation of (2.3.11).

5.2 FINITE ELEMENT DISCRETIZATION.

5.2.1 CONSTRUCTING EM FINITE ELEMENTS.

To deal with this particular axisymmetric problem a two-node "line" finite element is sufficient. This provides the C^o continuity for A_z that the variational formulation requires. In the following, individual elements and element properties are indentified by the superscript (e). The two element end nodes are denoted by the subscripts i and j. The magnetic potential A_z is interpolated over each element as

$$A_z = \mathbf{N}\mathbf{A}_z^{(e)} \tag{5.2.1}$$

Here the row vector $\mathbf{N}$ contains the isoparametric finite element shape functions for A_z. The elements of $\mathbf{N}$ are only functions of the isoparametric parameter ξ which varies between -1 at node i and +1 at node j. The shape functions are

$$\mathbf{N} = \tfrac{1}{2} \langle\, 1 - \xi \quad 1 + \xi \,\rangle \tag{5.2.2}$$

The shape functions are functions of the spatial variable r and the defining relation between r and $\mathbf{N}$ is

$$r = \mathbf{N} \left\{ \begin{array}{c} r_i^{(e)} \\ r_j^{(e)} \end{array} \right\} = \mathbf{N} \mathbf{r}^{(e)} \tag{5.2.3}$$

$\mathbf{A}_z^{(e)}$ contains the nodal values for A_z and are only functions of the time t, i.e.,

$$\mathbf{A}_z^{(e)} = \left\{ \begin{array}{c} A_{z_i}^{(e)} \\ A_{z_j}^{(e)} \end{array} \right\} \tag{5.2.4}$$

Substitution of these finite element assumptions into the previously derived Lagrangian, Equation (2.3.9), and then into Equation (2.2.14), yields the variational integral as the sum of elemental contributions $R = \Sigma_e R^{(e)}$, where

$$R^{(e)} = \int_{V^{(e)}} dV^{(e)} \left\{ \frac{1}{2\mu^{(e)}} \mathbf{A}_z^{(e)T} \frac{\partial \mathbf{N}^T}{\partial r} \frac{\partial \mathbf{N}}{\partial r} \mathbf{A}_z^{(e)} - \mathbf{A}_z^{(e)T} j_z^{(e)} \right\} \tag{5.2.5}$$

The nodal values $\mathbf{A}_z^{(e)}$ are constant with respect to time because this is a steady state problem. Therefore, the integration with respect to t disappears. Taking the variation with respect to the element node values of $\mathbf{A}_z^{(e)}$ gives

$$\delta R^{(e)} = \int_{V^{(e)}} dV^{(e)} \delta \mathbf{A}_z^{(e)T} \left\{ \frac{1}{\mu^{(e)}} \frac{\partial \mathbf{N}^T}{\partial r} \frac{\partial \mathbf{N}}{\partial r} \mathbf{A}_z^{(e)} - \mathbf{N}^T j_z^{(e)} \right\} \tag{5.2.6}$$

This can be written more simply as

$$\mathbf{K}^{\mathcal{U}(e)} \mathbf{u}^{(e)} = \mathbf{p}^{(e)} \tag{5.2.7}$$

where

$$\mathbf{K}^{\mathcal{U}^{(e)}} = \int_{V^{(e)}} dV^{(e)} \left\{ \frac{1}{\mu^{(e)}} \frac{\partial \mathbf{N}^T}{\partial r} \frac{\partial \mathbf{N}}{\partial r} \right\} \qquad \mathbf{u}^{(e)} = \mathbf{A}_z^{(e)}$$

$$\mathbf{p}^{(e)} = \int_{V^{(e)}} dV^{(e)} \left\{ \mathbf{N}^T j_z^{(e)} \right\} \tag{5.2.8}$$

Equation (5.2.7) is purposely written in a notation resembling the stiffness-force equations of statics. $\mathbf{K}^{\mathcal{U}^{(e)}}$ represents a stiffness matrix derived from a potential energy variational formulation, $\mathbf{u}^{(e)}$ the nodal displacements and $\mathbf{p}^{(e)}$ represents the external force vector. This form clearly illustrates that solution and assembly techniques developed for finite element mechanics problems can be used to solve four-potential based EM field problems.

5.2.2 APPLYING BOUNDARY CONDITIONS.

The finite element mesh is necessarily terminated at a finite size, which for this test problem is defined as the truncation radius r_t alluded to in Section 5.2. In order to make the boundary integrals of R vanish, it is necessary to look at the boundary integrals of (2.3.11). In the finite element formulation, the discretized version of these integrals is

$$\int_{\Gamma_2} d\Gamma_2 \delta A_{z_j}^{(numel)} \left\{ \frac{r}{\mu^{(e)}} \frac{\partial A_z}{\partial r} \right\} \bigg|_{r_t} - \int_{\Gamma_2} d\Gamma_2 \delta A_{z_i}^{(1)} \left\{ \frac{r}{\mu^{(e)}} \frac{\partial A_z}{\partial r} \right\} \bigg|_0 \tag{5.2.9}$$

where $d\Gamma_2$ is again $d\theta dz$, and $A_{z_i}^{(1)}$ and $A_{z_j}^{(numel)}$ represent the nodal values for A_z at $r = 0$ and $r = r_t$ respectively and $numel$ is the total number of finite elements. Simple observation shows that the first boundary integral vanishes at r equal to zero. To make the other term vanish, the nodal value for A_z at r equal to r_t can be constrained to zero. This is the essential boundary condition used for this particular problem.

5.3 NUMERICAL EXPERIMENTS.

5.3.1 THE FINITE ELEMENT MODEL.

The test problem consists of a wire conductor of radius r_c transporting a unit current density. For this problem, the finite element mesh is completely defined by specifying the radial node coordinates for each element e as $r_i^{(e)} = r_n^{(e)}$ and $r_j^{(e)} = r_{n+1}^{(e)}$. If the mesh contains N_{wire} elements inside the conductor, those elements are numbered $e = 1, 2, \ldots N_{wire}$ and nodes are numbered $n = 1, 2, \ldots N_{wire} + 1$ starting from the conductor center outwards. The first node ($n = 1$) is at the conductor center $r = 0$ and node $n = N_{wire} + 1$ is placed at the conductor boundary $r = r_c$. The mesh is then continued with N_{free} elements into free space to give a total of $N_{wire} + N_{free} + 1$ nodes and $N_{wire} + N_{free}$ elements. This type of mesh for EM field simulation is unique to four-potential based numerical methods. A single node is needed at material interfaces to model fields as opposed to the double nodes of field based simulations.

For the calculation of the element stiffness and force vectors, the material permeability μ and current density j_z are uniform over the element. Analytical integration over the element geometry gives

$$\mathbf{K}^{u(e)} = \frac{\mu^{(e)} r_m^{(e)}}{l^{(e)}} \begin{bmatrix} 1 & -1 \\ -1 & 1 \end{bmatrix}, \quad \mathbf{p}^{(e)} = j_z l^{(e)} \left\{ \begin{array}{c} \frac{1}{6}\left(2r_i^{(e)} + r_j^{(e)}\right) \\ \frac{1}{6}\left(r_i^{(e)} + 2r_j^{(e)}\right) \end{array} \right\} \quad (5.3.1)$$

where $r_m^{(e)} = \frac{1}{2}\left(r_i^{(e)} + r_j^{(e)}\right)$ is the mean radius of the element and $l^{(e)} = r_j^{(e)} - r_i^{(e)}$ the element radial length. For the test example, $\mu^{(e)}$ is a constant inside the conductor whereas outside, $\mu^{(e)}$ is assumed to be unity. For the analytical solution of Section 5.1.1, this requires that μ_o be replaced by one.

The longitudinal curent density is $j_z = I/(\pi r_c^2)$ inside the conductor whereas outside j_z vanishes.

The master stiffness matrix and force vector are assembled following standard finite element techniques. The only essential boundary condition requires setting the nodal potential on the truncation boundary to zero, as explained in Section 5.2.2. The modified master equations are processed by a conventional symmetric solver, which provided the value of the magnetic potential at the mesh nodes. The magnetic flux density B_θ, which is constant over each element, is recovered in element by element fashion through the simple finite element approximation

$$B_\theta^{(e)} = -\frac{\partial A_z}{\partial r} = -\frac{\partial \mathbf{N}}{\partial r}\mathbf{A}_z^{(e)} = \frac{A_{z_i}^{(e)} - A_{z_j}^{(e)}}{l^{(e)}} \qquad (5.3.2)$$

This value was assigned to the center of each element e for plotting purposes, although it is a step function due to its C^{-1} continuity.

5.3.2 NUMERICAL RESULTS.

The numerical results shown in Figures 5.1 through 5.6 pertain to a unit-radius conductor ($r_c = 1$), with the external mesh truncated at $r_t = 5$. The element radial lengths, $l^{(e)}$, were kept constant and equal to .25, which corresponds to four internal and sixteen external elements.

The computed values of the potential A_z are compared with the analytical solutions of Sections 1.1.1 and 1.1.2. As can be seen, the agreement between analytical and FE values is excellent. The comparison between computed values of the magnetic flux density B_θ shows excellent agreement

except for the last element near the wire center, at which point the FE approximation (5.3.1) loses accuracy.

Figures 5.1, 5.3, and 5.5 are for the case where μ_{wire} was 10.0, and Figures 5.2, 5.4, and 5.6 are for the case in which μ_{wire} was one, that is, the same as the space surrounding the wire. Figures 5.1 and 5.2 show computed and analytical magnetic potentials. The slope discontinuity at $r = 1$ in Figure 5.1 and the jump in B_θ in Figure 5.3 are a consequence of the change in permeability μ when crossing the conductor boundary. Figures 5.3 and 5.4 show the computed and analytical magnetic flux densities. Figures 5.5 and 5.6 show the computed and analytical magnetic flux densities in free space in more detail. Note that Figures 5.5 and 5.6 for $r > 1$ are identical; this is the expected result because as shown in Section 5.1.2, the free space magnetic flux field depends only upon the current enclosed by a surface integral around the wire and not on the details of the interior field distribution.

In summary, this finite element performed very accurately in the example problem and converged, as expected, to the analytical solution as the size of the elements decreased.
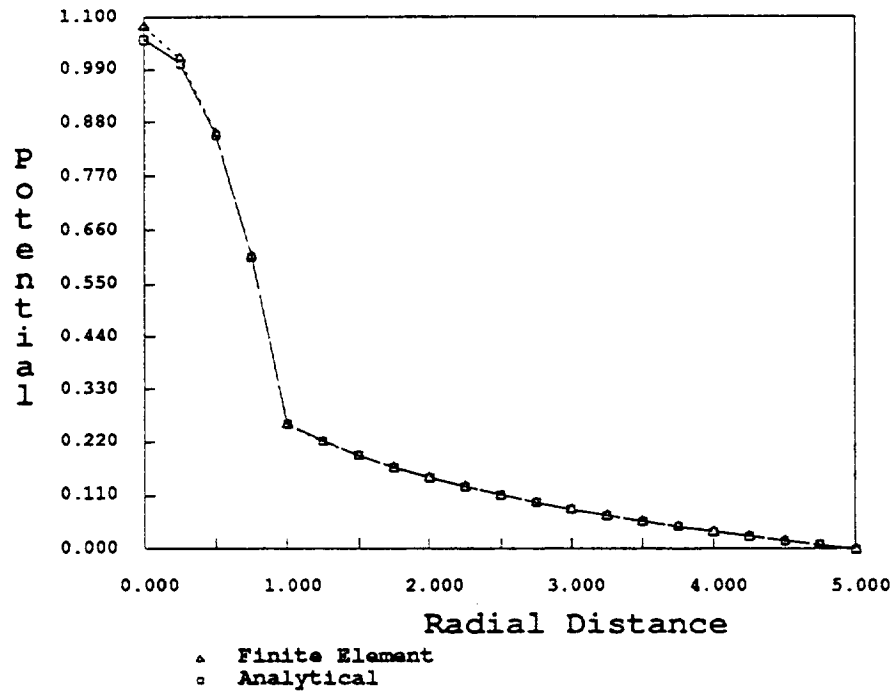
Figure 5.1: A_z vs. r, $\mu_{wire} = 10.0$.
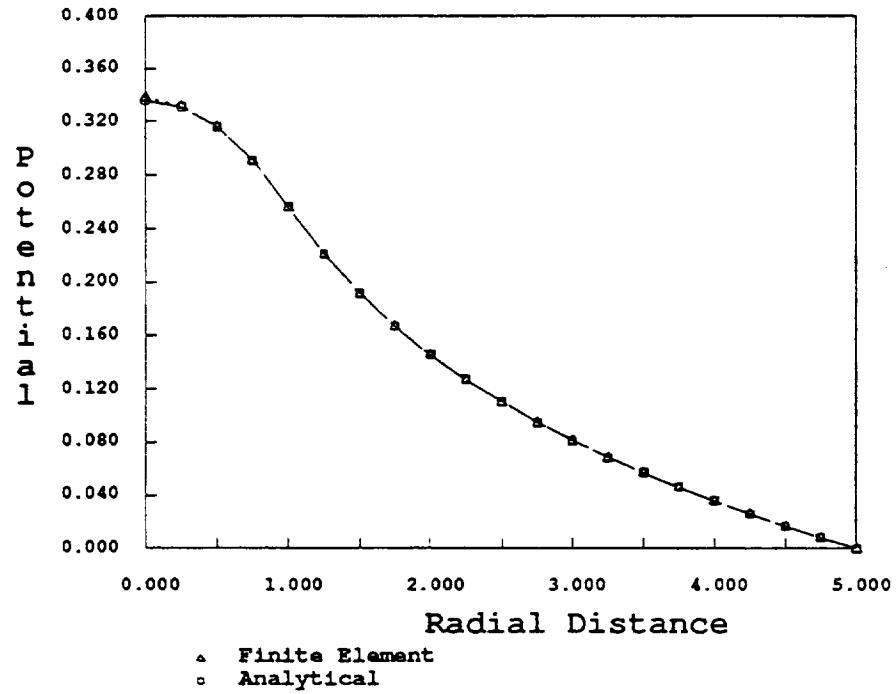
Figure 5.2: A_z vs. r, $\mu_{wire} = 1.0$.
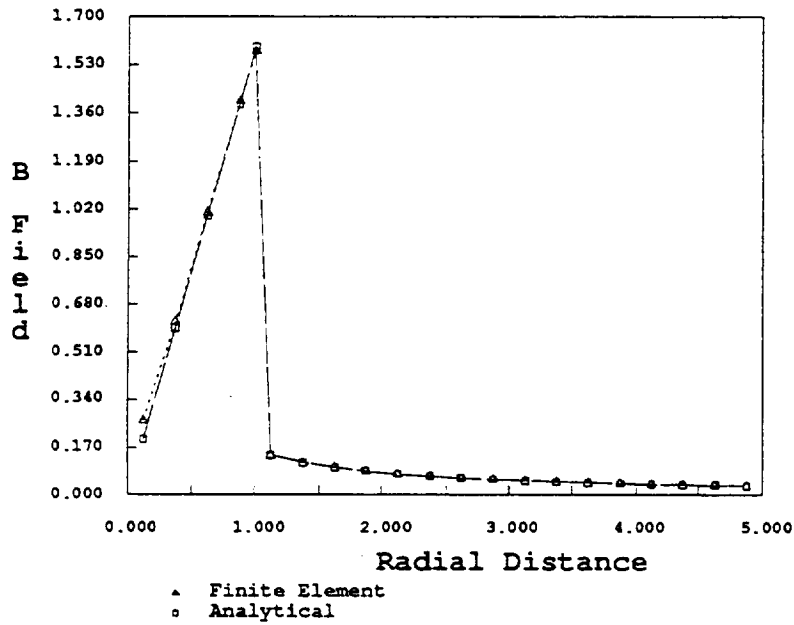
Figure 5.3: B_θ vs. r, $\mu_{wire} = 10.0$. Values shown on the interface $r = 1$ with dark symbols have been extrapolated from element center values to display the jump more accurately; this extrapolation scheme has not been used elsewhere.
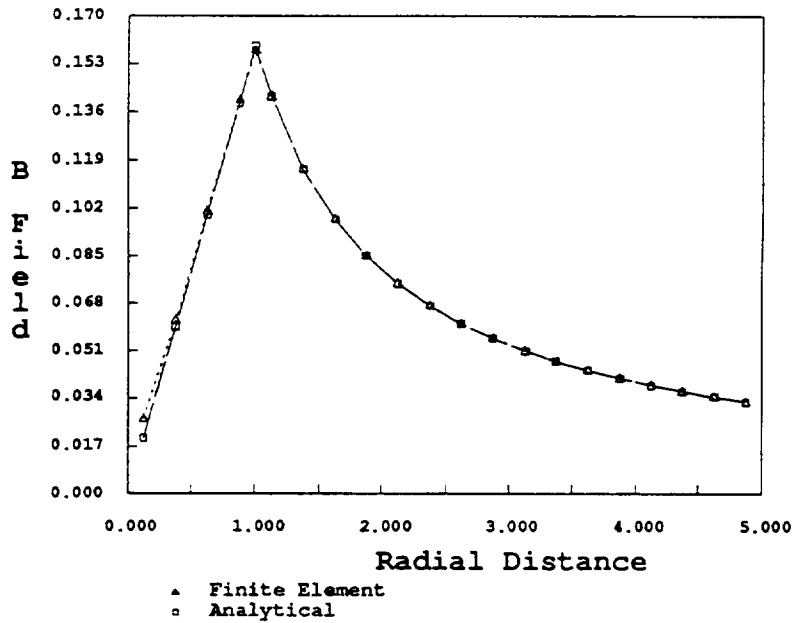
Figure 5.4: B_θ vs. r, $\mu_{wire} = 1.0$.
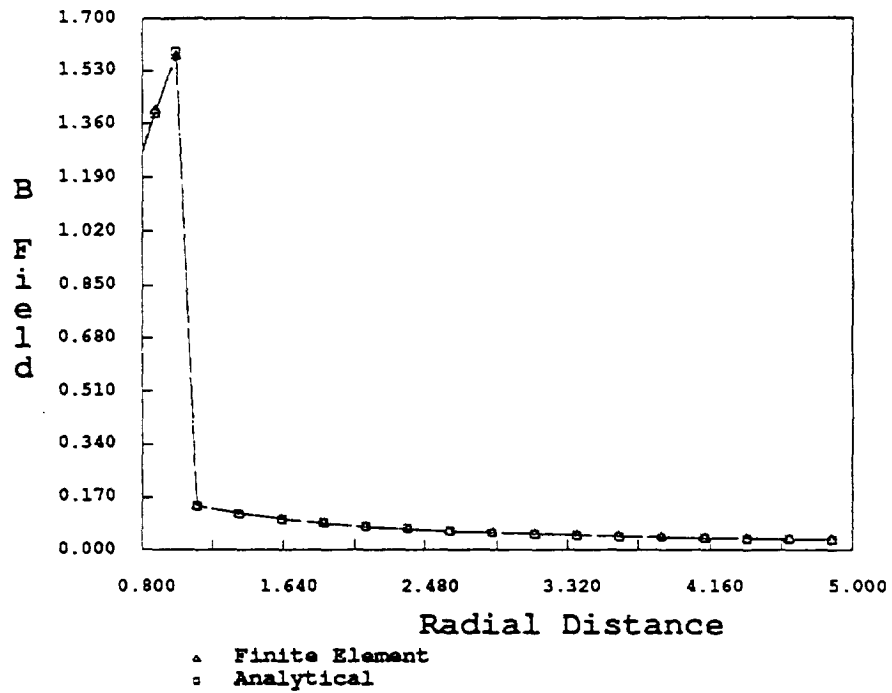
Figure 5.5: Figure 5.3 for $r > r_c = 1$, $\mu_{wire} = 10.0$, showing free space B_θ field in more detail.
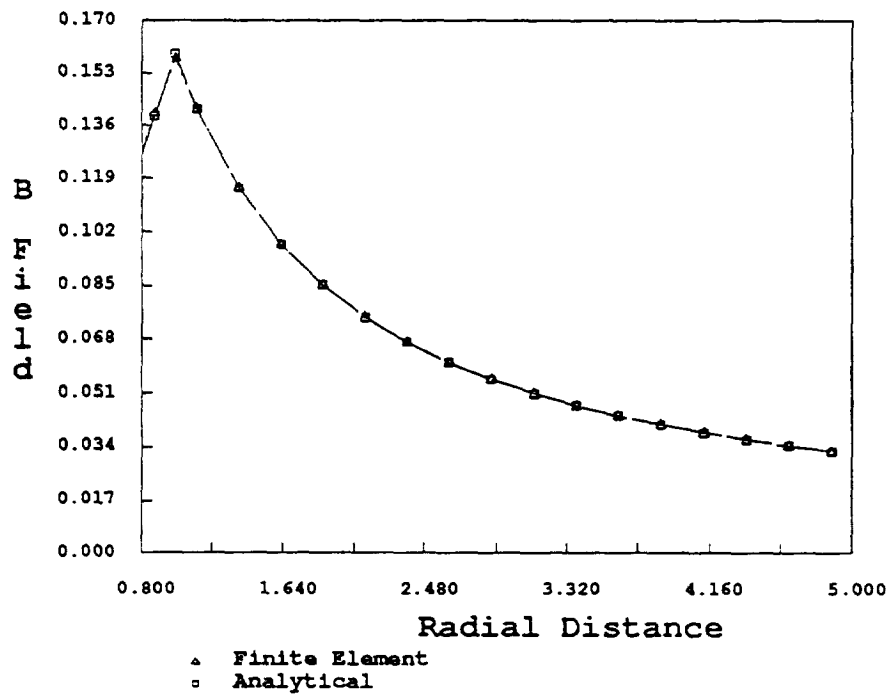
Figure 5.6: Figure 5.4 for $r > r_c = 1$, $\mu_{wire} = 1.0$, showing free space B_θ field in more detail.

5.4 SUMMARY.

In this chapter, the case of a simple one-dimensional infinite wire is tested. To perform this test, the linear functional of Section 2.3 is discretized using standard FE techniques and appropriate boundary conditions are determined. When the discretization is complete, it can be seen that the governing equations are of a standard form and present no problems to the use of standard FE solvers for linear systems.

Analytical solutions for the one-dimensional axisymmetric infinite conductor are also derived in this chapter. Presented in this chapter are graphs that compare results obtained from these analytical solutions and from the FE model. The two solutions are in excellent agreement except at the center of the conductor thereby validating the use of the four-potential method for the determination of EM fields. Most importantly, the four-potential method accurately predicts the B field across material interfaces without any special boundary treatment, unlike the conventional field based methods.

In the next chapter, the case of a two-dimensional problem with similar boundary conditions and a known current density is explored. The extension of the four-potential method to the two-dimensional case is done to offer further proof of the validity of this method for EM field analysis. It is also performed in order to show the effect of the Lorentz gauge, as the gauge effects disappear in the one-dimensional steady-state example.

THE CLEM2D FINITE ELEMENT

In this chapter, the four-potential FE element for axisymmetric two-dimensional problems is developed. The new elements show the relatively easy extension of the four-potential method through the use of Lagrange multiplier adjunction to a broader class of problems. This element was tested for two different geometries, a one-dimensional infinite conductor, and a cylindrical "can" connected to two infinite feed wires on the top and bottom.

For both geometries, the current density j is known, and the static charge density ρ is zero. The first geometry is the same as that of Chapter IV, and is used to provide a check on the element calculations. The second geometry is chosen to allow for a variation of B in more than one direction. For this geometry, there is no analytical solution, but the results can be examined to determine if they are physically realizable. For this reason, this chapter begins with a discussion of the construction of the two-dimensional axisymmetric finite element.

6.1 FINITE ELEMENT DISCRETIZATION.

In the previous chapter, the ungauged Lagrangian (2.2.13) is used to construct one-dimensional axisymmetric finite elements. In the present chapter, the four-potential method is extended to include two-dimensional

axisymmetric problems. In doing so, the basic four-potential does not necessarily satisfy the gauge condition (2.1.10) *a priori* and consequently, the gauged form of the four-potential (2.2.15) must be used.

6.1.1 CONSTRUCTING EM FINITE ELEMENTS.

For the finite element discretization of the two-dimensional case, quadrilateral axisymmetric elements defined by their geometry on the r-z plane are constructed. These elements are isoparametric with corner node points only. Additional construction details are provided in a later section of this chapter.

In the following, individual elements and element properties are again identified by the superscript e in parentheses. The element nodes are locally numbered $i = 1, \ldots n$, where n is the number of corner nodes ($n = 4$ for quadrilaterals). The magnetic potential components, A_r, A_θ and A_z are interpolated over each element as

$$A_r = \mathbf{N} \mathbf{A}_r^{(e)} \quad A_\theta = \mathbf{N} \mathbf{A}_\theta^{(e)} \quad A_z = \mathbf{N} \mathbf{A}_z^{(e)} \tag{6.1.1}$$

Here the row vector $\mathbf{N}$ contains the isoparametric quadrilateral shape functions, which are only functions of the radial and longitudinal coordinates r and z

$$\mathbf{N} = \langle\, N_1(r,z) \quad N_2(r,z) \quad N_3(r,z) \quad N_4(r,z) \,\rangle \tag{6.1.2}$$

and column vectors $\mathbf{A}_r^{(e)}$, $\mathbf{A}_\theta^{(e)}$, and $\mathbf{A}_z^{(e)}$ contain the nodal values of A_r, A_θ and A_z respectively, which are only functions of the independent variable t

$$\mathbf{A}_r^{(e)} = \langle\, A_{r1}(t) \quad A_{r2}(t) \quad A_{r3}(t) \quad A_{r4}(t) \,\rangle$$

$$\mathbf{A}_\theta^{(e)} = \langle\, A_{\theta 1}(t) \quad A_{\theta 2}(t) \quad A_{\theta 3}(t) \quad A_{\theta 4}(t) \,\rangle \tag{6.1.3}$$

$$\mathbf{A}_z^{(e)} = \langle\, A_{z1}(t) \quad A_{z2}(t) \quad A_{z3}(t) \quad A_{z4}(t) \,\rangle$$

where, as in the one-dimensional time-independent case, the nodal values for $A_r^{(e)}$, $A_\theta^{(e)}$ and $A_z^{(e)}$ become constants. Substitution of the above assumptions into the previously derived Lagrangian, Equation (2.4.1), and integration over the volume of the element yields the variational integral as a sum of element contributions $R = \Sigma_e R^{(e)}$, where

$$
R^{(e)} = \int_{V^{(e)}} dV^{(e)} \left\{ \frac{1}{2\mu^{(e)}} \left(\left(\frac{\partial \mathbf{N}}{\partial z} A_r^{(e)} - \frac{\partial \mathbf{N}}{\partial r} A_z^{(e)} \right)^T \left(\frac{\partial \mathbf{N}}{\partial z} A_r^{(e)} - \frac{\partial \mathbf{N}}{\partial r} A_z^{(e)} \right) \right. \right.
$$
$$
\left. + A_\theta^{(e)T} \left(\frac{1}{r} \frac{\partial}{\partial r} \left(r\mathbf{N}^T \right) \right) \left(\frac{1}{r} \frac{\partial}{\partial r} \left(r\mathbf{N} \right) \right) A_\theta^{(e)} + A_\theta^{(e)T} \frac{\partial \mathbf{N}^T}{\partial z} \frac{\partial \mathbf{N}}{\partial z} A_\theta^{(e)} \right)
$$
$$
- \left(j_r^{(e)} \mathbf{N} A_r^{(e)} + j_\theta^{(e)} \mathbf{N} A_\theta^{(e)} + j_z^{(e)} \mathbf{N} A_z^{(e)} \right)
$$
$$
\left. + \lambda_g \left(\left(\frac{1}{r} \frac{\partial}{\partial r} \left(r\mathbf{N} \right) \right) A_r^{(e)} + \frac{\partial \mathbf{N}}{\partial z} A_z^{(e)} \right) \right\}
$$

$$(6.1.4)$$

and $V^{(e)}$ again denotes the volume of the element. Varying the above equation with respect to the element node values $A_r^{(e)}$ produces

$$
\delta R(\delta A_r^{(e)}) = \int_{V^{(e)}} dV^{(e)} \delta A_r^{(e)T} \left\{ \frac{1}{\mu^{(e)}} \left(\frac{\partial \mathbf{N}^T}{\partial z} \frac{\partial \mathbf{N}}{\partial z} A_r^{(e)} - \frac{\partial \mathbf{N}^T}{\partial z} \frac{\partial \mathbf{N}}{\partial r} A_z^{(e)} \right) \right.
$$
$$
\left. + \lambda_g \left(\frac{1}{r} \frac{\partial}{\partial r} \left(r\mathbf{N}^T \right) \right) - \mathbf{N}^T j_r^{(e)} \right\}
$$

$$(6.1.5)$$

Taking the variation of (6.1.4) with respect to $A_\theta^{(e)}$ gives

$$
\delta R(\delta A_\theta^{(e)}) = \int_{V^{(e)}} dV^{(e)} \delta A_\theta^{(e)T} \left\{ \frac{1}{\mu^{(e)}} \left(\left(\frac{1}{r} \frac{\partial}{\partial r} \left(r\mathbf{N}^T \right) \right) \left(\frac{1}{r} \frac{\partial}{\partial r} \left(r\mathbf{N} \right) \right) A_\theta^{(e)} \right. \right.
$$
$$
\left. \left. + \frac{\partial \mathbf{N}^T}{\partial z} \frac{\partial \mathbf{N}}{\partial z} A_\theta^{(e)} \right) - \mathbf{N}^T j_\theta^{(e)} \right\}
$$

$$(6.1.6)$$

and taking the variation of (6.1.4) with respect to $\mathbf{A}_z^{(e)}$ produces

$$\delta R(\delta \mathbf{A}_z^{(e)}) = \int_{V^{(e)}} dV^{(e)} \delta \mathbf{A}_z^{(e)T} \left\{ \frac{1}{\mu^{(e)}} \left(\frac{\partial \mathbf{N}^T}{\partial r} \frac{\partial \mathbf{N}}{\partial r} \mathbf{A}_z^{(e)} - \frac{\partial \mathbf{N}^T}{\partial r} \frac{\partial \mathbf{N}}{\partial z} \mathbf{A}_r^{(e)} \right) \right.$$
$$\left. + \lambda_g \frac{\partial \mathbf{N}^T}{\partial z} - \mathbf{N}^T j_z^{(e)} \right\}$$

(6.1.7)

The variation of (6.1.4) with respect to the last independent variable λ_g is

$$\delta R(\delta \lambda_g) = \int_{V^{(e)}} dV^{(e)} \delta \lambda_g \left(\left(\frac{1}{r} \frac{\partial}{\partial r} (r\mathbf{N}) \right) \mathbf{A}_r^{(e)} + \frac{\partial \mathbf{N}}{\partial z} \mathbf{A}_z^{(e)} \right) \qquad (6.1.8)$$

To facilitate a more compact formulation, the introduction of the following matrix notation is used for the stiffness matrix

$$\mathbf{K}^{\mathcal{U}(e)} = \begin{bmatrix} \mathbf{K}^{(e)}{}_{A_r A_r} & 0 & \mathbf{K}^{(e)}{}_{A_r A_z} & \mathbf{K}^{(e)}{}_{A_r \lambda_g} \\ & \mathbf{K}^{(e)}{}_{A_\theta A_\theta} & 0 & 0 \\ & & \mathbf{K}^{(e)}{}_{A_z A_z} & \mathbf{K}^{(e)}{}_{A_z \lambda_g} \\ symm. & & & 0 \end{bmatrix} \qquad (6.1.9)$$

where

$$\mathbf{K}^{(e)}{}_{A_r A_r} = \int_{V^{(e)}} dV^{(e)} \left(\frac{1}{\mu^{(e)}} \frac{\partial \mathbf{N}^T}{\partial z} \frac{\partial \mathbf{N}}{\partial z} \right)$$

$$\mathbf{K}^{(e)}{}_{A_\theta A_\theta} = \int_{V^{(e)}} dV^{(e)} \frac{1}{\mu^{(e)}} \left(\left(\frac{1}{r} \frac{\partial}{\partial r} \left(r\mathbf{N}^T \right) \right) \left(\frac{1}{r} \frac{\partial}{\partial r} (r\mathbf{N}) \right) + \frac{\partial \mathbf{N}^T}{\partial z} \frac{\partial \mathbf{N}}{\partial z} \right)$$

$$\mathbf{K}^{(e)}{}_{A_r \lambda_g} = \int_{V^{(e)}} dV^{(e)} \lambda_g \left(\frac{1}{r} \frac{\partial}{\partial r} \left(r\mathbf{N}^T \right) \right) \quad \mathbf{K}^{(e)}{}_{A_z \lambda_g} \int_{V^{(e)}} dV^{(e)} \lambda_g \frac{\partial \mathbf{N}^T}{\partial z}$$

$$\mathbf{K}^{(e)}{}_{A_z A_z} = \left(\frac{1}{\mu^{(e)}} \frac{\partial \mathbf{N}^T}{\partial r} \frac{\partial \mathbf{N}}{\partial r} \right) \quad \mathbf{K}^{(e)}{}_{A_r A_z} = \int_{V^{(e)}} dV^{(e)} \left(\frac{1}{\mu^{(e)}} \frac{\partial \mathbf{N}^T}{\partial z} \frac{\partial \mathbf{N}}{\partial r} \right)$$

(6.1.10)

The following vector notation is also introduced to give a more compact formulation.

$$\mathbf{u}^{(e)} = \left\{ \begin{array}{c} \mathbf{A}_r^{(e)} \\ \mathbf{A}_\theta^{(e)} \\ \mathbf{A}_z^{(e)} \\ \lambda_g \end{array} \right\} \qquad \mathbf{p}^{(e)} = \int_{V^{(e)}} dV^{(e)} \mathbf{N}^T \left\{ \begin{array}{c} j_r^{(e)} \\ j_\theta^{(e)} \\ j_z^{(e)} \\ 0 \end{array} \right\} \qquad (6.1.11)$$

Using the new notation, it is apparent that the finite element system can be again written in the form of the stiffness-force equations of statics, $\mathbf{K}^{\mathcal{U}(e)}\mathbf{u}^{(e)} = \mathbf{p}^{(e)}$. Assembling these equations in the usual manner will produce the discrete finite element equations of magnetostatics, $\mathbf{K}^{\mathcal{U}}\mathbf{u} = \mathbf{p}$.

6.1.2 APPLYING BOUNDARY CONDITIONS.

In Section 5.2.2 it is seen that by constraining A_z to be zero at $r = r_t$, the boundary integrals for δA_z vanished. Examination of the boundary integrals for δA_z in the two-dimensional case, as shown earlier in Equation (2.4.6), show that utilization of the one-dimensional constraint will again allow both integrals over $d\Gamma_2$ to vanish. The physical interpretation of this phenomena is that at a large enough distance from any axisymmetric conductor, the field should always be the same as that of a straight wire independent of the conductor geometry. This will occur because at a sufficiently large distance, any effects, such as the end effects of the "can" of the second test example, will decay to zero.

Symmetry conditions also require that $\partial A_z / \partial r$ equal zero at $r = 0$. This is most easily achieved by constraining $\partial A_r / \partial z$ to zero at $r = 0$ because $\partial A_z / \partial r = \partial A_r / \partial z$ there. Constraining A_r at the axis to zero fulfills the symmetry requirement. Also constraining A_r to zero at z equal to the upper

and lower mesh boundaries will make the boundary integrals of Equation (2.2.2) disappear.

The application of these boundary conditions removes the rank deficiencies of the assembled master stiffness matrix. They are not the only boundary conditions that will work, as examination of Equations (2.4.2), (2.4.5) and (2.4.6) show, but they are the easiest to derive, being based upon simple physical and mathematical arguments. These are the boundary conditions that are used for the two-dimensional examples presented herein.

6.2 NUMERICAL EXPERIMENTS.

6.2.1 THE FINITE ELEMENT MODEL.

The finite element formulation described in the previous section has been applied to the solution of the two test examples described at the beginning of this chapter. Both problems are treated with quadrilateral elements. Each quadrilateral element has four corner points and one interior node. These nodes are defined by their radial and axial positions $r_i^{(e)}$ and $z_i^{(e)}$. At each corner i, there are three degrees of freedom, namely A_{ri}, $A_{\theta i}$, A_{zi}. From these values, the potential components are interpolated with the standard bilinear shape functions, which provide the C^o continuity required by the variational formulation. The centroidal node carries no physical significance and is used solely to provide the extra degree of freedom assigned to the Lagrange multiplier $\lambda_g^{(e)}$. Thus each quadrilateral element has $4 \times 3 + 1 = 13$ degrees of freedom.

For the calculation of the element stiffness and force vectors, it is assumed that the permeability $\mu^{(e)}$ and the current densities are uniform over

each element. The desired stiffness matrix and force vector are calculated by numerical quadrature using Gauss formulas. The portion associated with the potentials is always evaluated with the 2×2 rule. On the other hand, three different schemes were tried on the entries associated with λ_g:

Full Integration. The same 2×2 rule as for the potentials is used.

Selective Integration. A one-point rule is used for $\mathbf{K}^{(e)}_{A_r \lambda_g}$ and $\mathbf{K}^{(e)}_{A_z \lambda_g}$.

Zero Integration. The effect of λ_g is ignored by omitting the integration of the associated terms and placing ones on the diagonal. This numerical device effectively forces $\lambda_g = 0$, and thus "releases" the gauge constraint.

6.2.2   ASSEMBLY, SOLUTION AND FIELD RECOVERY.

The master stiffness matrix and force vector are assembled following standard finite element techniques. The boundary conditions are set as explained previously. The modified master equations modified for boundary conditions are processed by a standard symmetric skyline solver, which provides the value of the potentials at the mesh nodes.

The physical quantities of interest are not the potentials but the magnetic flux density $\mathbf{B}$. This is calculated by discretizing the curl of $\mathbf{A}$. Since $\partial \mathbf{A}/\partial\theta = 0$, the magnetic fields become, after discretization,

$$\left\{\begin{array}{c} B_r \\ B_\theta \\ B_z \end{array}\right\} = \left\{\begin{array}{c} -\frac{\partial \mathbf{N}}{\partial z}\mathbf{A}_\theta^{(e)} \\ \frac{\partial \mathbf{N}}{\partial z}\mathbf{A}_r^{(e)} - \frac{\partial \mathbf{N}}{\partial r}\mathbf{A}_z^{(e)} \\ \frac{1}{r^{(e)}}\frac{\partial(r\mathbf{N})}{\partial r}\mathbf{A}_\theta^{(e)} \end{array}\right\}. \qquad (6.2.1)$$

The nodal values for $\mathbf{B}$ are obtained by evaluation at the Gauss point followed by extrapolation to node locations. The average of these quantities is also reported as the centroidal value. As discussed below this value is found to

120

be more accurate than interelement-averaged node values. Consequently the centroidal value is used to report results.

For both test problems, the magnetic permeability $\mu^{(e)} = \mu_{wire}$ was constant inside the conductor whereas outside it the free-space permeability $\mu^{(e)} = \mu_{free}$ was assumed to be unity. The current densities were assumed to be uniformly distributed and consequently were calculated by dividing the assumed total current flowing through the conductor by the total cross-sectional areas of the conductors.

6.2.3 PROBLEM 1: A CONDUCTING INFINITE WIRE.

The first test problem is identical to that reported in the previous chapter with a one-dimensional axisymmetric discretization. As shown in Figure 2.1, it consists of a wire conductor of radius r_c transporting a total current of $I = 1$ ampere in the z direction. This current was assumed to be uniformly distributed over the wire cross section. For this problem one layer of quadrilateral elements in the z direction, extending from $z = 0$ through $z = d$, was sufficient; here the distance d was chosen arbitrarily. The radial direction is discretized with N_{wire} elements inside the wire and N_{free} elements outside the wire in free space. The mesh is terminated at a "truncation radius" $r_t \gg r_c$ where the potential component A_z is arbitrarily set to zero. Other boundary conditions are $A_r = 0$ on the nodes at $r = 0$, $z = 0$ and $z = d$.

The results obtained with $r_t = 5r_c$, $N_{wire} = 4$ and $N_{free} = 10$ for the potentials are identical to those reported in the previous chapter, thus providing a check on the element calculations. The same results were also obtained with the three integration schemes noted above for the λ_g term, which

verifies that the Lorentz gauge constraint (2.1.10) is automatically satisfied by the finite element shape function for one-dimensional magnetostatic fields.

The computed magnetic flux density B_θ at node points was not as accurate as could be expected, generally being too large, especially at $r = 0$. The centroidal values, on the other hand, were considerably more accurate as regards matching analytical results. Thus for the second problem field values at the element centroids are reported. The extrapolation of **B** to nodal locations is a disadvantage of the four-potential variational approach. Field based formulations can compute the value of the **B** field directly at the nodal locations while the four-potential method cannot.

6.2.4 PROBLEM 2: A CONDUCTING HOLLOW CAN.

The second test problem, shown in Figures 6.1 and 6.2, brings two-dimensional features. It is a hollow conducting cylindrical "can" with infinite feed wires connected to the center of its top and bottom faces. These wires carry a total current of $I = 1$ ampere in the $+z$ direction; this current was assumed to be uniformly distributed over the varying cross sections it traversed. For the ends of the can, it was assumed that the current flowed in the $\pm\hat{e}_r$ direction, forcing j_θ to be zero. For the areas where the feed wires join the "can", and the corners of the "can", it was assumed that the current turned ninety degrees and was uniformly distributed. This assumption is unrealistic physically, but warranted for the mesh used in this test problem. The mesh choice is discussed below. The wire radius r_c and the can wall thicknesses were assumed to be identical.

Because of the symmetry of the problem it is sufficient to model only the upper half $z \geq 0$. The results presented here were obtained by using a
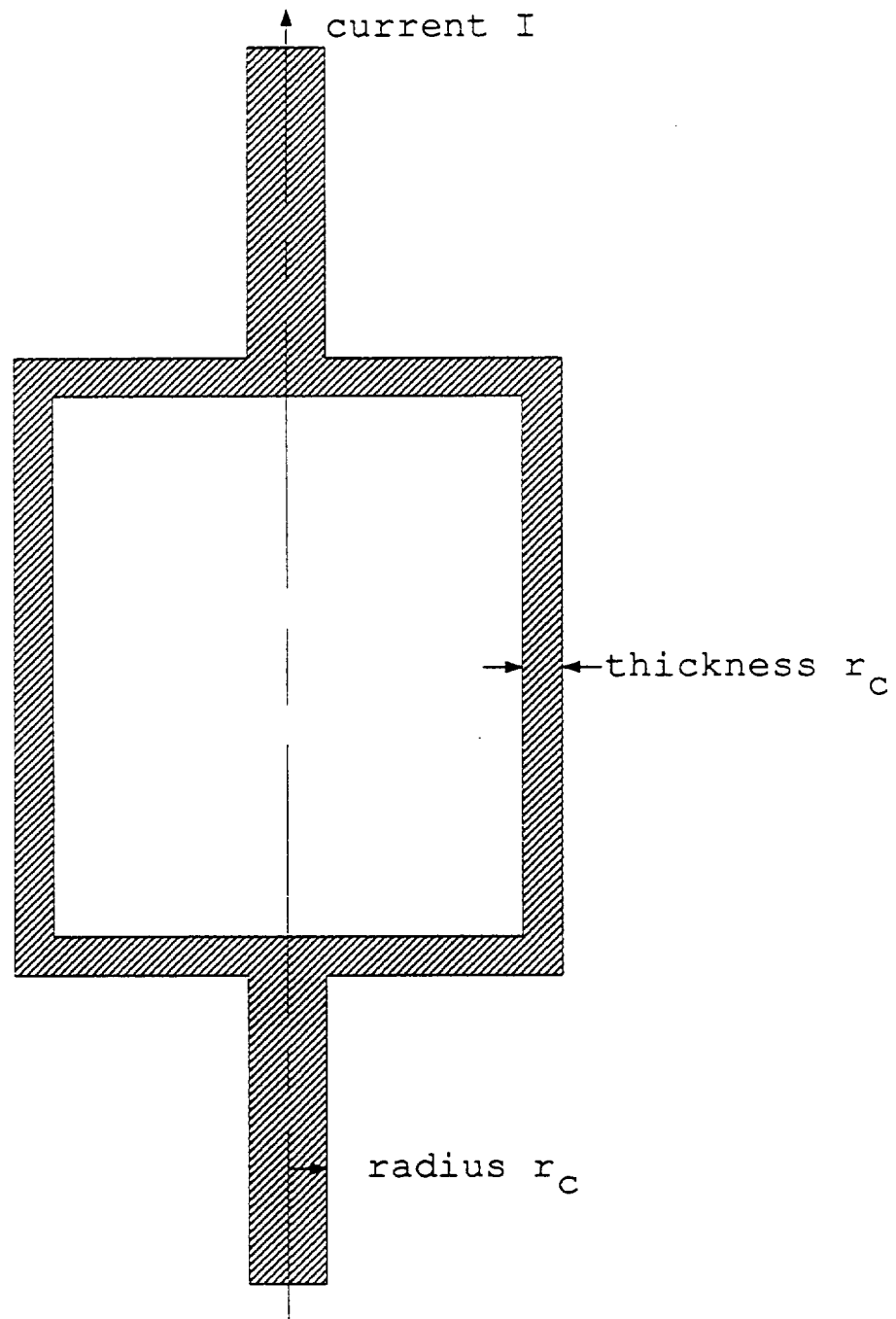
Figure 6.1: Cross-section of two-dimensional axisymmetric case. Cross-section taken through z axis.
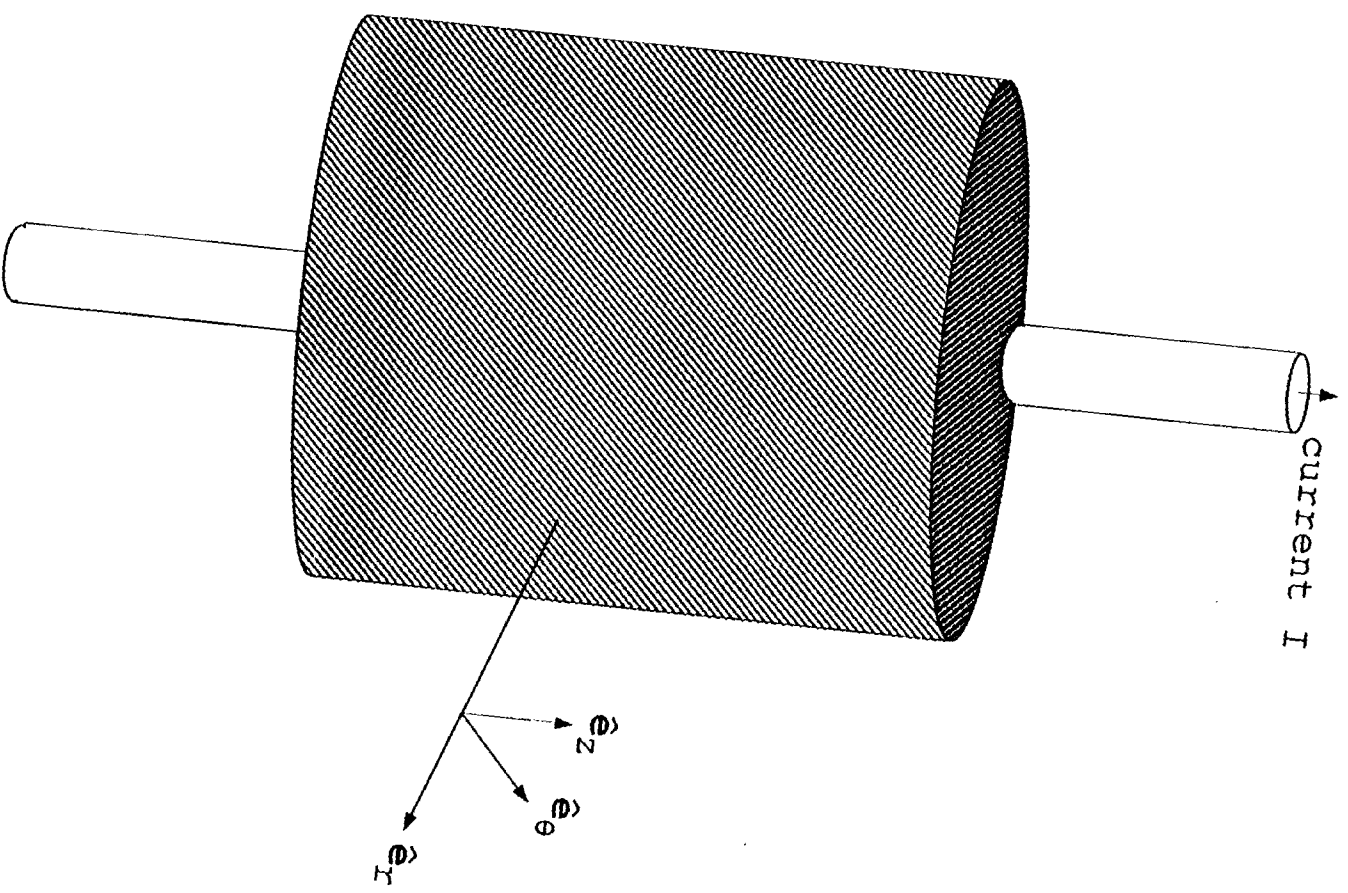
Figure 6.2: Solid Geometry of Two-Dimensional Axisymmetric Case.

current I

$|\hat{e}_z\rangle$

$|\hat{e}_\theta\rangle$

$|\hat{e}_r\rangle$

25×25 element mesh of square elements. Within this mesh, the wire as well as the can walls were modeled with only one element across the radius or thickness, respectively.

The regular mesh indeed represents an "overkill" for the free space while it is insufficiently refined to capture field distribution details inside and near the conducting material. This mesh was actually chosen to conform to limitations of the three-dimensional plotting functions of the software package Mathematica.

The problem was run using full, selective and zero integration schemes for the λ_g freedoms. The magnetic permeability μ_{free} in the free space outside the conducting material was chosen as unity. For the conducting material two different values for the permeability $\mu = \mu_{wire}$ were tried: 1.0 and 10.0; the latter to check whether flux jump conditions were automatically accommodated by the potential formulation. Selective results are reported graphically in Figures 6.3 through 6.8. Figures 6.3 and 6.4 show the magnitude of B_θ for $\mu_{wire} = \mu_{free} = 1$ obtained for the full and zero order integration schemes, respectively. Figures 6.5 and 6.6 show these results in contour plot form. Figures 6.7 and 6.8 correspond to $\mu_{wire} = 10$ and show the magnitude of B_θ from different viewing points. A discussion of the results follows.

The full integration scheme for λ_g performed well outside the conductor. Results were compared with those of the analytical solution for the infinite straight wire (the first test problem) to determine whether they were physically reasonable. As r becomes large compared to the can cross dimension (towards the outer radial edge of the mesh), the answers agreed. This is the expected behavior, because as r goes to ∞, the general axisymmetric

problem should behave as an infinite straight conductor. As one moved towards the top of the mesh, the solution again approached that of an infinite wire as can be observed in Figures 6.3 through 6.8. This behavior is expected because as we move parallel to the wire in the z direction, the effects of the current in the can ends should tend to zero and the only far-field effects should be from the total current. The results for the magnetic field within the feed wire were not accurate as it did not vanish for $r = 0$; this behavior was due to the use of only one element across the radius and the fact that only centroidal values are reported as noted above.

The selective integration scheme gave answers of the same general shape as the full integration scheme, but they only agreed to one or two significant digits; these results are not shown here as they are hard to distinguish in plots. The zero integration scheme (which in fact releases the Lorentz gauge coupling), gave solutions for the field that were larger than expected at the conductor boundary and a physically unrealizable field inside of the "can". This field grows sharply as the can axis is approached, as shown in Figures 6.4 and 6.6.
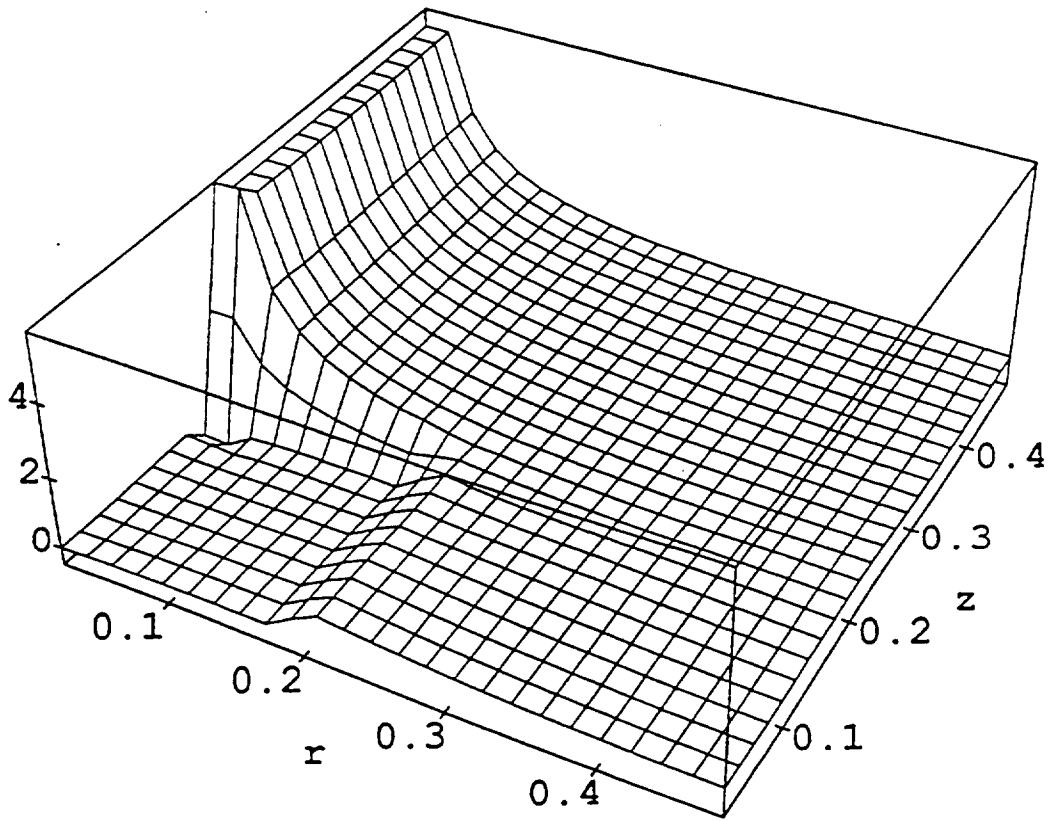
Figure 6.3: B_θ vs. r and z for $\mu_{wire} = 1$. Full integration scheme for λ_g. Intersections of mesh represent element centroids.
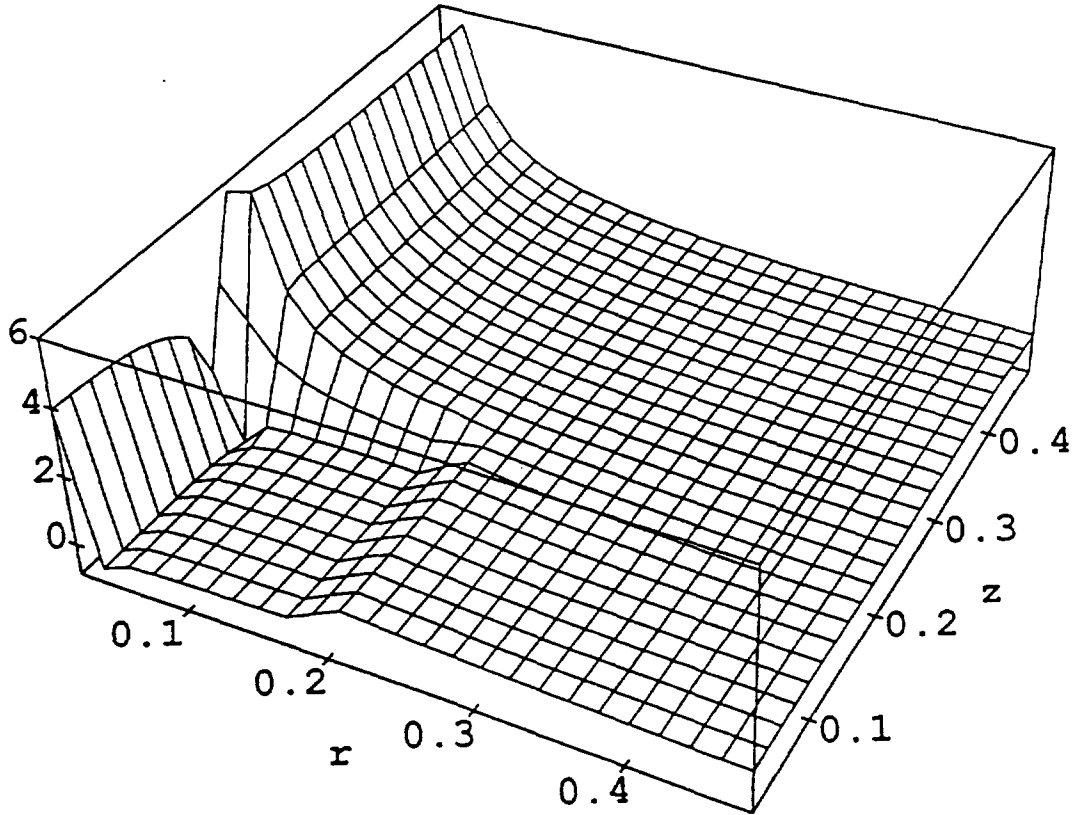
Figure 6.4: B_θ vs. r and z for $\mu_{wire} = 1$. Zero integration scheme for λ_g. Intersections of mesh represent element centroids.
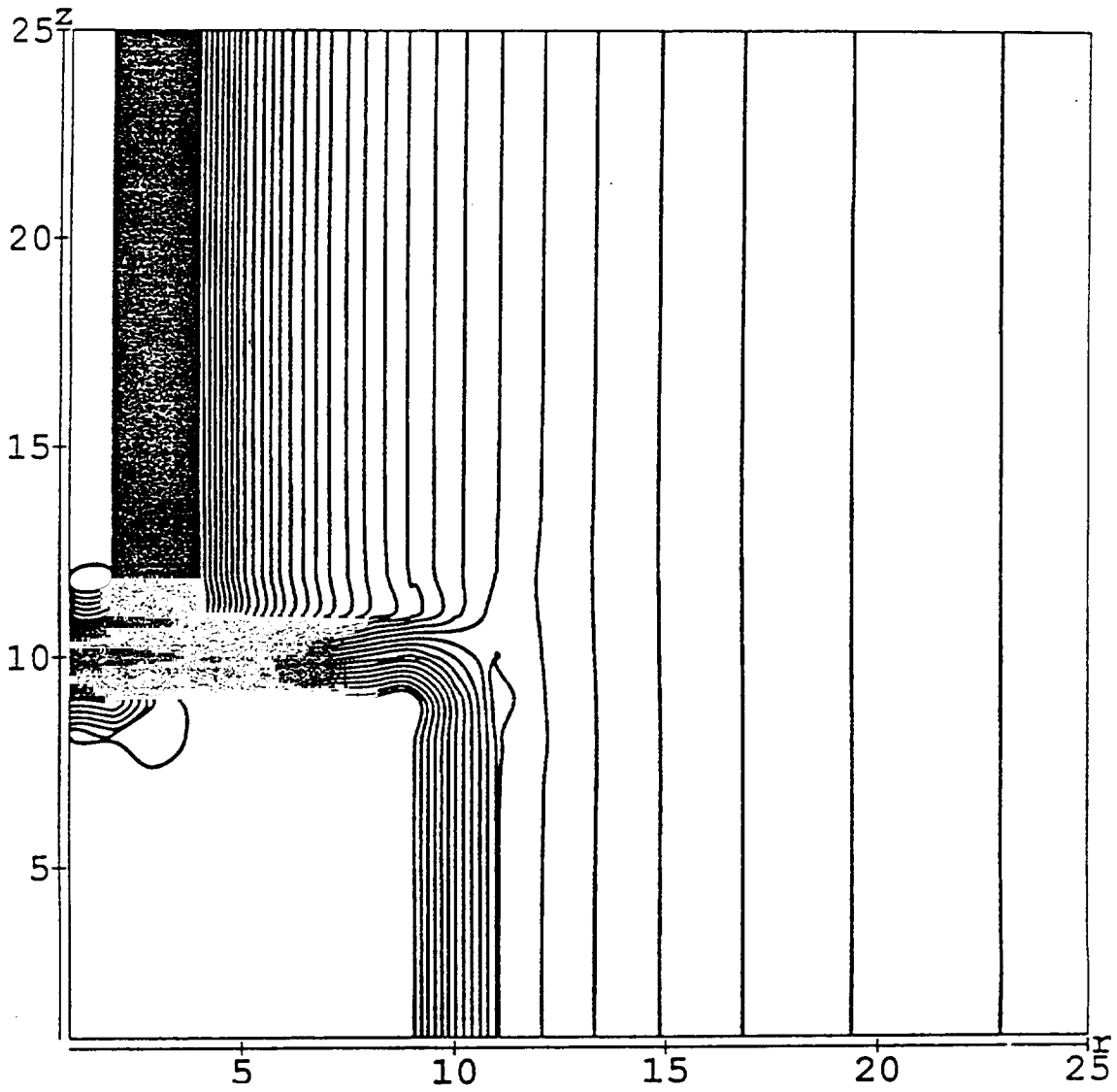
Figure 6.5: Contour plot of B_θ vs. r and z for $\mu_{wire} = 1$. Full integration scheme for λ_g. Numbers on axes represent the number of element centroids traversed from the center of the "can". Each element is .02 × .02 square. All contours are equally spaced and range from minumum to maximum values of the field.
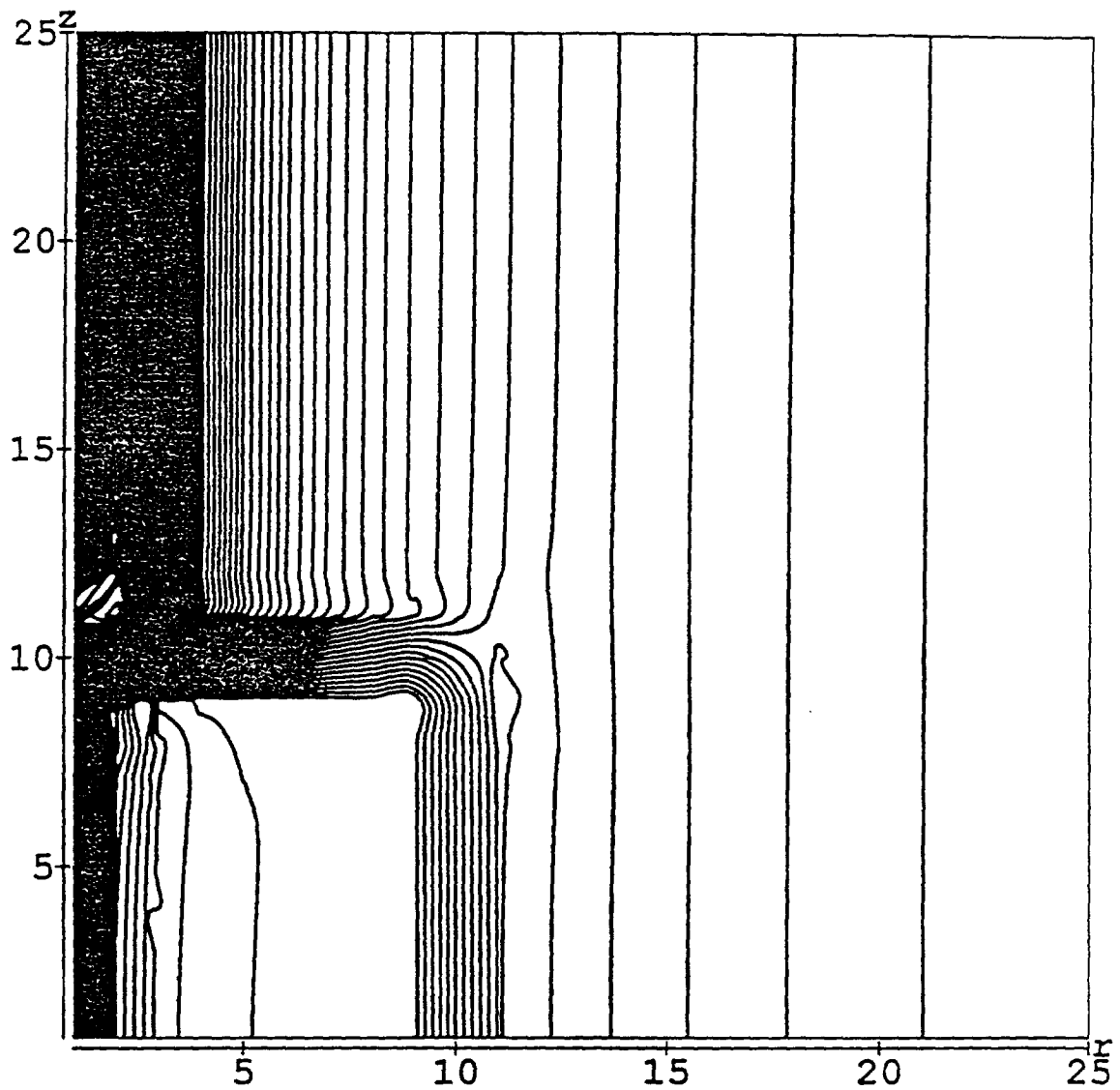
Figure 6.6: Contour plot of B_θ vs. r and z for $\mu_{wire} = 1.0$. Zero integration scheme for λ_g. Numbers on axes represent the number of element centroids traversed from the center of the "can". Each element is $.02 \times .02$ square. All contours are equally spaced and range from minumum to maximum values of the field.
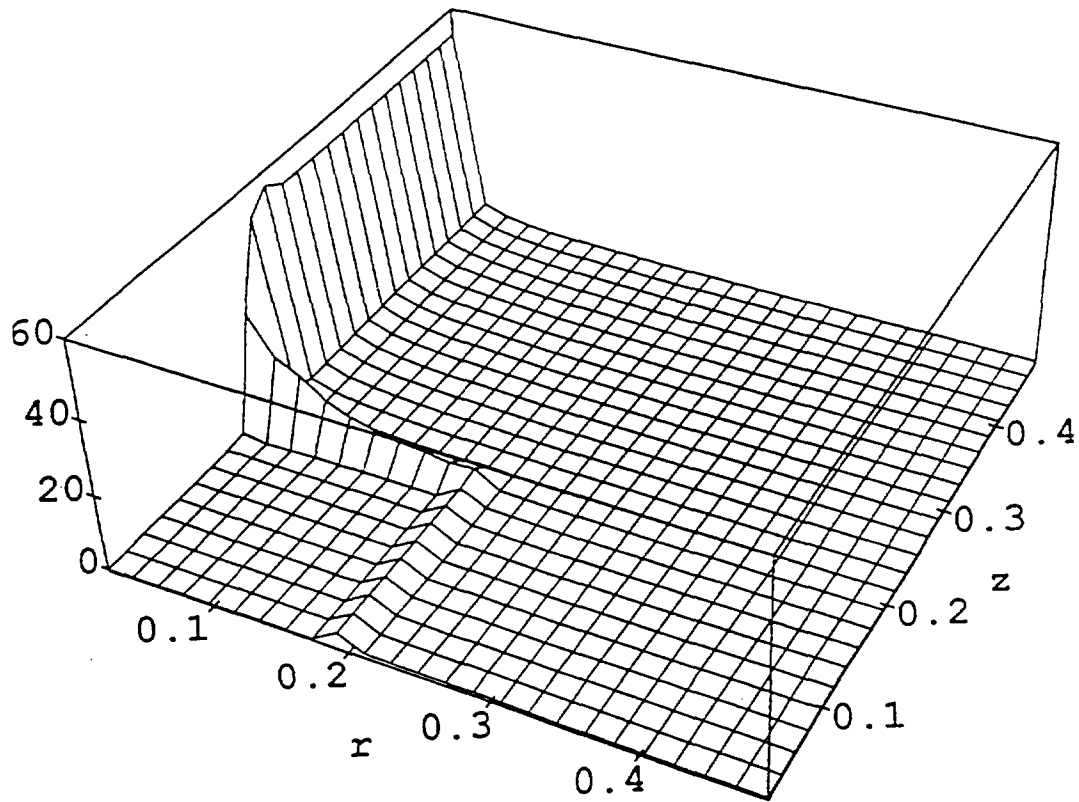
Figure 6.7: B_θ vs. r and z for $\mu_{wire} = 10$. Full integration scheme for λ_g. Intersections of mesh represent element centroids. Note sharp field jumps on conductor surfaces.
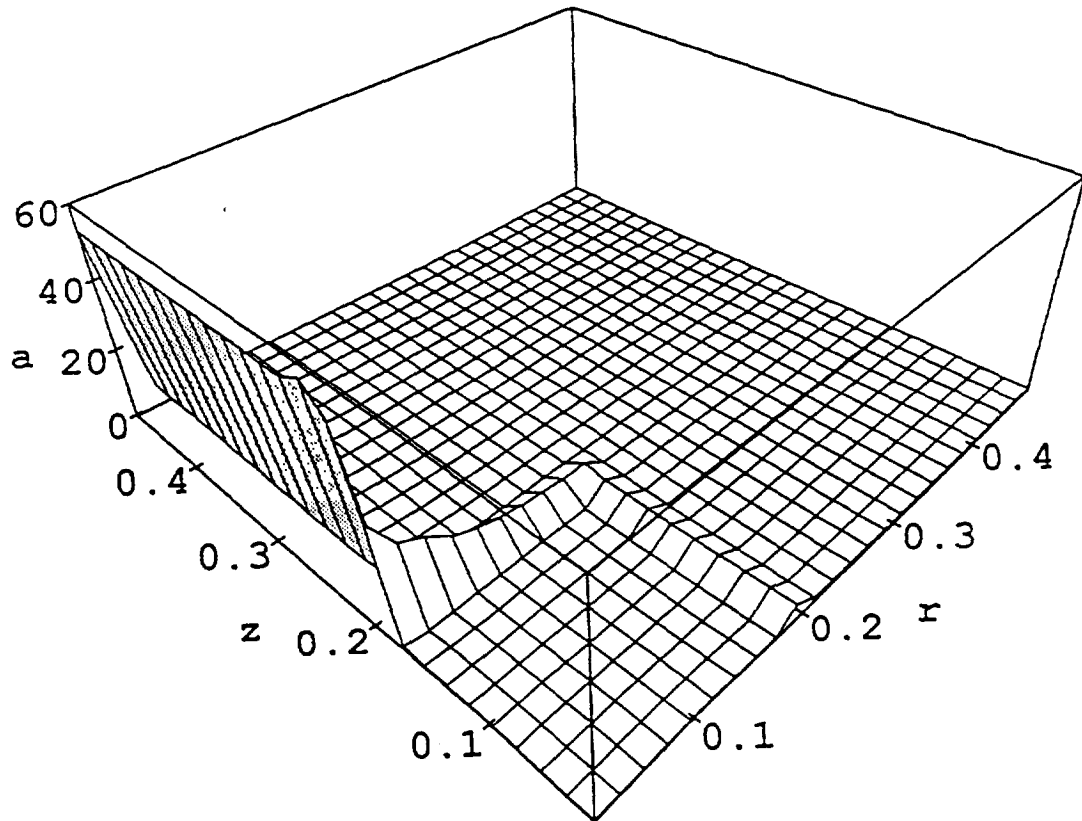
Figure 6.8: The same case as Figure 6.7 shown from a different viewing point to emphasize how B_θ fails to go to zero as r approaches zero because of the coarse conductor discretization.

132

6.3 SUMMARY.

The results of the CLEM2D finite element show that the four-potential variational principle can be applied to a broader class of problems than the simple one-dimensional axisymmetric conductor. Although no analytical solution is available for direct comparison, the physical behavior of the numerical results strongly suggest that they are accurate. The only point where the results are inaccurate are within the conductor itself. A finer mesh grading within the conductor can solve this problem, as results of the previous chapter illustrate.

The only truly unrealistic assumption about the second test problem was the assumption of the current density distribution. A physical current will in general not make a ninety degree turn and remain uniformly distributed. To address this problem, the CUPLE series of elements was developed. Given a known current I, these elements can determine the distribution of the current density j as well as the B and E fields. These finite element models are the subject of the next chapter.

THE CUPLE1D FINITE ELEMENT

In this chapter, the four-potential finite element for one-dimensional problems with an unknown current density vector is developed and tested for two examples. Both examples possess the same circular-wire geometry shown in Figure 2.1, no static charge density ($\rho = 0$), and a known current I in the positive z direction. In the first example, all elements have equal conductivities. This example gives the same type of fields encountered in Chapter V and is used to verify the accuracy of computed solutions. For the second example, the element conductivities are allowed to differ. An analytical solution to this problem exists and is compared with the numerical solution.

7.1 ANALYTICAL SOLUTION TO THE TEST PROBLEM.

7.1.1 MAGNETIC FIELD WITHIN THE CONDUCTOR.

The Euler equation for $\delta\lambda_c$ of Equation (3.1.11) states

$$I = \int_{\Gamma_1} d\Gamma_1 j_z \qquad (7.1.1)$$

This is the law of current conservation. For the examples presented here, it is assumed that j_z and ω are simple step functions where ω is known and j_z

is unknown. Using these assumptions, (7.1.1) becomes

$$I = \sum_{e=1}^{numel} \int_{\Gamma^{(e)}} d\Gamma^{(e)} j_z^{(e)} \qquad (7.1.2)$$

where a superscript letter or number in parentheses denotes the element number and *numel* is the total number of elements. The Euler equation for $\delta\kappa_\theta$ of Equation (3.1.11) over each volume disappears because $j_z^{(e)}$ and $\omega^{(e)}$ are step functions. If κ is constrained at $r = 0$ and $r = r_c$, the set of surface integrals for $\delta\kappa_\theta$ of (3.1.11) do not vanish and produces the following set of $numel - 1$ equations relating the $j_z^{(e)}$'s

$$j_z^{(e)}\omega^{(e)} = j_z^{(e+1)}\omega^{(e+1)} \qquad (7.1.3)$$

Insertion of (7.1.3) into (7.1.2) gives

$$I = \omega^{(1)} j_z^{(1)} \sum_{e=1}^{numel} \int_{\Gamma^{(e)}} d\Gamma^{(e)} \omega^{(e)} \left(\omega^{(1)} \right)^{-1} \qquad (7.1.4)$$

The above is used to determine $j_z^{(1)}$, and this value is then used with (7.1.3) to solve for the remainder of the undetermined $j_z^{(e)}$'s.

Equation (5.1.8) states

$$\oint \mu^{-1} \mathbf{B} \cdot ds = \int_\Gamma \mathbf{j} \cdot \hat{n}_c d\Gamma \qquad (7.1.5)$$

For this example, μ is a constant over the volume of the conductor. This assumption is discussed at the beginning of Chapter IV. For the one dimensional case, the contribution for each $j_z^{(e)}$ using (7.1.5) is

$$B_\theta^{(e)} = \frac{\mu}{2} j_z^{(e)} r \qquad (7.1.6)$$

where $r_i^{(e)} < r \leq r_j^{(e)}$ and $r_i^{(e)}$ and $r_j^{(e)}$ represent the inner and outer boundaries of $j_z^{(e)}$. For $r = r_i^{(e)}$, $B_\theta^{(e)}$ is zero. Using the principle of linear superposition, the total **B** field is

$$B_\theta = \frac{\mu}{2} \left(\sum_{n=1}^{e-1} \left\{ j_z^{(n)} \left(r_j^{(n)} - r_i^{(n)} \right) \right\} + j_z^{(e)} \left(r - r_i^{(e)} \right) \right) \qquad r_i^{(e)} \leq r \leq r_j^{(e)}$$

(7.1.7)

The value of $A_z^{(e)}$ is computed by integrating (7.1.6) over r and taking the negative of the answer, which is

$$A_z^{(e)} = -\int B_\theta dr = -\mu j_z^{(e)} \frac{r^2}{4} + C_0 \qquad (7.1.8)$$

where C_0 is again an integration constant. For $r_i^{(e)}$ equal to zero, C_0 is chosen as zero. To ensure the C^o continuity specified for A_z by the four-potential variational principle, $A_{z\,i}^{(2)}$ must equal $A_{z\,j}^{(1)}$ when both are evaluated at $r_j^{(1)} = r_i^{(2)}$. This requires that for $A_{z\,j}^{(1)} = A_{z\,i}^{(2)}$, C_0 equal $-\mu \left(r_j^{(1)} \right)^2 / 4 j_z^{(1)}$. The value of C_0 for each region where $j_z^{(e)}$ changes can be evaluated in a similar manner. Doing so will give the following expression for A_z

$$A_z = -\frac{\mu}{4} \left(j_z^{(e)} \left(r^2 - \left(r_i^{(e)} \right)^2 \right) + \sum_{n=1}^{e-1} \left\{ j_z^{(n)} \left(\left(r_j^{(n)} \right)^2 - \left(r_i^{(n)} \right)^2 \right) \right\} \right)$$

$$r_i^{(e)} < r \leq r_j^{(e)} \qquad (7.1.9)$$

7.1.2 THE FREE SPACE MAGNETIC FIELD.

Using Equations (7.1.5) and (7.1.1), the expression for B_θ in the free space outside of the conductor is

$$B_\theta = \frac{\mu_o I}{2\pi r} \qquad (7.1.10)$$

The value for the potential A_z is

$$A_z = -\int B_\theta dr = -\frac{\mu_o I}{2\pi} \ln r + C_0 \qquad (7.1.11)$$

Use of Equation (7.1.9) to determine C_0 gives the following expression for A_z

$$A_z = -\frac{I}{2\pi} \left(\mu_o \ln \left(\frac{r}{r_c} \right) + \mu \right) \qquad (7.1.12)$$

The above result differs from the previous solution of (5.1.5) by a constant. This is not surprising because, in the one-dimensional case, **A** is not unique and is determined solely by the boundary conditions. For the example of Chapter V, **A** is constrained to zero at r_t. For this example, **A** is constrained to zero at r equal to zero. For a one-dimensional bulk superconductor using the London gauge, **A** must vanish at $r = 0$ as discussed in Section 3.2.1. Because of this boundary constraint on a superconductor, **A** is also chosen as zero at $r = 0$ for the one-dimensional current density predicting case. This choice is made so that numerical coding that implements both elements to model the phase transition of a superconductor will require only one set of boundary conditions for **A**. The consequences of this choice are discussed in the subsection on applying boundary conditions.

7.2 FINITE ELEMENT DISCRETIZATION.

7.2.1 CONSTRUCTING EM FINITE ELEMENTS.

To deal with this particular axisymmetric problem, the two-node "line" finite element is again sufficient. Individual elements and their constitutive properties are denoted by a superscript (e). The element end nodes are also denoted by the subscripts i and j again. A_z and κ_θ are interpolated over each element as

$$A_z = \mathbf{N}\mathbf{A}_z^{(e)} \qquad \kappa_\theta = \mathbf{N}\kappa_\theta^{(e)} \tag{7.2.1}$$

The row vector $\mathbf{N}$ contains the isoparametric shape functions for the interpolation of A_z and κ_θ. The elements of $\mathbf{N}$ are only functions of the spatial coordinate r. $\mathbf{A}_z^{(e)}$ and $\kappa_\theta^{(e)}$ contain the nodal values for A_z and κ_θ and are only functions of the time t, and for the time-independent problem studied here, become constants with respect to time. Substitution of these finite element assumptions into the previously derived variational functional of Equation (3.1.10) gives

$$R_p^{(e)} = \int_{V^{(e)}} dV^{(e)} \left\{ \frac{1}{2\mu^{(e)}} \mathbf{A}_z^{(e)T} \frac{\partial \mathbf{N}^T}{\partial r} \frac{\partial \mathbf{N}}{\partial r} \mathbf{A}_z^{(e)} - \frac{1}{2} \epsilon^{(e)} \omega^{(e)2} j_z^{(e)2} - j_z^{(e)} \mathbf{A}_z^{(e)T} \mathbf{N}^T \right.$$

$$\left. + \omega^{(e)} j_z^{(e)} \kappa_\theta^{(e)T} \left(\frac{1}{r} \frac{\partial}{\partial r} \left(r \mathbf{N}^T \right) \right) \right\} - \int_{\Gamma_2^{(e)}} d\Gamma_2^{(e)} \omega^{(e)} r j_z^{(e)} \mathbf{N} \kappa_\theta^{(e)} \Big|_0^{r_c}$$

$$+ \lambda_c \left(I - \int_{\Gamma_1^{(e)}} d\Gamma_1^{(e)} j_z^{(e)} \right)$$

$$\tag{7.2.2}$$

where $d\Gamma_2$ and $d\Gamma_1$ are again $d\theta dz$ and $rdrd\theta$ respectively. Variation with respect to $\mathbf{A}_z^{(e)}$, $\kappa_\theta^{(e)}$, λ_c and $j_z^{(e)}$ produces the following expression for the

138

elemental stiffness matrix

$$
\mathbf{K}^{\mathcal{U}(e)} =
\begin{bmatrix}
\mathbf{K}^{(e)}{}_{AA} & \mathbf{K}^{(e)}{}_{Aj} & 0 & 0 \\
\mathbf{K}^{(e)}{}_{Aj}^{T} & K^{(e)}_{jj} & \mathbf{K}^{(e)}{}_{j\kappa} & K^{(e)}_{j\lambda_c} \\
0 & \mathbf{K}^{(e)}{}_{j\kappa}^{T} & 0 & 0 \\
0 & K^{(e)}_{j\lambda_c}{}^{T} & 0 & 0
\end{bmatrix}
\tag{7.2.3}
$$

where

$$
\mathbf{K}^{(e)}{}_{AA} = \int_{V^{(e)}} dV^{(e)} \left\{ \frac{1}{\mu^{(e)}} \frac{\partial \mathbf{N}^{T}}{\partial r} \frac{\partial \mathbf{N}}{\partial r} \right\}
\qquad
\mathbf{K}^{(e)}{}_{Aj} = -\int_{V^{(e)}} dV^{(e)} \mathbf{N}^{T}
\tag{7.2.4}
$$

$$
K^{(e)}_{jj} = -\int_{V^{(e)}} dV^{(e)} \epsilon^{(e)} \omega^{(e)^2}
\qquad
K^{(e)}_{j\lambda_c} = -\int_{\Gamma_1^{(e)}} d\Gamma_1^{(e)}
\tag{7.2.5}
$$

$$
\mathbf{K}^{(e)}{}_{j\kappa} = \int_{V^{(e)}} dV^{(e)} \omega^{(e)} \left(\frac{1}{r} \frac{\partial}{\partial r} \left(r \mathbf{N} \right) \right)
\tag{7.2.6}
$$

The above expression for $\mathbf{K}^{\mathcal{U}(e)}$ is not complete because it neglects contributions to $\mathbf{K}^{(e)}{}_{j\kappa}$ from the boundary integral over $d\Gamma_2$. The discussion of this contribution is deferred to the subsection devoted to the application of boundary conditions. Following the notation of previous chapters, $\mathbf{u}^{(e)}$ is expressed as

$$
\mathbf{u}^{(e)} =
\left\{
\begin{array}{c}
\mathbf{A}_z^{(e)} \\
j_z^{(e)} \\
\kappa_\theta^{(e)} \\
\lambda_c
\end{array}
\right\}
\tag{7.2.7}
$$

It is important to note that λ_c is a global degree of freedom. This condition must be met when the elemental matrices are assembled to form the master stiffness matrix.

Taking the second variation of $R_p^{(e)}$ with respect to the independent variables produces the *tangent* stiffness matrix $\mathbf{K}$, which is identical to $\mathbf{K}^{\mathcal{U}(e)}$. This occurs because $\mathbf{K}^{\mathcal{U}(e)}$ is only a function of the radial coordinate r and

not the independent variables. This fact is important when non-linear solution techniques, such as the corrective Newton-Raphson method, are used for the thermally coupled superconducting problem. To use the non-linear solution techniques, the tangent stiffness matrix is required, and the equivalency of $\mathbf{K}^{\mathcal{U}(e)}$ and $\mathbf{K}$ means that $\mathbf{K}^{\mathcal{U}(e)}$ may be used in the normally conducting portion with no modification.

7.2.2 APPLYING BOUNDARY CONDITIONS.

As mentioned in the previous subsection, $\mathbf{K}^{\mathcal{U}(e)}$ is not complete because the boundary integral term over $d\Gamma_2$ is not evaluated. The expanded form of this term is

$$2\pi H\, r N_1 \kappa_{\theta_i}^{(1)} \omega^{(1)} j_z^{(1)} \Big|_{r_i^{(1)}} - 2\pi H\, r N_2 \kappa_{\theta_j}^{(numel+1)} \omega^{(numel)} j_z^{(numel)} \Big|_{r_j^{(numel)}} \tag{7.2.8}$$

where H is the height of the element, $numel$ is the total number of elements, N_1 and N_2 are the shape functions of $\mathbf{N}$ for the two-node "line" finite element and the superscript terms in parentheses represent an element number again. Taking the variation of (7.2.8) with respect to the independent variables $\kappa_{\theta_i}^{(1)}$, $\kappa_{\theta_j}^{(numel)}$, $j_z^{(1)}$ and $j_z^{(numel)}$ and evaluating at the specified values for r gives

$$2\pi H\, r_i^{(1)} \delta\kappa_{\theta_i}^{(1)} \omega^{(1)} j_z^{(1)} - 2\pi H\, r_j^{(numel)} \delta\kappa_{\theta_j}^{(numel)} \omega^{(numel)} j_z^{(numel)}$$
$$+2\pi H\, r_i^{(1)} \kappa_{\theta_i}^{(1)} \omega^{(1)} \delta j_z^{(1)} - 2\pi H\, r_j^{(numel)} \kappa_{\theta_j}^{(numel)} \omega^{(numel)} \delta j_z^{(numel)} \tag{7.2.9}$$

There remains in $R_p^{(e)}$ a volume term that contains $\kappa_\theta^{(e)}$ as an independent variable. The variation of this term with respect to $j_z^{(e)}$ and $\kappa_\theta^{(e)}$ produces

$$\delta j_z^{(e)} \mathbf{K}^{(e)}{}_{j\kappa} \kappa_\theta^{(e)} = 0$$
$$\delta \kappa_\theta^{(e)T} \mathbf{K}^{(e)T}{}_{j\kappa} j_z^{(e)} = 0 \tag{7.2.10}$$

Evaluation of $K^{(e)}{}_{j\kappa}$ for a two-node element gives

$$K^{(e)}{}_{j\kappa} = 2\pi H \omega^{(e)} \left\langle -r_i^{(e)} \quad r_j^{(e)} \right\rangle \tag{7.2.11}$$

Using this equation, $\delta j_z^{(e)} K^{(e)}{}_{j\kappa} \; \kappa_\theta^{(e)}$ for $e = 1$ and $e = numel$ is

$$\delta j_z^{(1)} K_{j\kappa}^{(1)} \kappa_\theta^{(1)} = \delta j_z^{(1)} \left\{ 2\pi H \omega^{(1)} \left\langle -r_i^{(1)} \quad r_j^{(1)} \right\rangle \kappa_\theta^{(1)} \right\}$$

$$\delta j_z^{(numel)} K_{j\kappa}^{(numel)} \kappa_\theta^{(numel)} \tag{7.2.12}$$

$$= \delta j_z^{(numel)} \left\{ 2\pi H \omega^{(numel)} \left\langle -r_i^{(numel)} \quad r_j^{(numel)} \right\rangle \kappa_\theta^{(numel)} \right\}$$

Addition of the third and fourth terms of (7.2.9) to the above gives

$$\delta j_z^{(1)} K_{j\kappa}^{(1)} \kappa_\theta^{(1)} = \delta j_z^{(1)} \left\{ 2\pi H \omega^{(1)} \left\langle 0 \quad r_j^{(1)} \right\rangle \kappa_\theta^{(1)} \right\}$$

$$\delta j_z^{(numel)} K_{j\kappa}^{(numel)} \kappa_\theta^{(numel)} \tag{7.2.13}$$

$$= \delta j_z^{(numel)} \left\{ 2\pi H \omega^{(numel)} \left\langle -r_i^{(numel)} \quad 0 \right\rangle \kappa_\theta^{(numel)} \right\}$$

Evaluation of $\delta \kappa_\theta^{(e)T} K^{(e)T}{}_{j\kappa} j_z^{(e)}$ at $e = 1$ and $e = numel$ and the addition of the first two terms of Equation (7.2.9) reproduces the transpose of the above results.

These results have three consequences. The first is that for $e = 1$ and $e = numel$, zeros should be inserted in the appropriate positions of the stiffness matrix to account for the effects of the boundary integral over Γ_2. Performing this operation creates a rank deficiency in the master stiffness matrix. A solution to this problem is to insert a one (1) on the diagonal element of K at the appropriate degrees of freedom and to then constrain $\kappa_{\theta_i}^{(1)}$ and $\kappa_{\theta_j}^{(numel)}$ to zero. This is easily accomplished and causes no major difficulties for finite element analysis. Second, we now have a system of $numel - 1$ equations for κ_θ. The physical significance of this is that a

Lagrangian multiplier is assigned to each of the boundaries in the conductor where ω may change, thereby ensuring the verification of the Maxwell equation $\nabla \times \mathbf{E} = 0$. Again, no difficulties ensue and the formulation still matches the actual physics of the problem. Third, there are now $numel - 1$ equations relating the $numel$ degrees of freedom associated with the $j_z^{(e)}$'s. The latter consequence is the most important because it shows that the constraint λ_c is necessary to remove the rank deficiency of the master stiffness matrix associated with the $j_z^{(e)}$'s.

As mentioned earlier, the boundary condition on A_z has been changed so that the interior node of the conductor is constrained instead of the truncation node. The appropriate boundary integral of (3.1.11) is

$$\int_{\Gamma_2} \delta A_z \left\{ \frac{r}{\mu} \frac{\partial A_z}{\partial r} \right\} \bigg|_{r_t} - \int_{\Gamma_2} \delta A_z \left\{ \frac{r}{\mu} \frac{\partial A_z}{\partial r} \right\} \bigg|_0 \qquad (7.2.14)$$

As assumed in Section 7.1.1 and at the beginning of Chapter IV, μ is assumed to be constant for the examples of this work. Equation (5.1.8) is then used to produce the following result

$$H_\theta = -\mu^{-1} \frac{\partial A_z}{\partial r} = \frac{I}{2\pi r} \qquad (7.2.15)$$

A minimum amount of algebra and the above relation changes (7.2.14) to

$$-\int_{\Gamma_2} d\Gamma_2 \delta A_z \frac{I}{2\pi} \bigg|_{r_t} = -H I \delta A_z \bigg|_{r_t} \qquad (7.2.16)$$

where the first integral is again allowed to vanish at $r = 0$.

In Chapter V, the truncation node at $r = r_t$ is constrained to zero. This will produce a reaction force at that node of magnitude HI because the imposed constraint is an essential boundary condition. On the other

hand, at the degree of freedom associated with $A_z{}_i^{(1)}$ there is no boundary force because the boundary integral vanishs there. In the case presented in Chapter V, the reaction force at the last degree of freedom for A_z was not necessary for the analysis of the example problem. This information is needed here for the determination of the new boundary forces. If A_z is constrained to zero at r equal to zero, a reaction force of $-HI$ is produced at the degree of freedom associated with $A_z{}_i^{(1)}$. This situation is analogous to changing the end constraint for a one-dimensional bar with a point force on the free end from one end to the other.

For this example, it is necessary to achieve the same loading that was exhibited for the example of Chapter V when $A_z{}_j^{(numel)}$ was constrained. This loading will produce the same B fields but different values for A. Again, it is easier to visualize the rational for the above statement by again examining the example of a one-dimensional bar again. For a one-dimensional bar, this would require that the same stresses be produced in the bar for the different set of displacements produced by constraining first one end and then the other. The validity of this comparison is shown by an examination of (5.2.1). The expression for $\mathbf{K}^{\mathcal{U}(e)}$ is the same as that for a one-dimensional FE "bar" element with a linearly varying cross-sectional area. Young's modulus has been replaced by $1/\mu^{(e)}$, and the cross-sectional area is denoted by $r_m^{(e)}$. For the forcing vector $\mathbf{p}^{(e)}$, we see that j_z is a uniformly distributed constant loading force.

For our problem, to maintain the same boundary forces that are exhibited when $A_z{}_j^{(numel)}$ is constrained, a reaction force of $-HI$ is added at this degree of freedom, and another reaction force of HI is added at the

first degree of freedom for A_z. The second force is added to cancel the force of $-HI$ produced when $A_{z_i}^{(1)}$ is constrained.

The above reaction forces can also be used for a one-dimensional superconductor. The forces are the same because variation of the terms in ΔF associated with A_z will produce boundary integrals that are identical to those in Equation (7.2.14). The use of (5.1.8) to determine an analytical expression for these integrals will still apply because the integral on the right hand side of (5.1.8) requires only the knowledge of the current I within the conductor and not its distribution. The only limitation for the correct determination of the boundary integral of (7.2.14) is that $r \geq r_c$.

Finally, one more reaction force appears from the variation of $R_p^{(e)}$ with respect to λ_c. This force has a magnitude of $-I$ and is applied at the degree of freedom associated with λ_c. Consequently, only three non-zero values appear in the global external force vector **p**.

7.3 NUMERICAL EXPERIMENTS.

7.3.1 THE FINITE ELEMENT MODEL.

The finite element formulation derived in the previous section has been applied to two test problems described below. Both problems are treated with one-dimensional axisymmetric elements. Each of these "line" elements has two end nodes and a common shared glodal node. These nodes are defined by their axial positions $r_i^{(e)}$ and $r_j^{(e)}$. Each end node has three degrees of freedom. The first degree of freedom corresponds to $\kappa_\theta^{(e)}$ and the third degree of freedom corresponds to $A_z^{(e)}$. From these values, the components of the magnetic potential and the Lagrangian multiplier κ_θ are

144

interpolated with the standard linear shape functions, which provide the C^o continuity required by the variational formulation. The second degree of freedom corresponds to $j_z^{(e)}$ on the interior node while the exterior node has no independent variable associated with it on the elemental level and is considered "empty". This second degree of freedom has no physical significance and $j_z^{(e)}$ is carried on the interior node so that an extra node per element does not have to be injected to account for this independendent variable. This scheme is used because it matches the format of the STEP1D finite element which carries no injected interior nodes. The use of this scheme makes downstream coupling of these elements, when modeling the complete, coupled EM-thermal problem, more computationally efficient. All entries in $K^{u(e)}$ associated with the "empty" degree of freedom are assigned the value of zero. The common shared global node is injected at the end of the finite element mesh. It carries no physical significance and is used solely to provide the extra degree of freedom assigned to λ_c. Consequently, each element has $2 \times 3 + 1 = 7$ degrees of freedom.

For the calculation of the element stiffnesses, it is assumed that the permeability μ, the resistivity ω, the permittivity ϵ and the current density j_z are constant over the element. The desired stiffness matrix is calculated by numerical quadrature using a two point Gauss rule. As mentioned at the end of the preceding section, only three non-zero values appear in p and the calculation of $p^{(e)}$ is not necessary.

7.3.2 APPLYING BOUNDARY CONDITIONS.

The finite element mesh is necessarily terminated at a finite size. For the two test problems, the outer radial end of the mesh is defined as the truncation radius $r = r_t$. The outer radial end of the conductor's mesh is defined as the wire radius r_c. Since current is only carried in the conductor, the degrees of freedom for j_z between r_c and r_t are constrained to zero. Similarly, the degrees of freedom for κ_θ between r_c and r_t are also constrained to zero. The degrees of freedom corresponding to $\kappa_{\theta_i}^{(1)}$ and $\kappa_{\theta_j}^{(numel)}$ are also constrained to zero as explained in Section 7.2.2. A_z is constrained to zero at r equal to zero and HI is injected into p at the degree of freedom corresponding to $A_{z_i}^{(1)}$. At the degrees of freedom corresponding to $A_{z_j}^{(numel)}$ and λ_c, $-HI$ and $-I$ are injected into p. The use of the seven degrees of freedom format for each finite element results in a rank deficiency of one for the assembled master stiffness equations. This occurs because there are only $numel$ $j_z^{(e)}$'s but the elemental degree of freedom format used produces $numel+1$ equations when assembled. The last element only contributes zeros to the master stiffness matrix for the second degree of freedom of the external (j) node. To remove the rank deficiency, the second degree of freedom on the outer node of the last element is constrained to zero.

7.3.3 ASSEMBLY, SOLUTION AND FIELD RECOVERY.

The master stiffness matrix is assembled following standard finite element techniques. During the assembly, the elemental entries for $\kappa_{\theta_i}^{(1)}$ and $\kappa_{\theta_j}^{(numel)}$ are modified as discussed in Section 7.2.2. The external force vector is assembled by injecting its three non-zero entries as described in the

previous section. The remainder of the boundary conditions are set as explained previously. The modified master equations, modified for boundary conditions, are processed by a standard symmetric skyline solver, which provides the value of A_z and κ_θ at the mesh nodes, λ_c at the injected node, and the mean current density over each element.

As in previous chapters, the physical quantity of interest is the magnetic flux density B_θ. The finite element approximation of Equation (5.3.2) is used again. However, this time B_θ is plotted as a step function to avoid the extrapolations necessary to determine the value of B_θ at r_c.

The ability of the potential formulation to model the discontinutiy in the **B** field at a conductor/free space has already been established in previous chapters. For this reason, in both test problems μ and ϵ were set equal to one (1) inside the conductor and in the free space surrounding it. The first test problem set all of the $\omega^{(e)}$'s to one, and the second problem set each $\omega^{(e)}$ to equal the inverse of the element number (*i.e.*, $\sigma^{(e)}$ equaled the element number).

7.3.4 <u>PROBLEM 1: EQUAL CONDUCTIVITIES.</u>

The first test problem is identical to that reported in Chapter V and possesses a one-dimensional axisymmetric geometry. As shown in Figure 2.1, it consists of a wire conductor of radius r_c transporting a total current $I = 1$ ampere in the positive z direction. The elements were given a unit thickness in the z direction. The radial direction is discretized with N_{wire} elements inside the wire and N_{free} elements outside the wire in free space. The mesh is truncated at a "truncation radius" r_t. Boundary conditions were set as previously defined.

The results obtained with $r_t = 2r_c$, $N_{wire} = 20$, $N_{free} = 20$ for the potentials differed from those generated by the previous EM finite elements of Chapter V by a constant, as expected. These results are shown in Figure 7.1. They illustrate what appears to be an almost exact matching of the computed solution to the analytical solution. Analysis of the data values shows that at r equal to zero the error is about 33 per cent. The error declines rapidly to .2 per cent at r_c and even further to .08 percent at r_t. This error is attributed to the relatively coarse mesh used for the example problem.

Figure 7.2 shows the results obtained for the computed current density. The result obtained is lower than the true value by less than one ten thousandth of a percent, thus providing a check on the element calculations. Because these results were so close to the exact solution, they were plotted as a series of points, rather than a line, so that they could be distinguished from the exact solution.

Figure 7.3 shows the results obtained for the B_θ field. To evaluate how closely the finite element solution matches the exact solution, it must be observed where the analytical solution intersects the tops of the finite element "steps". For an exact matching, the analytical solution will intersect the middle of the "step" tops. Although difficult to see, at r equal to zero, to approximately r equal to .1, the exact solution moves right of center on the "steps". This means that the computed solution is larger than the exact solution. The error in the computed solution ranges from 33 percent at the center of the conductor to 4.6 percent at the conductor boundary. Outside of the conductor, the error trailed off to .02 per cent. The high error at the center of the conductor is due to the relatively coarse mesh discretization used

for this problem. Finer meshes were tested and the finite element solution converged to the exact solution as expected.

7.3.5 PROBLEM 2: DIFFERENT CONDUCTIVITIES.

This problem's geometry and the values for r_t, r_c, N_{free} and N_{wire} are identical to those used in Problem 1. The only difference is that the element conductivity is set to the element number. The values obtained for the current densities shown in Figure 7.4 are as accurate as those obtained in the first test problem.

The computed potential shown in Figure 7.5 displays a behavior that is different from that exhibited in the first example. The error ranges from a maximum of about 33 per cent at r_c to zero per cent at r equal to zero. The error at r_t is approximately 13.4 per cent. But the primary quantity of interest is B_θ, not A_z.

The behavior of B_θ is shown in Figure 7.6 and displays much less absolute error than A_z. The error at r equal to zero is about 33 per cent, at r_c .064 per cent and at r_t .016 per cent. The reason for such better results for B_θ is that the rate of change of A_z is the quantity of interest, and not its magnitude. Referring again to Figure 7.5, it can be seen that the computed value for the rate of change of A_z appears to be close to the analytical value for over half of the range of r. This accounts for the good values of B_θ that occured for $r > .2$. Much of the error that occured in the computation of A_z can be attributed to the large change in ω $(= \sigma^{-1})$ for this example. From the first conducting element to the last, there occured a 1900 per cent change in the value of ω. Put into this context, the errors that did occur for the finite element values of A_z are reasonable. Several more examples with

more slowly varying resistivities were performed to verify that this was the source of the error. They are not presented here because Figure 7.3 illustrates what occurs in the limiting case where the conductivity does not vary at all; the analytical and finite element solutions converge. Although some error remains at the center of the conductor, finer mesh discretizations can be used to generate computed solutions that lie within a desired tolerance.

It is recognized that the error at the center of the conductor for both test problems appears large. This is because the error measured is the absolute error. Other error estimators are available, but this topic is deferred to Section 10.2.3 because of similar errors that occur for both the STEP1D and LINT1D finite elements. As in the problems studied in this chapter, the error measured is the absolute error and appears large. The discussion in Section 10.2.3 shows that the error produced by using the STEP1D, LINT1D, CUPLE1D and LET1D finite elements to solve EM and thermal problems is within acceptable limits and that the absolute error alone is not always the best measure of a computed solution's accuracy.
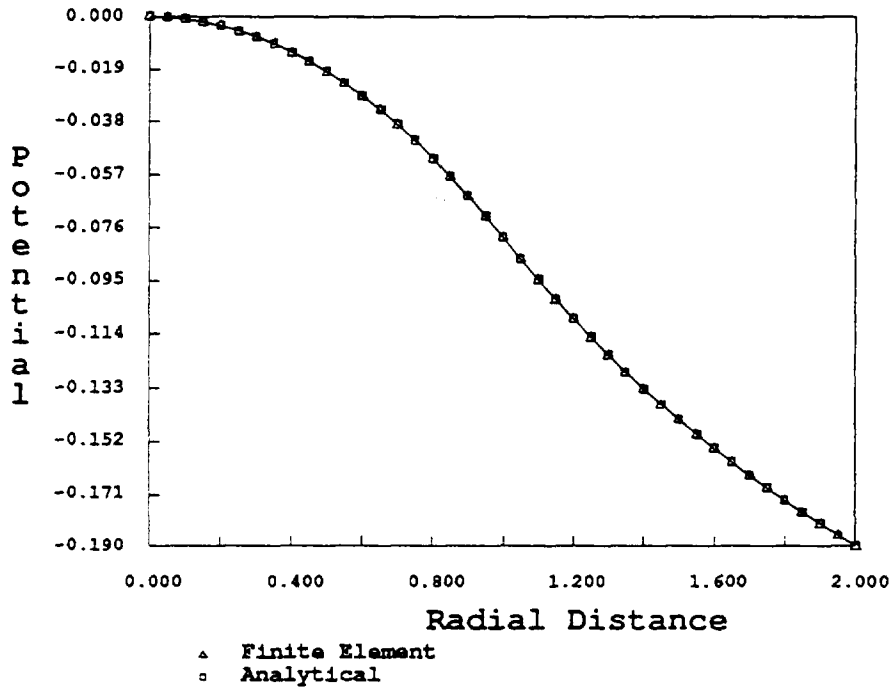
Figure 7.1: A_z vs. r, all elements equal conductivities.
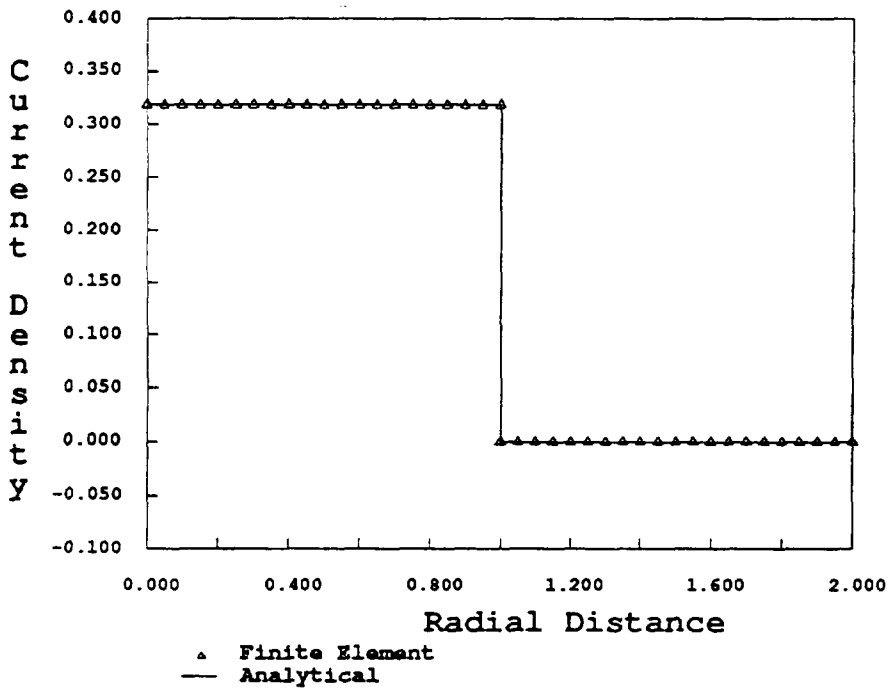
Figure 7.2: j_z vs. r, all elements equal conductivities. Finite element solution plotted as points to highlight accuracy of method in matching analytical solution.

151
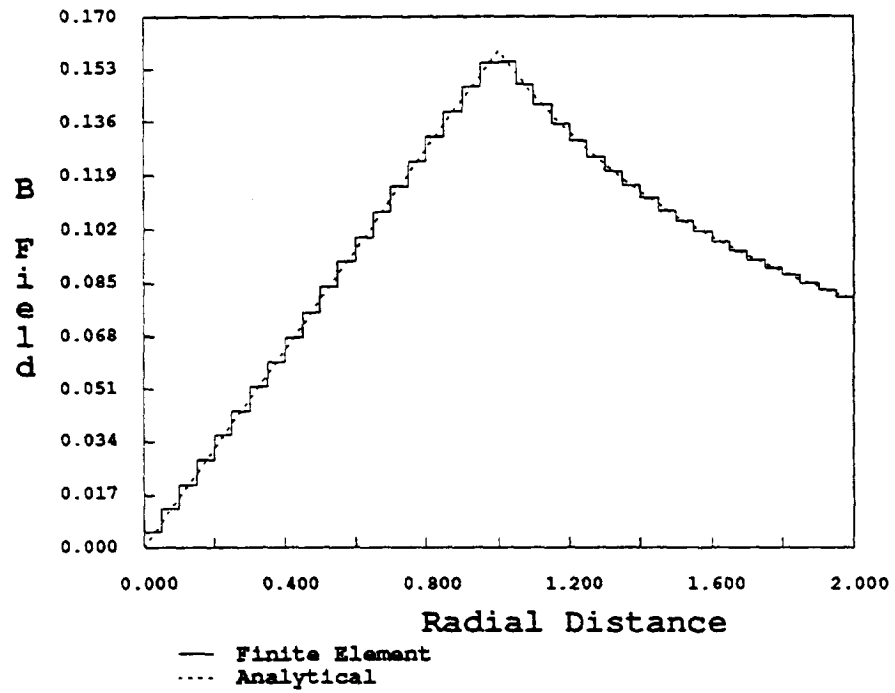
Figure 7.3: B_θ vs. r, all elements equal conductivities.

Figure 7.4: j_z vs. r, element conductivity equal to element number. Finite element solution plotted as points to highlight accuracy of method in matching analytical solution.
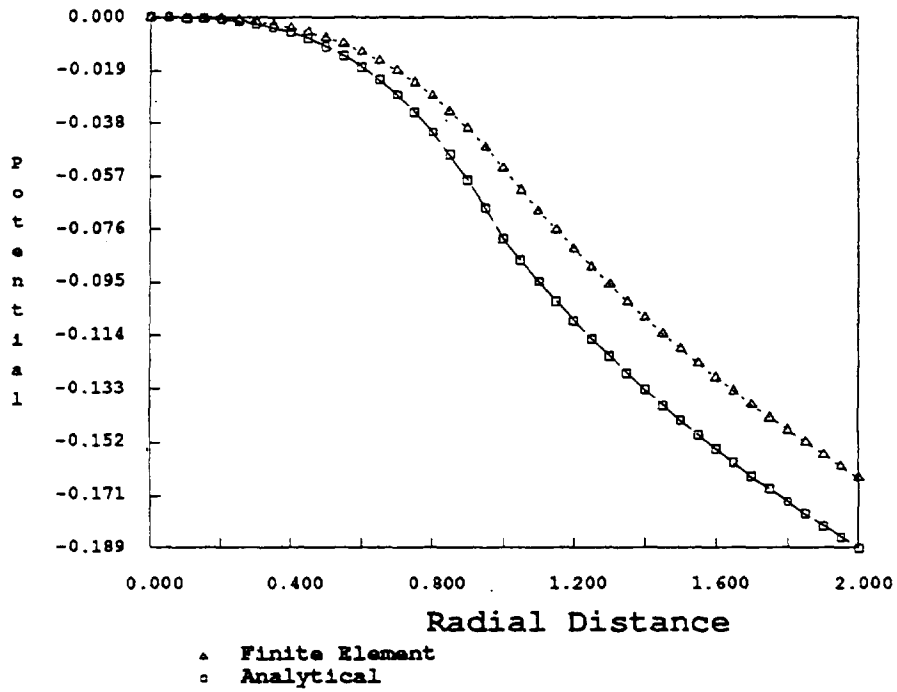
Figure 7.5: A_z vs. r, element conductivities equal to element number

Figure 7.6: B_θ vs. r, element conductivities equal to element number

153
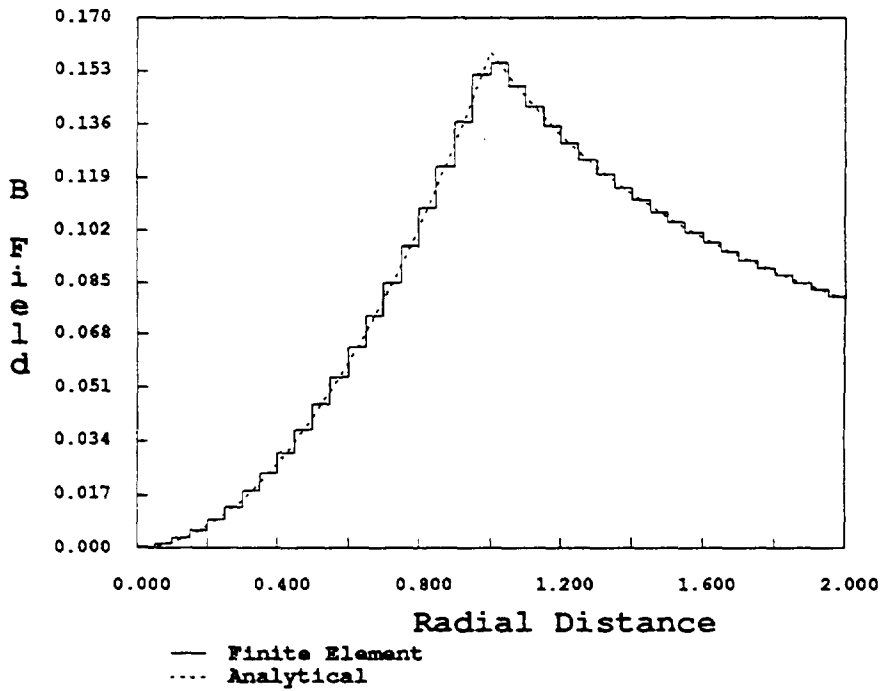
7.4 SUMMARY.

The results obtained in the previous two problems show that it is possible to extend the four-potential formulation to the case where the current density distribution is unknown. This is important since this means that it is now possible to solve problems where material and geometric non-linearities preclude a linear current distribution. It also means that whereas before a knowledge of how the current was distributed within a conductor was necessary, with this extension of the four-potential variational principle, all that is needed is the total current I through the conductor, its material properties μ and ω, and the conductor geometry.

Having shown the validity of this extension of four-potential theory to the prediction of electromagnetic quantities, one is now prepared to construct a nonlinear conductor, the superconductor. This is the topic of the next chapter.

THE SUPERCONDUCTING FINITE ELEMENT

In this chapter, the four-potential formulations of the Ginzburg-Landau and London type superconductors are discussed. Both elements use for the example problem the geometry of the one-dimensional infinite conductor shown in Figure 2.1. Because the London type superconductor is only an approximation to the more exact Ginzburg-Landau equations, only the computational results for the Ginzburg-Laundau superconductor are presented here. We restrict our consideration to the time-independent (static) case.

For both superconductors, the total current I is known, $\mathbf{j}$ is unknown, and the static charge density ρ is zero. Because the four-potential method has shown in the past three chapters that it can easily model the conductor/free space boundary discontinuity for B_θ, only the region within the conductor is modeled. The stiffness and tangent stiffness matrices for the Ginzburg-Landau superconductor contain the independent variables $|\psi|$ and $\mathbf{A}$ and therefore represent a set of non-linear equations. A short discussion of non-linear solution techniques is included in this chapter as well as a discussion on how $|\psi|$ and $\mathbf{A}$ are scaled to reduce the ill-conditioning of the system of nonlinear superconducting finite element equations.

No analytical solution is available for the chosen problem. However, numerical results can be examined to determine if they are physically realizable. As a second check on the accuracy of the results, the $\mathbf{B}$ field as

determined by the finite element approximation using **A** can be compared to the **B** field determined by **j** of the finite element formulation and Equation (7.1.5). Because no analytical solution is available, the first topic to be discussed is the construction of the one-dimensional axisymmetric superconducting finite element.

8.1 FINITE ELEMENT DISCRETIZATION.

As mentioned in the introduction to this chapter, the discretization of the Ginzburg-Landau equations results in a set of nonlinear equations. To solve these equations, expressions for the residual **r**, the internal force vector **f**, the external force vector **p** and the tangent stiffness matrix **K** are needed. For this problem, **f** and **r** are determined by taking the first variation of the governing functional, **p** by boundary integrals, and **K** by taking the second variation of the governing functional. The relationship between **r**, **f** and **p** is

$$\mathbf{r} = \mathbf{f} - \mathbf{p} \qquad (8.1.1)$$

In this section, **r**, **f** and **K** are determined and in the discussion of the boundary terms, **p** is determined.

8.1.1 CONSTRUCTING EM FINITE ELEMENTS.

For the finite element discretization of a one-dimensional superconductor, the two-node "line" element is again sufficient. Individual elements are denoted by the superscript (e). As mentioned in Section 3.2.1, μ may be replaced by μ_o with little loss of accuracy and this substitution is performed for the superconducting finite elements derived here. The material parameters α and β are dependent upon $\mathcal{T}$. Also mentioned in Section 4.1 is that

156

for the steady state heat conduction problem, $\mathcal{T}$ is a constant throughout a superconductor. Consequently, the material parameters α, β and μ_o are the same for every element and the superscript (e) is omitted for these quantities. The element end nodes are denoted by the subscripts i and j. A_z and $|\psi|$ are interpolated over each element as

$$A_z = \mathcal{A}^{(e)} = \mathbf{N} \mathbf{A}_z^{(e)} \qquad |\psi| = |\Psi^{(e)}| = \mathbf{N}|\psi|^{(e)} \tag{8.1.2}$$

where the symbols $\mathcal{A}^{(e)}$ and $|\Psi^{(e)}|$ have been introduced to simplify notation later. The row vector $\mathbf{N}$ contains the isoparametric shape functions for the interpolation of A_z and $|\psi|$. The elements of $\mathbf{N}$ are only functions of the spatial coordinate r. $\mathbf{A}_z^{(e)}$ and $|\psi|^{(e)}$ contain the nodal values of A_z and $|\psi|$ respectively, and are time-independent. Substitution of these finite element assumptions into the previously derived variational functional of Equation (3.2.13) gives

$$\Delta F_g^{(e)} = \int_{V^{(e)}} dV^{(e)} \left\{ -\alpha |\psi|^{(e)T} \mathbf{N}^T \mathbf{N} |\psi|^{(e)} + \tfrac{1}{2}\beta \left(|\psi|^{(e)T} \mathbf{N}^T \mathbf{N} |\psi|^{(e)} \right)^2 \right.$$
$$+ \frac{\hbar^2}{2m^*} |\psi|^{(e)T} \frac{\partial \mathbf{N}^T}{\partial r} \frac{\partial \mathbf{N}}{\partial r} |\psi|^{(e)} + \frac{1}{2\mu_o} \mathbf{A}_z^{(e)T} \frac{\partial \mathbf{N}^T}{\partial r} \frac{\partial \mathbf{N}}{\partial r} \mathbf{A}_z^{(e)}$$
$$\left. + \frac{q^{*2}}{2m^*} |\psi|^{(e)T} \mathbf{N}^T \mathbf{N} |\psi|^{(e)} \mathbf{A}_z^{(e)T} \mathbf{N}^T \mathbf{N} \mathbf{A}_z^{(e)} \right\}$$

$$\tag{8.1.3}$$

Taking the first variation of $\Delta F_g^{(e)}$ gives a set of equations, which collectively represent the internal force vector $\mathbf{f}$ for each finite element. The portion of $\mathbf{f}^{(e)}$ obtained by varying $|\psi|^{(e)}$ is

$$\mathbf{f}^{(e)}|_{|\psi|} = \int_{V^{(e)}} dV^{(e)} \left\{ -2\alpha \mathbf{N}^T \mathbf{N} |\psi|^{(e)} + 2\beta |\Psi^{(e)}|^2 \mathbf{N}^T \mathbf{N} |\psi|^{(e)} \right.$$
$$\left. + \frac{\hbar^2}{m^*} \frac{\partial \mathbf{N}^T}{\partial r} \frac{\partial \mathbf{N}}{\partial r} |\psi|^{(e)} + \frac{q^{*2}}{m^*} \mathbf{N}^T \mathbf{N} |\psi|^{(e)} \mathcal{A}^{(e)2} \right\} \tag{8.1.4}$$

157

The portion of the internal force vector associated with $\mathbf{A}_z^{(e)}$ is

$$\mathbf{f}^{(e)}{}_{A_z} = \int_{V^{(e)}} dV^{(e)} \left\{ \frac{1}{\mu_o} \frac{\partial \mathbf{N}^T}{\partial r} \frac{\partial \mathbf{N}}{\partial r} \mathbf{A}_z^{(e)} + \frac{q^{*2}}{m^*} |\Psi^{(e)}|^2 \mathbf{N}^T \mathbf{N} \mathbf{A}_z^{(e)} \right\} \quad (8.1.5)$$

The total internal force for each element is now

$$\mathbf{f}^{(e)} = \left\{ \begin{array}{c} \mathbf{f}^{(e)}{}_{|\psi|} \\ \mathbf{f}^{(e)}{}_{A_z} \end{array} \right\} \quad (8.1.6)$$

This expression applies to a Ginzburg-Landau superconductor. For a London type superconductor $|\psi|^2$ is constant and equal to $|\psi_\infty|^2$. Consequently, the only nonzero portion of $\mathbf{f}^{(e)}$ is $\mathbf{f}^{(e)}{}_{A_z}$.

Taking the derivative of $\mathbf{f}^{(e)}$ with respect to the independent variables produces the tangent stiffness matrix $\mathbf{K}^{(e)}$ for each element. The expression for a Ginzburg-Landau superconductor is

$$\mathbf{K}^{(e)} = \begin{bmatrix} \mathbf{K}^{(e)}{}_{A_z A_z} & \mathbf{K}^{(e)}{}_{A_z |\psi|} \\ \mathbf{K}^{(e)T}{}_{A_z |\psi|} & \mathbf{K}^{(e)}{}_{|\psi||\psi|} \end{bmatrix} \quad (8.1.7)$$

where

$$\mathbf{K}^{(e)}{}_{A_z A_z} = \int_{V^{(e)}} dV^{(e)} \left\{ \frac{1}{\mu_o} \frac{\partial \mathbf{N}^T}{\partial r} \frac{\partial \mathbf{N}}{\partial r} + \frac{q^{*2}}{m^*} |\Psi^{(e)}|^2 \mathbf{N}^T \mathbf{N} \right\} \quad (8.1.8)$$

$$\mathbf{K}^{(e)}{}_{A_z |\psi|} = \int_{V^{(e)}} dV^{(e)} \left\{ 2 \frac{q^{*2}}{m^*} \mathcal{A}^{(e)} |\Psi^{(e)}| \mathbf{N}^T \mathbf{N} \right\} \quad (8.1.9)$$

$$\mathbf{K}^{(e)}{}_{|\psi||\psi|} =$$
$$\int_{V^{(e)}} dV^{(e)} \left\{ \left(-2\alpha + 6\beta |\Psi^{(e)}|^2 + 2 \frac{q^{*2}}{m^*} \mathcal{A}^{(e)2} \right) \mathbf{N}^T \mathbf{N} + \frac{\hbar^2}{m^*} \frac{\partial \mathbf{N}^T}{\partial r} \frac{\partial \mathbf{N}}{\partial r} \right\}$$
$$(8.1.10)$$

For the London superconductor $\mathbf{K}^{(e)}$ is reduces to $\mathbf{K}^{(e)}{}_{A_z A_z}$.

Examination of $\mathbf{K}^{(e)}{}_{|\psi||\psi|}$ and $\mathbf{K}^{(e)}{}_{A_z A_z}$ shows that an internal inconsistency can appear because both of the independent variables, $|\psi|$ and

A_z, and their derivatives use the same shape functions. This inconsistency can sometimes cause a "locking" problem. For the one-dimensional cases considered here, this does not occur and is discussed further in Section 8.2.4.

For mechanical elements $\mathbf{u}^{(e)}$ is the displacement field in the element. In non-linear finite elements, $\mathbf{v}^{(e)}$ are the visible degrees of freedom. The nodal degrees of freedom $\mathbf{v}^{(e)}$ cannot be solved for directly because the internal forces are nonlinear functions of $\mathbf{v}^{(e)}$, which in turn is a function of the "loading parameter" ζ. The general technique to handle such nonlinear problems is to convert the assembled residual force equations (8.1.0) to incremental form by differentiating them with respect to a loading parameter ζ, $i.e.$,

$$\frac{\partial \mathbf{f}}{\partial \zeta} = \frac{\partial \mathbf{f}}{\partial \mathbf{v}} \frac{\partial \mathbf{v}}{\partial \zeta} = \frac{\partial \mathbf{p}}{\partial \zeta} \quad \text{or} \quad \mathbf{Kw} = \mathbf{q} \qquad (8.1.11)$$

where $\mathbf{w}$ is the set of incremental rates and $\mathbf{q}$ is the loading vector. $\mathbf{w}$ and $\mathbf{q}$ represent the rate of change of $\mathbf{v}$ and $\mathbf{p}$ with respect to a loading parameter ζ. The response $\mathbf{v}(\zeta)$ is obtained by numerically integrating the above equation in conjunction with Newton-Raphson iteration procedures as described later in this chapter. The purpose of introducing these new quantities here is that they are necessary for the topic of the next section, the application of boundary conditions. In keeping with the new notation, for a Ginzburg-Landau superconductor, $\mathbf{v}^{(e)}$ and $\mathbf{w}^{(e)}$ are

$$\mathbf{v}^{(e)} = \left\{ \begin{array}{c} A_z^{(e)} \\ |\psi|^{(e)} \end{array} \right\} \qquad \mathbf{w}^{(e)} = \left\{ \begin{array}{c} \dfrac{\partial A_z^{(e)}}{\partial \zeta} \\ \dfrac{\partial |\psi|^{(e)}}{\partial \zeta} \end{array} \right\} \qquad (8.1.12)$$

For a London superconductor, $\mathbf{v}^{(e)}$ and $\mathbf{w}^{(e)}$ are

$$\mathbf{v}^{(e)} = \left\{ A_z^{(e)} \right\} \qquad \mathbf{w}^{(e)} = \left\{ \frac{\partial A_z^{(e)}}{\partial \zeta} \right\} \qquad (8.1.13)$$

159

8.1.2 APPLYING BOUNDARY CONDITIONS.

The boundary conditions for A_z are addressed first. As discussed in the latter half of Section 7.2.2, the discrete boundary terms for the CU-PLE1D finite element are the same as those of a one-dimensional supercon-ductor. The only non-zero values for p_{A_z} occur at the degrees of freedom corresponding to the first and last nodal displacements of A_z. They both have a magnitude of HI and differ in the direction of their application. In the past, I has been used to represent the *total* current load. It is now split into two distinct parts to give

$$I = I_o + \zeta I_L \qquad (8.1.14)$$

where I_o represents the *initial* current and I_L the *loading* current. When the loading parameter ζ is zero, the only load upon the system results from the initial current load. When ζ equals one, by convention the system is regarded as being fully loaded. Using the new notation, the forcing vector p_{A_z} is

$$\mathbf{p}_{A_z} = (I_o + \zeta I_L) H \left\{ \begin{array}{c} 1 \\ 0 \\ \vdots \\ 0 \\ -1 \end{array} \right\} \qquad (8.1.15)$$

where 1 and -1 correspond to the first and last degrees of freedom for A_z respectively, and the vertical dots represent a continuation of zeros over the remaining degrees of freedom for A_z. The expression for q_{A_z} is

$$\mathbf{q}_{A_z} = \frac{\partial \mathbf{p}_{A_z}}{\partial \zeta} = -I_L H \left\{ \begin{array}{c} 1 \\ 0 \\ \vdots \\ 0 \\ -1 \end{array} \right\} \qquad (8.1.16)$$

The above expressions for q_{A_z} and p_{A_z} are valid for *any* one-dimensional conductor where the first degree of freedom of A_z is constrained to zero.

As discussed in Section 3.2.1, $\nabla|\psi|$ on the boundaries is equal to zero. Consequently, the boundary terms dependent upon $|\psi|$ of (3.2.14) are zero and make no contribution to p. The expressions for $p_{|\psi|}$ and $q_{|\psi|}$ are therefore

$$\mathbf{p}_{|\psi|} = 0 \qquad \mathbf{q}_{|\psi|} = 0 \qquad (8.1.17)$$

and the total external force and loading vectors are

$$\mathbf{p} = \left\{ \begin{array}{c} \mathbf{p}_{A_z} \\ \mathbf{p}_{|\psi|} \end{array} \right\} \qquad \mathbf{q} = \left\{ \begin{array}{c} \mathbf{q}_{A_z} \\ \mathbf{q}_{|\psi|} \end{array} \right\} \qquad (8.1.18)$$

for a Ginzburg-Landau superconductor. To ensure that there are no superconducting charge carriers in the free space surrounding the Ginzburg-Landau superconductor, $|\psi|$ is constrained to zero at r equal to r_c. For a London superconductor, p and q reduce to $\mathbf{p}_{A_z}$ and $\mathbf{q}_{A_z}$ respectively.

8.2 NUMERICAL EXPERIMENTS.

The finite element formulation for a Ginzburg-Landau superconductor has been applied to the solution of a one-dimensional axisymmetric infinite wire. Each element contains two end nodes and a common global node that is located at the truncation radius r_t. These nodes are defined by their radial positions $r_i^{(e)}$ and $r_j^{(e)}$. The glodal node carries an "empty" degree of freedom and is used only to provide the same number of degrees of freedom as contained in the CUPLE1D finite element. Similarly, each end node contains three degrees of freedom. The first and third degree of freedoms carry the nodal values for $|\psi|$ and A_z respectively. The second degree of freedom is also

"empty". This choice provides for easier downstream coupling of the super and normal conducting finite elements by reducing computational effort.

The computational effort is reduced because nodal connectivity and freedom tables used to generate the diagonal location pointer array for the skyline symmetric stored system of equations are only generated once. The "empty" degree of freedom on each end node also allows for the easy addition of the variable ϖ if the gauge choice used is not the London gauge. With the "empty" degrees of freedom, each element carries seven degrees of freedom like the CUPLE1D finite element. The actual number of degrees of freedom used per element is $2 \times 2 = 4$ degrees of freedom.

For the calculation of $\mathbf{K}$, $\mathbf{p}$, $\mathbf{q}$ and $\mathbf{f}$ the permeability μ is set to μ_o, as discussed in the introduction to Chapter IV. The values for α, β and $|\psi_\infty|^2$ for each element are determined by using the formulas presented in Section 4.4. The tangent stiffness matrix and internal force vector are calculated by numerical quadrature using a two point Gauss formula.

8.2.1 APPLYING BOUNDARY CONDITIONS.

The finite element mesh is terminated at r_t, as in the linear conductor. To ensure that no superconducting flux can cross the conductor's outer edge into free space, the degrees of freedom corresponding to $|\psi|$ between r_c and r_t are set to zero. At $r = r_c$, $|\psi|$ is also set to zero. By doing this, the boundary terms of (3.2.14) vanish. At $r = 0$, A_z is set to zero as required by the London gauge choice. Any "empty" degrees of freedom are also constrained to zero to prevent rank deficiencies of the assembled master stiffness matrix.

8.2.2 ASSEMBLY AND SOLUTION.

The tangent stiffness and internal force vector are assembled following standard finite element techniques. The tangent stiffness K is stored using a symmetric skyline storage scheme, and then modified for boundary conditions. The external force and loading vectors are inititalized to zero and the two non-zero values for each are injected at the appropriate degrees of freedom.

Solution Technique.

For linear finite elements, the displacements v can be solved for directly by inverting the stiffness matrix $K^{\mathcal{U}}$ and multiplying it by the external force vector p, i.e.,

$$v = \left(K^{\mathcal{U}}\right)^{-1} p \tag{8.2.1}$$

The standard technique shown above to solve for v does not work for the Ginzburg-Landau superconducting finite element because $K^{\mathcal{U}}$ is a function of $|\psi|$ and A_z. To begin our discussion of nonlinear solution techniques, the residual equations are rewritten as

$$f - p \quad = \quad r \quad = \quad 0 \tag{8.2.2}$$

where f and r represent the internal force and residual vectors respectively. It can be seen that when the residual vector is zero, the solution vector v lies upon an equilibrium curve or path called the response. The central idea of non-linear solution techniques is to find a solution that lies upon a physically correct equilibrium path and to then advance the solution along it. For the cases examined in this work, the position along the equilibrium path is determined by the loading parameter, also known as the control parameter, ζ.

The displacements **v** are also called the state variables because they represent the state of the system along an equilibrium path. For the cases presented here, an initial solution that lies upon the physically correct equilibrium path is not always known in advance. For these cases, we are required to guess a "neighboring" state from which to start an iterative process that takes us to the path. The initial solution, or "guess", is named the *reference* state of the system.

For the Ginzburg-Landau superconducting finite element (STEP1D), it was found that the best choice for the reference state is that where A_z is set to 0 and all unconstrained values of $|\psi|$ are set to $|\psi_\infty|$. The value for $|\psi_\infty|$ is determined from the formula presented in Section 4.4. This state closely approximates a Ginzburg-Landau superconductor with the total current I and external **B** fields equal to zero, the difference for our choice occuring primarily in the boundary layer. The true state can be closely approximated by a step function for $|\psi|$ over the interior of the conductor with a magnitude of $|\psi_\infty|$. However, the chosen reference state is close enough to the true state that the same techniques used to advance the solution can also be used to bring this reference state onto the desired equilibrium path.

To find how the solution vector **v** changes as the solution advances along an equilibrium path, the partial of **r** with respect to the loading parameter ζ is taken to give

$$\begin{aligned}
\frac{\partial \mathbf{r}}{\partial \zeta} &= \frac{\partial \mathbf{f}}{\partial \zeta} - \frac{\partial \mathbf{p}}{\partial \zeta} \\
&= \frac{\partial \mathbf{f}}{\partial \mathbf{v}} \frac{\partial \mathbf{v}}{\partial \zeta} - \frac{\partial \mathbf{p}}{\partial \zeta} \\
&= \mathbf{K} \frac{\partial \mathbf{v}}{\partial \zeta} - \mathbf{q} \\
&= \mathbf{K}\mathbf{w} - \mathbf{q} = 0
\end{aligned} \qquad (8.2.3)$$

The last equation shown above is known as the *incremental rate* equation. K defines the tangent to the equilibrium path and is known as the tangent stiffness matrix; w represents the rate of change of the solution vector along the equilibrium path and is named the *incremental velocity* vector; and q is the *loading* vector that represents the rate of change of the system's external forces as the external loads of the system are varied.

To advance the solution along an equilibrium path, the values of the solution vector at the current known state are used to determine the tangent stiffness matrix. The loading vector is also determined and the following system of equations is solved to determine the incremental rates.

$$\mathbf{w} = \mathbf{K}^{-1}\mathbf{q} \qquad (8.2.4)$$

Numerical problems arise, however, if the current position of the solution on the equilibrium path is a stationary (critical) point. At these points, K is singular. For the STEP1D finite element, this occurs when ΔF_g is zero. There is no difference between the Helmholtz free energies for the superconducting and normal states of a conductor at this point. This point represents a crossing of the equilibrium paths for the Helmholtz free energy functionals of the normal and superconducting states and is called a bifurcation point. If this point is reached or exceeded, because the free energies are equal, the LET1D finite element is used. The LET1D formulation is not singular at this point because it does not contain the quantum parameter $|\psi|$; consequently it does not model the true state of the system at this point. The true state is a mixture of normal and superconducting phases that lies beyond the modeling ability of one-dimensional finite elements as it is in fact a multidimensional problem.

Assuming that a current value of **v** on the equilibrium path is known, as a first step to obtaining another solution, an increment along the tangent to the equilibrium path is taken. That is, the solution is moved Δ**v** in the **v** direction and $\Delta\zeta$ in the ζ direction of the hyperspace defined by **v** and ζ. The step is named the *predictor* step. New values for **v** and ζ are computed at the point that lies at the end of the predictor step. A corrector procedure, called the *corrector* step, is then invoked to iterate the solution back onto the equilibrium path. The distances traversed in the **v** and ζ directions for each iteration are designated as $\mathbf{d}^k$ and η^k respectively, where superscript k designates the iteration number. The equilibrium path is reached when **r** = 0. To ensure at each step n that the solution does not travel too far from the equilibrium path, a distance l_n is specified. The distance l_n is also used to ensure that the distance along the equilibrium path traversed is not too large. This distance is limited so that the solution procedure does not accidentally step over a stationary point or move too far from the equilibrium path. Detecting stationary points becomes important when they are branching or bifurcation points because it is desired that the solution procedure follow the equilibrium path that matches the true physics of the system. If the solution procedure steps over one of these points, it may follow a non-physical equilibrium path.

The addition of the length constraint adds an extra equation to the original system of equations:

$$|\Delta s_n| - l_n = c = 0 \qquad\qquad (8.2.5)$$

where $|\Delta s_n|$ is an approximation to the distance s travelled on the equilibrium path. For the finite elements of this work, the initial values for **v** and

166

ζ are computed using a Forward Euler scheme. The corrector step uses the Conventional Newton-Raphson (CNR) method to iterate to a solution under the arclength constraint (8.2.5). The formulas used for the forward Euler integration and the arclength constraint are reproduced below. Subscripts n represent the step number and superscripts k represent the iteration number.

Arclength Constraint

$$|\Delta s_n| - l_n = \frac{1}{f_n} \left| \mathbf{w}_n^T \Delta \mathbf{v}_n + \Delta \zeta_n \right| - l_n = 0$$

$$f_n = \sqrt{1 + \mathbf{w}_n^T \mathbf{w}_n} \qquad (8.2.6)$$

$$\frac{\partial c}{\partial \mathbf{v}} = \mathbf{a}^T = \frac{\mathbf{w}_n}{f_n} \qquad \frac{\partial c}{\partial \zeta} = g = \frac{1}{f_n}$$

Foward Euler Method with Arclength Constraint

$$\zeta_{n+1} = \zeta_n + \Delta \zeta_n \qquad \Delta \zeta_n = l_n / f_n \, sign \left(\mathbf{q}_n^T \mathbf{w}_n \right)$$

$$\mathbf{v}_{n+1} = \mathbf{v}_n + \Delta \mathbf{v}_n \qquad \Delta \mathbf{v}_n = \mathbf{K}_n^{-1} \mathbf{q}_n \Delta \zeta_n \qquad (8.2.7)$$

$$= \mathbf{w}_n \Delta \zeta_n$$

To implement the Conventional Newton-Raphson technique, the original equations for $\mathbf{r}$ must be augmented by the constraint equation c and solved. This gives the linear system

$$\begin{bmatrix} \mathbf{K} & -\mathbf{q} \\ \mathbf{a}^T & g \end{bmatrix} \begin{Bmatrix} \mathbf{d} \\ \eta \end{Bmatrix} = - \begin{Bmatrix} \mathbf{r} \\ c \end{Bmatrix} \qquad (8.2.8)$$

Because this augmented system is not symmetric, the two linear symmetric systems below are solved for instead

$$\mathbf{K} \mathbf{d}_r = -\mathbf{r} \qquad \mathbf{K} \mathbf{d}_q = \mathbf{q} \qquad (8.2.9)$$

to get

$$\eta = -\frac{c + \mathbf{a}^T \mathbf{d}_r}{g + \mathbf{a}^T \mathbf{d}_q} \qquad \mathbf{d} = \mathbf{d}_r + \eta \mathbf{d}_q \qquad (8.2.10)$$

which finally gives

$$\mathbf{v}_n^{k+1} = \mathbf{v}_n^k + \mathbf{d} \qquad \zeta_n^{k+1} = \zeta_n^k + \eta \qquad (8.2.11)$$

Iterations are performed until the 2-norm of $\mathbf{r}$ is less than a specified tolerance τ. For cases where the 2-norm will not go below τ, a limit is set on the maximum number of iterations by another input parameter. Because the Newton-Raphson technique can also diverge instead of converge upon a solution, limits on the maximum value for the 2-norm of $\mathbf{v}$ are also specified. To stop the solution process, another input parameter limits the maximum value of ζ. When this value for ζ is surpassed, the solution process is terminated.

The solution procedure may be summarized as follows:

(1) Initialize $\mathbf{v}$ and ζ to the reference state.

(2) Solve for $\mathbf{w}$.

(3) Update $\mathbf{v}$ and ζ using the Forward Euler integration scheme

(4) Evaluate $\mathbf{r}$ and c at step $n + 1$ by using $\mathbf{v}_{n+1}$ and ζ_{n+1}.

(5) Solve (8.2.9) for $\mathbf{d}_r$ and $\mathbf{d}_q$.

(6) Using (8.2.10) with the values for $\mathbf{d}_r$ and $\mathbf{d}_q$, solve for η and $\mathbf{d}$.

(7) Update $\mathbf{v}$ and ζ using (8.2.11).

(8) Find the 2-norm of $\mathbf{v}$

(9) If the maximum value for the 2-norm of $\mathbf{v}$ or ζ is exceeded, terminate the solution procedure.

(10) Find the 2-norm of $\mathbf{r}$ and c.

(11) If the 2-norm of (10) is less than or equal to τ, restart the solution procedure over at step (2) until the desired value for ζ is reached or exceeded. If the 2-norm of (10) is greater than τ, go back to step (5) and repeat the solution procedure until the 2-norm is less than or equal to τ or the maximum number of iterations is surpassed.

8.2.3 SCALING TECHNIQUES.

The solution procedure of the previous section is particularly sensitive to heterogeneous physical dimensions in the solution vector $\mathbf{v}$. In addition, off-diagonal terms of $\mathbf{K}$ may be either considerably larger or smaller than the diagonal terms, giving $\mathbf{K}$ a high condition number. This means that a small change in one degree of freedom may produce a large, non-physical displacement at another degree of freedom. The STEP1D finite element solves the above problems by implementing several different scaling techniques. The first technique gives the elements of $\mathbf{v}$ the same physical dimensions. The second scaling makes off-diagonal terms of the same order of magnitude as the diagonal terms. The third scaling is used to further improve the condition number of $\mathbf{K}$. Finally, the fourth scaling adjusts the dimensions of $\mathbf{v}$ and ζ in the solution hyperspace to improve convergence rates and accuracy.

To perform the first, third and fourth scalings, the solution vector $\mathbf{v}$ is scaled by a diagonal matrix $\mathbf{S}_n$

$$\tilde{\mathbf{v}}_n = \mathbf{S}_n \mathbf{v} \qquad (8.2.12)$$

where subscript n indicates either the first, third or fourth scaling and the superposed tilde denotes a scaled quantity. If the stiffness-force equation is

169

premultiplied by S_n^{-1} and the scaled form of $\mathbf{v}$ is substituted, the results are

$$S_n^{-1} K^{\mathcal{U}} S_n^{-1} \tilde{\mathbf{v}} = S_n^{-1} \mathbf{p}$$

$$\tilde{K}^{\mathcal{U}} \tilde{\mathbf{v}} = \tilde{\mathbf{p}} \tag{8.2.13}$$

where $\tilde{K}^{\mathcal{U}}$ and $\tilde{\mathbf{p}}$ are the scaled versions of $K^{\mathcal{U}}$ and $\mathbf{p}$. The scaled versions of other relevant quantities can be derived in a similar manner and are presented below.

$$\tilde{\mathbf{r}} = S_n^{-1} \mathbf{r} \qquad \tilde{\mathbf{f}} = S_n^{-1} \mathbf{f} \qquad \tilde{\mathbf{q}} = S_n^{-1} \mathbf{q}$$

$$\tilde{\mathbf{w}} = S_n^{-1} \mathbf{w} \qquad \tilde{\Delta} \mathbf{v} = S_n^{-1} \Delta \mathbf{v} \qquad \tilde{K} = S_n^{-1} K S_n^{-1}$$

$$|\Delta \tilde{s}| = \left| \tilde{\mathbf{w}}^T S_n^2 \tilde{\Delta} \tilde{\mathbf{v}} + \Delta \zeta \right| = \left| \tilde{\mathbf{w}}^T \tilde{\Delta} \tilde{\mathbf{v}} + \Delta \zeta \right| / \tilde{f} \tag{8.2.14}$$

$$\tilde{f} = \sqrt{1 + \mathbf{w}^T S_n^2 \mathbf{w}} = \sqrt{1 + \tilde{\mathbf{w}}^T \tilde{\mathbf{w}}}$$

First Scaling.

The first scaling is performed element by element at an element level, and is used to scale $|\psi|$ and A_z to have the same dimensions. Let L, M, T and Q represent units of distance, mass, time and charge respectively. It can be seen that A_z has units of ML/TQ and $|\psi|$ has units of $L^{-3/2}$. Numerical experiments showed that letting the units of $\mathbf{v}$ be $L^{-1/2}$ improved the stability of the solution process. For this scaling, S_1 for *each* element is expressed as

$$S_1^{(e)} = \begin{bmatrix} S_{11}^{(e)} & 0 & 0 & 0 & 0 & 0 & 0 \\ & 1 & 0 & 0 & 0 & 0 & 0 \\ & & S_{33}^{(e)} & 0 & 0 & 0 & 0 \\ & & & S_{44}^{(e)} & 0 & 0 & 0 \\ & & & & 1 & 0 & 0 \\ & & symm. & & & S_{66}^{(e)} & 0 \\ & & & & & & 1 \end{bmatrix} \tag{8.2.15}$$

$$S_{11}^{(e)} = S_{44}^{(e)} = \sqrt{\mu_0 \frac{q^{*2}}{m^*}} \qquad S_{33}^{(e)} = S_{66}^{(e)} = \frac{q^*}{\hbar}$$

where ones have been placed at the degrees of freedom corresponding to the "empty" degrees of freedom. This allows for the inversion of $\mathbf{S}_1^{(e)}$. Both scaling factors are constants over the domain of the superconductor and do not affect the assembled scaled master stiffness equations if this scaling is performed at the elemental level.

Second Scaling.

The second scaling is performed to make off diagonal elements of $\mathbf{K}$ of the same order of magnitude as the diagonal elements. It also serves the dual purpose of bringing steps in the $\mathbf{v}$-ζ hyperspace into a more reasonable range. The second scaling is essentially a conversion of units from one system to another. After performing the first scaling, the units of $\mathbf{v}$ are L^{-1} where L is measured in meters, the appropriate unit of length for the rationalized MKS system of measurement. However, most of the material parameters for a superconductor are of the order of about 10^{-8} meters. To make the order of magnitude of the off diagonal terms approximately the same as the diagonal terms, it was observed that on an element level this could be done by changing the units of length to micrometers (10^{-6} meters). To perform this conversion, all of the nodal positions, $r_i^{(e)}$ and $r_j^{(e)}$, are multiplied by 10^6. The permeability of free space has units of $M L/Q^2$ and is also multiplied by 10^6, whereas $\hbar$ has units of $M L^2/T$ and is multiplied by 10^{12}. The effective penetration depth λ_{eff} has units of L and is also multiplied by 10^6. These are the only quantities that are changed to perform the units conversion. The remaining material parameters α, β and $|\psi_\infty|^2$ are calculated using the new values for μ_o and λ_{eff} while the scaled value of $\hbar$ is used for calculating $\mathbf{S}_1$

and $K^{(e)}$. B has units of M/TQ and is not affected by this unit conversion, so scaled quantities can be used "as is" for field recovery.

Third Scaling.

The third scaling is performed on the assembled tangent stiffness matrix **K**. It is a simple diagonal scaling where nonzero elements of the diagonal matrix S_3 are equal to the square root of the absolute value of the corresponding diagonal element of **K**, *i.e.*, $S_{ii} = \sqrt{|K_{ii}|}$. For the "empty" degrees of freedom, the diagonal elements of S_3 are set to one to give full rank to the matrix so that it can be inverted. This is a common scaling technique that will reduce the condition number of a symmetric positive definite matrix. Although the constrained stiffness matrix for the superconductivity problem is negative definite, this technique works well here.

Fourth Scaling.

The fourth scaling is also performed on a global level. Again a diagonal matrix S_4 is used, but this time all of the elements are the same. The purpose of this scaling is to make $\Delta\zeta$ approximately equal to l_n. To meet this requirement, f must be approximately one. It is ensured with this requirement that no matter what the value of the product $\mathbf{w}^T\mathbf{w}$ may be, the scaled distance traversed along the equilibrium path will be approximately equal to the desired input distance l_n. The value for each element of S_4 that gave the best results for the STEP1D finite element numerical examples presented here was 10^4.

8.2.4 MESH GENERATION.

The superconductivity problem exhibits boundary layer characteristics because most of the physics occur in a relatively narrow region close to the conductor/free space boundary. The finite element mesh must have a fine grading in this region to model superconductivity accurately. Eighteen months of research and numerous numerical experiments have shown that if the mesh grading there is inappropriate, the solution generated will suffer accordingly. The problem most often encountered by poor mesh choices was that of a high condition number for $\mathbf{K}$. This generally causes the solution method to fail because the 2-norm of the residual vector $\mathbf{r}$ and the arclength constraint c cannot be brought below a reasonable value for the input tolerance τ. The solution "dances" around the $\mathbf{v} - \zeta$ hyperspace until the maximum number of corrector iterations is reached or the 2-norm of $\mathbf{v}$ is exceeded. In a few rare cases, with a poor mesh choice, the solution actually did converge. These solutions were rarely of any value because the condition number was estimated to be in the to range of 10^6 to 10^{16}! Another difficulty encountered with a poor mesh choice is that $|\psi|$ and A_z will oscillate around their equilibrium values. To solve these problems, it is necessary to reexamine the theory of superconductivity.

In the previous discussion of superconductivity, the effective London penetration depth λ_{eff} was introduced. The London penetration depth provides a measure of how far the $\mathbf{B}$ field penetrates into a superconductor from the conductor/free space interface. This is significant because λ_{eff} provides a minimum depth for the boundary layer that is being modeled. This is the

range over which A_z should decay to approximately zero. It is also necessary to know the range in which the other variable, $|\psi|$, decays from its bulk layer value of $|\psi_\infty|$ to zero. To accomplish this goal, the Ginzburg-Landau equations must be examined once again. The following is an abstraction of material presented in Reference[21], pp. 111-114, and is used to determine the range of decay of $|\psi|$.

The variation of ΔF_g for a one-dimensional superconductor in Cartesian coordinate space will produce the Euler equation

$$\frac{\hbar^2}{2m^*} \frac{\partial^2 |\psi|}{\partial x^2} + \alpha|\psi| - \beta|\psi|^3 = 0 \qquad (8.2.16)$$

where x is the one-dimensional spatial coordinate and $\mathbf{A}$ has been set equal to zero because we are primarily interested in the behavior of $|\psi|$. If the normalized wave function $|\psi|_N$ which equals $|\psi|/|\psi_\infty|$ is introduced, and some algebra is performed, Equation (8.2.16) becomes

$$\frac{\hbar^2}{2m^*\alpha} \frac{\partial^2 |\psi|_N}{\partial x^2} + |\psi|_N - |\psi|_N^3 = 0 \qquad (8.2.17)$$

Linearizing this equation by setting $|\psi|_N$ equal to $1 + b(x)$, where $b(x) \ll 1$, gives the first order expansion of this equation as being

$$\frac{\hbar^2}{2m^*\alpha} \frac{\partial^2 b(x)}{\partial x^2} = -(1 + b(x)) + (1 + 3b(x))$$

$$\frac{\partial^2 b(x)}{\partial x^2} = \frac{2m^*\alpha}{\hbar^2} b(x), \quad b(x) \sim \exp\left(\pm x\sqrt{2m^*\alpha/\hbar^2}\right) \qquad (8.2.18)$$

The first term of the equation shows that the decay of $|\psi|_N$ is determined by $\sqrt{\hbar^2/2m^*\alpha}$. This length is referred to as the Ginzburg-Landau coherence length $\xi(T)$. Appropriate substitutions from Chapter IV will give

$$\xi(T) = \frac{\hbar}{\sqrt{2}|q^*|} B_c^{-1}(0) \lambda_{eff}^{-1}(0) \left[\frac{1 + (T/T_c)^2}{1 - (T/T_c)^2}\right]^{\frac{1}{2}} \qquad (8.2.19)$$

To avoid confusion with the isoparametric coordinate ξ, this length shall always be referred to as $\xi(\mathcal{T})$. The dimensionless Ginzburg-Landau parameter $\kappa(\mathcal{T})$ is also introduced, which is the ratio of the two lengths $\xi(\mathcal{T})$ and $\lambda_{eff}(\mathcal{T})$.

$$\kappa(\mathcal{T}) = \frac{\lambda_{eff}(\mathcal{T})}{\xi(\mathcal{T})} = \frac{\sqrt{2}|q^*|}{\hbar} B_c(0)\lambda^2_{eff}(0) \left[1 + \left(\frac{\mathcal{T}}{\mathcal{T}_c}\right)^2\right]^{-1} \qquad (8.2.20)$$

where $\kappa(\mathcal{T})$ shall be used for this ratio to distinguish it from the Lagrange multiplier vector $\boldsymbol{\kappa}$. A superconductor with $\kappa(\mathcal{T}) < 1/\sqrt{2}$ is called a type I superconductor, while a superconductor with $\kappa(\mathcal{T}) > 1/\sqrt{2}$ is called a type II superconductor. Figure 8.1 shows the difference between $\xi(\mathcal{T})$ and λ_{eff} for type I and II superconductors.

For the particular case of high purity aluminum, $\kappa(0) \approx .1$. This makes it a type I superconductor and shows that the decay depth for $|\psi|$ is approximately ten times the decay depth of A_z, where λ_{eff} is the approximate decay depth for A_z. Consequently, the boundary layer region to be modeled must have a depth of at least $10 \times \lambda_{eff}$ to capture $|\psi|$, furthermore $\xi(\mathcal{T})$ determines the size of the boundary layer mesh. For a type II superconductor $\lambda_{eff}(\mathcal{T}) > \xi(\mathcal{T})$ and the size of the boundary mesh is determined by $\lambda_{eff}(\mathcal{T})$. Numerical experiments confirm that for aluminum the mesh choice of $10 \times \lambda_{eff}$ reduces the condition number of the system. Numerical experiments also show that the mesh generated must be a function of $\mathcal{T}$ because λ_{eff} and $\xi(\mathcal{T})$ are both functions of $\mathcal{T}$. The results obtained with the above mesh show realistic values for $|\psi|$, but both $|\psi|$ and A_z exhibit oscillatory behavior. Expanding the boundary layer depth to $200 \times \lambda_{eff}$ caused the oscillations in $|\psi|$ to disappear. All elements generated in the
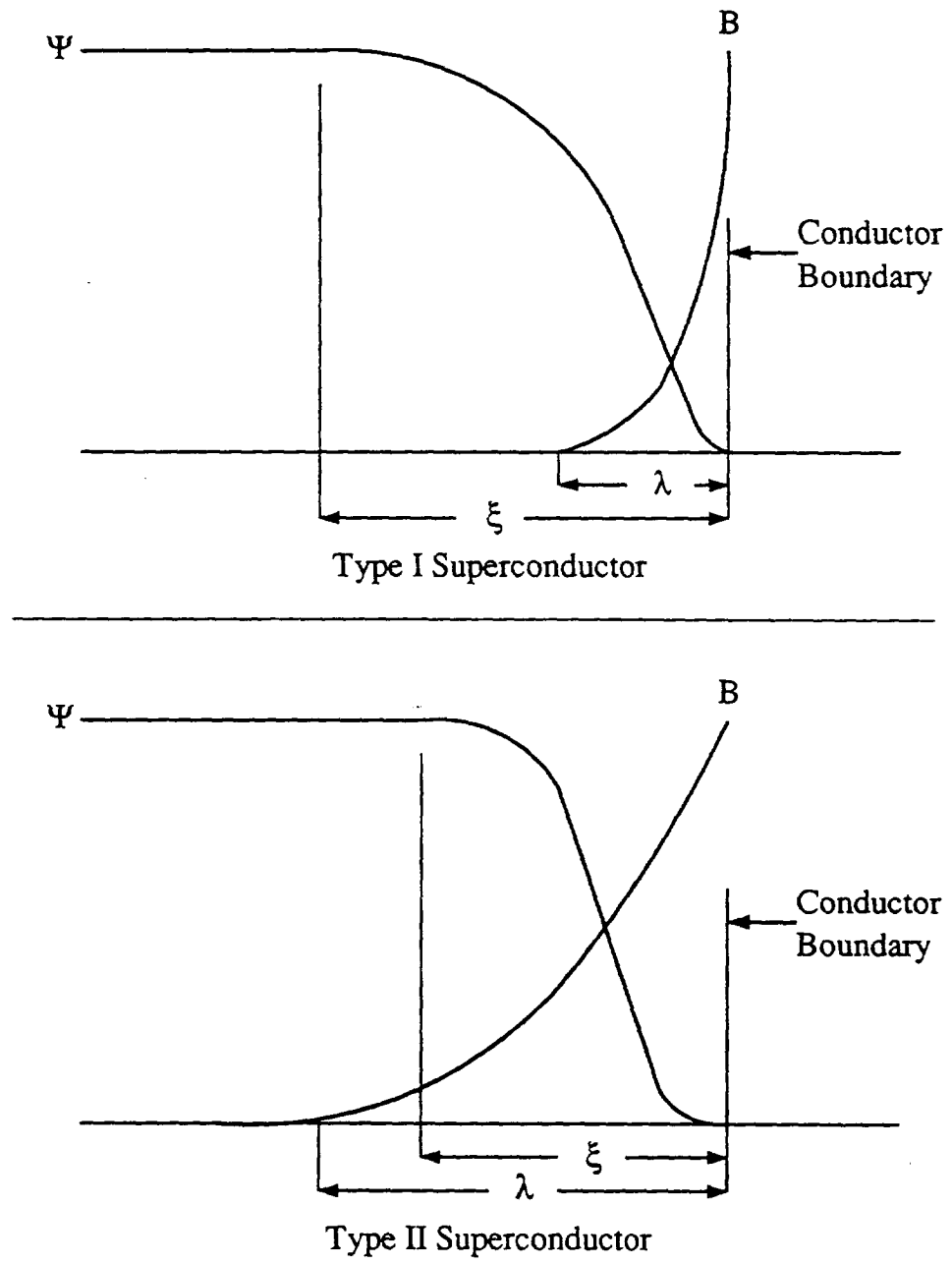
Figure 8.1: Differences between $\mathbf{B}$, ψ, $\xi(\mathcal{T})$ and λ_{eff} for type I and II super-conductors.

176

boundary layer were equal length elements, where the element length was equal to the depth of the boundary layer divided by the number of boundary layer elements N_{bound}. The elements used to model the bulk layer were also "regular", their length being equal to $(r_c - 200 \times \lambda_{eff}(T))/N_{bulk}$, with N_{bulk} representing the number of bulk layer elements.

The oscillations are triggered by three different error sources. The first one comes from the approximation that is made for (8.2.18). The Ginzburg-Landau equations are linearized there to get an idea of the penetration depth of the magnetic field. The coherence length is only a rough approximation to the true penetration depth and not an exact one because only the linearized system of equations has been solved and not the exact system. The second source of error arises because the finite element model is not exact. It merely tries to approximate the continuous case by discretizing the region of interest. The third source of error is that finite precision mathematics are used when a solution to the discretized superconductor is attempted. The solution procedure and the scaling procedures used all introduce numerical error into the computed solution because of the machine's inability to resolve numbers beyond 16 significant numbers. The expansion of the boundary layer helps to push the oscillations induced by the numerical error of the solution and scaling techniques below machine limits and more importantly, accurately captures the physics of the problem.

After the oscillations in $|\psi|$ are removed, A_z may still exhibit oscillations close to the conductor/free space boundary. It was thought that they were induced by the mesh being too coarse for that region. Numerical experiments showed that this was indeed the case. There are three methods that can be used to resolve this problem. The first method consists of generating

another boundary layer of regular elements near the conductor/free space boundary. The second method involves changing the length of each element so that the mesh is more finely graded at the conductor/free space boundary than at the interior edge of the boundary layer. The third method is to simply insert more elements into the boundary layer. All three methods add extra node points at the conductor/free space boundary and serve to make the finite element approximation more accurate. The third method was used for the examples here to expedite the research. This is the least computationally efficient of the three, but time constraints limited the author to using this choice.

It is mentioned earlier in Section 8.1.1 that the use of the same shape functions for the calculation of $|\psi|$ and A_z and their derivatives can lead to internal inconsistencies that can cause a "locking" problem. As the length of the element $l^{(e)}$ goes to zero, the polynomial shape function approximation of the independent variable tries to match the approximation of its first derivative, which is a constant, when 'locking" is present. This leads to the oscillatory behavior described above. But as more and more nodal points are added, $i.e.$, more finite elements are added, oscillations of the independent variable will still persist if "locking" is present. These oscillations disappear for the STEP1D finite element as the mesh is refined and show that "locking" is not present for the one-dimensional cases studied here.

To summarize, the depth of the boundary layer mesh is determined by the larger of λ_{eff} and $\xi(T)$. This is the starting point for determining the boundary layer depth. Numerical experiments are then used to expand the boundary layer until oscillations of $|\psi|$ disappear. Finally, additional

elements are inserted into the boundary layer until oscillations of A_z also vanish.

8.2.5 FIELD RECOVERY.

The primary quantity of interest is again **B**. For this problem, there is no analytical solution, but the results can be checked to determine if they are physically correct. There are also two methods by which **B** can be determined from the finite element solution. Comparison of the results of these two methods determines if an internally consistent solution has been reached.

The first method of determining the B_θ field is the finite element approximation of Equation(5.3.2). The second method uses Equation(3.2.16) inserted into Equatition (7.1.5). The one dimensional form of this equation that gives the value for B_θ at the outer node of each element e is

$$B_\theta{}^{(e)} = -\frac{\mu_o}{r_j^{(e)}} \sum_{n=1}^{e} \left\{ \int_{r_i^{(e)}}^{r_j^{(e)}} \left(\frac{q^{*2}}{m^*} |\Psi^{(n)}|^2 \mathcal{A}^{(n)} \right) r\,dr \right\} \qquad (8.2.21)$$

where the superscript letter in parentheses represents an element number. The integration over each element is performed by numerical quadrature using a two point Gauss rule.

8.2.6 TEST PROBLEM.

The test material used for this example was high purity aluminum. The material constants α and β for each element were evaluated at $\mathcal{T}$ equal to zero degrees Kelvin using the formulas of Section 4.4. The permeability μ of each element was set to μ_o as discussed earlier in this chapter. The reference state of **v** was set as described in Section 8.2.2. The mesh was discretized

as desribed in Section 8.2.4 with a regular mesh of N_{bulk} elements in the region $0 \geq r \geq r_c - 200\lambda_{eff}$. Another regular mesh of N_{bound} elements was generated in the region $r_c - 200\lambda_{eff} \geq r \geq r_c$. N_{bulk} and N_{bound} denote the number of elements in the bulk and boundary layers respectively. N_{bulk} and N_{bound} were 2 and 98 for this problem respectively. Because the free-space magnetic field element has been validated previously, all elements were within the conductor. The conductor radius r_c was 1.15×10^{-4}. The value of I_o was 5.0 amperes and the value of I_L was 0.0 amperes for the results presented here. The choice of these values ensures that an actual specified current loading for results presentation was attained. The element has been tested many times by loading from zero to full load and has worked extremely well. The only problem that was experienced was when the current loading appoached a magnitude that was large enough to move the solution close to the stationary point. In this region, Δv and $\Delta \zeta$ became increasingly smaller. To rectify this problem, the coding was modified to ensure that the step size at step $n + 1$ does not fall below an arbitrary value. If the step size became too small, $.9 \times l_n \times I_L$ was added to I_o, the reference state was reset, and the solution proccedure was restarted at step n. The only disadvantage to this scheme was determining the correct value of I at each step for output purposes. This problem was easily circumvented by outputting the value for I_o when it changed, and the step where the change took place.

The main disadvantage with using the incremental solution methods for results presentation was that the solution process did not always stop at the desired full load value, but usually exceed it by some fraction of the step size l_n. This is a consequence of the solution procedure used, and is inherent

in arclength schemes. By setting I_L equal to zero and I_o equal to I, this problem was bypassed here.

For the results presented below, the solution procedure required 9 iterations to converge, with the solution tolerance τ being 4×10^{-17}. The 2-norm for r did not include the value for the constrained degree of freedom of $|\psi|$. The value of r there ranged between 10^{-3} to 10^{-7} depending on how close the finite elements came to modeling a zero slope for $|\psi|$ at the conductor/free space boundary. To more accurately match this slope requirement, all that was needed was a more refined mesh for this area. However the results obtained were judged accurate enough for our purposes. Finally, the estimated condition number of the system was 228.

Figures 8.2 and 8.3 show the results obtained for the normalized values of $|\psi|^2$ plotted over the whole conductor and the boundary layer of the conductor respectively. If a London type superconductor had been modeled, an exact step function would have been expected. Because aluminum is an extreme type I superconductor, $|\psi|$ should exhibit behavior that is almost "step"-like. Figure 8.2 illustrates that the finite element does model physical behavior by returning values that closely match a step function. The boundary conditions are seen to match well in Figure 8.3 in that the slope of $|\psi_N|^2$ is zero at the interior boundary and is very close to zero at the exterior boundary.

Results for A_z are shown in Figures 8.4 and 8.5. Figure 8.4 shows the behavior over the whole mesh and Figure 8.5 the behavior in the boundary layer. The physical behavior of A_z should approximately be the opposite of $|\psi|$. Over the bulk of the conductor, A_z should be zero, and where $|\psi|$
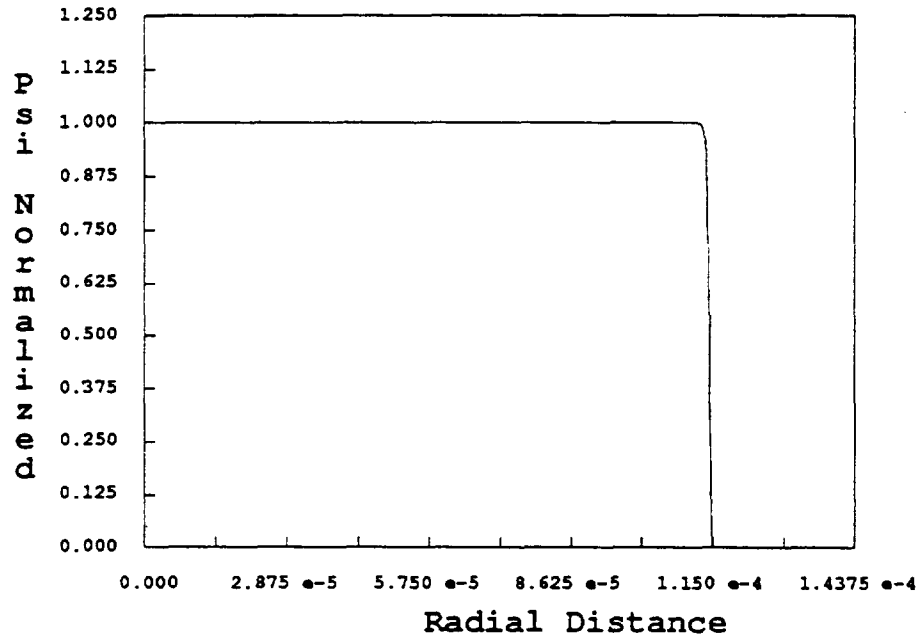
Figure 8.2: $|\psi|^2/|\psi_\infty|^2$ vs. r, values for complete mesh plotted.
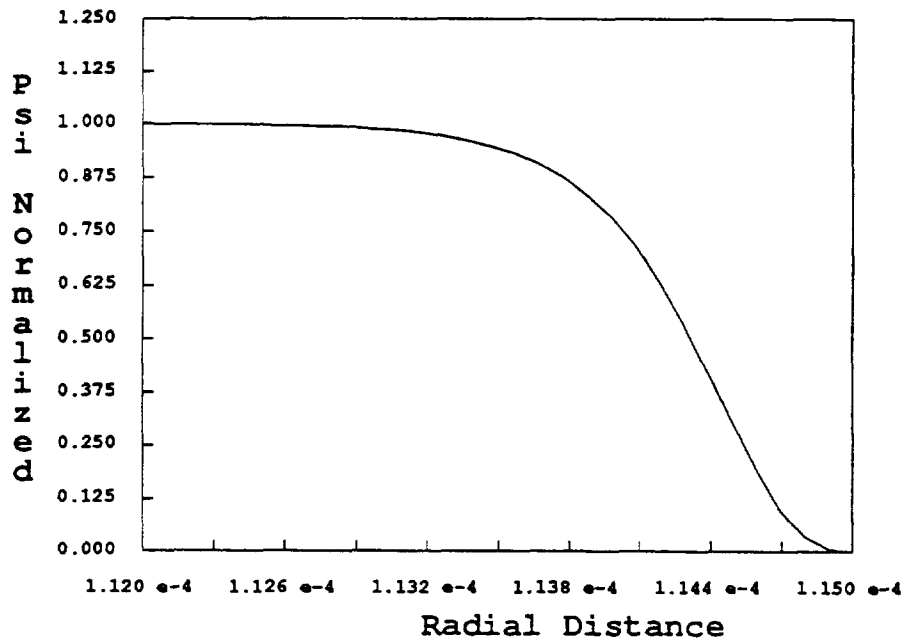
Figure 8.3: $|\psi|^2/|\psi_\infty|^2$ vs. r, values for boundary layer plotted.
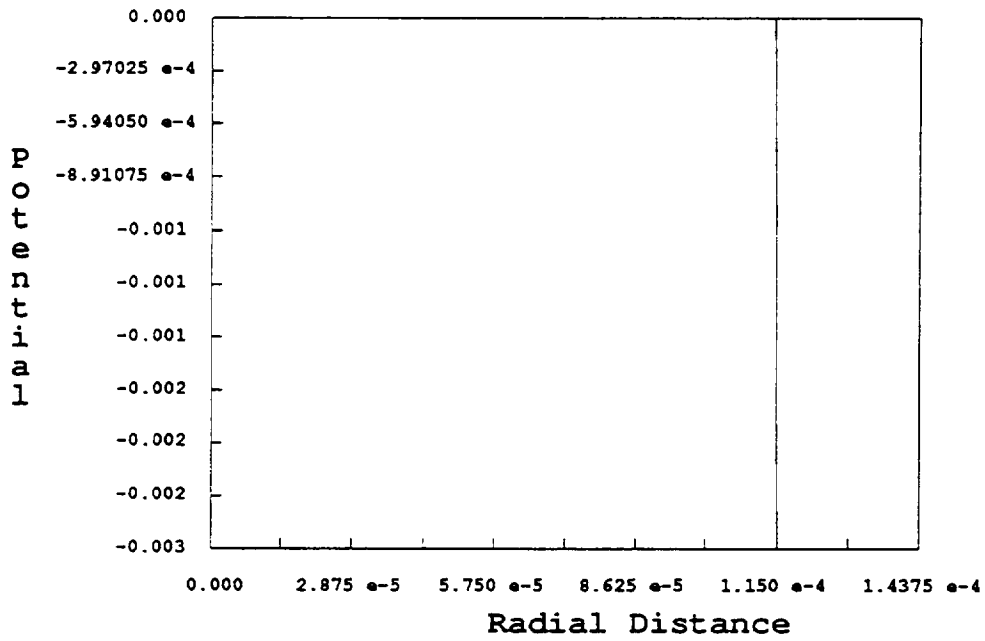
Figure 8.4: A_z vs. r, values for complete mesh plotted.
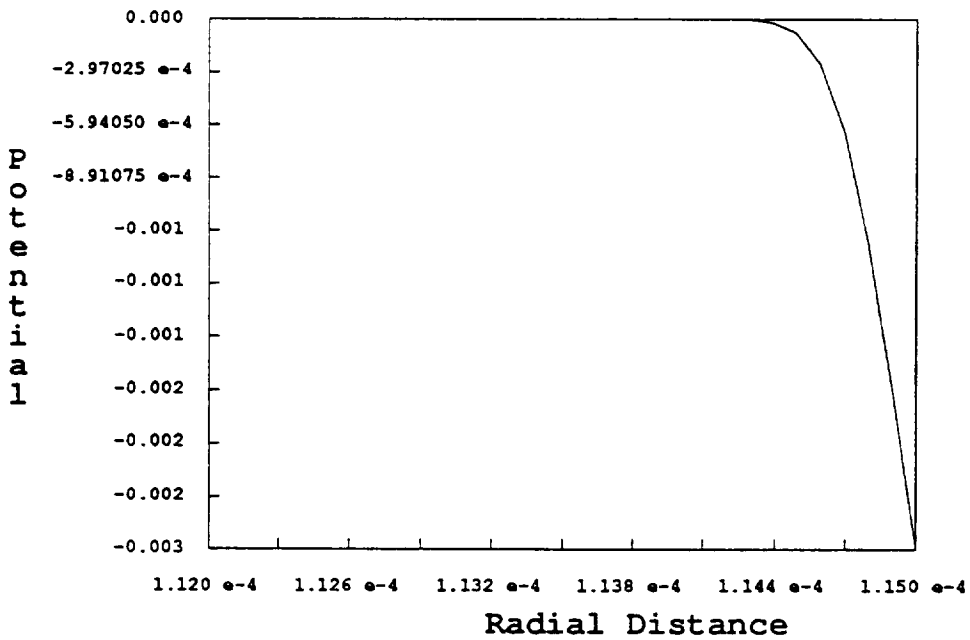
Figure 8.5: A_z vs. r, values for boundary layer plotted.

decreases, the magnitude of A_z should increase as kinetic momentum is exchanged for magnetic field momemtum. Figure 8.4 shows this expected physical behavior. Figure 8.5 shows this behavior in more detail, and illustrates one difference in behavior between A_z and $|\psi|$. The slope of A_z is zero at the interior edge of the boundary layer, but nonzero at the exterior edge. This is expected because the boundary conditions for A_z and $|\psi|$ are different at the exterior edge, the behavior of A_z matching its expected physical behavior.

Figures 8.6 and 8.7 display the results for j_z over the entire conductor and the boundary layer respectively. The behavior of j_z can best be described by making an analogy to a similar problem in fluid mechanics. The medium of the problem would be a large pool of water contained between two infinitely long straight walls. For convenience, the walls are aligned so that one is on our left side and the other on our right. To make the analogy correlate to the results presentation, the left wall would be the center of the superconductor, and the right wall would be the conductor/free space boundary. The bottom of the pool would be shaped so that the density of water molecules matches the density of the superconducting charge carriers. The walls and the bottom of the pool would present no resistance to water flow. Assuming laminar flow, a rapidly moving stream of water is injected into the pool along the right wall. For the EM problem, j_z is analogous to the velocity of the water molecules, v_w in the pool. Where the stream is injected, it is expected that a large, rapid change in v_w would exist, which upon first examination would appear to be a Dirac delta function.

This behavior is exactly matched by the velocities of the superconducting electron pairs of the finite element model, and is shown in Figure 8.6. At the conductor/free space boundary, a Dirac delta-like "spike" appears for
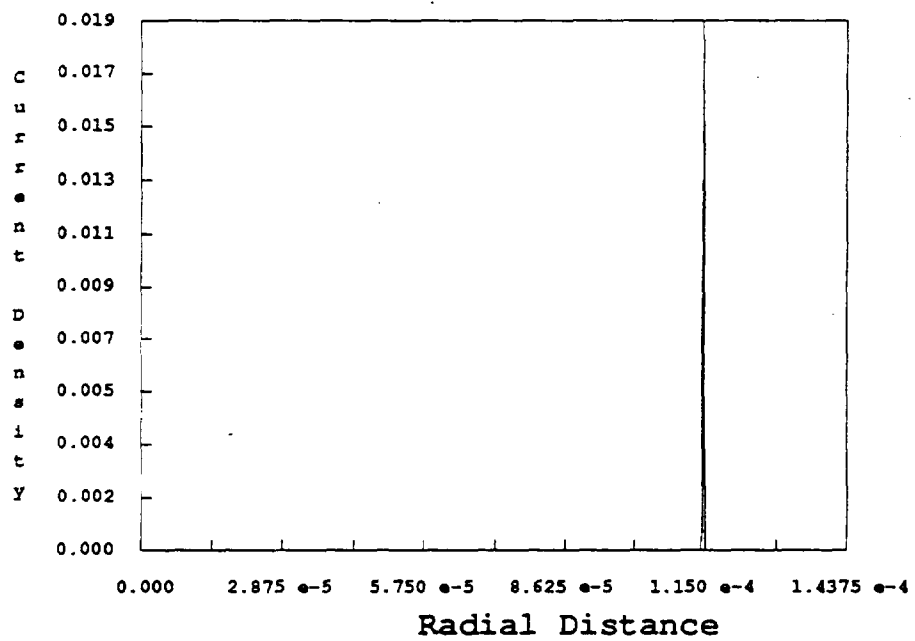
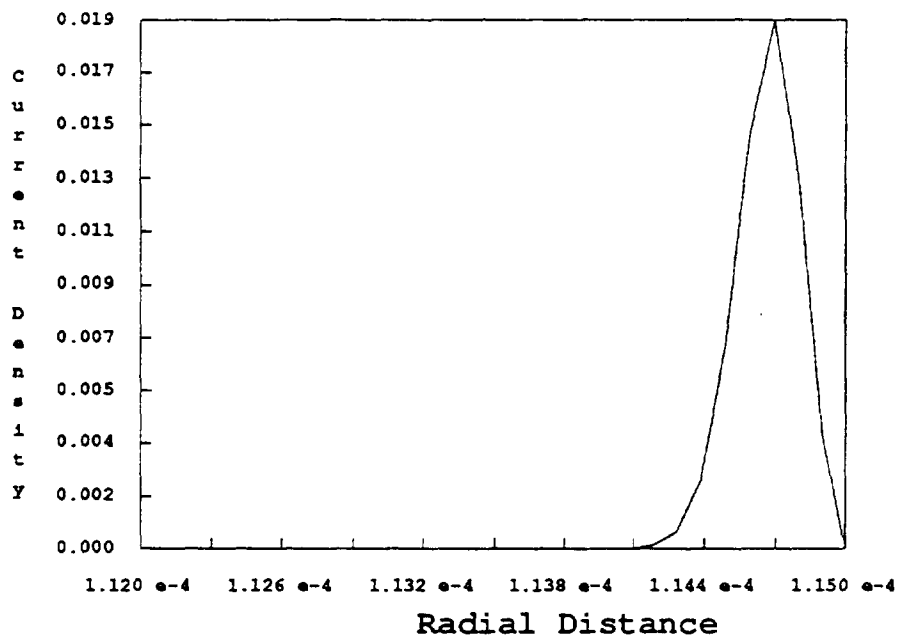Figure 8.6: j_z vs. r, values for complete mesh plotted.

Figure 8.7: j_z vs. r, values for boundary layer plotted.

j_z, which is zero otherwise. A closer examination of the fluid velocities for the imaginary example would reveal that v_w would rise rapidly on both sides of the stream, but a more gradual rise in v_w would occur on the side of the stream facing the left wall as momentum is exchanged with the other water molecules there. Again j_z mimics this behavior as shown in Figure 8.7 and validates the ability of the STEP1D element to model the expected physics of a superconductor.

This comparison of a fluid flow to a Ginzburg-Landau superconductor is a particularly enlightening one because, if this superconductivity model is correct, it explains the source of the miniscule resistivity in superconductors. The resistivity is a result of a momentum exchange produced by collisions of Cooper pairs, the supeconductor's charge carriers, as required by the residual equation (3.2.6). Because the collisions are relatively infrequent, a "spike" in the current density appears in the boundary layer, rather than a "smearing" of the current density to an approximate step function. The position of the spike is determined by the density of charge carriers, the current density vector choosing the point where the fewest collisions can take place. The fact that the density of Cooper pairs is higher on the interior of the boundary layer than the exterior explains why j_z changes more slowly towards the center of the conductor. The Cooper pairs in the current stream j_z are simply experiencing more collisions with stationary Cooper pairs because the density of pairs is higher towards the center of the conductor. Its position also determines that there is an expulsion of the B field from the interior of the conductor (the Meissner effect) because there is no current there to generate a field in accordance with Maxwell's equations.
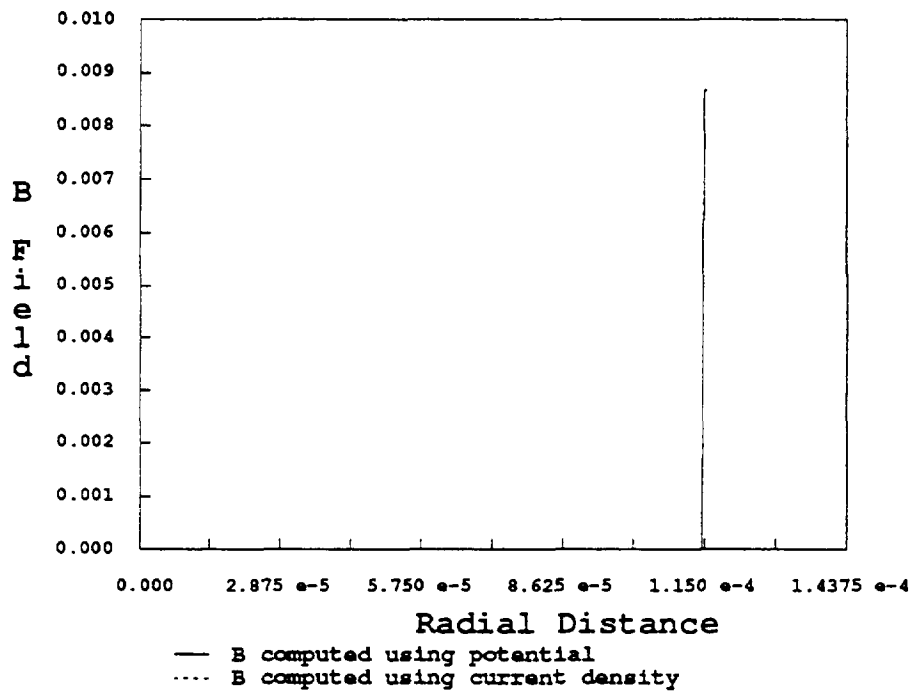
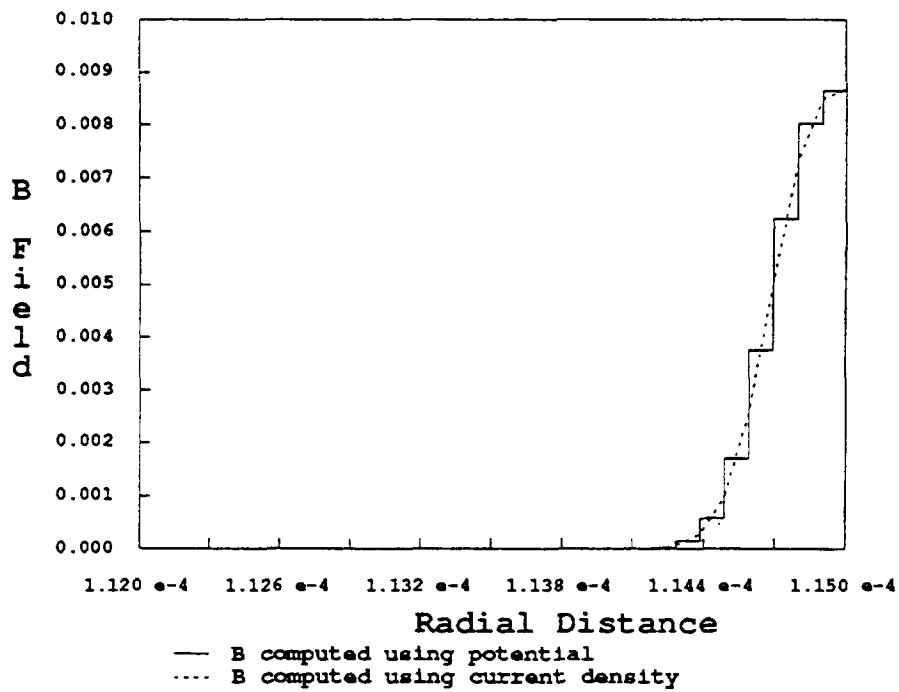Figure 8.8: B_θ vs. r, values for complete mesh plotted.

Figure 8.9: B_θ vs. r, values for boundary layer plotted.

187

Figures 8.8 and 8.9 show the B_θ field generated there. Figure 8.8 shows B_θ over the whole conductor and Figure 8.9 shows B_θ in the boundary region. Because no analytical solution is available, the **B** field has been plotted using the two different methods cited previously and finite element values for $|\psi|$ and A_z. As in Chapter VII, the B_θ field calculated using Equation (5.3.2) is plotted as a step function. Both sets of values match fairly well over most of the region, but show some divergence towards the maximum and minimum values of B_θ. No reason exists to prefer one set of values over the other, but using $j_z^{(e)}$ to recover B_θ has the advantage of being able to directly compute B_θ at element nodes.

Expected physical behavior is matched by both curves. The value of B_θ computed by using (8.2.21) also matches the necessary analytical value, derived from an integral form of Maxwell's equations, of $\mu_o I/2\pi r_c$. A comparison of these values with values obtained by using the London model of superconductivity does not allow any statement to be made about the accuracy of the Ginzburg-Landau model because the former neglects the gradient of $|\psi|$. The important point is that the Ginzburg-Landau model must achieve a specific magnitude at r_c, and this is verified by Equation (5.3.2). For the above reasons, the London values are not compared to the finite element values obtained here.

8.3 FURTHER DISCUSSION OF RESULTS.

A word of caution is necessary here with regard to the author's physical interpretation of results. Because no analytical solution is available for

comparison with the numerical results, these results and their physical interpretation must be treated with some suspicion pending experimental verification. However, there is a good evidence to suggest that the results are valid.

First, the numerical approach has been based upon the Ginzburg-Landau theory of superconductivity. This theory, while not being thoroughly validated experimentally for cases away from the critical temperature, has been able to predict superconducting phenomena with a great deal of accuracy (Ref. [21, pp.104-191]). This provides a great deal of credibilty to the ability of the Ginzburg-Landau theory for the prediction of EM and quantum phenomena within a superconductor. It is *universally accepted* as an accurate model of the macroscopic quantum-mechanical and electomagnetic properties of a superconductor near its critical temperature T_c.

Second, the results of this chapter and Chapter XI exhibit behavior that is in qualitative agreement with the physics of superconductors. These behaviors are the appearance of the Meissner effect and a current carried at the surface of a superconductor. The Meissner effect is the almost total expulsion of a magnetic field from the interior of a conductor, and this behavior is shown in Figures 8.8 and 11.12. The cause of this effect is that the current is carried at the surface of the conductor (Ref. [31, p.335]). In order to satisfy Maxwell's law $\nabla \times \nabla \times \mathbf{B} = \mathbf{j}$, no current can be carried within the bulk of the conductor or a magnetic field will be present there. Again, the STEP1D finite element shows this behavior in Figure 8.6.

Finally, there is some quantitative agreement between the STEP1D finite element and a known physical value. The value of the B_θ field at the

conductor radius is known to be $\mu_o I / 2\pi r_c$. As mentioned at the end of the previous section, the finite element model achieves this value at r_c.

8.4 SUMMARY.

In this chapter, a broad range of topics necessary to the solution of the superconductivity problem by the finite element method are discussed. The topics include the four-potential formulation of superconductivity, appropriate boundary conditions, nonlinear solution techniques, scaling techniques, and appropriate mesh choices for finite element models. The most important aspect of this research is the insight that is gained about superconductivity. For the Ginzburg-Landau model, it is possible to think of the current that moves through a superconductor as a "stream" of charge carriers called Cooper pairs that moves through a "sea" of static Cooper pairs. This "sea" acts like an extremely low viscosity fluid, and the "stream" moves through the region of the "sea" where the density of the Cooper pairs is the smallest. This region represents the place where the least amount of energy is expended by the collisions of moving Cooper pairs with stationary Cooper pairs. Unlike the London approximation, or linearized forms of the Ginzburg-Landau model, the physics of the system as described above are shown only by modeling the exact Ginzburg-Landau equations so that a complete description of j_z can be obtained. The STEP1D model shows this behavior well, and from the limited search of literature that the author has performed, it is believed that this is the first model that shows the physics in such good detail.

Now that reasonable models for the normal and superconducting states of a conductor have been developed, the next step in the complete

modeling of a conductor is to add thermal effects. This is the topic of discussion of the next chapter.

THE THERMAL PROBLEM

It is first necessary to model the temperature distribution within a conductor before the effects a temperature field has on the EM fields and the quantum properties of a conductor can be determined. Appropriately, the first topic of discussion in this chapter is the modeling of the temperature field of the steady state heat conduction problem with convection cooling boundary conditions. The one-dimensional case is the case of interest for this work's examples and is the only case discussed. In Chapter IV it is mentioned that there are no temperature gradients within a one-dimensional steady state superconductor. Because no gradients are present, the temperature distribution of a superconductor is known and the calculation of the temperature distribution by finite element methods is not necessary. Therefore, this chapter is concerned with the finite element modeling of a *normal* conductor. The temperature distribution within a conductor is a function of the current I and the thermal boundary conditions at r_c. In the current chapter, it is assumed that the current I is steady and does not change. Cases where the current load I changes are discussed in the following chapter. For this chapter, the discussion is about the physics of a conductor as the thermal boundary loads are varied.

The discussion begins by first developing the finite element model for the temperature distribution of a one-dimensional conductor, and then determining the analytical solution of that problem. The analytical solution

to this problem is developed later because certain assumptions about the
finite element model have a direct effect on the analytical solution.

9.1 FINITE ELEMENT DISCRETIZATION.

9.1.1 CONSTRUCTING THE LINT1D FINITE ELEMENT.

Using the two-node "line" finite element again provides the C^o continuity required by the variational functional of (4.1.7) for $\mathcal{T}$. Again individual elements and elemental properties are identified by the superscript (e). The two element end nodes are denoted by the subscripts i and j. The temperature $\mathcal{T}$ is interpolated over each element as

$$\mathcal{T} = \mathbf{N}\underline{\mathcal{T}}^{(e)} \tag{9.1.1}$$

where the row vector $\mathbf{N}$ contains isoparametric shape functions for the interpolation of $\mathcal{T}$. The elements of $\mathbf{N}$ are functions only of the spatial coordinate r. The column vector $\underline{\mathcal{T}}^{(e)}$ contains the nodal values of $\mathcal{T}$, which are constants with respect to time. Substitution of these finite element assumptions into the variational functional of Equation (4.1.7) gives

$$\Omega_d^{(e)} = \int_{V^{(e)}} dV^{(e)} \left\{ \frac{k}{2}\underline{\mathcal{T}}^{(e)T} \frac{\partial \mathbf{N}^T}{\partial r} \frac{\partial \mathbf{N}}{\partial r}\underline{\mathcal{T}}^{(e)} - \omega^{(e)} j_z^{(e)2}\underline{\mathcal{T}}^{(e)T}\mathbf{N}^T \right\}$$
$$- \int_{\Gamma_2^{(e)}} d\Gamma_2^{(e)} \left\{ r\, Q_r \underline{\mathcal{T}}^{(e)T}\mathbf{N}^T \right\} \bigg|_{r_i^{(e)}}^{r_j^{(e)}} \tag{9.1.2}$$

Variation of the above with respect to $\underline{\mathcal{T}}^{(e)}$ will produce

$$\delta\Omega_d^{(e)} = \int_{V^{(e)}} dV^{(e)} \delta\underline{\mathcal{T}}^{(e)T} \left\{ k\frac{\partial \mathbf{N}^T}{\partial r} \frac{\partial \mathbf{N}}{\partial r}\underline{\mathcal{T}}^{(e)} - \omega^{(e)} j_z^{(e)2}\mathbf{N}^T \right\}$$
$$- \int_{\Gamma_2^{(e)}} d\Gamma_2^{(e)} \delta\underline{\mathcal{T}}^{(e)T} \left\{ r\, Q_r \mathbf{N}^T \right\} \bigg|_{r_i^{(e)}}^{r_j^{(e)}} \tag{9.1.3}$$

Quantities k and $\omega^{(e)}$ are functions of the spatial coordinate r and *not* of the independent variable T. This assumption is made because the variational functional $\Omega_d^{(e)}$ does not give the correct residuals for the heat conduction problem if the thermal conductivity and the electrical resistivity are allowed to be functions of T. This approximation can be corrected by using the nonlinear solution procedures of Chapter VIII. During the solution phase, k and $\omega^{(e)}$ are held constant at their values for step n, and after the solution vector $\mathbf{v}$ at step $n + 1$ is determined, k and $\omega^{(e)}$ are updated using the new temperature distribution of step $n + 1$. If the step size l_n is small, $\mathbf{v}$ does not move too far from the true equilibrium path and the values of $\underline{T}^{(e)}$ are close enough to the exact values that any error is negligible. This assumption is the reason for discussing the finite element model first instead of the analytical solution. No analytical solution exists for the set of coupled EM-thermal equations where k and ω are functions of T. By making the approximation that k and ω are functions of the spatial coordinate r, an analytical solution can be developed.

The spatial approximations used are the ones discussed in previous chapters, *i.e.*, ω is a step function or constant over an element, and k is interpolated linearly across the element. In terms of our shape functions, k may be written as

$$k = \mathbf{N}\mathbf{k}^{(e)} \qquad (9.1.4)$$

where $\mathbf{k}^{(e)}$ contains the nodal values of the thermal conductivity. The values for $\mathbf{k}^{(e)}$ are obtained by using Equation (4.2.1). Equation (4.2.1) is a function of T, and is evaluated at $T_i^{(e)}$ and $T_j^{(e)}$ to obtain the respective components of $\mathbf{k}^{(e)}$, $k_i^{(e)}$ and $k_j^{(e)}$. For the evaluation of $\mathbf{k}^{(e)}$ and $\omega^{(e)}$, $T_i^{(e)}$ and $T_j^{(e)}$

are the two components of $\underline{T}^{(e)}$ at step n. The elemental value for $\omega^{(e)}$ is determined by the formula

$$\omega^{(e)} = \omega_o + \tfrac{1}{2}\left(\omega_i(T_i^{(e)}) + \omega_i(T_j^{(e)})\right) \qquad (9.1.5)$$

where ω_o is the residual resistivity, and $\omega_i(T)$ is the ideal resistivity. The ideal resistivity is calculated as described in Section 4.3.

All but two of the boundary integrals of (9.1.3) can be ignored by noticing that the heat flux Q_r between interelement boundaries in the radial direction must be C^o continuous; this point is shown later by the analytical solution. The two remaining boundary integrals occur at r equal to zero and r_c. At r equal to zero, it can be seen that the boundary integral there vanishes, and the only remaining boundary integral occurs at r_c. The remaining integral is a function of the boundary heat flux loading where $Q_r(\zeta^T)$ represents this load and ζ^T is the thermal loading paramter.

Because non-linear solution techniques are used, expressions for $\mathbf{K}^{(e)}$, $\mathbf{f}^{(e)}$, $\mathbf{r}^{(e)}$, $\mathbf{p}^{(e)}$ and $\mathbf{q}^{(e)}$ must be determined. The Euler equations of (9.1.3) give the following expressions for $\mathbf{r}^{(e)}$, $\mathbf{p}^{(e)}$ and $\mathbf{f}^{(e)}$

$$\mathbf{f}^{(e)} = \int_{V^{(e)}} dV^{(e)} \left\{ k\frac{\partial \mathbf{N}^T}{\partial r}\frac{\partial \mathbf{N}}{\partial r}\underline{T}^{(e)} \right\}$$

$$\mathbf{p}^{(e)} = \int_{V^{(e)}} dV^{(e)} \left\{ \omega^{(e)} j_z^{(e)^2} \mathbf{N}^T \right\} + \delta_{me} \left\{ 2\pi r_c Q_r(\zeta^T) \right\}\bigg|_{r_c} \left\{ \begin{matrix} 0 \\ 1 \end{matrix} \right\} \qquad (9.1.6)$$

$$\mathbf{r}^{(e)} = \mathbf{f}^{(e)} - \mathbf{p}^{(e)}$$

where the Kronecker delta δ_{ij} is defined as

$$\begin{aligned} \delta_{ij} &= 0 \qquad i \neq j \\ &= 1 \qquad i = j \end{aligned} \qquad (9.1.7)$$

$1 m = N_{wire} + 1$, with N_{wire} again representing the number of elements in the conductor. Taking the partials of $\mathbf{r}$ with respect to $\underline{T}^{(e)}$ and ζ^T produces the following expressions for $\mathbf{K}^{(e)}$ and $\mathbf{q}^{(e)}$.

$$\mathbf{K}^{(e)} = \int_{V^{(e)}} dV^{(e)} \left\{ k \frac{\partial \mathbf{N}^T}{\partial r} \frac{\partial \mathbf{N}}{\partial r} \right\}$$

$$\mathbf{q}^{(e)} = \delta_{me} \left\{ 2\pi r_c \frac{\partial Q_r(\zeta^T)}{\partial \zeta^T} \right\} \bigg|_{r_c} \left\{ \begin{matrix} 0 \\ 1 \end{matrix} \right\}$$

(9.1.8)

where $j_z^{(e)}$ and $\omega^{(e)}$ have been assumed to be only functions of the nodal position r and therefore vanish.

9.1.2 APPLYING BOUNDARY CONDITIONS.

In the previous section, expressions for $\mathbf{p}^{(e)}$ and $\mathbf{q}^{(e)}$ are determined. They contain the boundary heat flux term $Q_r(\zeta^T)$. The heat flux at r_c for the one-dimensional steady state convection cooling problem is expressed by the Euler equation of (4.1.10)

$$Q_r = h_{conv} \left(T_\infty - T(r_c) \right) \tag{9.1.9}$$

Because the free stream temperature T_∞ is known, it is natural to choose this variable as the load to be varied. To make T_∞ a variable load, it is split into two parts where T_o is the initial loading temperature, and T_L is the variable loading temperature. The free stream temperature is now expressed as

$$T_\infty = T_o + \zeta^T T_L \tag{9.1.10}$$

The value of the temperature at r equal to r_c can also be expressed as

$$T(r_c) = N_j T_j^{(m)} \bigg|_{r_c} = T_j^{(m)}; \qquad m = N_{wire} + 1 \tag{9.1.11}$$

196

where N_j is the second component of the shape function vector $\mathbf{N}$, $T_j^{(m)}$ is the nodal value of the temperature at r_c, and the superscript letter in parentheses represents an element number and not an exponential. When the new expressions for T_∞ and $T(r_c)$ are substituted into (9.1.9), the expression for $Q_r(\zeta^T)$ becomes

$$Q_r(\zeta^T) = h_{conv}\left(T_o + \zeta^T T_{\mathrm{L}} - T_j^{(m)}\right) \tag{9.1.12}$$

and the expression for $\partial Q_r(\zeta^T)/\partial\zeta^T$ is

$$\frac{\partial Q_r(\zeta^T)}{\partial\zeta^T} \;=\; h_{conv}\left(T_{\mathrm{L}} - \frac{\partial T_j^{(m)}}{\partial\zeta^T}\right) \;=\; h_{conv}\left(T_{\mathrm{L}} - w_j^{(m)}\right) \tag{9.1.13}$$

where $w_j^{(m)}$ is the nodal value of the incremental rate of change of T at r_c.

By convention, any terms of a set of finite element equations that include the incremental rates and the nodal displacements are usually moved to the left hand side of the system of equations. Doing this, and making substitutions for $Q_r(\zeta^T)$ in the previously derived vectors $\mathbf{p}^{(e)}$ and $\mathbf{f}^{(e)}$ gives

$$\mathbf{f}^{(e)} = \int_{V^{(e)}} dV^{(e)} \left\{ k\frac{\partial\mathbf{N}^T}{\partial r}\frac{\partial\mathbf{N}}{\partial r}\mathcal{T}^{(e)} \right\} + \delta_{me}\left\{2\pi r_c\right\}\begin{bmatrix} 0 & 0 \\ 0 & 1 \end{bmatrix}\underline{\mathcal{T}}^{(e)}$$

$$\mathbf{p}^{(e)} = \int_{V^{(e)}} dV^{(e)} \left\{ \omega^{(e)} j_z^{(e)^2}\mathbf{N}^T \right\} + \delta_{me}\left\{2\pi r_c h_{conv}\left(T_o + \zeta^T T_{\mathrm{L}}\right)\right\}\begin{Bmatrix} 0 \\ 1 \end{Bmatrix} \tag{9.1.14}$$

Similarly, $\mathbf{K}^{(e)}$ and $\mathbf{q}^{(e)}$ are

$$\mathbf{K}^{(e)} = \int_{V^{(e)}} dV^{(e)} \left\{ k\frac{\partial\mathbf{N}^T}{\partial r}\frac{\partial\mathbf{N}}{\partial r} \right\} + \delta_{me}\left\{2\pi r_c\right\}\begin{bmatrix} 0 & 0 \\ 0 & 1 \end{bmatrix}$$

$$\mathbf{q}^{(e)} = \delta_{me}\left\{2\pi r_c h_{conv} T_{\mathrm{L}}\right\}\begin{Bmatrix} 0 \\ 1 \end{Bmatrix} \tag{9.1.15}$$

The addition of the boundary term Q_r makes this system of equations, when assembled, determinate and no nodal values need to be constrained.

9.2 ANALYICAL SOLUTION TO THE TEST PROBLEM.

Equation (4.1.14) states that the temperature distribution for a linearly interpolated k and step function ω and j_z may be expressed as

$$T = \frac{\omega j_z^2}{2}\left(\frac{r\Delta r}{\Delta k} - \frac{k_i\Delta r^2}{\Delta k^2}\ln\left(k_i + \frac{\Delta k}{\Delta r}r\right)\right) + C_1\frac{1}{k_i}\ln\left(\frac{r\Delta r}{k_i\Delta r + \Delta k}\right) + C_2$$

$$(9.2.1)$$

where C_1 and C_2 are integration constants and

$$k = k_i + \frac{k_j - k_i}{r_j - r_i}r = k_i + \frac{\Delta k}{\Delta r}r \qquad (9.2.2)$$

where k_i and k_j are the values of k at the inner and outer boundaries of integration respectively. To adapt this solution for each element, the integration constants C_1 and C_2 are first replaced by the constants $C^{(e)}_{\text{odd}}$ and $C^{(e)}_{\text{even}}$ where the superscript (e) represents an individual element number again. For notational convenience, the following equalities are also defined: $a^{(e)} = k_i^{(e)}$, $b^{(e)} = \Delta k/\Delta r$ and $\dot{q}^{(e)} = -\omega^{(e)}j_z^{(e)^2}$. The function $ft^{(e)}$ is also defined as

$$ft^{(e)}(r) = \frac{\dot{q}^{(e)}}{2b^{(e)}}\left(\frac{a^{(e)}}{b^{(e)}}\ln(k) - r\right) + \frac{C^{(e)}_{\text{odd}}}{a^{(e)}}\ln\left(\frac{r}{k}\right) \qquad (9.2.3)$$

Using the new notation, the temperature T over each element is expressed as

$$T^{(e)}(r) = ft^{(e)}(r) + C^{(e)}_{\text{even}} \qquad (9.2.4)$$

Using a little physics, it can be seen that the heat flux out of an element *must* equal the heat flux into adjacent elements because the system is conservative and energy *must* be conserved. This requires that the heat

flux Q_r be C^o continuous and gives the following series of equations that relate the heat flux transferred across adjacent element boundaries

$$\frac{C^{(e)}_{odd}}{r^{(e)}_i} - \frac{\dot{q}^{(e)}r^{(e)}_i}{2} = \frac{C^{(e-1)}_{odd}}{r^{(e-1)}_j} - \frac{\dot{q}^{(e-1)}r^{(e-1)}_j}{2} \qquad (9.2.5)$$

This equation can be rearranged to give

$$C^{(e)}_{odd} = \frac{\dot{q}^{(e)}r^{(e)2}_i}{2} + C^{(e-1)}_{odd} - \frac{\dot{q}^{(e-1)}r^{(e-1)2}_j}{2} \qquad (9.2.6)$$

by using the relation $r^{(e-1)}_j = r^{(e)}_i$. At r equal to zero, $C^{(1)}_{odd}$ must also be zero for the system of equations to remain bounded. This gives for $C^{(e)}_{odd}$

$$\begin{aligned} C^{(e)}_{odd} &= \frac{\dot{q}^{(e)}r^{(e)2}_i}{2} - \sum_{p=1}^{(e-1)} \left\{ \frac{\dot{q}^p}{2} \left(r^{p2}_i - r^{p2}_j \right) \right\} & e > 1 \\ &= 0 & e = 1 \end{aligned} \qquad (9.2.7)$$

The values for $C^{(e)}_{even}$ may be derived in a similar manner by ensuring that T is C^o continuous across element boundaries. The result is

$$C^{(e)}_{even} = T_s - ft^{(e)}(r^{(e)}_i) - \sum_{p=e}^{N_{wire}} \left\{ ft^p(r^p_j) - ft^p(r^p_i) \right\} \qquad (9.2.8)$$

where T_s is the temperature at the surface of the conductor and equals the nodal value $T^{(m)}_j$. T_s is determined by using the discretized version of Equation (4.1.21), which is

$$T_s = T_0 + \zeta^T T_L + \frac{1}{h_{conv}r_c} \sum_{e=1}^{N_{wire}} \left\{ \int_{r^{(e)}_i}^{r^{(e)}_j} \omega^{(e)}j^{(e)2}_z r\,dr \right\} \qquad (9.2.9)$$

The preceding analytical solution is only valid for cases where $b^{(e)}$ is nonzero. As $k^{(e)}_i$ approaches $k^{(e)}_j$, the first two terms of (9.2.3) diverge. For

cases where $b^{(e)}$ is zero, the methodology used to derive (9.2.1) in Chapter IV can be used to determine that $ft^{(e)}(r)$ becomes

$$ft^{(e)}(r) = -\frac{\dot{q}^{(e)}}{4}r^2 + C^{(e)}_{\text{odd}}\ln(r) \qquad (9.2.10)$$

The methods of this section can then be used to show that the solutions for T_s, $C^{(e)}_{\text{odd}}$, and $C^{(e)}_{\text{even}}$ are identical to those of Equations (9.2.7), (9.2.8) and (9.2.9).

The above solutions to the heat conduction problem were originally loaded into a Fortran subroutine and solutions to the example problem were computed. For the example problem and material values used, it was found that incorrect solutions were being determined. One source of error was that the magnitude of the first two terms of (9.2.3) were much greater than the last term. Finite precision numerics caused the last term to be virtually ignored when determining $C^{(e)}_{\text{even}}$ and $ft^{(e)}(r)$ although this term should have made a noticeable contribution to both. All of the formulas were rearranged so that $C^{(e)}_{\text{even}}$ and $ft^{(e)}(r)$ were computed in a term by term manner, i.e., first all of the $\ln(k)$ terms were computed, then all of the $\ln(r/k)$ terms, etc.. This improved the solution marginally, and the problem was examined further. The largest source of error came from the finite precision mathematics again. The term $b^{(e)}$ was seen to be extremely small and caused the first two terms of (9.2.3) to diverge. Although the divergence of individual terms should cancel when summed during the computation of $C^{(e)}_{\text{even}}$, it was beyond the machine's capability to resolve the minute differences between the large individual terms. False zero values or random values were being assigned for the difference by the machine. To correct this problem, when the absolute value of the percentage difference between $k_i^{(e)}$ and $k_j^{(e)}$ dropped

below 2.2×10^{-9}, k was assumed constant over an element. The value of $k_j^{(e)}$ was then used for the elemental value of k, and Equation (9.2.10) was used to calculate $ft^{(e)}(r)$ and $C^{(e)}_{\text{even}}$.

The numerical results became much better, and both of the above corrective procedures are implemented in existing coding. Results presented in this work as the analytical solution to thermal problems used the above methods to control numerical errors.

9.3 NUMERICAL EXPERIMENTS.

9.3.1 THE FINITE ELEMENT MODEL.

The finite element model derived in the previous section has been applied to the test problem described later in this section. The LET1D finite element is used for determining EM quantities and the LINT1D element is used to determine the temperature distribution. Both of these elements are treated as one-dimensional axisymmetric elements. The LET1D element is identical to the CUPLE1D element except that $\omega^{(e)}$ is allowed to change during the solution process. The description of the nodal degrees of freedom and the variables associated with each degree of freedom for the CUPLE1D element can be found at the beginning of Section 7.3.1. The permeability $\mu^{(e)}$, the resistivity $\omega^{(e)}$ and the current density $j_z^{(e)}$ are uniform over each element.

For the LINT1D element, the "line" type element has only two end nodes which are defined by their axial positions $r_i^{(e)}$ and $r_j^{(e)}$. They each have one degree of freedom corresponding to the temperature T which results in a total of two degrees of freedom per element. These nodal values are

determined by interpolation with standard linear shape functions that provide the C^o continuity required by the variational formulation. The thermal conductivity of each element is also calculated by interpolation with standard linear shape function where the nodal values of k are determined by the nodal temperatures at step n and use of Equation (4.2.1). The resistivity of each element, for both the LET1D and the LINT1D elements, is calculated by using Equation (4.3.1) and the nodal temperature values at step n to determine ω at each node, and then taking the mean of the two ω's. The value of $j_z^{(e)}$ for the LINT1D elements is determined by use of the LET1D finite element.

9.3.2 APPLYING BOUNDARY CONDITIONS.

As shown earlier, no nodes are constrained for the thermal part of this problem. The thermal flux terms that contain the Kronecker delta are directly injected at their appropriate positions when assembling $\mathbf{f}^{(e)}$, $\mathbf{p}^{(e)}$, $\mathbf{r}^{(e)}$, $\mathbf{K}^{(e)}$ and $\mathbf{q}^{(e)}$ to account for boundary conditions. The electromagnetic boundary conditions are set as described in Section 7.3.2.

9.3.3 ASSEMBLY AND SOLUTION.

Both tangent stiffness matrices $\mathbf{K}^{EM}$ and $\mathbf{K}^T$ are assembled in an element by element fashion following standard finite element techniques. $\mathbf{K}^{EM}$ and $\mathbf{K}^T$ are used here to represent the master electromagnetic and master thermal tangent stiffness matrices respectively. The superscripts EM and T are also used in the sequel to distinguish between assembled electromagnetic and thermal vector quantities (*e.g.*, $\mathbf{v}^{EM}$ is the electromagnetic solution vector). $\mathbf{K}^{EM}$ is stored in a symmetric skyline form and $\mathbf{K}^T$ is stored as three

vectors because it is a tridiagonal matrix. Systems of electromagnetic equations are modified for boundary conditions as described in Section 7.3.2 and are processed by a standard symmetric skyline solver. After the solution procedure that is described later has been used, $\mathbf{v}^{EM}$ provides the desired nodal values of A_z for field recovery and the elemental values of j_z for calculation of the electromagnetic heating loads of the heat conduction problem.

Systems of thermal equations are modified for boundary conditions, as discussed in the preceding section, and are then processed by a standard tridiagonal solver. The solution procedure then returns $\mathbf{v}^T$ which contains nodal values of $\mathcal{T}$.

Solution Technique

Because the values for k and $\omega^{(e)}$ are actually functions of the temperature $\mathcal{T}$ and not the spatial coordinate r, the LINT1D finite element is nonlinear, and the nonlinear solution techniques of Section 8.2.2 are used to solve problems. These techniques work well for thermal problems if the rate of change of temperature across an element is not too large.

The solution procedure is started by choosing a reference state for $\mathcal{T}$. The reference state chosen for the examples of this work is set by initializing $\mathbf{v}^T$ to $\mathcal{T}_o$ and $\mathbf{v}^{EM}$ to zero. For cases where $\mathcal{T}_o$ is not sufficiently close to the equilibrium path, the reference state may be chosen by use of Equation (4.1.22). For the latter case, the thermal conductivity and electrical resistivity are evaluated as constants over the whole domain of the conductor and evaluated at some mean representative temperature such as $\mathcal{T}_o$. The current density becomes a constant with these assumptions and is equal to $I/\pi r_c^2$.

To advance the solution to the next step, the set of incremental rate equations

$$K_n w_n = q_n \qquad (9.3.1)$$

is solved. This system can be written as

$$\begin{bmatrix} K_n^{EM} & 0 \\ 0 & K_n^{T} \end{bmatrix} \begin{Bmatrix} w_n^{EM} \\ w_n^{T} \end{Bmatrix} = \begin{Bmatrix} q_n^{EM} \\ q_n^{T} \end{Bmatrix} \qquad (9.3.2)$$

where the subscript n represents the current step number. The solution vector v_n is equal to $\langle v_n^{EM} \quad v_n^{T} \rangle^{T}$. The rest of the solution procedure is identical to the procedure outlined in Section 8.2.2. except that K, r, f and p at step $n + 1$ are calculated by using the values of $\mathcal{T}$ and $j_z^{(e)}$ from the previous step n. The solution must be calculated in this manner because the variational formulation assumes that k, ω and j_z are all functions of the spatial coordinates and not the independent variable $\mathcal{T}$. This device holds the material properties and j_z constant for K, r, f and p so that a new temperature distribution at step $n + 1$ can be determined. This means that the solution procedure is not solving the correct set of equations for the true equilibrium path of the heat conduction problem.

Unfortunately, this is the current level of advancement of heat conduction analysis. To solve this problem, a relatively small step size l_n is taken. This "fix" allows the computed solution to remain close to the correct equilibrium path. This problem can also be corrected by holding $\zeta^{\mathcal{T}}$ constant and taking several steps. The result is that the quantities K, r, f and p are all updated until the correct equilibrium path is reached. For the examples presented here, the last "fix" was not required as taking a small step size l_n brought the solution sufficiently close to the true equilibrium path.

9.3.4 SCALING TECHNIQUES.

The tridiagonal solver that was implemented does not include any method for the estimation of the conditioning of a system of equations. Because no estimate was available, no attempt was made to scale any of the thermal systems of equations that were processed. The skyline solver did include the capability to estimate the condition number of $\mathbf{K}^{EM}$. Choosing realistic values for the material properties $\omega^{(e)}$, $\epsilon^{(e)}$ and $\mu^{(e)}$ made $\mathbf{K}^{EM}$ so highly ill-conditioned that the solution method failed, and showed that the values used in the example problems of Chapter VII were rather simplistic.

Some of this ill-conditioning is alleviated by employing a scaling scheme similar to the first scaling technique of Section 8.2.3. This scaling is performed at an elemental level before $\mathbf{K}^{EM}$ is assembled. Using L, M, T and Q to represent units of length, mass, time and charge respectively, the units of A_z, j_z, κ_θ and λ_c are seen to be $ML/(TQ)$, $Q/(TL^2)$, Q/L and $ML^2/(TQ)$ respectively. Many scaling schemes were tried, but the one that reduced the condition number the most gave the scaled displacements of A_z, j_z, and κ_θ dimensions of $M^{1/2}L/T$ and λ_c dimensions of $M^{1/2}L^{3/2}/T$. The elemental scaling matrix $\mathbf{S}_1^{(e)}$ for each element is

$$
\mathbf{S}_1^{(e)} =
\begin{bmatrix}
S_{11}^{(e)} & 0 & 0 & 0 & 0 & 0 & 0 \\
& S_{22}^{(e)} & 0 & 0 & 0 & 0 & 0 \\
& & S_{33}^{(e)} & 0 & 0 & 0 & 0 \\
& & & S_{44}^{(e)} & 0 & 0 & 0 \\
& & & & S_{55}^{(e)} & 0 & 0 \\
& & symm. & & & S_{66}^{(e)} & 0 \\
& & & & & & S_{77}^{(e)}
\end{bmatrix}
\tag{9.3.3}
$$

$$S_{11}^{(e)} = S_{44}^{(e)} = 2/\sqrt{\epsilon_o} \quad S_{33}^{(e)} = S_{66}^{(e)} = 1/\sqrt{\mu_o}$$

$$S_{22}^{(e)} = \sqrt{\epsilon_o}\omega^{(e)}l^{(e)} \quad S_{77}^{(e)} = 2/\sqrt{\mu_o}$$

$$S_{55}^{(e)} = 0 \quad e \le N_{wire}; \quad S_{55}^{(e)} = 1 \quad e > N_{wire}$$

where $l^{(e)}$ is the elemental length $r_j^{(e)} - r_i^{(e)}$. The inclusion of the elemental length in the scaling parameter for j_z does not cause any difficulties because the only diagonal terms affected by $S_{22}^{(e)}$ of $\mathbf{K}^{EM}$ correspond to the j_z degrees of freedom which do not couple through the diagonal terms.

To illustrate this point, consider the diagonal terms corresponding to the degrees of freedom for A_z of a two element system that contains a total of three element end nodes. If $A_z^{(e)}$ is scaled for each element by $l^{(e)}$, $A_z^{(e)}$ at the shared center node will be scaled on an elemental level by $l^{(1)}$ for the first element and $l^{(2)}$ for the second element. Note that the bracketed superscript numbers represent the element number and not an exponent. This causes no problem in determining scaling factors if $l^{(1)}$ equals $l^{(2)}$. It is simply $l^{(1)}$ or $l^{(2)}$. But if the lengths differ, problems will occur because A_z at the shared node will be scaled into two different dimensions! Trying to assemble the scaled elemental diagonal terms of A_z with this scaling would result in an error because each scaled variable represents a single scaled independent variable.

The scaling matrix of (9.3.3) avoids these difficulties due to a careful choice of its elements. $S_{55}^{(e)}$ ensures no coupling of adjacent values of $j_z^{(e)}$ and also ensures that there are no zero diagonal terms of the assembled scaling matrix for degrees of freedom of $j_z^{(e)}$ that are constrained to zero. $S_{55}^{(e)}$ also ensures that no zero diagonal term appears for the extra "empty" degree of freedom of $\mathbf{K}^{EM}$ that is discussed in Section 7.3.

The scaled elemental electromagnetic tangent stiffness matrix for $1 < e < N_{wire}$ is

$$\tilde{K}^{(e)} = \frac{1}{l^{(e)}} \begin{bmatrix} 0 & -r_i^{(e)} & 0 & 0 & 0 & 0 & 0 \\ & -r_m^{(e)} & K_{23} & r_j^{(e)} & 0 & K_{26} & K_{27} \\ & & r_m^{(e)} & 0 & 0 & -r_m^{(e)} & 0 \\ & & & 0 & 0 & 0 & 0 \\ & & & & 0 & 0 & 0 \\ & \text{symm.} & & & & r_m^{(e)} & 0 \\ & & & & & & 0 \end{bmatrix} \qquad (9.3.4)$$

$$K_{23} = -\frac{l^{(e)}}{2} \frac{\mu_o c_o}{\omega^{(e)}} \left(r_m^{(e)} - l^{(e)}/6 \right) \qquad K_{26} = -\frac{l^{(e)}}{2} \frac{\mu_o c_o}{\omega^{(e)}} \left(r_m^{(e)} + l^{(e)}/6 \right)$$

$$K_{27} = -\frac{l^{(e)}}{2} \frac{\mu_o c_o}{\omega^{(e)}} r_m^{(e)}$$

where $r_m^{(e)} = (1/2)(r_i^{(e)} + r_j^{(e)})$ is the mean radius of the element and c_o is the speed of light in vacuum. As can be seen by inspection, the closer $(l^{(e)}/2)(\mu_o c_o/\omega^{(e)})$ is to one, the better the conditioning of the matrix. If this occurs, it can also be seen that all of the terms become proportional to approximately $r_m^{(e)}/l^{(e)}$. Using the test material of high purity aluminum does not allow $(l^{(e)}/2)(\mu_o c_o/\omega^{(e)})$ to come as close to one as is desired, and other means are used to reduce the conditioning of the scaled electromagnetic system of equations. It was found that the choice of mesh discretiztion greatly affected the conditioning of the system, and this is the next topic of discussion.

9.3.5 MESH GENERATION.

The thermal conduction problem is similar to the superconductivity problem because a finer mesh discretization is required near r_c to accurately determine the nodal values of the independent variables. The independent variable for the thermal conduction problem is T and the electromagnetic quantity ω in the temperature range of interest is proportional to T^5. This behavior suggests that electromagnetic quantities vary either much more quickly or more slowly than T depending on whether the system is above or below 1° Kelvin. This behavior also suggests the use of separate meshes for the electromagnetic and thermal equations. Separate meshes were not used for the examples of this work because they require a transfer of data between the thermal mesh and the electromagnetic mesh and are subject to extrapolation errors. Separate meshes also require more computational effort and memory storage. For the above reasons, it was decided to use a single mesh for both the linear electromagnetic and thermal system of equations. As mentioned above, there is a finer grading of the thermal mesh at r_c. This grading was determined to be a source of ill-conditioning for the assembled EM equations.

Originally, a small region near r_c was discretized with regular finite elements and the remainder of the conductor volume was descretized with larger regular finite elements. It was seen that at the node where the two meshes joined, off-diagonal terms were generated that were substantially larger than diagonal terms. Other off-diagonal terms that were substantially smaller than diagonal terms were also generated. To cure this problem, the scaling scheme of the previous section is used to make off-diagonal terms of

the same order of magnitude as the diagonal terms on an elemental level. A new mesh discretization scheme is also used to eliminate the substantially larger and smaller off-diagonal terms. The third scaling technique of Chapter VIII does this for a system of positive definite equations, but this technique was tried and did not work here because the system is positive semi-definite due to the Lagrangian multiplier λ_c.

By observing that all of the terms in the elemental EM matrices are approximately proportional to $r_m^{(e)}/l^{(e)}$, a basis for the mesh discretization can be determined. By minimizing the rate of change of $r_m^{(e)}/l^{(e)}$, "bad" off-diagonal terms can either be eliminated or changed to more closely approximate the magnitude of the diagonal terms.

For convenience, a regular mesh of N_{fine} elements is used in the region near r_c. The remaining region uses a special mesh that contains N_{coarse} elements. This choice determines $d(r_m^{(e)}/l^{(e)})/de$ to be 1.0 in the "fine" region. It also specifies that $r_m^{(e)}/l^{(e)}$ equals $(r_{ncp1}/l^{(e)}) + .5$ at e equal to $N_{coarse} + 1$ where r_{ncp1} is the value of r at the node where the coarse mesh ends. This choice also determines that the length of each element in the "fine" region be equal to $(r_c - r_{ncp1})/N_{fine}$. An additional boundary condition for the axisymmetric problem is that $r_m^{(e)}/l^{(e)}$ is always equal to .5 at e equal to 1.

To satisfy the three boundary conditions and still have a varible input for the mesh discretization, a cubic curve fit for $r_m^{(e)}/l^{(e)}$ is required. Using these requirements gives the following equation for $r_m^{(e)}/l^{(e)}$.

$$\frac{r_m^{(e)}}{l^{(e)}} = \tfrac{1}{2}\left(\mathcal{A}_1 e^3 + \mathcal{A}_2 e^2 + \mathcal{A}_3 e + \mathcal{A}_4\right) \qquad (9.3.5)$$

$$\mathcal{A}_1 = \mathcal{B}_3^{-1}\left(2\mathcal{C}_1 - \mathcal{B}_1 N_{coarse}(N_{coarse} - 1) - 2\mathcal{C}_2(N_{coarse} + 1) + N_{coarse} - 1\right)$$

$$\mathcal{A}_2 = \mathcal{B}_1 + \mathcal{B}_2 \mathcal{A}_1 \qquad \mathcal{A}_3 = 2\mathcal{C}_2 - 7\mathcal{A}_1 - 3\mathcal{A}_2 - 1$$

$$\mathcal{A}_4 = 1 - (\mathcal{A}_1 + \mathcal{A}_2 + \mathcal{A}_3)$$

$$\mathcal{B}_1 = \left(\frac{2\mathcal{C}_3 - 2\mathcal{C}_2 + 1}{2N_{coarse} - 1} \right) \qquad \mathcal{B}_2 = \left(\frac{4 - 6N_{coarse} - 3N_{coarse}^2}{2N_{coarse} - 1} \right)$$

$$\mathcal{B}_3 = (N_{coarse} + 1)^3 + \mathcal{B}_2(N_{coarse} + 1)^2 - (7 + 3\mathcal{B}_2)(N_{coarse} + 1) + 2\mathcal{B}_2 + 6$$

$$\mathcal{C}_1 = (r_{ncpl}/l^{(e)}) + .5; e = N_{coarse} + 1 \qquad \mathcal{C}_2 = (r_m^{(e)}/l^{(e)}); e = 2$$

$$\mathcal{C}_3 = \frac{\partial}{\partial e} \left(\frac{r_m^{(e)}}{l^{(e)}} \right); e = N_{coarse} + 1$$

where the subscripted $\mathcal{A}$'s, $\mathcal{B}$'s and $\mathcal{C}$'s represent constants. The constant $\mathcal{C}_2$ is an input value and represents the value of $r_m^{(e)}/l^{(e)}$ for the second element. The value of $r_m^{(e)}/l^{(e)}$ for the second element is chosen as in input variable because at the first element, this value is determined by the problem geometry as always being 0.5. It is also easier to determine the size of the second element with this formula. If $\mathcal{C}_2$ is larger (smaller) than 1.5 the second element is smaller (larger) than the first, and if $\mathcal{C}_2$ equals 1.5, it has the same size. The value for r where the two meshes meet (r_{ncpl}) is also an input value. For the numerical experiments presented here, it was found that $r_{ncpl} = .75r_c$ and $\mathcal{C}_2 = 1.5$ produced the best results.

To determine the values of r at each node in the coarse mesh region, the following additional formula is used

$$r_i^{(e)} = r_j^{(e)} \left(\frac{r_m^{(e)}/l^{(e)} - 1}{r_m^{(e)}/l^{(e)} + 1} \right); \qquad e = (N_{coarse} + 1), N_{coarse}, \dots, 2, 1 \quad (9.3.6)$$

9.3.6 FIELD RECOVERY.

For the thermal part of the problem, the T field is recovered by using the values of $\mathbf{v}^T$. The electromagnetic fields are determined by using the simple finite element approximation of Chapter V, Equation (5.3.6). This value was plotted as a step function due to its C^{-1} continuity.

9.3.7 TEST PROBLEM.

In this example, high purity aluminum was again used for the test material. The values for k and $\omega^{(e)}$ were calculated as discussed earlier in this chapter. The permeability and permittivity for all elements were set to μ_o and ϵ_o as explained at the beginning of Chapter IV. The reference state for $\mathbf{v}$ was set as described in Section 9.3.3. The geometry was that of a one-dimensional axisymmetric wire as shown in Figure 2.1 with a radius r_c transporting a total current I equal to 5 amperes in the positive z direction. The mesh was discretized as described in Section 9.3.5 with r_c equal to 1.15×10^{-4}, N_{coarse} equal to 50 elements and N_{fine} equal to 30 elements. This gave a total of N_{wire} equal to 80 elements. Because the element for the free space magnetic fields had been validated before, no elements were generated external to the conductor. The solution tolerance τ was 9.0×10^{-4} and required about 2 iterations per step to converge. The estimated condition number for $\mathbf{K}^{EM}$ ranged from 10816 to 65888. The initial temperature was chosen as 1° Kelvin and the loading temperature was 1° Kelvin. The step size l_n was chosen as .025 and 40 steps were necessary to move the solution from the starting temperature of 1° Kelvin to 2° Kelvin.

The results for the analytical solution and the finite element solution for T were so close as to be indistinguishable on a plot. Consequently, Figure

9.1 shows the results for the finite element solution for the temperature distribution and Figure 9.2 shows the percentage error of the finite element solution from the analytical solution as functions of the radial distance at the final step ($T_\infty = 2^o$ Kelvin). A comparison of the Euler equations of the EM problem (Equation (2.3.11)) and the thermal problem (Equation (4.1.8)) shows that they are of an identical form. If k is nearly constant and $\omega^{(e)} j_z^{(e)}/k$ approximates a constant, then the behavior of A_z and T within the example wire should be the same. A comparison of Figure 9.1 with Figures 5.2 and 7.2 show that this is indeed the case. Figure 9.2 shows the deviation of the computed solution from the analytical solution as a percentage error, and it ranges from a maximum at $r = 0$ of 2.860×10^{-3} to zero at $r = r_c$.

The primary variables of interest for this research were the **B** fields, and they are the only EM results that are shown here. Figure 9.3 and 9.4 show the results for the B_θ field at the final step. Figure 9.3 shows the B_θ field over the whole conductor and Figure 9.4 shows the B_θ field for the volume of the mesh with the finer discretization. The percent error ranged from 33.1 percent at $r = 0$ to 5.89×10^{-4} at $r = r_c$. By observing where the analytical solution intersects the "steps" in Figures 9.3 and 9.4, a rough estimate of the accuracy of the finite element solution can be made. The finite element solution is exact when the analytical solution intersects the center of the "step tops". It can be seen that the analytical solution intersects the majority of the "steps" at their center points. It can also be seen that the error quickly diminishes as the distance from the center of the conductor increases.

As mentioned earlier, the solution procedure is not exact. Also mentioned was that the exact solution can be computed by setting T_o to the full
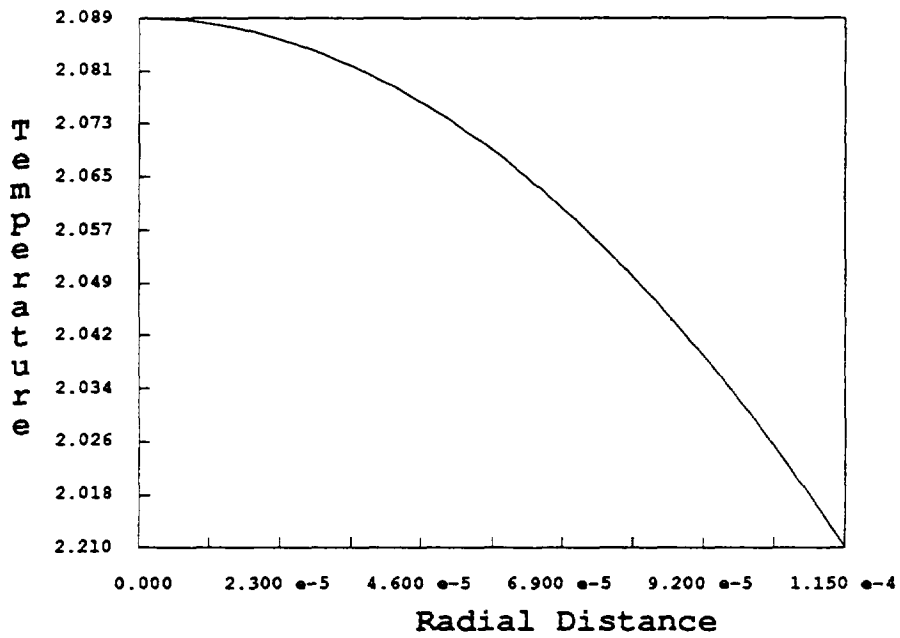
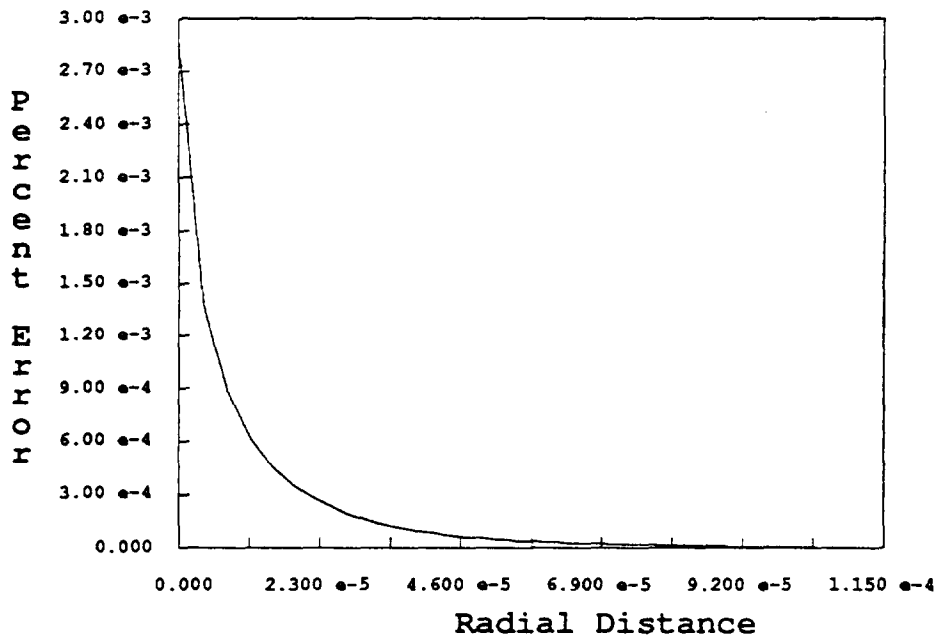Figure 9.1: T vs. r, values for the finite element solution plotted.

Figure 9.2: Percent error of the finite element solution from the analytical solution for T vs. r.

213

load, T_L to zero and using the corrective Newton-Raphson method to iterate onto the equilibrium path.

The above technique was tried for this numerical example and it was found that the finite element results presented here differed from the exact solution by 4.65×10^{-2} and 3.43×10^{-5} percent for the temperature at r equal to zero and r_c respectively. The B_θ field differed from the exact solution by 33.3 and 5.60×10^{-4} percent at r equal to zero and r_c respectively.

A brief word must be said here about the analytical solution of Section 9.2. In general, the analytical solution does not match the exact solution because it uses the nodal values of T from the previous step to compute k, $\omega^{(e)}$ and $j_z^{(e)}$. The analytical solution only becomes the exact solution when ζ^T is held constant and the solution is allowed to iterate onto the equilibrium path. This brings about the rhetorical question, why bother computing the analytical solution?

The analytical solution is computed because it gives some measure of how close the finite element solution is to an exact solution. It will always give the correct form of the solution, but not the correct magnitude if the solution lies close to the true equilibrium path. This is the first step in assessing the accuracy of the solution vector produced by the non-linear path-following techniques used in this work. The second step is to hold the loading parameter constant and then use the corrective Newton-Raphson technique to iterate to the exact solution. The exact solution is then compared to the original incremental solution. If the difference between the two solutions is too large, then the solution procedure has moved too far from the correct equilibrium path and a smaller step size needs to be chosen. The solution process is attempted again with the new step size and ζ^T reset to zero.
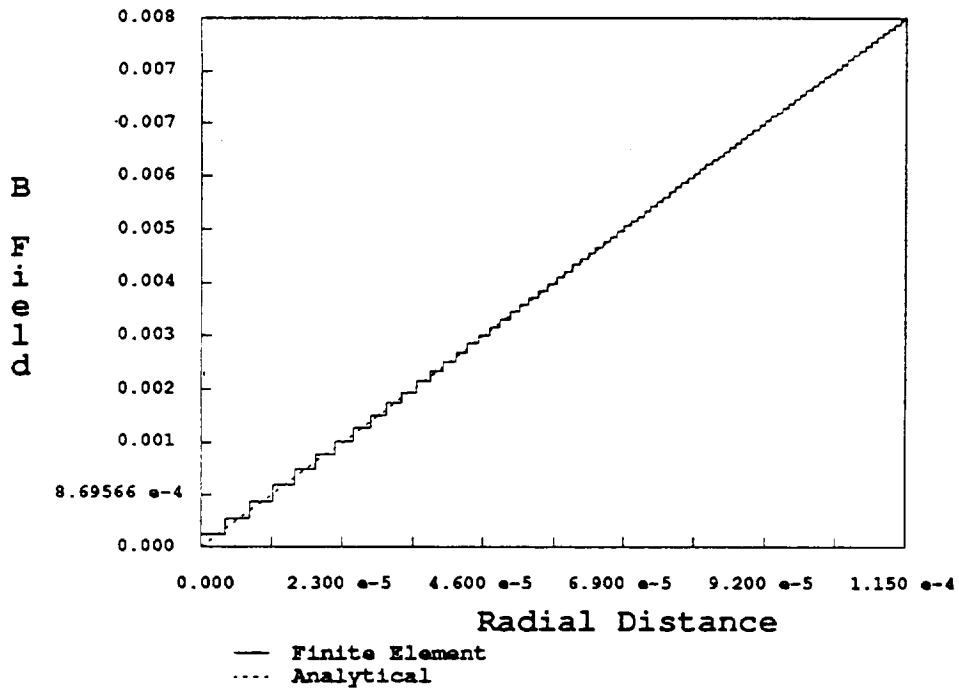
Figure 9.3: B_θ vs. r, values for complete mesh plotted.

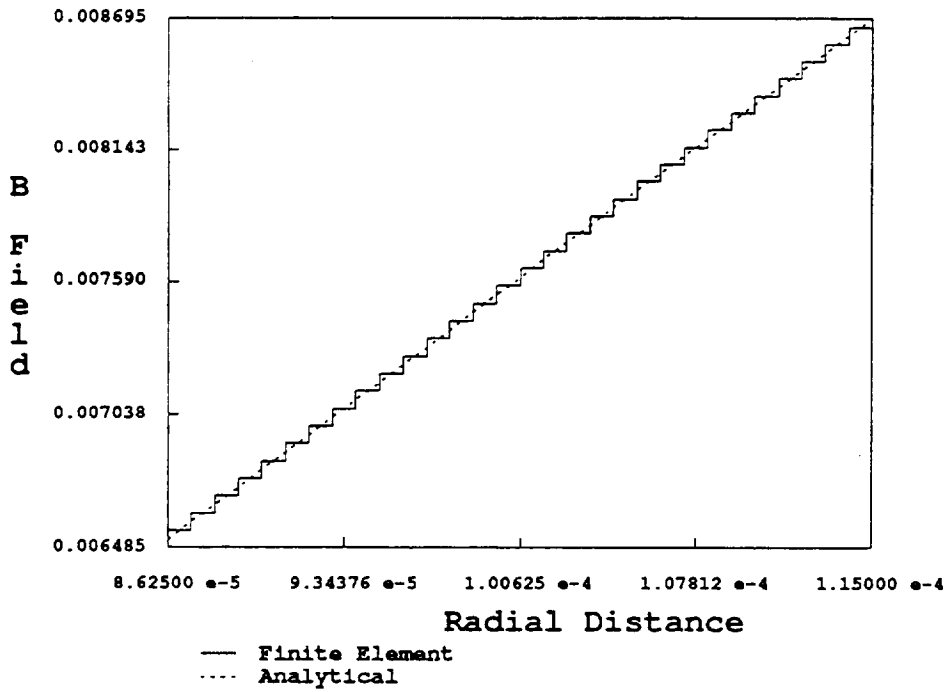Figure 9.4: B_θ vs. r, values for finer discretization plotted.

215

In general, it is not possible to hold the loading parameter constant at its final value and iterate onto the exact solution without first following the incremental path to that point. There may be bifurcation points or other stationary points on the equilibrium path that will not allow the solution method to converge to the correct solution by this simple iterative process. The problem of the thermally loaded conductor presented here does allow the above method to converge because it can be determined where the only critical point for this problem lies, that point being the superconducting phase transition point.

The plots for T and B_θ presented here show that with an appropriate mesh choice, a reasonable step size and a slowly varying temperature distribution that the solution technique presented here is adequate for the author's purposes and little accuracy is lost with this solution procedure.

9.4 SUMMARY.

In this chapter, it is shown how thermal fields may be modeled with the LINT1D finite element. The CUPLE1D finite element is also adapted to the nonlinear solution techniques of Chapter VIII to become the LET1D element. This demonstrates the usefulness of the four-potential method and the solution techniques for modeling the coupling that occurs between thermal and EM fields. The four-potential theory is also validated for computing the desired EM quantity, the B fields and the effects of temperature on these fields by the results presented in this chapter. The use of real values for ω, μ and ϵ make the problem more difficult to solve, but by using a different mesh discretization and scaling techniques, good solutions for the B field can still be realized.

For this chapter, the case where only thermal loads are allowed to vary is solved. In the next chapter, the case where the EM load I is allowed to vary is examined.

COUPLED THERMAL-EM PROBLEM IN NORMAL CONDUCTOR

In the previous chapter, the consequences of varying the thermal loading on a conductor are discussed. In this chapter, the thermal-electromagnetic coupling in a normal conductor loaded by varying the current I is discussed. Most of the necessary ground work to consider this problem is developed in the previous chapters. Analytical solutions to both problems are discussed in previous chapters and are not presented here. The solution, mesh discretization and scaling techniques of the previous chapter are also implemented for the varying current load problem. The only parts of this problem that change are parts of the LINT1D finite element that depend explicitly upon j, which is a function of the current load I, and the parts of the LET1D finite element that are dependent upon I. The first topic of discussion is the modification of the LET1D finite element to include cases where I is allowed to vary.

10.1 FINITE ELEMENT DISCRETIZATION.

10.1.1 MODIFICATIONS TO THE LET1D FINITE ELEMENT.

The first step in adapting the LET1D finite element for a varying current load is to split I into an initial current I_o and a loading current I_L as was done for the superconductor. Thus $I = I_o + \zeta^{EM} I_L$, where ζ^{EM} is the electromagnetic loading parameter. By using the Kronecker delta with

218

the boundary terms, the new equality for I, and Equation (7.2.2), $\mathbf{f}^{(e)}$, $\mathbf{p}^{(e)}$ and $\mathbf{v}^{(e)}$ are expressed as

$$\mathbf{f}^{(e)} = \left\{ \mathbf{K}^{\mathcal{U}(e)} + \mathbf{K}^{*(e)} \right\} \mathbf{v}^{(e)} \tag{10.1.1}$$

$$\mathbf{K}^{*(e)} = 2\pi H \begin{bmatrix} 0 & \delta_{1e} r_i^{(1)} \omega^{(1)} & 0 & 0 & 0 & 0 & 0 \\ & 0 & 0 & -\delta_{me} r_j^{(m)} \omega^{(m)} & 0 & 0 & 0 \\ & & 0 & 0 & 0 & 0 & 0 \\ & & & 0 & 0 & 0 & 0 \\ & & & & \delta_{me} & 0 & 0 \\ & & symm. & & & 0 & 0 \\ & & & & & & 0 \end{bmatrix}$$
$$\tag{10.1.2}$$

$$\mathbf{v}^{(e)} = \left\{ \begin{array}{c} \kappa_{\theta}^{(e)}{}_i \\ j_z^{(e)} \\ \mathbf{A}_z^{(e)}{}_i \\ \kappa_{\theta}^{(e)}{}_j \\ 0 \\ \mathbf{A}_z^{(e)}{}_j \\ \lambda_c \end{array} \right\} \qquad \mathbf{p}^{(e)} = \left(I_o + \zeta^{EM} I_L \right) \left\{ \begin{array}{c} \delta_{1e} H \\ 0 \\ 0 \\ 0 \\ 0 \\ -\delta_{me} H \\ -\delta_{me} \end{array} \right\} \tag{10.1.3}$$

where m again equals $N_{wire} + 1$ and H represents the element height. The matrix $\mathbf{K}^{*(e)}$ is used here to add the boundary terms for κ to $\mathbf{K}^{(e)}$ discussed in Section 7.2.2. $\mathbf{K}^{*(e)}$ also removes the rank deficiency generated by the "empty" degree of freedom discussed in Section 7.3.2. The correct value of $\mathbf{K}^{\mathcal{U}(e)}$ is given by Equations (7.2.3), (7.2.4), (7.2.5) and (7.2.6). Taking the partials of $\mathbf{f}^{(e)}$ and $\mathbf{p}^{(e)}$ with respect to the independent variables contained in $\mathbf{v}^{(e)}$ gives the tangent stiffness matrix and loading vector, respectively. Therefore the tangent stiffness matrix $\mathbf{K}^{(e)}$, the loading vector $\mathbf{q}^{(e)}$ and the

incremental rate vector $\mathbf{w}^{(e)}$ are:

$$\mathbf{K}^{(e)} = \mathbf{K}^{\mathcal{U}(e)} + \mathbf{K}^{*(e)}; \quad \mathbf{q}^{(e)} = I_L \left\{ \begin{array}{c} \delta_{1e}H \\ 0 \\ 0 \\ 0 \\ 0 \\ -\delta_{me}H \\ -\delta_{me} \end{array} \right\}; \quad \mathbf{w}^{(e)} = \left\{ \begin{array}{c} \dfrac{\partial \kappa_\theta^{(e)}{}_i}{\partial \zeta^{EM}} \\[6pt] \dfrac{\partial j_z^{(e)}}{\partial \zeta^{EM}} \\[6pt] \dfrac{\partial \mathbf{A}_z^{(e)}{}_i}{\partial \zeta^{EM}} \\[6pt] \dfrac{\partial \kappa_\theta^{(e)}{}_j}{\partial \zeta^{EM}} \\[6pt] 0 \\[6pt] \dfrac{\partial \mathbf{A}_z^{(e)}{}_j}{\partial \zeta^{EM}} \\[6pt] \dfrac{\partial \lambda_c}{\partial \zeta^{EM}} \end{array} \right\}$$

$$(10.1.4)$$

It can be seen that $\mathbf{K}^{(e)}$ is exactly the same as the stiffness matrix, modified for boundary conditions and the extra "empty" degree of freedom of Chapter VII thereby justifying the statement at the end of Section 7.1.1 that the two are equivalent. A word of caution is necessary here because the expressions for $\mathbf{p}^{(e)}$ and $\mathbf{q}^{(e)}$ are only valid for cases where the first degree of freedom for A_z is constrained. For the examples presented in the sequel, this is always the case and no further information is needed to solve the EM system of equations except that the "empty" degree of freedom for the fifth element of $\mathbf{v}^{(m)}$ must also be constrained to zero as explained in Section 7.3.2.

10.1.2 MODIFICATIONS TO THE LINT1D FINITE ELEMENT.

The expressions derived in Chapter IX for $\mathbf{K}^T$, $\mathbf{p}^T$ and $\mathbf{f}^T$ for the LINT1D finite element do not depend upon the current load I explicity and may be used without modification to solve the current loading problem. Because $\mathbf{p}^{(e)}$ for the LINT1D element does contain $j_z^{(e)}$, it must be varied with respect to the loading parameter ζ^{EM} to determine what happens to the thermal system of equations as I is varied. The result for $\mathbf{q}^{(e)}$ is

$$\mathbf{q}^{(e)} = \int_{V^{(e)}} dV^{(e)} \left\{ 2\omega^{(e)} \frac{\partial j_z^{(e)}}{\partial \zeta^{EM}} \mathbf{N}^T \right\} \tag{10.1.5}$$

The assembled system of coupled thermal and EM equations with this form for $\mathbf{q}$ can be expressed as

$$\begin{bmatrix} \mathbf{K}^{EM} & 0 \\ 0 & \mathbf{K}^T \end{bmatrix} \left\{ \begin{matrix} \mathbf{w}^{EM} \\ \mathbf{w}^T \end{matrix} \right\} = \left\{ \begin{matrix} \mathbf{q}^{EM} \\ \mathbf{q}^T \end{matrix} \right\} \tag{10.1.6}$$

where $\mathbf{q}^T$ is now a function of $\mathbf{w}^{EM}$. This form of the equations is undesirable because terms of the incremental rate vector appear on both sides of the equality sign. Moving $\mathbf{q}^T$ to the left hand side produces

$$\begin{bmatrix} \mathbf{K}^{EM} & 0 \\ \mathbf{K}^{EMT} & \mathbf{K}^T \end{bmatrix} \left\{ \begin{matrix} \mathbf{w}^{EM} \\ \mathbf{w}^T \end{matrix} \right\} = \left\{ \begin{matrix} \mathbf{q}^{EM} \\ 0 \end{matrix} \right\} \tag{10.1.7}$$

where $\mathbf{K}^{EMT}$ contains the elements of $-\mathbf{q}^T$ at the appropriate positions.

This form of the equations is also undesirable for two reasons. First, the extra matrix $\mathbf{K}^{EMT}$ must be assembled which requires more computational effort and memory storage. It also ruins the sparsity and the symmetry of the original system of equations and a tridiagonal solver can no longer be used to process the thermal equations. Second, $\mathbf{K}^{EMT}$ is also a function of the independent variable j_z. This affects adversely the conditioning of the

221

coupled system and typically requires more iterations to converge upon a solution than a set of linear equations, which only requires a single iteration to converge.

If the form of Equation (10.1.6) is preserved by making $\mathbf{q}^T$ a function of ζ^{EM}, the original sparsity of the system is retained and computational effort and memory storage are reduced. To accomplish this goal, Equations (7.1.2) and (7.1.3) are used. Insertion of (7.1.3) into (7.1.2) gives

$$ I = I_o + \zeta^{EM} I_L = \omega^{(e)} j_z^{(e)} \sum_{p=1}^{N_{wire}} \int_{\Gamma_1^{(p)}} d\Gamma_1^{(p)} \frac{\omega^{(p)}}{\omega^{(e)}} \qquad (10.1.8) $$

where the superscripts (p) and (e) again represent element numbers and N_{wire} is the total number of elements within the conductor. Rearranging Equation (10.1.8) and taking the partial of $j_z^{(e)}$ with respect to ζ^{EM} gives

$$ \frac{\partial j_z^{(e)}}{\partial \zeta^{EM}} = \frac{1}{\omega^{(e)}} \left\{ \frac{I_L}{\int_{\Gamma_1^{(p)}} d\Gamma_1^{(p)} \frac{\omega^{(p)}}{\omega^{(e)}}} \right\} \qquad (10.1.9) $$

The bracketed term of the above expression is evaluated when assembling $\mathbf{K}^{EM}$ and requires less computational effort and memory storage than the scheme presented in Equation (10.1.7). The thermal loading vector $\mathbf{q}^T$ is still a function of the EM solution vector $\mathbf{v}^{EM}$ but does not cause difficulties in the example problems. The value of $\mathbf{v}^{EM}$ at step n is used to compute $\mathbf{w}$ at step $n+1$ in the same manner that $\mathbf{v}^T$ is used at step n to compute k and ω for $\mathbf{K}^T$ and $\mathbf{K}^{EM}$ at step $n+1$.

The coupled system of thermal and EM equations is conservative and the variation of the discretized functionals that describe this system should produce a symmetric system of equations. The fact that (10.1.7) is

not symmetric is caused by the use of approximations that render them incomplete. In Chapter IX, it is assumed that **j** is only a function of I but not of the temperature $\mathcal{T}$, an approximation responsible for the unsymmetry 0f (10.1.7). This point is mentioned here to emphasize the importance of using the nonlinear solution procedure of Chapter VIII and equilibrium path following procedures to generate correct solutions. For small incremental steps, the methods described in this and the last chapter work well for determining solutions for the coupled system of thermal and EM equations although the complete set of equations is not solved. Because the solution never moves too far from the equilibrium path, the missing terms have little effect on determining a correct solution.

10.2 NUMERICAL EXPERIMENTS.

10.2.1 THE FINITE ELEMENT MODEL.

The finite element model described in the previous section has been applied to the infinite axisymmetric normal conductor of the previous chapter. The modifed LET1D and LINT1D finite elements are used to determine EM quantities and the temperature distribution, respectively. Both of these elements are treated as one-dimensional axisymmetric two node "line" type elements. The description of the nodal degrees of freedom and the variables associated with each degree of freedom for the LET1D element are the same as the CUPLE1D element and are found at the beginning of Section 7.3.1. The permeability μ, the resistivity ω and the current density j_z are all assumed to be uniform over each element.

For the modified LINT1D finite element, the description of the nodal degrees of freedom and the variables associated with each degree of freedom are found in Section 9.3.1. The material constants k and ω are also determined by the same methods discussed in that section. The value used for $j_z^{(e)}$ to determine $q^{(e)}$ at step $n + 1$ comes from the EM solution vector at step n and $\partial j_z^{(e)}/\partial \zeta^{EM}$ for $q^{(e)}$ is determined by use of Equation (10.1.9).

The boundary conditions for this system are the same as described in Section 9.3.2 and are set in the same manner.

10.2.2 ASSEMBLY AND SOLUTION.

The assembly and solution of the coupled EM-thermal normal conducuctor with a variable current loading is identical to a conductor with variable thermal loading except that Equation (10.1.5) is used to determine q^T. The scaling techniques implemented for $\mathbf{K}^{EM}$ for the thermally loaded conductor are also used on $\mathbf{K}^{EM}$. The mesh generation and field recovery techniques used here are also identical to the techniques of Sections 9.3.5 and 9.3.6 respectively.

10.2.3 TEST PROBLEM.

A one-dimensional axisymmetric wire made of high purity aluminum was used as test example. The geometry is shown in Figure 2.1. The radius of the wire r_c is 1.15×10^{-4}. The wire transports a total current of $I_o + \zeta^{EM} I_L$ in the positive z direction where I_o is zero amperes and I_L is 5 amperes. The free stream temperature of the system T_∞ is held constant at 2° Kelvin by setting the initial temperature T_0 equal to 2° Kelvin and the loading temperature T_L equal to zero. The convection heat transfer coefficient h_{conv},

the thermal conductivity k and the resistivity are calculated as described previously in Chapters IV and IX. The permeability $\mu^{(e)}$ and the permittivity $\epsilon^{(e)}$ for each element were set to μ_o and ϵ_o respectively, which are the free space or vacuum values, as discussed at the beginning of Chapter IV.

The mesh was discretized as described in Section 9.3.5 with N_{coarse} equal to 50 elements and N_{fine} equal to 30 elements to give the total of elements within the conductor, N_{wire} equal to 80 elements. Because the element for the free space magnetic field had been validated before, none were used outside of the conductor. The incremental step size l_n chosen was .1 and 21 steps were taken to give a final value for ζ^{EM} of ≈ 0.97. The solution tolerance τ was 1.0×10^{-4} and the solution procedure averaged 2.381 iterations per step to converge. The condition number of $\mathbf{K}^{EM}$ was estimated to range from a low of 14826 to a high of 70969.

The results of the analytical solution and the finite element solution for $\mathcal{T}$ are indistinguisable on a plot. Figure 10.1 shows the results of the finite element solution and Figure 10.2 shows the percentage deviation of the finite element solution from the analytical solution for the final value of ζ^{EM}. The maximum error from the analytical solution occured at r equal to zero and was 2.67×10^{-3}.

To converge upon the exact solution another four incremental steps using 14 iterations per step was required. For these four steps ζ^{EM} was held constant. The results of this final process showed that the finite element solution presented in Figure 9.1 differed by 9.36×10^{-3} percent at r equal to zero and 5.27×10^{-6} percent at r equal to r_c from the exact solution. For all increments, the initial or reference state was the finite element solution obtained *after* following the incremental path to ζ^{EM} equal to ≈ 0.97. The

225

state at $\zeta^{EM} \approx 0.97$ was actually quite close to the equilibrium path. The high iteration number required to move the solution back onto the equilibrium path illustrates the difficulty associated with finding an exact solution by simply using the corrective Newton-Raphson process. Sometimes, direct iteration is not possible or more expensive computationally than just using the incremental "path following" solution method presented here.

Figures 10.3 and 10.4 show the finite element and analytical solutions for B_θ. Figure 10.3 shows the two solutions plotted over the whole domain of the conductor, and Figure 10.4 shows the solutions over the domain of the finely graded mesh. At r equal to zero, B_θ differs from the analytical and exact solutions by 33.3 percent. At r equal to r_c, B_θ has errors of 5.91×10^{-4} and 5.85×10^{-4} perecent when compared to the analytical and exact solutions respectively.

Although not mentioned until this point, the 33.3 percent error at r equal to zero appears to be large. Subtracting out the temperature at r equal r_c from all of the finite element and analytical values for T and then recomputing the percent error for T will give the same error at r equal to zero of 33.3 percent. This observation has led the author to believe that the error is the same for all systems of equations of the form $\nabla \cdot (a\nabla b) = f(b)$ when this system is modeled with finite elements. Here a represents some material constant, b the independent variable, and $f(b)$ some function of the independent variable b. If the above observation is correct, it should always be possible to correct any error when modeling a system of this form.

A quick look at Figures 5.3, 5.4, 7.3, 7.6, 9.3 and 10.3 shows that the correction is probably unnecessary. The divergence of the computed solution
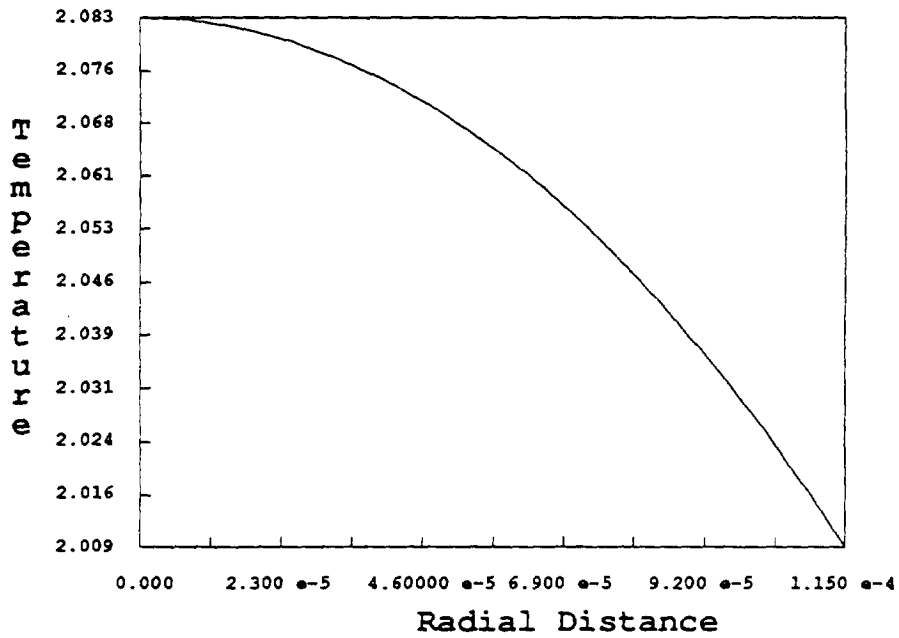
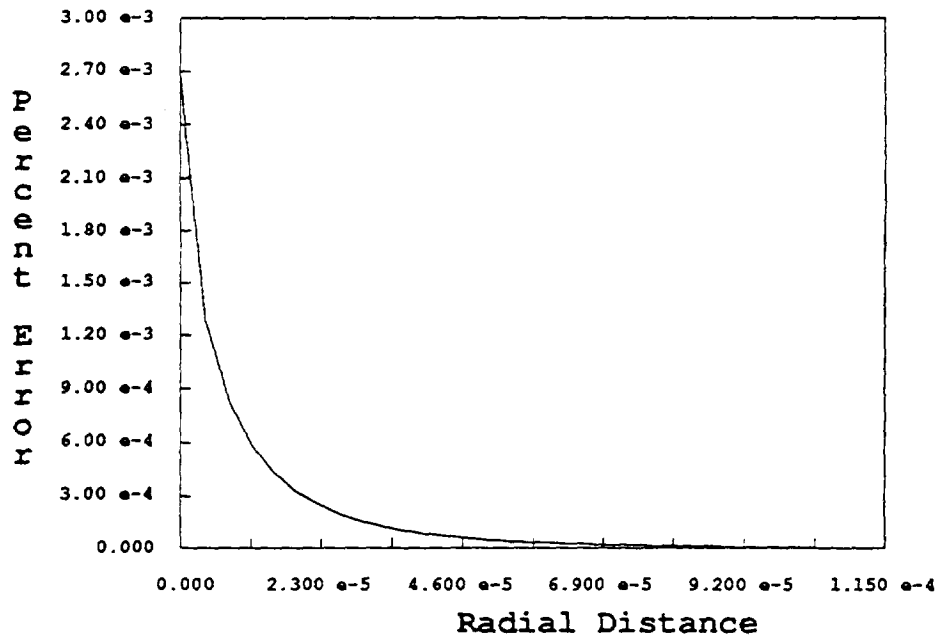Figure 10.1: T vs. r, values for the finite element solution plotted.

Figure 10.2: Percent error of the finite element solution from the analytical
solution for T vs. r.

from the exact solution is so small as to be almost unnoticeable and from a practical engineering standpoint, the error is not noticeable.

The reason that the 33.3 percent error appears to be large is because the computed solution is compared to the exact solution on a node to node basis. This is formally expressed as

$$\% \ error = \frac{B_{FE}(r) - B_{EX}(r)}{B_{EX}(r)} \times 100 \qquad (10.2.1)$$

where B_{FE} and B_{EX} are the finite element and exact values respectively for the B_θ field. A more realistic error estimator for engineering purposes is

$$\% \ error = \frac{B_{FE}(r) - B_{EX}(r)}{B_{EX}(r) + B_{EX}(r_c)} \times 100 \qquad (10.2.2)$$

This type of error estimate has been used to compute the error for T in this and previous chapters. When computing T on a node by node basis, the boundary loading has already been factored into the estimator. The conclusion of this brief digression is that an error estimator by itself is not always a good indicator of the accuracy of a finite element model. Graphics, a relationship of numerical answers to the actual physics of a modeled problem and good engineering common sense should all be used with an error estimator to judge the validity and usefulness of each finite element model.

10.3 SUMMARY.

In this chapter, a form of the LINT1D finite element is derived for the case where I is varied instead of T. The LET1D finite element is modified, and using a nonlinear solution technique it is possible to compute some good values for the thermal and magnetic fields of a one-dimensional axisymmetric conductor.
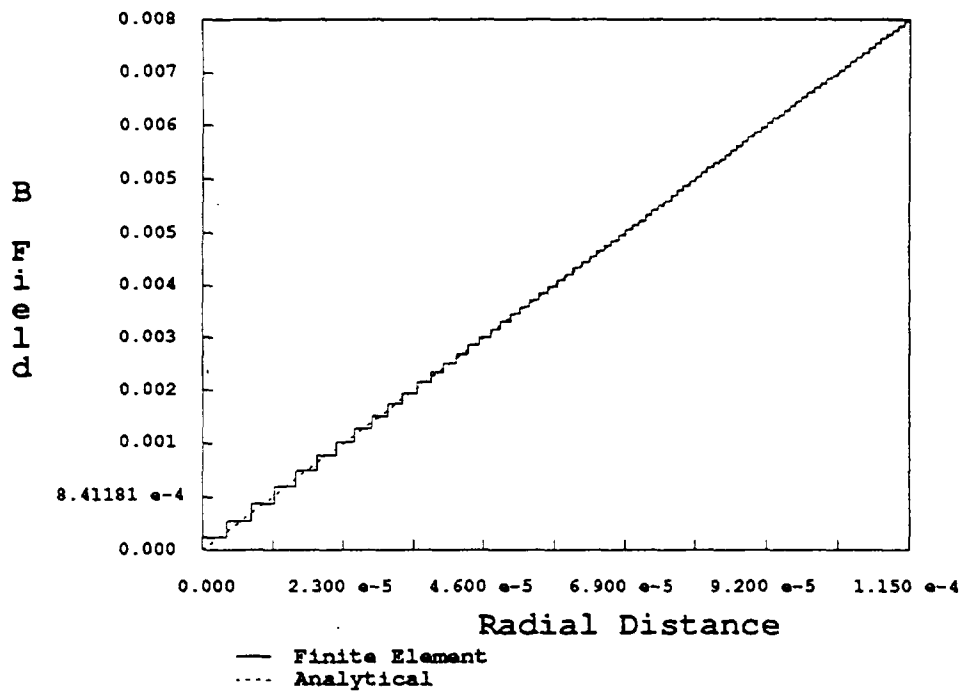
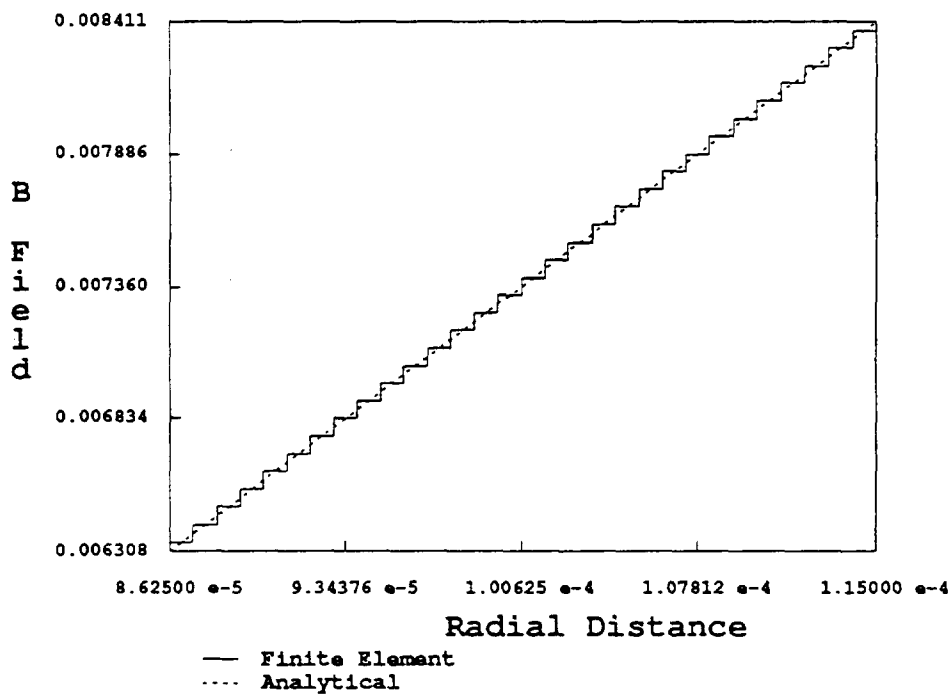Figure 10.3: B_θ vs. r, values for complete mesh plotted.

Figure 10.4: B_θ vs. r, values for finer discretization plotted.

229

This represents the next to the last phase of this work's analysis of the coupled quantum phase-EM-thermal problem for superconductors. It is now possible to generate models of the superconducting material in its normal and superconducting phases. It is also possible to determine the effect of varying either the thermal T or current I loading of that material.

The next chapter is concerned with the use of the final versions of the LINT1D and LET1D finite elements with the STEP1D finite element in a single computer program. This program is used to determine the correct state of a superconducting material and the values of the thermal and magnetic fields.

THE COMPLETE COUPLED PROBLEM.

This chapter is concerned with the correct application of the LINT1D, CUPLE1D and the STEP1D finite elements to the the specific problem of determining the electromagnetic and thermal fields within a superconducting material. The main limitation on this model is that it is only one-dimensional and cannot realistically model the state where B and T reach their critical values because, as noted previously, the solution at the transition state is a multi-dimensional problem. At this bifurcation point, a mixed normal and superconducting state appears that needs to at least include variations of ψ in the z direction to obtain an accurate model of the physics that occur within a conductor [21, pp.99-103; pp.127-191]. This point also marks where the computed solution must change equilibrium paths to accurately model the physics of the electron transport within a conductor.

The methodology required to model a superconductor when the thermal loading is varied is first discussed in some detail. Then the question of how to determine if a computed solution lies above or below the bifurcation point is discussed. Means to determine whether or not such a solution is correct are also presented. These means form the basis of an equilibrium path changing criteria. Finally, results that show the model changing state as I and T_∞ are varied are presented to validate the path changing criteria.

11.1 A SUPERCONDUCTOR WITH A VARYING $\mathcal{T}$ LOAD.

To use the incremental approach to solve the superconductor with a varying thermal load, f^{EM} and p^{EM} are varied with respect to $v^{\mathcal{T}}$ and $\zeta^{\mathcal{T}}$. The thermal quantities $f^{\mathcal{T}}$ and $p^{\mathcal{T}}$ are also varied with respect to v^{EM}. Doing so produces a system of incremental equations that can be partitioned in the following manner:

$$\begin{bmatrix} \mathbf{K}^{EM} & \mathbf{K}^{EM\mathcal{T}} \\ \mathbf{0} & \mathbf{K}^{\mathcal{T}} \end{bmatrix} \left\{ \begin{array}{c} \mathbf{w}^{EM} \\ \mathbf{w}^{\mathcal{T}} \end{array} \right\} = \left\{ \begin{array}{c} \mathbf{0} \\ \mathbf{q}^{\mathcal{T}} \end{array} \right\} \qquad (11.1.1)$$

where $\mathbf{K}^{EM}$ and $\mathbf{K}^{\mathcal{T}}$ are the previously derived tangent stiffness matrices for the superconducting and thermal conduction problems respectively and $\mathbf{q}^{\mathcal{T}}$ is the previously derived loading vector for the thermal conduction problem with convection boundary conditions. The matrix $\mathbf{K}^{EM\mathcal{T}}$ is $\partial f^{EM}/\partial v^{\mathcal{T}}$ and the zero entries on the left and right hand sides of the equality sign appear because $\partial f^{\mathcal{T}}/\partial v^{EM} = \mathbf{0}$ and $\partial \mathbf{q}^{EM}/\partial \zeta^{\mathcal{T}} = 0$. Because the resistivity of each element $\omega^{(e)}$ is zero for a superconductor, only one nonzero term appears in $\mathbf{q}^{\mathcal{T}}$. This term has a magnitude of $\mathcal{T}_{\mathrm{L}}$ and appears at the degree of freedom for $\mathcal{T}$ associated with the radial distance r_c.

Solving the set of thermal equations produces the simple result that $\mathcal{T}$ is a constant over the whole conductor, the value of $\mathcal{T}$ at each node being equal to $\mathcal{T}_0 + \zeta^{\mathcal{T}}_{n+1}\mathcal{T}_{\mathrm{L}}$. This simplifies the solution procedure considerably because the thermal equations $\mathbf{K}^{\mathcal{T}}\mathbf{w}^{\mathcal{T}} = \mathbf{q}^{\mathcal{T}}$, need not be solved by assembling and inverting $\mathbf{K}^{\mathcal{T}}$. Instead of solving (11.1.1), which also requires the assembly and storage of $\mathbf{K}^{EM\mathcal{T}}$, the corrective Newton-Raphson technique is used to directly iterate to a solution for v^{EM}. This is accomplished by solving the superconductor problem with the current load I held constant. The value for $\mathcal{T}$ at each node is the value of $\mathcal{T}$ at the $n+1$ step, $\mathcal{T}_0 + \zeta^{\mathcal{T}}_{n+1}\mathcal{T}_{\mathrm{L}}$,

where ζ_{n+1}^{T} equals $\zeta_{n}^{T} + l_n$ and the quantity l_n is the input step size. This is the value of T that is also used to determine α and β, since they are both functions of T and their values are required to obtain the correct EM tangent stiffness matrix $\mathbf{K}^{EM}$.

Essentially this is the same incremental/iterative solution method used in the two previous chapters to generate the exact solutions for $\underline{T}^{(e)}$, $j_z^{(e)}$ and $\mathbf{A}_z^{(e)}$. The loading parameters ζ^{EM} and ζ^{T} are held constant and the system is allowed to iterate onto the equilibrium path. As mentioned in those chapters, this technique can fail or become computationally expensive when a large number of corrective iterations is required. Early in the testing of the STEP1D element, it was observed that a reasonable solution for $|\psi|^{(e)}$ and $\mathbf{A}_z^{(e)}$ could be obtained in this manner if the reference state is set so that all unconstrained values of $|\psi|^{(e)}$ are equal to $|\psi_\infty|$ and all values of $\mathbf{A}_z^{(e)}$ are set equal to zero. The number of iterations needed for convergence with this reference configuration was usually less than ten. This configuration is also identical to the initial reference state that is used to start the solution procedure for a superconductor when the current loading I is varied. This means that the subroutine that generates the initial reference state for the varying current problem can also be used to generate a reference state for the varying T problem thereby reducing the logic and memory requirements of a code that solves both problems.

The computational cost of using the above solution method is that more iterations are required at each step and the reference configuration must be recomputed at each step. There is also no guarantee that the solution method will convege but numerical experiments strongly suggest that it will.

The corrective Newton-Raphson technique is therefore used to solve the problem of a superconductor with a varying thermal boundary load for the following reasons:

1. Assembly and storage of $\mathbf{K}^{EMT}$ is unnecessary.

2. The number of iterations required per step is relatively modest.

3. Convergence, as determined by numerical experiments, always occured.

4. The reference state is identical to the initial configuration of the I loading problem, allowing the use of one subroutine to set either configuration.

11.2 DETERMINATION OF THE CORRECT EQUILIBRIUM PATH.

To check whether the conductor is in the normal or superconducting state, one determines the critical temperature T_c and the critical magnetic field $\mathbf{B}_c$. Then $\mathbf{B}_c$ and T_c are compared to the largest magnitude of $\mathbf{B}$ and the highest temperature T (typically T_∞) field within the conductor. If either T_c or $\mathbf{B}_c$ is exceeded, a superconductor changes quantum states and becomes a normal conductor. This change of state occurs because at T equal to T_c or $\mathbf{B}$ equal to $\mathbf{B}_c$ a bifurcation point for the equilibrium paths of a superconductor and a normal conductor exists.

The existence of this bifurcation point also means that if the conductor is originally in the normal state and T_∞ falls below T_c *and* the largest value of $\mathbf{B}$ within the conductor is less than $\mathbf{B}_c$, the material becomes superconducting. It is therefore important to know the values of T_c and $\mathbf{B}_c$ so that the position of the bifurcation point along the equilibrium path can be determined. The critical temperature T_c is a material constant, and is determined either by experimentation or by referencing previous experimental

data. The critical **B** field $\mathbf{B}_c$ is determined by using Equation (4.4.1) which is a function of the temperature T.

An alternative method for finding the correct conductor state is to compute the Helmholtz free energy for the superconducting and normal states of a conductor for the same thermal and current loading conditions. After finding the free energies of both systems, the state of the system can be determined by choosing the system that has the lower free energy. This approach is computationally inefficient because it requires solving for the degrees of freedom **v** of both states at every incremental step. It also requires knowledge of the heat capacity of the material for the superconducting and normal states of the material, and finding these values can be a task of considerable difficulty because of the dearth of experimental data. The first approach is therefore chosen here.

Following the first approach, the **B** fields and T distribution as determined by $\mathbf{v}_{n+1}$ are checked at the end of each incremental step to see if they are sufficiently small so that a superconducting state is possible. If that is the case and the system was originally in the *normal* state at step n, then $\mathbf{v}_{n+1}$ is solved for again at step $n+1$ using the superconducting finite element STEP1D. If that is not the case and the condutor was in the normal state at step n, then the solution at step $n+1$ is accepted and the program proceeds to the next step keeping the normal conducting state element LET1D. If the **B** fields and the T distribution are small enough at step $n+1$ and the system was originally in the *superconducting* state at step n, the solution vector $\mathbf{v}_{n+1}$ is accepted and the solution process moves to the next step using the STEP1D finite element. Finally, if either of the two fields are too large for a superconducting state to exist, then $\mathbf{v}_{n+1}$ is recomputed

using the LET1D finite element and the solution method moves to the next step using the LET1D finite element.

For the one-dimensional problem, this methodology appears to be optimal and is the one used for the present numerical experiments. It has the key advantage that knowledge of the heat capacity of the material is unnecessary. Furthermore, the solution vector **v** only needs to be computed twice when the system changes state. If the second path determination method that involves computing the Helmholtz free energies of the normal and superconducting states is used, the solution vector **v** must be computed twice at *every* step.

The first approach naturally delineates the tests for the proper equilibrium state of the system into four separate cases where a change of state may occur. These cases are:

1. System originally in the superconducting state, thermal load increasing.
2. System originally in the superconducting state, current load increasing.
3. System originally in the normal state, thermal load decreasing.
4. System originally in the normal state, current load decreasing.

For cases where the system is originally in the superconducting state and the current or thermal loading is decreasing, the system remains in the superconducting state because the solution is moving away from the bifurcation point and no problems involving equilibrium path changing are posed. Similarly, when the system is originally in the normal state and the current or thermal loading is increasing, the solution remains in the normal state because it is moving along the normal state equilibrium path away from the bifurcation point. Again, this poses no problems to the solution procedure.

The comparison of $\mathcal{T}_c$ to $\mathcal{T}_\infty$, the first path changing criterion, is relatively straightforward and only involves the computation of $\mathcal{T}_\infty$ at each step. The second criterion can cause problems. This criterion states that **B** for every element of the conductor must be below $\mathbf{B}_c$ for a superconducting state to exist. Comparing **B** over each element to $\mathbf{B}_c$ can become computationally expensive as the number of elements used to model a problem increases. This computational expense can be reduced by finding *a priori* where **B** attains its largest value within the conductor. For the one-dimensional axisymmetric infinite conductor, **B** attains its largest value at r_c. A cursory examination of Equation (5.1.8) verifies that the preceding statement is correct. Equation (5.1.8) can also be used to determine that

$$B_\theta(r_c) = \frac{\mu_o I}{2\pi r_c} \qquad (11.2.1)$$

where μ_o replaces μ for example conductors of this work, as discussed in previous chapters, and $\int_\Gamma \mathbf{j} \cdot \hat{\mathbf{n}}_c d\Gamma$ is equal to I. By using this analytical solution for $B_\theta(r_c)$, a simple means exists for determining if a superconducting state is possible.

The only situation not discussed so far is when the incremental solution falls directly upon the bifurcation point. As explained previously, at this point the physical solution cannot be modeled by one-dimensional elements and the LET1D element is used to model EM quantities although the solution generated does not represent the correct physical state of the system. This method is used so that the solution method can proceed to the next step without failing. The LET1D element does not fail at this point because it is based upon a potential energy formulation. The STEP1D element fails because it is based upon the difference of the Helmholtz free energies of the

237

superconducting and normal states. At the bifurcation point, this difference is zero and the tangent stiffness matrix $\mathbf{K}^{EM}$ becomes singular.

The physical significance of what is occuring is that both the normal and superconducting states possess the same energy. In the actual physics, a variation of ψ occurs in the z direction, and the system chooses the eigenstate that possesses the lowest possible energy and entropy. To extend the current superconducting model to this problem, an adaptive mesh appears to be necessary to determine the boundary between parts of the conductor that are normal and superconducting. The adaptive mesh is also required to make $\mathbf{K}^{EM}$ well-conditioned enough that reasonable values of EM quantities can be generated by standard nonlinear solution techniques. Unfortunately, time limitations on the thesis research precluded the development of an adaptive two-dimensional mesh and the examination of the physics of this most interesting and challenging problem was foregone.

The STEP1D finite element used for the thesis research should possess a rank deficiency of one at the bifurcation point. In an effort to gain a better understanding of what was occuring at the bifurcation point with the finite element model, the model was forced to converge upon this point by setting the thermal loading to the critical temperature $\mathcal{T}_c$ and setting the current loading to a value that would generate the critical field $\mathbf{B}_c$ at the outer conductor boundary r_c. The corrective Newton-Raphson solution method was then used to iterate to the bifurcation point. The finite element model actually converged and returned a quantum state that carried no current and an applied external field of $\mathbf{B}_c$ at r_c. Even though $\mathbf{K}^{EM}$ should be singular at this point, a fact that precludes convergence, it is believed that

the STEP1D model converged for two reasons. First, the CNR iterative procedure is stopped when the 2-norm of $\mathbf{r}$ is smaller than the input tolerance τ. Second, the scalings and the factorization of $\mathbf{K}^{EM}$ introduce numerical round off errors that perturb the generated solution off of the bifurcation point just enough to render $\mathbf{K}^{EM}$ nonsingular.

The STEP1D model returned the result of an applied external field and no current in the conductor because it does not enforce the current conservation constraint $I - \int_\Gamma d\Gamma \hat{n}_c \cdot \mathbf{j} = 0$. The addition of this constraint automatically allows an EM model to distinguish between cases where the field at r_c is generated by a current I or by an externally applied $\mathbf{B}$ field. The eigenvalue analysis of $\mathbf{K}^{EM}$ for earlier versions of Ginzburg-Landau and London superconducting finite elements that contained the current conservation constraint showed that the current conservation constraint is redundant when no external fields are applied to the system or when $\mathbf{v}^{EM}$ does not lie upon the bifurcation point. These two cases are not considered in this work and are not presented here.

To summarize, the basic path determination process is as follows:

A.   Solve system of equations for $\mathbf{v}_{n+1}$.

B.   Find $\mathcal{T}_\infty$ by using $\mathcal{T}_\infty = \mathcal{T}_o + \zeta_{n+1}^{\mathcal{T}} \mathcal{T}_L$.

C.   Find $\mathbf{B}_c$ at $\mathcal{T}_\infty$ by using Equation (4.4.1).

D.   Find I by using $I = I_o + \zeta^{EM}_{n+1} I_L$.

E.   Find B_θ at r_c by using Equation (11.2.1).

F.   If $B_\theta(r_c) \geq \mathbf{B}_c$, go to H.; if not, go to G.

G.   If $\mathcal{T}_\infty \geq \mathcal{T}_c$, go to H.; if not, go to I.

H.   If the current EM element type is STEP1D, change it to LET1D and go back to A.; if it is not, go to J.

I. If the current EM element type is LET1D, change it to STEP1D, reset the reference state of $\mathbf{v}^{EM}$ and go back to A.; if it is not, go to J.

J. Accept solution vector $\mathbf{v}_{n+1}$ for the current step.

Additional logic statements are included in the actual coding to help prevent the STEP1D element from exceeding the bifurcation point. Beyond the bifurcation point, the element will "zero in" upon the same type of solution that occurs when the element is forced to converge upon the bifurcation point. A quantum state is generated where there is no current in the conductor and a boundary B_θ field loading of magnitude $(\mu_o I)/(2\pi r_c)$ exists. This state usually requires more iterations to converge upon a solution and a larger solution tolerance τ than physical states that lie below the bifurcation point on the equilibrium path. Non-physical solutions for the superconductor that lie beyond the bifurcation point can also cause the CNR procedure to fail if τ is too small or if the maximum number of allowed iterations for the solution procedure is exceeded.

To prevent the STEP1D element from moving past the bifurcation point and encountering these problems when the current load I is being incremented, steps C through E of the path determination procedure are performed prior to each corrector iteration. The current iteration value of ζ^{EM}_{n+1} is used for step D because the actual step size along the equilibrium path may change with each iteration. If the step size changes, then ζ^{EM}_{n+1} changes for each iteration and so does the value of I. If $\mathbf{B}_c$ is exceeded at r_c for any iteration, the program changes the element type to LET1D, and the solution procedure restarts at step n and attempts to increment the loading to step $n+1$.

For the case where the thermal loading is varied, steps B through E are performed prior to each predictor step. For this case where the temperature $\mathcal{T}$ is being incremented, the current I is held steady and causes no problems because ζ^{EM} is held constant and is known before the predictor and corrector steps are taken. $\mathcal{T}$ is also known *a priori* as being $\mathcal{T}_o + (\zeta_n^{\mathcal{T}} + l_n)\mathcal{T}_L$ at step $n + 1$ as discussed in Section 11.1. Because $\zeta_{n+1}^{\mathcal{T}}$ is known before the solution procedure begins, steps B through E of the path determination process can be used to determine if the solution vector will move past the bifurcation point *before the solution process begins*. Inserting this test before the predictor step keeps the program from performing an unnecessary solution step. After steps B through E of the path determination process are performed, $\mathbf{B}_c(\mathcal{T}_{n+1})$ and $\mathcal{T}_c$ are compared to $B_\theta(r_c)$ and $\mathcal{T}_{n+1}$ respectively. If either of the two latter quantities exceed their critical values the EM element type is changed to LET1D and the solution procedure is allowed to continue. If the critical values are not exceeded, the solution procedure is allowed to continue unaffected.

11.3 NUMERICAL EXAMPLES.

The LINT1D, LET1D and STEP1D finite elements derived in previous chapters have been applied to the solution of the test problems described later in this section. The CUPLE1D and STEP1D elements were used to determine EM quantities and the LINT1D element was used to determine the thermal distribution for the normal state of the superconductor. The temperature of each node of the superconductor is calculated as described in Section 11.1 of this chapter. The description of the nodal degrees of freedom and the calculation of the material properties of each element may be found

241

in their respective chapters. The application of boundary conditions, scaling techniques, mesh generation techniques and the assembly and solution techniques are also described in the respective chapters. For the graphical results generated in this chapter, B_θ was calculated by using the integral form of Maxwell's inhomogeneous equation for magnetic fields, Equation (7.1.5). This equation requires knowledge of $j_z^{(e)}$ to determine B_θ. For the superconducting phase, $j_z^{(e)}$ is calculated by using Equation (3.2.16) and for the normal phase $j_z^{(e)}$ is calculated by using the elemental values returned in the solution vector $\mathbf{v}$. The integral of Equation (7.1.5) is evaluated by 2 point Gaussian integration.

11.3.1 PROBLEM 1: VARYING T LOAD.

For this problem and the next, the test material is high purity aluminum. Reference and initial states of the system are set as described in previous chapters. The geometry is that of a one-dimensional axisymmetric wire as shown in Figure 2.1. The wire radius r_c is 1.15×10^{-4} meters and transported a total current I in the positive z direction. The initial current I_o is 1 ampere and the loading current I_L is 0 amperes. The initial free stream temperature is $.5625^o$ Kelvin and the loading temperature I_L is 1° Kelvin. Because the free-space magnetic field element has been validated previously, all elements are within the wire. The mesh for the superconducting phase has 98 elements in the boundary layer and 2 elements in the bulk layer while the mesh for the normal phase of the conductor has 50 elements in the coarse mesh and 50 elements in the fine mesh. As in Chapters IX and X the depth of the fine mesh was $.25\ r_c$ for the normal conductor. The depth of the boundary layer mesh for the superconducting phase varies with

temperature as discussed in Chapter VIII. The step size l_n is chosen as .0125 and 80 steps are used to increment ζ^T from 0.0 to 1.0. A solution tolerance τ of 4×10^{-17} is used for the superconducting state and 9×10^{-4} is used for the normal state.

The solution procedure required 41 steps in the superconducting phase averaging 4.61 iterations per step. The estimated condition number for these steps ranges between 181 and 834. The solution procedure then required 39 steps in the normal phase with an average of 2 iterations per step. The estimated condition number varies between 29861 and 204664.

Data output files for all of the figures to be shown for all examples in this chapter are saved every tenth step and all graphical representations of this data are labeled with the appropriate values of ζ^T or ζ^{EM} when it was possible. Graphical representations of each data set are generated by using the PLOT2D utility to produce a raster file and then using the raster files to create a PostScript language file. This is mentioned because the graphical representations of data sets are subject to the limits of the PLOT2D utility. The data sets for each variable were then loaded into a single file, and PostScript language commands were used to generate axes and data set labels and legends. This is mentioned for researchers who wish to duplicate the graphical results because the PLOT2D utility does not possess the ability to add the desired labels and font types or graph 10 sets of data on a single graph.

Results for the temperature distribution within the wire are shown in Figure 11.1 and match the expected physical behavior. The results for $|\psi|^2/|\psi_\infty|^2$ in the region $1.023 \times 10^{-4} \leq r \leq r_c$ are presented in Figure 11.2. The value of the normalized value of $|\psi|$ is not shown over the whole

conductor because all of the physics of interest occured within the boundary layer. The value for $|\psi|^2/|\psi_\infty|^2$ for r in the region $0 \leq r \leq 1.023 \times 10^{-4}$ is a constant equal to 1.0. The expected physical behavior for the normalized value of $|\psi|$ in the boundary layer was that as the temperature increased, the boundary layer depth would increase and $|\psi|^2/|\psi_\infty|^2$ would vary over a wider range of r. This physical behavior is accurately captured by the STEP1D element and is shown in Figure 11.2. Figures 11.3 and 11.4 show the value of the current density $j_z^{(e)}$ in the normal and superconducting phases respectively. For the superconducting phase, only the boundary layer values are shown with all other values of $j_z^{(e)}$ being equal to zero. The value of $j_z^{(e)}$ at each node for the superconducting phase is calculated by use of Equation (3.2.16). Because the current I was steady, the magnitude of the current density should decrease as the temperature increases for the superconducting phase. The boundary layer depth should also increase. Again both physical characteristics are accurately depicted by the STEP1D model.

For the normal phase of the conductor, $j_z^{(e)}$ is depicted as a step function in Figure 11.4. The step function represention is necessary because the current density is approximated by a step function over an element by the LET1D finite element. The results for the steps where ζ^T equals 0.7 and 0.9 were omitted for clarity. By referring back to Figure 11.1 some determinations can be made about the behavior of $j_z^{(e)}$ for the normal phase. It can be seen that the temperature is higher at the center of the conductor than at r_c. The resistivity should also be higher at the center and $j_z^{(e)}$ should be smaller there.

As the temperature of the wire increases, the amount of thermal energy produced by the current I through a wire should remain almost constant. The rest of the thermal energy in this system comes from the free stream temperature boundary conditions. The significance of this is that the temperature distribution in the wire should become more homogeneous and the magnitude of the heat absorbed by the system from the free stream boundary conditions should eventually become greater than the magnitude of the heat produced by resistance to the current I. The resistivity will also be determined more by the boundary conditions than by the heat generated by the steady current I. The temperature should become more homogeneous throughout the wire and the resistivities and current densities should follow suit. This expected behavior is accurately modeled by the finite element approximation as can be observed in Figure 11.4.

The only behavior that at first appears to be non-physical is the jump in the magnitude of the current density as the conductor changes from the normal to the superconducting phase. This is easily explained because $j_z^{(e)}$ is a function of the resistivity ω and the $\mathbf{E}$ field for the normal state while it is a function of $\mathbf{A}_z^{(e)}$ and $|\psi|$ for the superconducting state. The easiest way to verify that the current density predicted by the finite element method is exact is the use of the integral form of Maxwell's inhomogeneous magnetic field equation (Equation (7.1.5)) to evaluate B_θ at r_c. This equation requires that no matter what the j_z distribution may be, that for wires carrying the same current I, the value of B_θ at r_c will always be the same. Because the current I is held steady for this example, B_θ should always be the same at r_c independent of the quantum state of the conductor. Figure 11.5 shows this expected behavior accurately and also demonstrates why Equation (7.1.5)

has been used to compute the B_θ field for the results presentation of this chapter. Equation (7.1.5) allows the value of B_θ to be computed at each node while the equation used in previous chapters, Equation (5.3.2), only allows the computation of the mean value of B_θ over each element. By using Equation (7.1.5), the accuracy of computed values of $j_z^{(e)}$ can easily be verified by comparing values of B_θ at r_c.

Figures 11.5 and 11.6 show the distribution of the B_θ field within the conductor as the temperature was increased. Figure 11.5 shows only values of B_θ that lie within the boundary layer while Figure 11.6 shows values for the normal state of the conductor for r between 0 and r_c. In Figure 11.5, it can be seen that the B_θ field penetrates more deeply into the conductor as the temperature of the conductor increases. This is the desired and expected physical behavior. In Figure 11.6, it can be seen that the small increase in the temperature for ζ^T equal to .6 to 1.0 produces no significant changes in the B_θ field. The changes are so small that the PLOT2D utility connot discern changes in B_θ as the temperature increased although there is a small change in the B_θ field that follows changes in $j_z^{(e)}$. The maximum nodal change of B_θ as ζ^T is varied from .6 to 1.0 was $\sim 2 \times 10^{-4}$ percent. This percent difference of B_θ occurred between the states where ζ^T was equal to .6 and 1.0.

11.3.2   PROBLEM 2: VARYING I LOAD.

As mentioned earlier, the test material is high purity aluminum. Reference and initial states are set as described in previous chapters. The geometry is the same as that of Problem 1 of this chapter with r_c being equal to 1.15×10^{-4} meters, $N_{coarse} = N_{fine} = 50$ elements for the normal

state and N_{bulk} and N_{bound} being equal to 2 and 98 elements respectively for the superconducting state. The initial current I_o is 1 ampere and the loading current I_L is 2.1 amperes. The initial free stream temperature T_o is 1° Kelvin and the loading temperature T_L is 0° Kelvin. Again no elements were generated external to the conductor/free space boundary located at r_c. Meshes for both states are generated as described in Chapters VIII and IX. The step size l_n is chosen to be .01 and 80 steps were used to increment ζ^{EM} from 0.0 to .73. The solution tolerances τ of 4×10^{-17} and 9×10^{-4} are used for the superconducting and normal states respectively.

The solution procedure required 40 steps in the superconducting phase averaging 3.65 iterations per step. The estimated condition number for these steps ranged between 231 and 10935. The solution procedure then required 40 steps in the normal phase averaging 2.05 iterations per step. The estimated K condition number for these steps varied between 28146 to 181319. Data output files were saved every tenth step as stated in the previous section.

Results for the temperature distribution in the whole wire are shown in Figure 11.7. Because the free stream temperature T_∞ is held constant at 1° Kelvin, the major source of heat energy comes from resistance of the current flow I through the wire rather than from boundary loading. This caused the temperature differential between the center of the wire and r equal to r_c to be greater than in Problem 1 of the previous section. This expected physical behavior is shown in Figure 11.7.

Figure 11.8 depicts the behavior of $|\psi|^2/|\psi_\infty|^2$ for the region where r varies between 1.0597×10^{-4} and 1.1887×10^{-4} meters. For r between 0 and 1.0597×10^{-4} meters, $|\psi|^2/|\psi_\infty|^2$ is unity. Graphical results of the data

obtained for ζ^{EM} equal to .16 and .30 are omitted for clarity. Physically it is expected that as the current I is increased, the system will move to a higher energy state. As the energy of the system increases, the boundary layer should widen independently of whether the energy source is thermal or electromagnetic in nature. This behavior is accurately reflected in Figure 11.8, but comparison of this plot with Figure 11.2 shows that for the current I loading case, it appears that there was more of a shifting of the distribution of the Cooper pairs towards the center of the conductor rather than a reordering of the distribution. An explanation of the physics of these two cases can be made by invoking the London model of superconductivity.

With the London model, the number density of Cooper pairs $|\psi|^2$ is only a function of the temperature T and is equal to $|\psi_\infty|^2$. Using this information and refering to Equation (4.4.4), it can be seen that as the temperature increases, the total number of the Cooper pairs will decrease. This is the general behavior of the Ginzburg-Landau superconductor as well. As the temperature increases in Figure 11.2, the number of Cooper pairs in the current stream must also remain constant because I is constant. To maintain the same number of Cooper pairs within the current stream as T increases, the system must reorder itself and impart a kinetic momentum to pairs that lie deeper within the boundary layer.

For the case of an increasing current I and steady temperature T, the total number and distribution of the Cooper pairs must remain approximately constant. As the current I is increased, the number of the Cooper pairs remains essentially constant, but the number of Cooper pairs with a kinetic momentum increases. This increase in the energy of the system destroys some of the Cooper pairs. The annihilation of Cooper pairs occurs at

the most energetically favorable position, within the boundary layer. This also serves the dual purpose of widening the boundary layer, upon which an increased number of Cooper pairs with kinetic momentum is allowed to move more easily. This expected behavior explains why there is more of a "shifting" of the distribution of the Cooper pairs in Figure 11.8 than a reordering of the distribution. The boundary layer is widening in response to the increasing number of pairs with a kinetic momentum. In Problem 1, the amount of Cooper pairs annihilated by the increasing thermal energy is much greater than those destroyed by the increasing EM energy of Problem 2. This relative change in the number of Cooper pairs as an incremental step is taken explains the nature of the difference of the two plots.

Figures 11.9 and 11.10 show the change in $j_z^{(e)}$ as ζ^{EM} was incremented. Figure 11.9 shows the superconducting state and Figure 11.10 shows the normal state. Figure 11.9 only shows values in the boundary layer. Outside of this layer, the plotted values of $j_z^{(e)}$ for the superconducting state vanish. For this figure, different line types and a legend are used so that the plots for ζ^{EM} equal to .30 and .32 are more easily distinguishable. The graphical representation of $j_z^{(e)}$ in Figure 11.9 matches the expected physical behavior. As I is increased, the boundary layer should spread and the magnitude of $j_z^{(e)}$ should also increase. The STEP1D finite element also captured this expected behavior well. As in Problem 1, the current density should be higher at r_c than the center of the conductor for the normal state. There should also be an increase in the magnitude of $j_z^{(e)}$ as the current I is increased. The LET1D element performed as expected and modeled this expected physical behavior.

Figures 11.11 and 11.12 show the Finite Element values of B_θ plotted over the boundary layer and the whole conductor respectively. Figure 11.11 omits the labels for ζ^{EM} equal to .50 and .66 for clarity. Similarly, Figure 11.12 omits the labels for ζ^{EM} equal to .16, .23, .30, .50 and .66. The expected physical behavior for the superconducting state is that as the current increases, the magnitude of B_θ will increase and penetrate more deeply into the boundary layer. For the normal state, the magnitude of B_θ should keep on increasing but it should also be an almost linear function of the distance r from the center of the conductor. Both of these physical behaviors are again modeled well by the finite element computed solutions and illustrate the ability of the four-potential based finite elements to model EM fields.
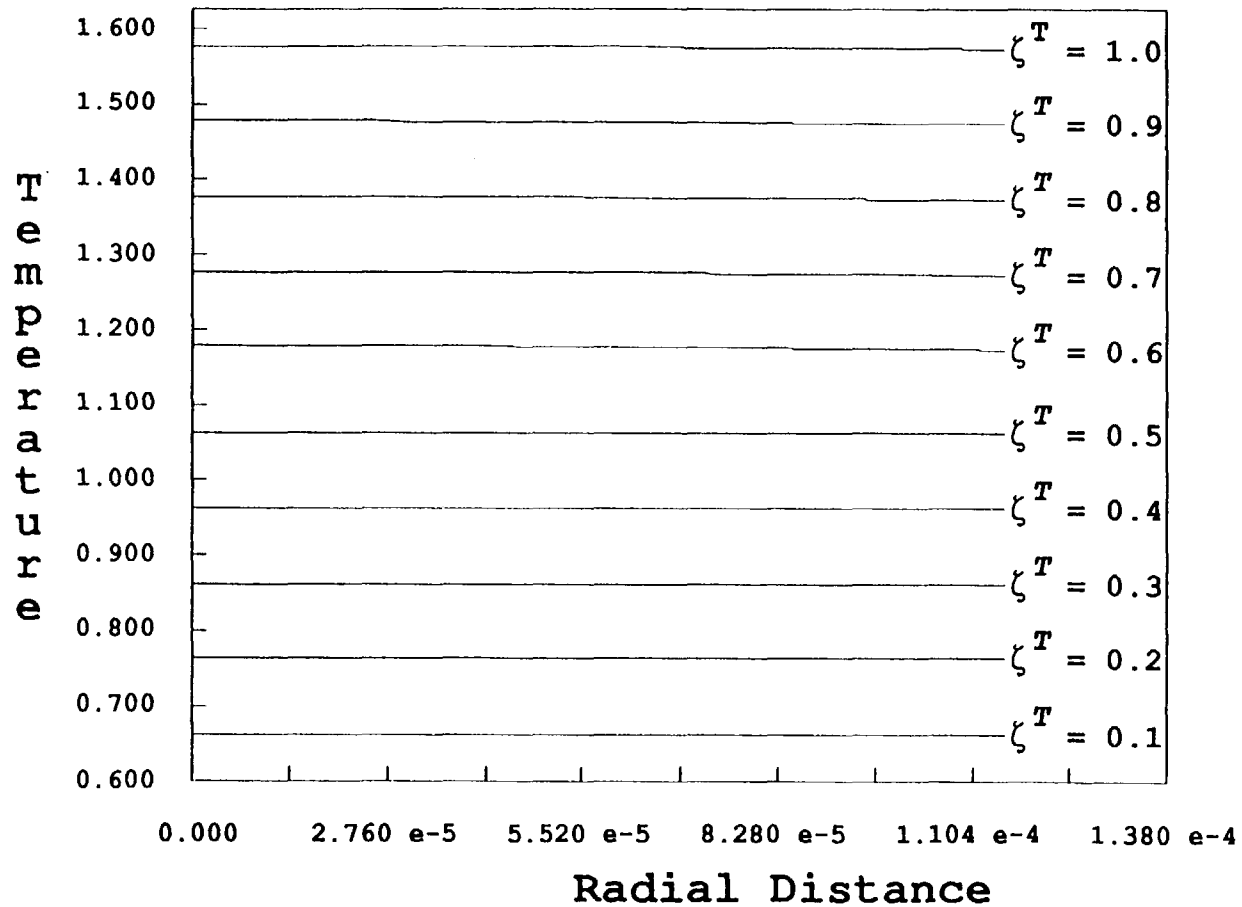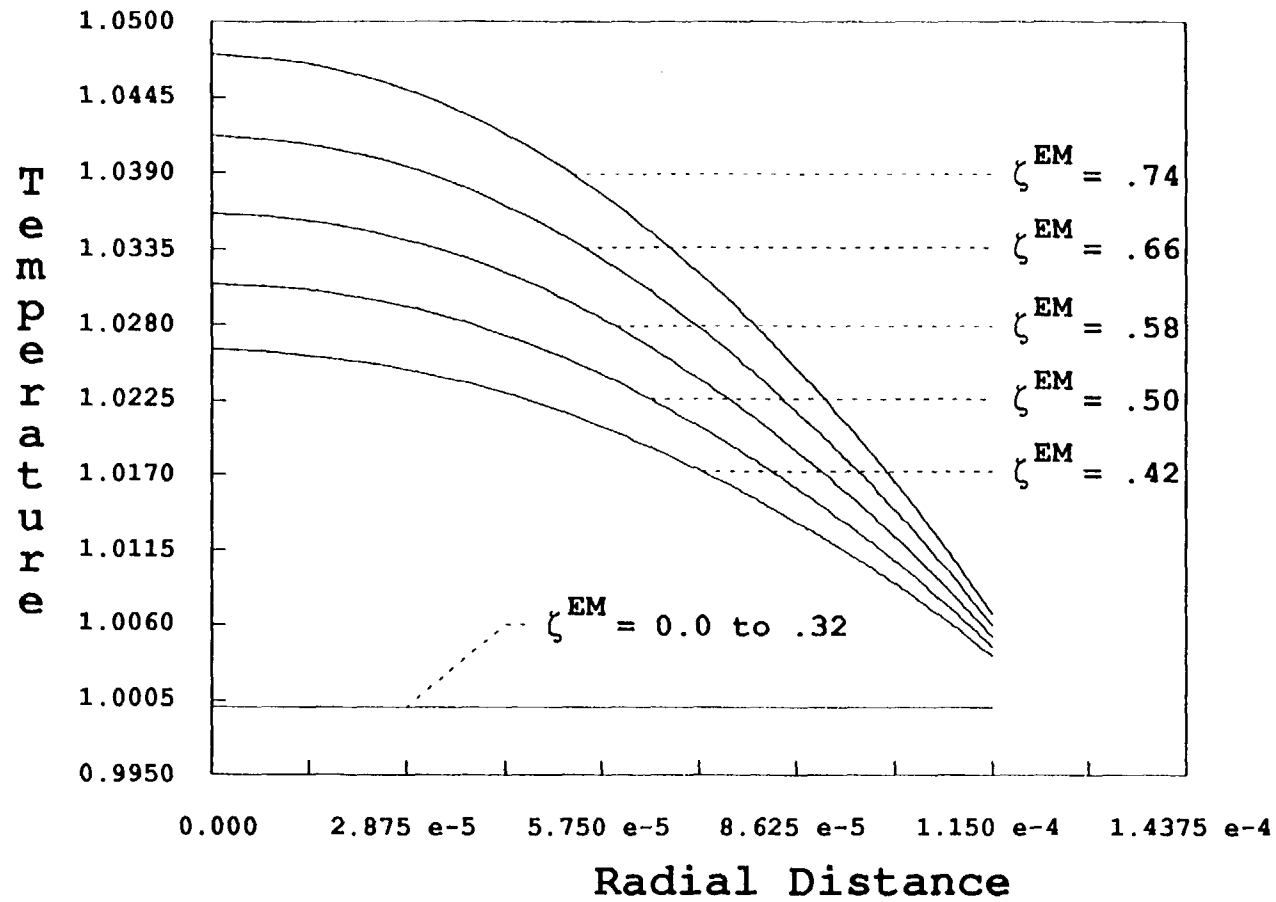
Figure 11.1: T vs. r. Values of T for complete mesh plotted.
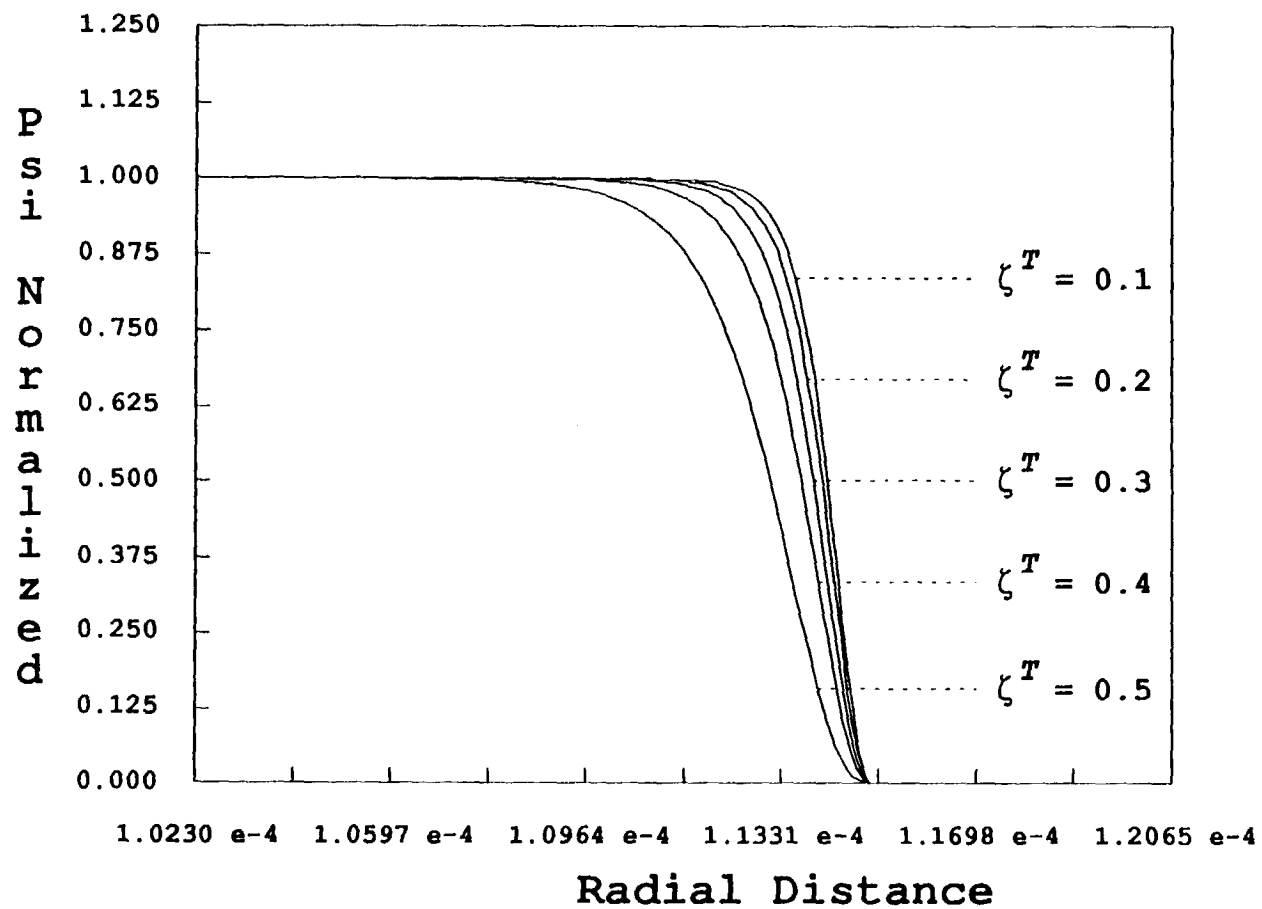
Figure 11.2: $|\psi|^2/|\psi_\infty|^2$ vs. r. Values for $|\psi|^2/|\psi_\infty|^2 \neq 1$ plotted.
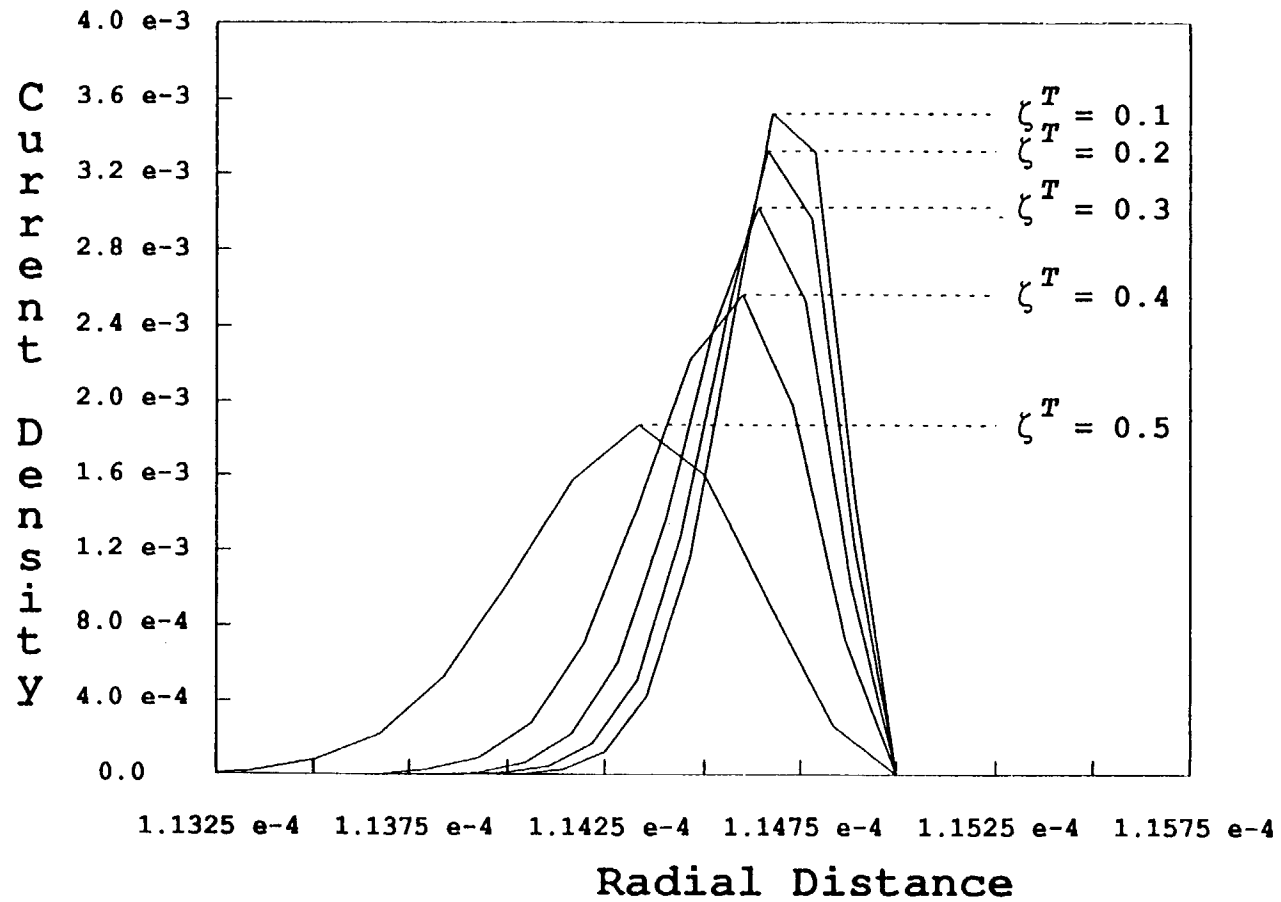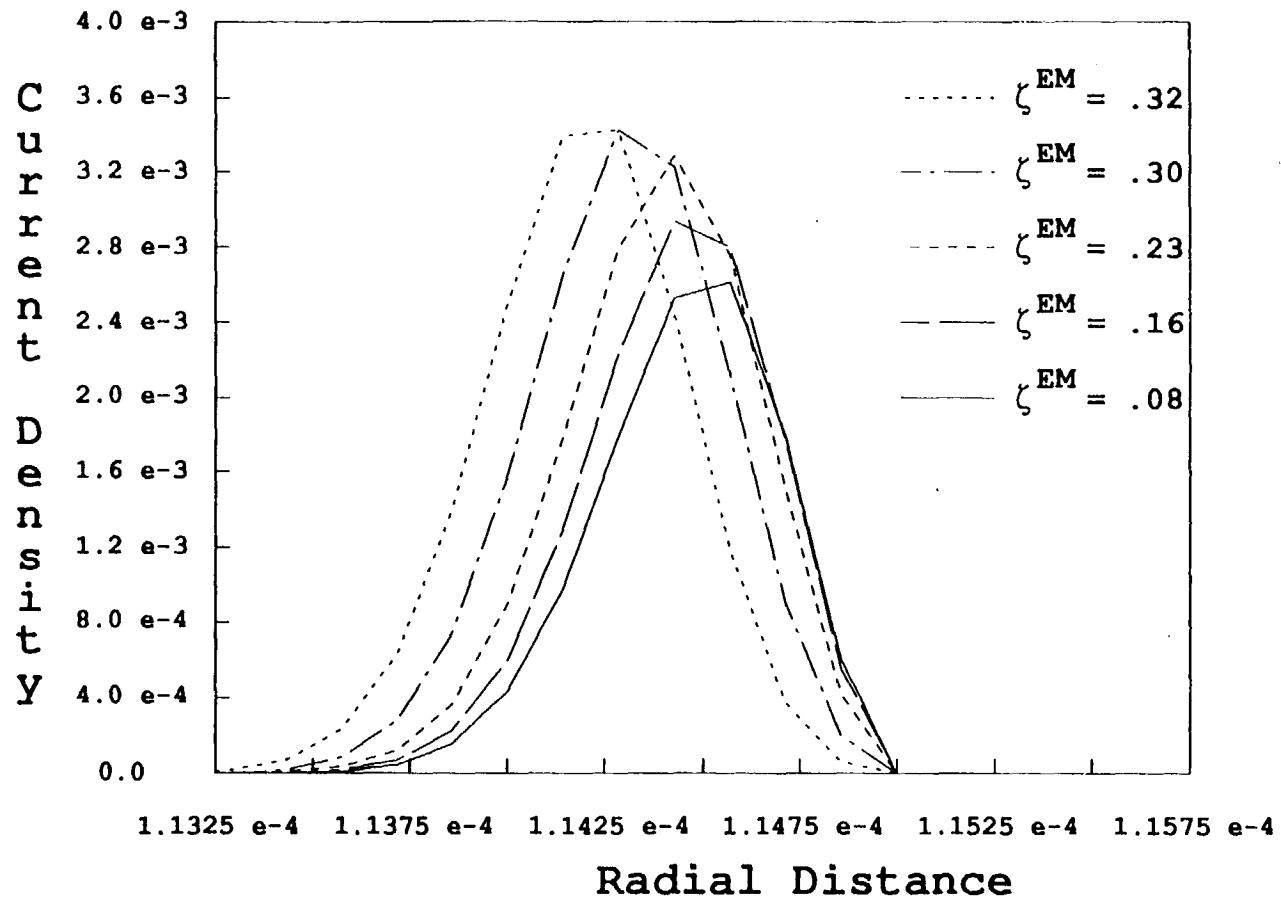
Figure 11.3: j_z vs. r. Nonzero values for j_z plotted for the superconducting state.
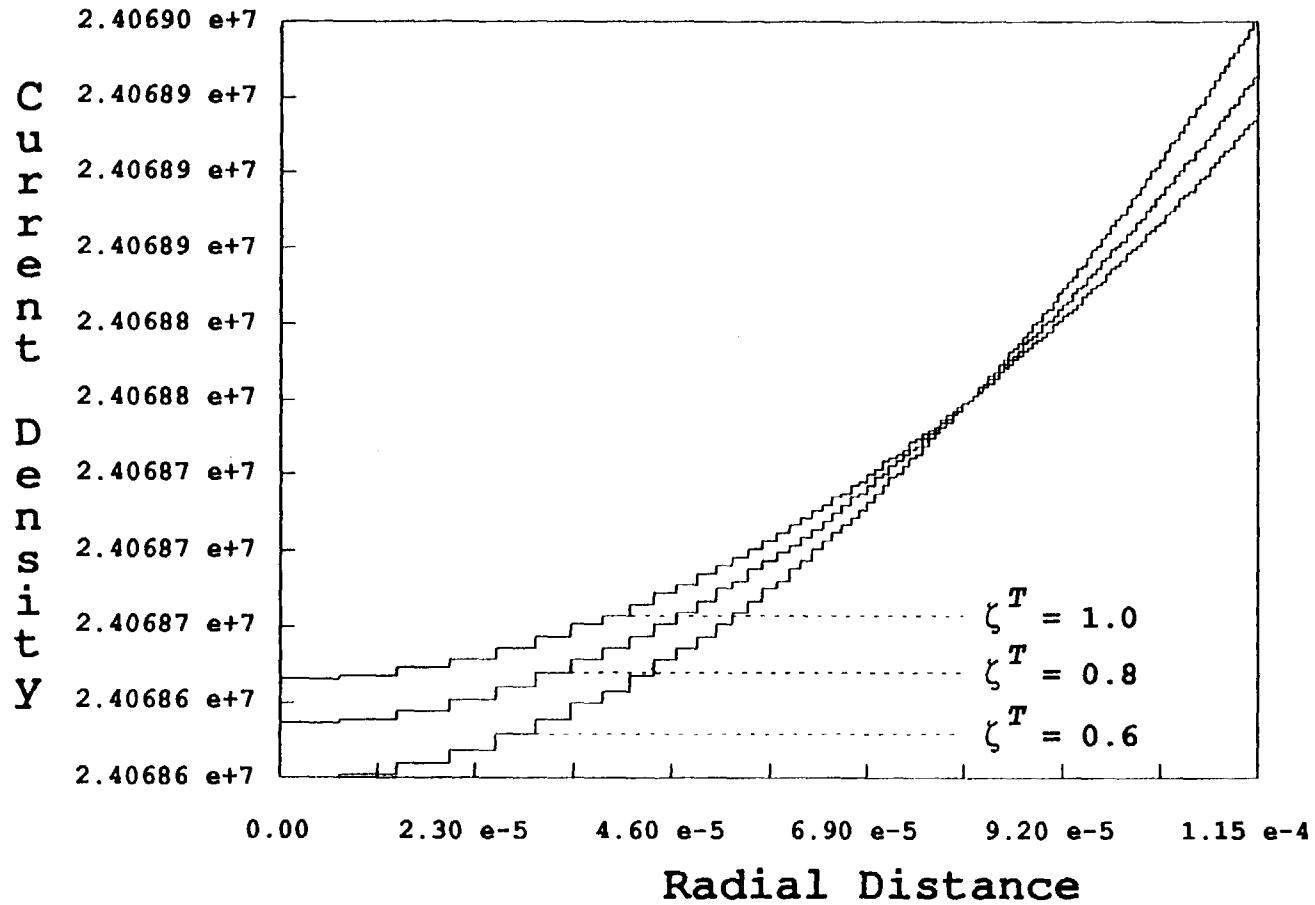
Figure 11.4: j_z vs. r. Values of j_z for complete mesh plotted for the normal conducting state. Graphs for $\zeta^T = .7$ and .9 omitted for clarity.
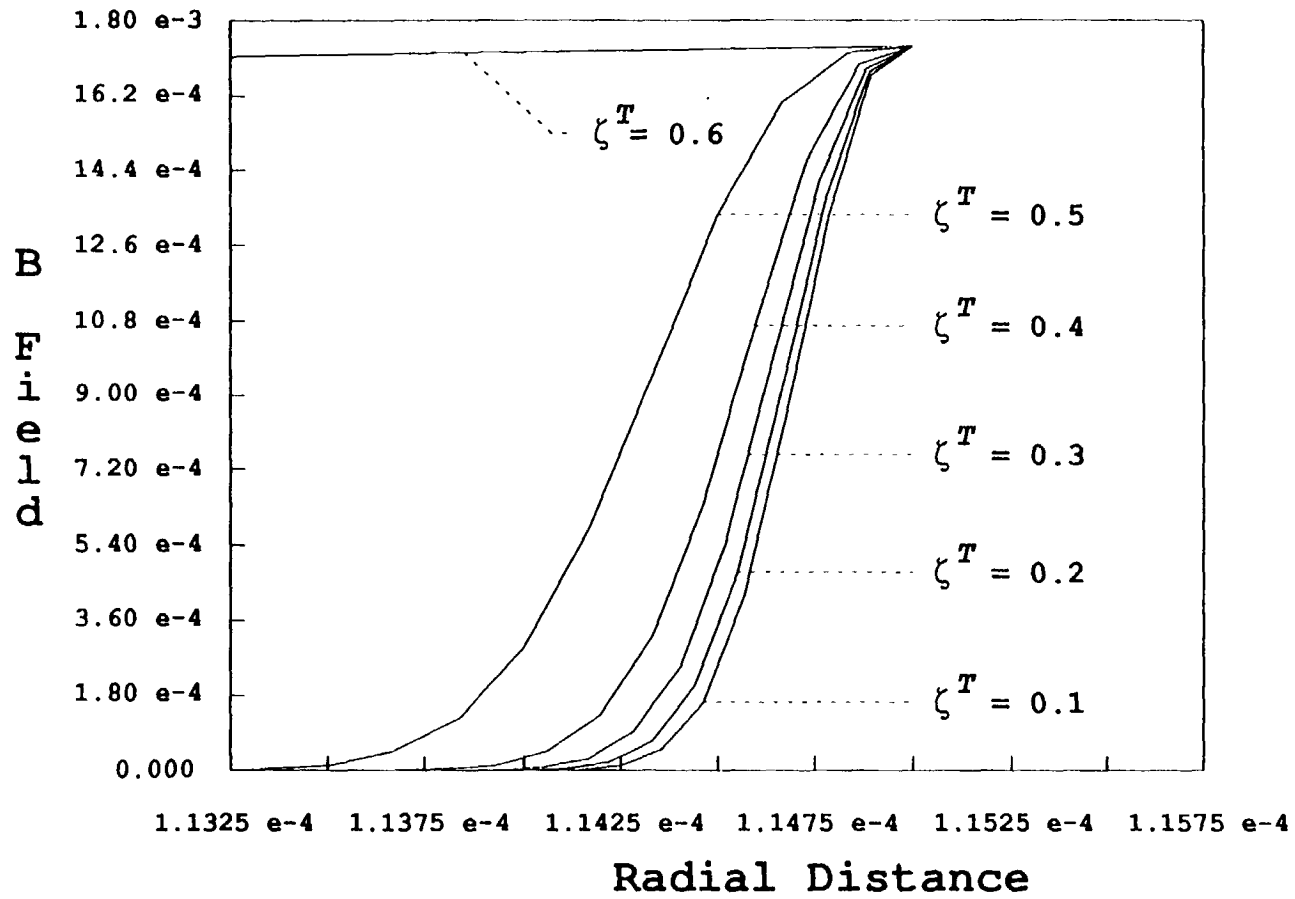
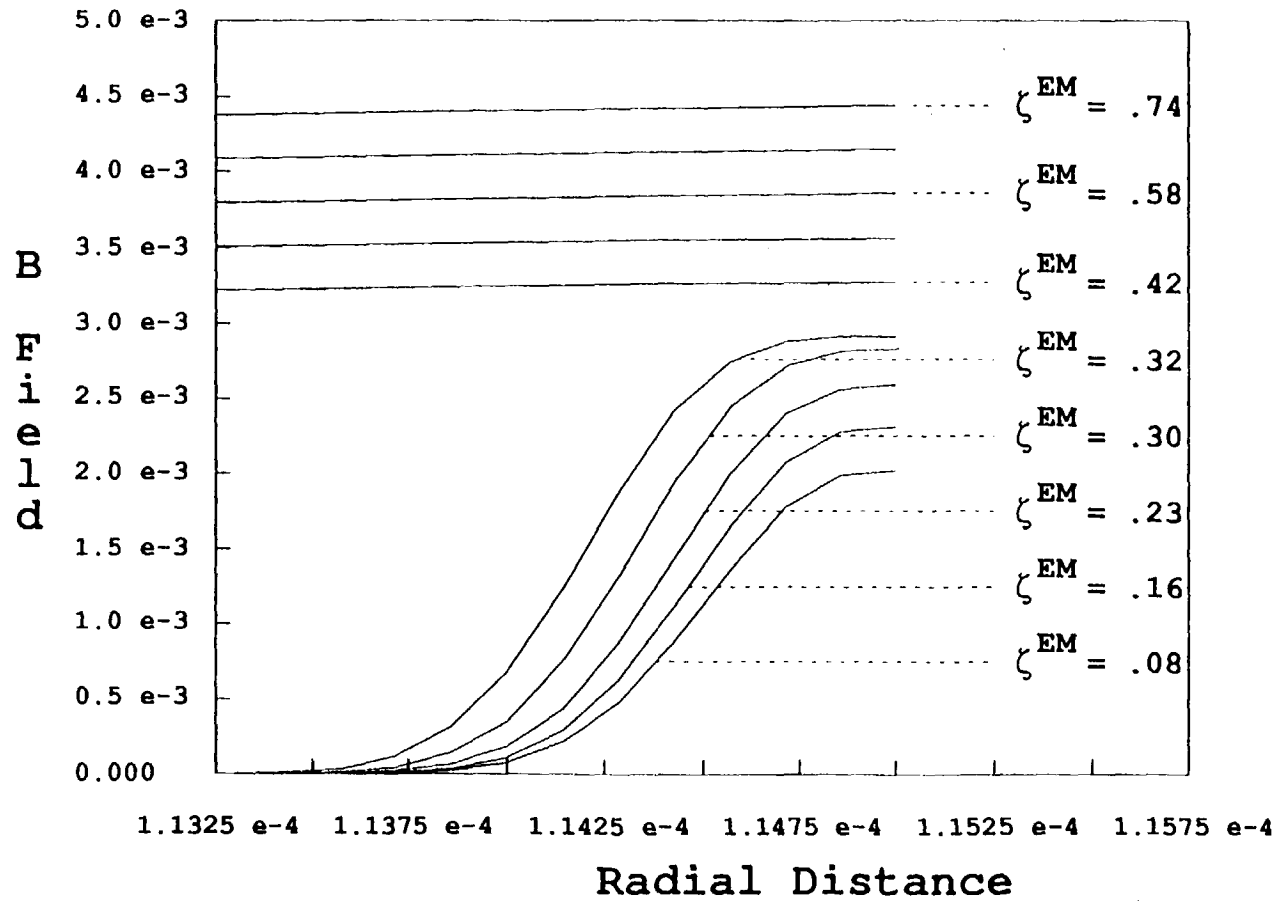Figure 11.5: B_θ vs. r. Nonzero values for the superconducting state plotted. One graph for the normal state also plotted in the same range.
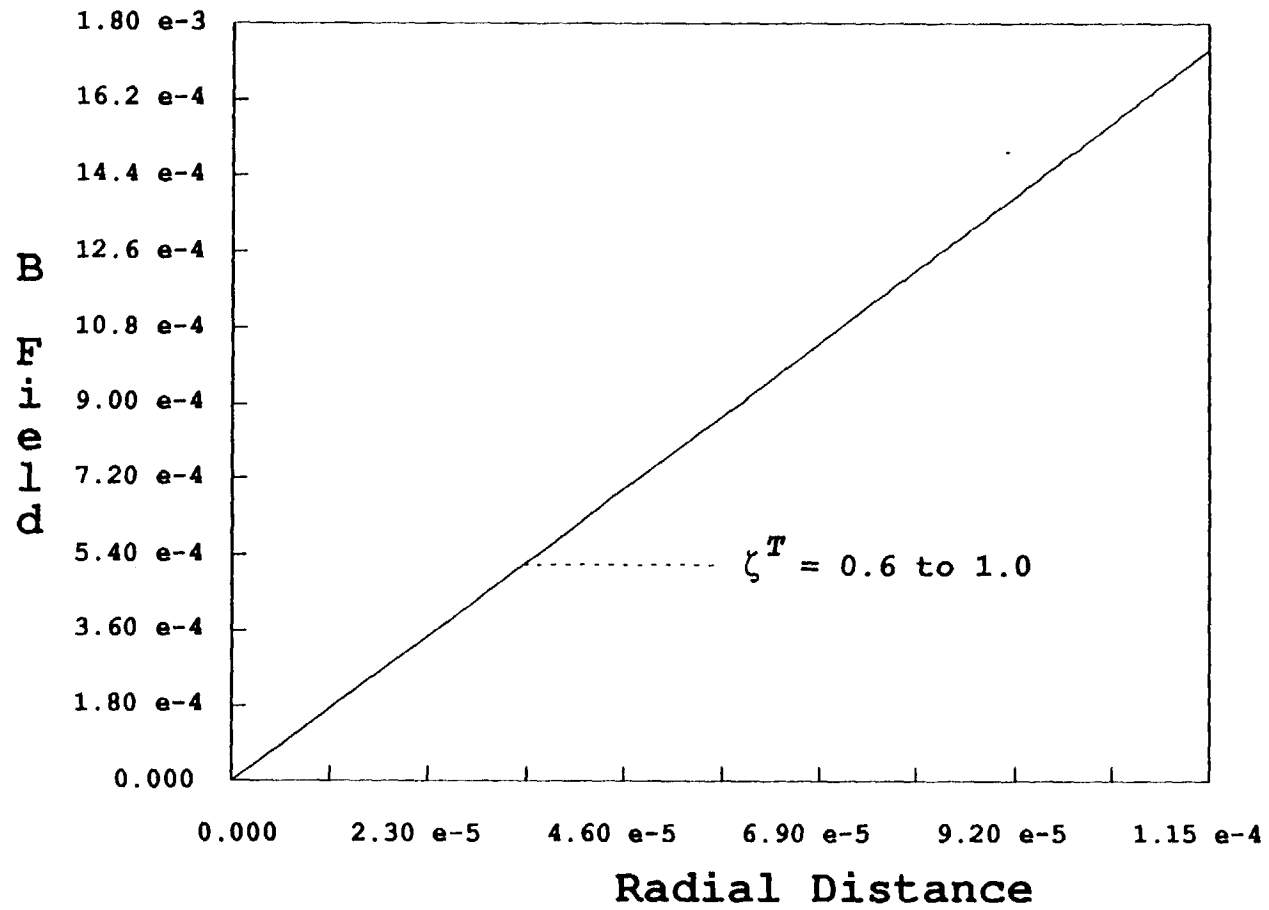
Figure 11.6: B_θ vs. r. Values of B_θ for complete mesh plotted for the normal conducting state.

Figure 11.7: T vs. r. Values of T for complete mesh plotted.
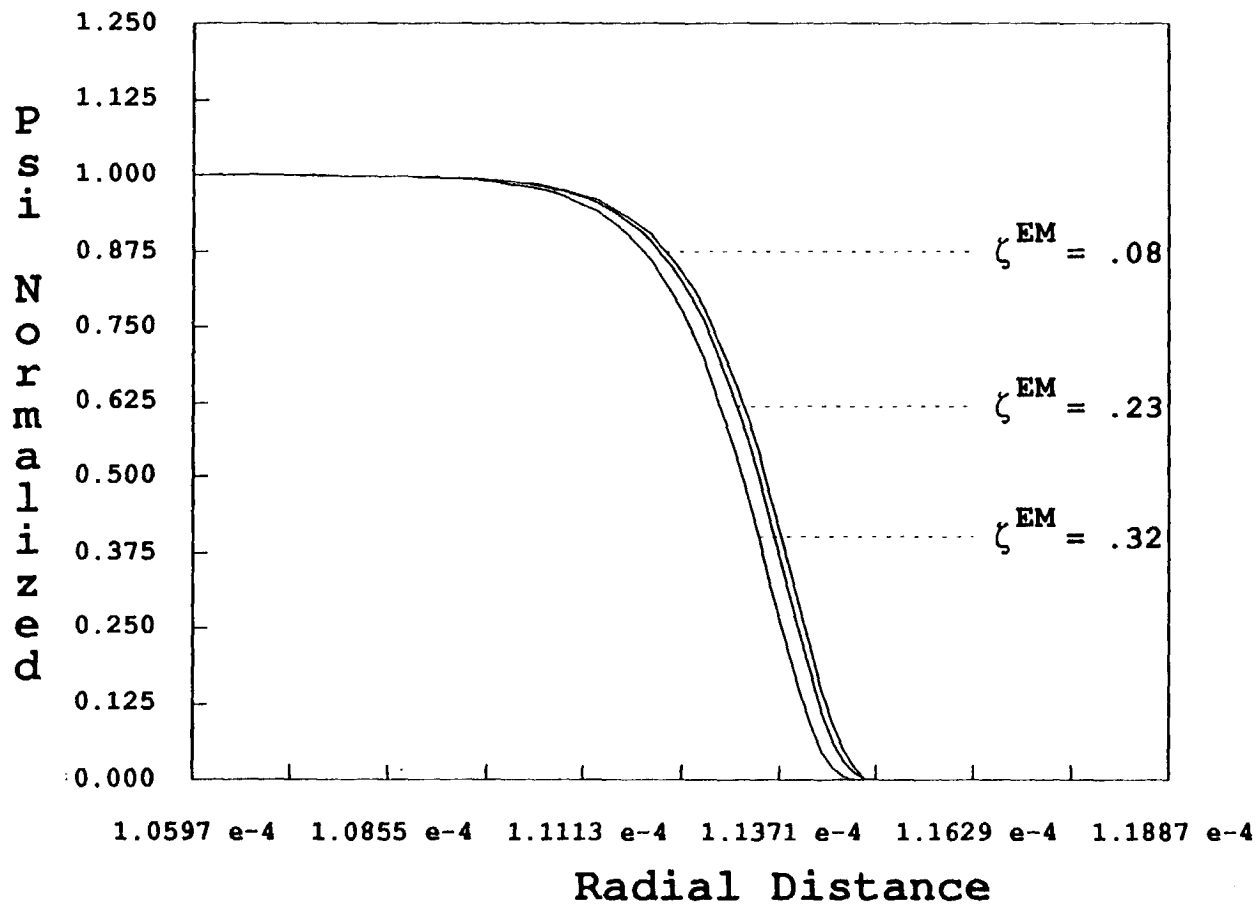
Figure 11.8: $|\psi|^2/|\psi_\infty|^2$ vs. r. Values for $|\psi|^2/|\psi_\infty|^2 \neq 1$ plotted. Graphs for $\zeta^{EM} = .16$ and $.30$ omitted for clarity.

Figure 11.9: j_z vs. r. Nonzero values for j_z plotted for the superconducting state.
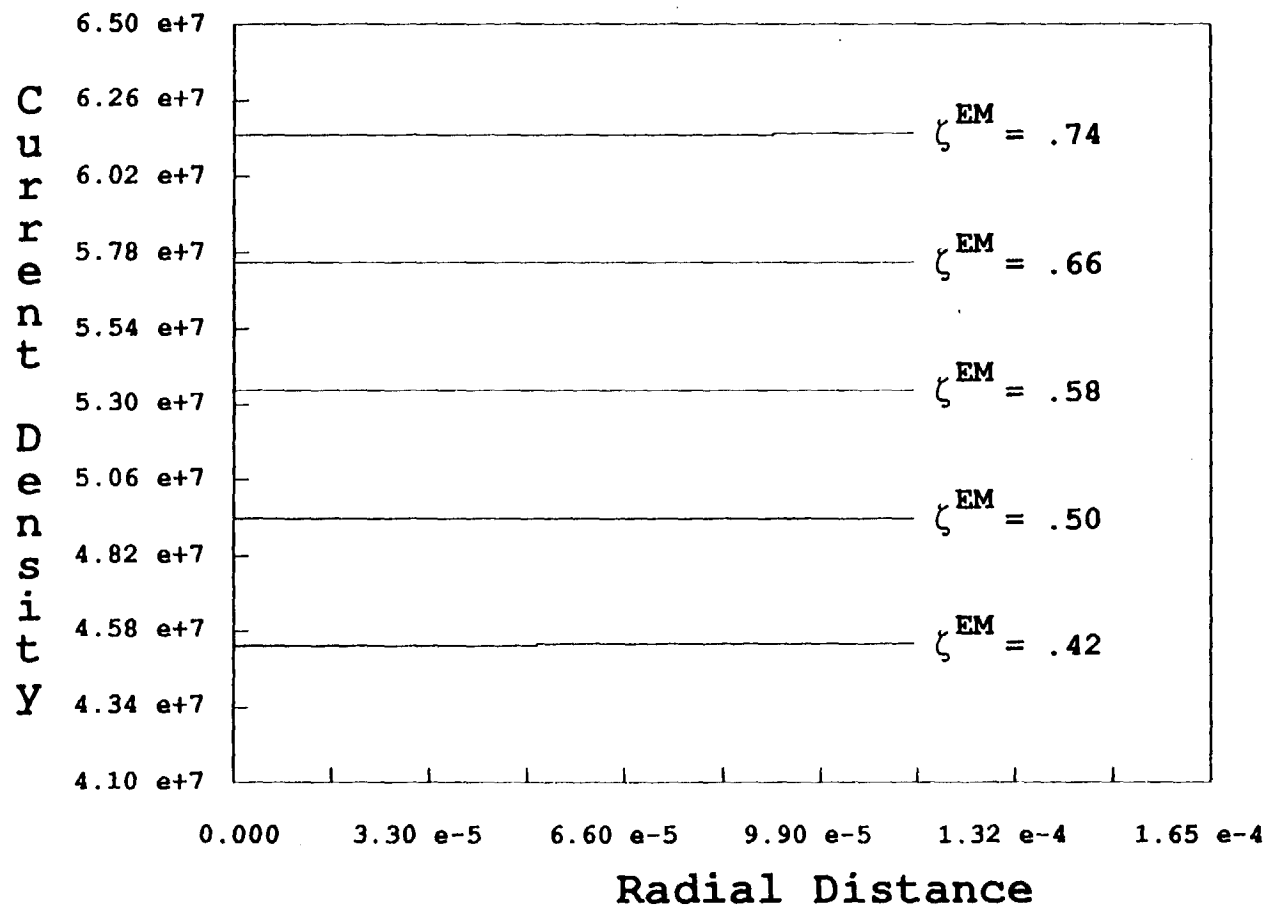
Figure 11.10: j_z vs. r. Values of j_z for complete mesh plotted for the normal conducting state.

Figure 11.11: B_θ vs. r. Nonzero values for the superconducting state plotted. Values for the normal state also plotted in the same range. Labels for $\zeta^{EM} = .50$ and $.66$ omitted for clarity.
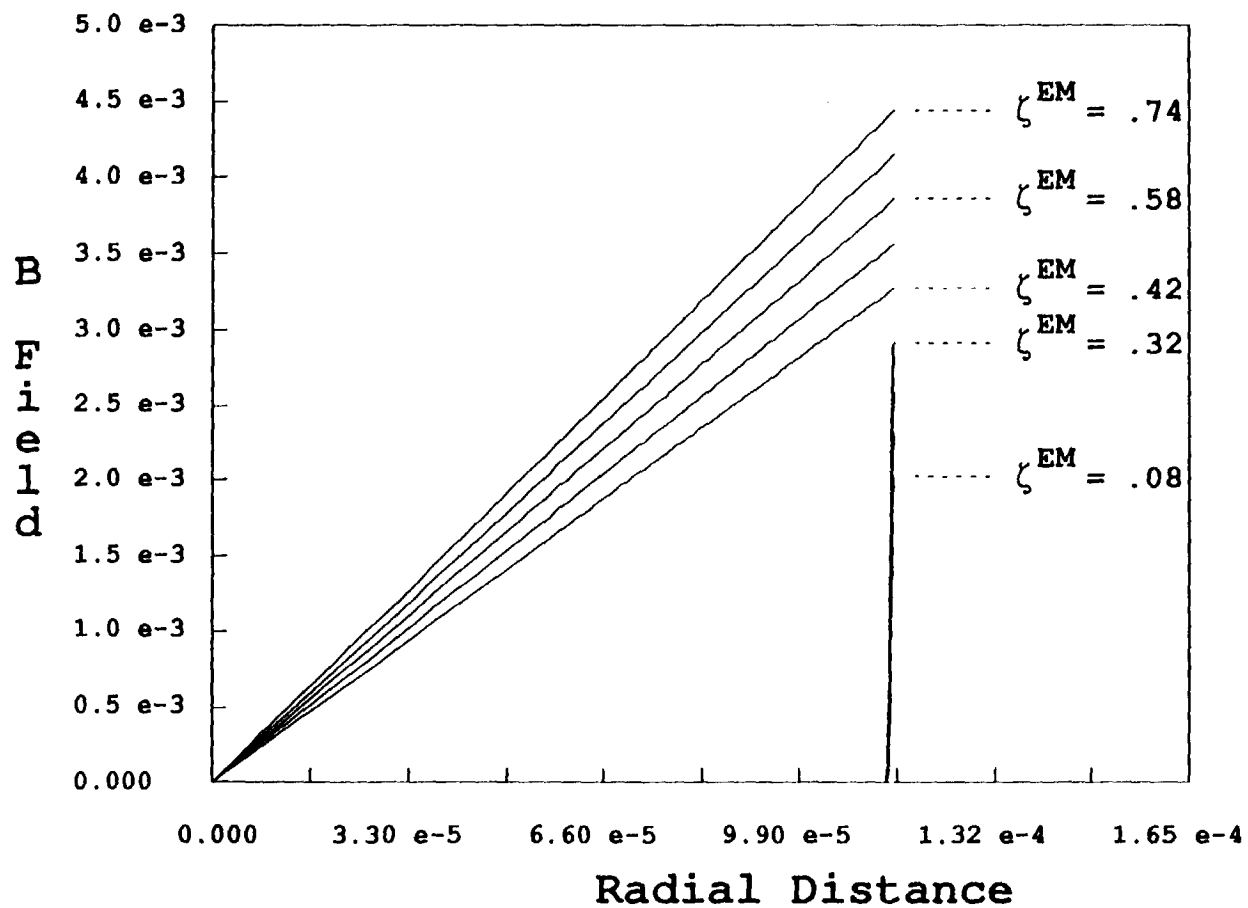
Figure 11.12: B_θ vs. r. Values of B_θ for complete mesh for both normal and superconducting states plotted. Legends for ζ^{EM} = .16, .23, .30, .50 and .66 omitted for clarity.

11.4 SUMMARY.

This chapter "glues" together all of the previously derived finite elements into a comprehensive program that can determine the correct equilibrium state of a thermally and quantum mechanically coupled EM system. The primary emphasis is the discussion of the results for two different coupled problems but two other topics are also discussed: the solution of the superconducting problem where I is constant and T_∞ is varied, and the determination of whether an EM system is in the superconducting or normal state.

The constant I, varying T_∞ problem mentioned above is solved rather easily as is the determination of the correct quantum state. The only real problem and failing of the final model that is developed here is its inability to accurately model a system within a conductor that has mixed normal and superconducting states near the transition point. Fortunately, the four-potential method is readily extensible to the solution of this problem although it is not addressed in this thesis primarily because the development of an adaptive two-dimensional mesh to deal with conditioning problems of the tangent stiffness matrix would have required a considerable investment of time and effort.

CONCLUSIONS.

12.1 SUMMARY OF WORK.

As mentioned in Chapter 1, the primary purpose of this work is to develop a finite element model for types I and II superconductivity that can accurately predict EM quantities. This model is to include thermal effects and to have the ability to change between superconducting and normal phases when necessary. Originally, this model was to be based upon the four-potential variational principle to reduce the number of degrees of freedom per element node. However, it was discovered during the course of research that the four-potential variational principle offered more advantages for the analysis of EM problems than just the simple reduction of element nodal degrees of freedom. More important is the ability of the four-potential method to model *any* EM problem that has been posed here through the adjunction of constraints by a Lagrangian multiplier. An equally important advantage of the four-potential method is that **B** and **D** discontinuities at material interfaces are enforced automatically and require no special attention from the user. The current predicting elements presented in this work required a special boundary treatment solely because **j** is used as an independent variable instead of Φ. This choice was made originally to simplify the current conservation constraint and was not changed. The simpler Φ formulation

given by Equation (3.1.5) reduces the number of degrees of freedom required by a one-dimensional current predicting finite element by two.

To produce the desired four-potential based EM finite element mentioned in the first paragraph, a functional that used $\mathbf{A}$ and Φ is first developed for any arbitrary material. This functional is then augmented by the Lorentz gauge constraint to ensure that $\mathbf{A}$ is unique. The augmented functional is then applied to one and two-dimensional geometries and the natural boundary conditions of the two geometries are determined. At this point, it was determined that a further extension of the new functional was necessary to model the more general case of an unknown current density $\mathbf{j}$. This extension is necessary because the arbitrary nature of geometries for EM problems does not always permit *a priori* knowledge of the distribution of a current within a conducting medium. It was also realized that temperature differentials within a conductor make the resistivity within a conductor inhomogeneous. The varying resistivities also preclude an *a priori* knowledge of $\mathbf{j}$ within a conductor.

To model the thermal effects that are eventually added to the EM model of a normal state conductor it was therefore necessary to extend the previously derived four-potential functionals to include cases where $\mathbf{j}$ is unknown. This is accomplished by augmenting a gauged form of the four-potential functional by an additional constraint, the current conservation constraint. The functional is also modified by making $\mathbf{j}$ a primary variable instead of Φ through the use of the constitutive relation between Φ and $\mathbf{j}$. This substitution requires the additional augmentation of the functional by a boundary continuity constraint. The additional constraint is necessary because the previous substitution for Φ inhibits a necessary integration by

parts that ensures the continuity of the E field across material interfaces. The final functional is a four-potential based functional for determining EM fields in linear conducting materials.

The next phase extends the four-potential variational principle to cover type I and II superconducting materials. The Ginsburg-Landau equations provide the necessary basis for this extension. The variational functional used to derive these equations contains the magnetic vector potential **A**. This functional also contains terms that represent a Landau expansion of the Helmholtz free energy of the quantum wave order parameter ψ around the critical temperature T_c. To adapt this functional to the four-potential method the electric field energy U_E is added and the gauge constraint adjoined. The gauge constraint used here is the London gauge which is identical to the Lorentz gauge for magnetostatic problems. Because all of the superconductivity cases that are considered here are free of electrostatic charge, the electric field energy U_E is zero and this term is not included in the functionals of this work. After the augmentation of the Ginzburg-Landau variational functional by the London gauge constraint is complete, the two material parameters α and β of the Landau expansion are determined as functions of the effective penetration depth λ_{eff} and the critical magnetic field $\mathbf{B}_c$ of a superconducting material.

Conventional thermal field variational functionals are then used to describe the thermal energy of the EM systems under consideration. The temperature dependence of material parameters is also developed for conductors in both the superconducting and normal states.

This modeling work completes the necessary background for the development of EM finite elements that are thermally and quantum phase

coupled. Elements and solution procedures are then developed. The most significant features of the finite elements are:

1. The normal element has the ability to predict current densities with a high degree of accuracy.

2. The superconducting element has the ability to show the current density distribution in much greater detail than ever before. The significance of this feature is that if the Ginzburg-Landau model of superconductivity is correct, there is a greater understanding of the physics that occur within a superconductor.

3. A nonlinear superconducting finite element that does not require path following procedures to determine equilibrium states if the correct reference state and mesh are chosen.

4. A superconducting finite element that also is rapidly convergent upon a solution, well conditioned and, as far as the author has been able to determine, generally convergent upon the equilibrium solution provided the correct reference state and mesh have been selected.

5. The combined use of the thermal, normal, and superconducting elements provides for a comprehensive program that can analyze any physical equilibrium state of a conductor except for the mixed normal/superconducting state. Appropriate modifictions to allow for the modeling of this state are also suggested.

6. Finite element models that can model any EM media provided that the thermal and EM properties of the medium are known.

7. Finite element models that are modular and employ standard linear and nonlinear assembly, scaling, and solution techniques.

8. Finite element models that require no special boundary treatment for adjacent elements that possess differing EM or thermal properties.

9. EM finite elements that can predict electric and magnetic fields with a high degree of accuracy.

10. EM Finite elements that require fewer degrees of freedom for the analysis of two and three-dimensional field problems than the conventional field based finite elements currently in use.

12.2 DIRECTIONS FOR FURTHER RESEARCH.

The focus of this work is upon the analysis of magnetostatic EM field problems. These cover a significant but small part of the range of EM field problems that are of interest to scientists and engineers. The ready extension of the four-potential variational principle to a wide range of EM field problems provides a powerful tool for the solution of difficult EM problems.

An unsolved problem of most interest to the author is the one where normal and superconducting state coexist near the transition state. A realistic treatment of this problem requires two- and three-dimensional space discretization and consequently follows outside the scope of this work. To extend the present work to that problem, a multidimensional adaptive mesh appears to be necessary to determine the interface between normal and superconducting portions of a conductor as well as to improve the conditioning of the tangent stiffness matrix.

Another direction that scientific research can take from the results of this work is experimental verification of these results. This verification would

add considerably more evidence for the validity of the Ginzburg-Landau theory of superconductivity as well as a greater understanding of superconductivity in general. Even without this verification, the results herein that compare the current density to a low viscosity fluid stream might be applied to the analysis and eventual development of a model of high temperature superconductivity.

Other problems of active interest to the engineering community are dynamical in nature. These problems include the analysis of time-dependent EM waves moving through fixed (static) EM media, as well as EM media coupled with rapid mechanical motions. These problems are highly comples, but the general applicability of the four-potential method to EM problems in general appears to be well suited for the numerical treatment of these problems.

Finally, the thermal functionals that are used to analyze the temperature distribution within the conductor are adequate for the relatively minor loadings and changes of loadings that are presented here. A direction of further research that the author has already undertaken is the development of thermal finite elements that are nonlinear in nature. These elements allow the thermal conductivity k and the electrical resistivity ω to be functions of the temperature T rather than the spatial coordinates. It is hoped that these elements will permit a more accurate analysis of the temperature distribution within a normal conductor and allow larger "steps" to be taken with solution path following techniques.

In conclusion, the EM finite elements that are presented here have performed well and confirmed the ability of the four-potential variational

principle to solve a range of problems. The author believes that this method-ology is relatively simple to use and exhibits key advantages over current field based formulations. Potential based formulations and variational principles show promise for the treatment of unsolved EM problems and should both be given due consideration over field-based formulations.

REFERENCES

1. Schuler, J., and Felippa, C., "Electromagnetic Axisymmetric Finite Elements Based on a Gauged Four-Potential Variational Principle", *Computing Systems in Engineering*, 1990, 1, pp. 273-284

2. Felippa, C. A. and T. L. Geers, "Partitioned Analysis of Coupled Mechanical Systems," *Engineering Computations*, 5, 1988, pp. 123-133

3. Park, K. C. and C. A. Felippa, "Partitioned Analysis of Coupled Systems," Chapter 3 in *Computational Methods for Transient Analysis*, ed. by T. Belytschko and T. J. R. Hughes, North-Holland, Amsterdam–New York, 1983

4. Felippa, C. A.,, "The Extended Free Formulation of Finite Elements in Linear Elasticity," *Journal of Applied Mechanics*, 56, 3, 1989, pp. 609–616

5. Felippa, C. A. and C. Militello, "Developments in Variational Methods for High-Performance Plate and Shell Elements," in *Analytical and Computational Models for Shells*, CED Vol. 3, ed. by A. K. Noor, T. Belytschko and J. C. Simo, The American Society of Mechanical Engineers, ASME, New York, 1989, pp. 191-216

6. Felippa, C. A. and C. Militello, "The Variational Formulation of High-Performance Finite Elements: Parametrized Variational Principles," (with C. Militello), *Computers & Structures*, 36, 1990, pp. 1-11

7. Militello, C. and C. A. Felippa, "A Variational Justification of the Assumed Natural Strain Formulation of Finite Elements: I. Variational Principles," (with C. Militello), *Computers & Structures*, 34, 1990, pp. 431-438

8. Militello, C. and C. A. Felippa, "A Variational Justification of the Assumed Natural Strain Formulation of Finite Elements: II. The C^0 4-Node Plate Element," *Computers & Structures*, 34, 1990, pp. 439-444

9. Farhat, C. and Park, K.C., "An Unconditionally Stable Staggered Algorithm for Transient Finite Element Analysis of Coupled Thermoelastic Problems", *Computer Methods in Applied Mechanics and Engineering*, 85, 1991, pp. 349-365

10. Davies, J. B., "The Finite Element Method," Chapter 2 in *Numerical Techniques for Microwave and Millimeter-Wave Passive Structures*, ed. by T. Itoh, Wiley, New York, 1989

11. Trowbridge, C. W., "Numerical Solution of Electromagnetic Field Problems in Two and Three Dimensions," Chapter 18 in *Numerical Methods in Coupled Problems*, ed. by R. Lewis *et.al.*, Wiley, London, 1984

12. Jackson, J. D., *Classical Electrodynamics*, 2nd. ed, Wiley, New York, 1975

13. Mosig, J. R., "Integral Equation Technique", Chapter 3 in *Numerical Techniques for Microwave and Millimeter-Wave Passive Structures*, ed. by T. Itoh, Wiley, New York, 1989

14. Grant, I.S. and Phillips, W. R., *Electromagnetism*, Wiley, New York, 1984

15. Baird, D.C. and Mukherjee, B. K., "Destruction of Superconductivity by a Current", *Physics Letters*, **25A**, 1967, pp. 137-138

16. Mukherjee, B. K., Allen, J. F. and Baird, D.C., "Destruction of Superconductivity by a Current", *Proceedings of the 11th. International Conference on Low Temperature Physics*, University of St. Andrews, Physics Dept., St. Andrews, Scotland, 1967, pp. 827-830

17. Yuan, K.-Y., Moon, F. C. and Abel, J. F., "Elastic Conducting Structures in Pulsed Magnetic Fields", Chapter 19 in *Numerical Methods in Coupled Problems*, ed. by R. Lewis *et.al.*, Wiley, London, 1984

18. Bossavit, A., "Solving Maxwell Equations in a Closed Cavity, and the Question of 'Spurious Modes'", *IEEE Transactions on Magnetics*, **26**, 1990, pp. 702-705

19. Gelfand, I. M. and Fomin, S. V., *Calculus of Variations*, Prentice-Hall, Englewood Cliffs, N. J., 1963

20. Yourgrau, W., and Mandelstam, S., *Variational Principles in Dynamics and Quantum Theory*, Dover Publications, Inc., New York, 1968

21. Tinkham, M., *Introduction to Superconductivity*, Krieger Pub. Co., Malabar, Florida, 1975

22. Felippa, C. A. and Ohayon, R., "Treatment of Coupled Fluid-Structure Interaction Problems by a Mixed Variational Principle," *Proceedings 7th International Conference on Finite Element Methods in Fluids*, ed. by T. J. Chung *et.al.*, University of Alabama Press, Huntsville, Alabama, April 1989, pp. 555-563

23. Felippa, C. A. and Ohayon, R., "Mixed Variational Formulation of Finite Element Analysis of Acousto-Elastic Fluid-Structure Interaction," *Journal of Fluids & Structures*, 1990, 4, pp. 35-37

24. Wilson, Edward L., and Nickell, Robert E., "Application of the Finite Element Method to Heat Conduction Analysis", *Nuclear Engineering and Design*, 1966, 4, pp. 276-286.

25. Schuler, James J., "Infinite Axisymmetric Elements for Electromagnetostatics", *Term Projects in Advanced Finite Element Methods*, Felippa, C. A., ed., May 1990, Vol. II.

26. Eyges, L., *The Classical Electromagnetic Field*, Dover, New York, 1980

27. Rojanski, V., *The Electromagnetic Field*, Dover, New York, 1979

28. Shadowitz, A., *The Electromagnetic Field*, Dover, New York, 1975

29. Lorentz, H. A., *Theory of Electrons*, 2nd. ed, Dover, New York, 1952

30. Lanczos, C., *The Variational Principles of Mechanics*, Univ. of Toronto Press, Toronto, 1949

31. Kittel, C., *Introduction to Solid State Physics*, 6th. ed, Wiley, New York, 1986

32. Schuler, J., and Felippa, C., "Analysis of Superconducting Electromagnteic Finite Elements Based on a Magnetic Vector Variational Principle", CSSC report CU-CSSC-91-28, October 1991

33. Incropera, Frank P., and De Witt, David P., *Fundamentals of Heat and Mass Transfer*, Wiley, New York, 1985

34. Serway, Raymond A., *Physics for Scientists and Engineers*, Saunders College Publishing, New York, 1983

REPORT DOCUMENTATION PAGE

1. AGENCY USE ONLY (Leave blank)	2. REPORT DATE	3. REPORT TYPE AND DATES COVERED
	January 1996	Final Contractor Report

4. TITLE AND SUBTITLE

Coupled Structural, Thermal, Phase-Change and Electromagnetic Analysis for Superconductors, Volume II

5. FUNDING NUMBERS

WU–505–10–11
G–NAG3–934

6. AUTHOR(S)

C.A. Felippa, C. Farhat, K.C. Park, C. Militello, and J.J. Schuler

7. PERFORMING ORGANIZATION NAME(S) AND ADDRESS(ES)

College of Engineering
University of Colorado
Campus Box 429
Boulder, Colorado 80309

8. PERFORMING ORGANIZATION REPORT NUMBER

E–8471–1

9. SPONSORING/MONITORING AGENCY NAME(S) AND ADDRESS(ES)

National Aeronautics and Space Administration
Lewis Research Center
Cleveland, Ohio 44135–3191

10. SPONSORING/MONITORING AGENCY REPORT NUMBER

NASA CR–194457
CU–CSSC–93–06–II

11. SUPPLEMENTARY NOTES

12a. DISTRIBUTION/AVAILABILITY STATEMENT

Unclassified - Unlimited
Subject Category 39

This publication is available from the NASA Center for Aerospace Information, (301) 621–0390.

12b. DISTRIBUTION CODE

13. ABSTRACT (Maximum 200 words)

Described are the theoretical development and computer implementation of reliable and efficient methods for the analysis of coupled mechanical problems that involve the interaction of mechanical, thermal, phase-change and electromagnetic subproblems. The focus application has been the modeling of superconductivity and associated quantum-state phase-change phenomena. In support of this objective the work has addressed the following issues: (1) development of variational principles for finite elements, (2) finite element modeling of the electromagnetic problem, (3) coupling of thermal and mechanical effects, and (4) computer implementation and solution of the superconductivity transition problem. The main accomplishments have been: (1) the development of the theory of parametrized and gauged variational principles, (2) the application of those principled to the construction of electromagnetic, thermal and mechanical finite elements, and (3) the coupling of electromagnetic finite elements with thermal and superconducting effects, and (4) the first detailed finite element simulations of bulk superconductors, in particular the Meissner effect and the nature of the normal conducting boundary layer. The theoretical development is described in two volumes. Volume I describes mostly formulations for specific problems. Volume II describes generalization of those formulations.

14. SUBJECT TERMS

Superconductivity; Coupled descriptions; Phase change; Mechanical; Thermal electromagnetic; Finite elements; Computer codes; Solution methods

15. NUMBER OF PAGES

279

16. PRICE CODE

A13

17. SECURITY CLASSIFICATION OF REPORT	18. SECURITY CLASSIFICATION OF THIS PAGE	19. SECURITY CLASSIFICATION OF ABSTRACT	20. LIMITATION OF ABSTRACT
Unclassified	Unclassified	Unclassified	

35. Morse, Philip M., *Thermal Physics*, The Benjamin/Cummings Publishing Co., Inc., Reading, Mass., 1969

36. Touloukian, Y.S., Powell, R. W., Ho, C.Y., and Klemens, P. G., *Thermophysical Properties of Matter*, Vol. 1, Plenum Publishing Co., New York, N.Y., 1970

37. Blatt, Frank J., *Physics of Electronic Conduction in Solids*, McGraw-Hill Book Co., New York, 1968

38. Doss, James D., *Engineer's Guide to High-Temperature Superconductivity*, Wiley, New York, 1989

39. Meaden, George Terence, *Electrical Resistance of Metals*, Plenum Press, New York, 1965

40. Boorse, H.A., and Niewodniczanski, H., "The Electrical Resistance of Aluminum at Low Temperatures", *Proceedings of the Royal Society of London*, SeriesA, 1936, 879, pp. 463-475

41. *Handbook of Mathematical Functions*, ed. by Milton Abramowitz and Irene A. Stegun, U.S. Dept. of Commerce, National Bureau of Standards, Washington, D.C., 1965

42. Lynton, E.A., *Superconductivity*, Methuen & Co. Ltd., London, 1969

43. Purcell, Edward M., *Electricity and Magnetism*, Vol. 2, McGraw-Hill Book Co., New York, 1985

National Aeronautics and
Space Administration

Lewis Research Center
21000 Brookpark Rd.
Cleveland, OH 44135-3191